Université du Québec
Institut National de la Recherche Scientifique
Centre Énergie, Matériaux et Télécommunications

Engineered semiconducting nanomaterials for photovoltaic applications

Par

Daniele Benetti

Thèse présentée pour l'obtention du grade

de Philosophiae Doctor (Ph.D.)

en sciences de l'énergie et des matériaux

Jury d'évaluation

Président du jury et examinateur interne	Prof. Shuhui Sun INRS-EMT, Université du Québec
Examinateur externe	Prof. Rafik Naccache Concordia University
Examinateur externe	Prof. Clara Santato Polytechnique Montréal
Directeur de recherche	Prof. Federico Rosei INRS-EMT, Université du Québec

ACKNOWLEDGMENTS

The research effort behind this thesis is not a single-man work. Therefore, I would like to acknowledge those people who had, in different ways, contributed to its construction.

I want to express my deep gratitude to my research advisor Prof. Federico Rosei. Federico not only helped me with suggestion on my research projects but also provide me with trust, freedom and encouragement to let me explore and try my own ideas. I have grown a lot, as scientist and as a person, under your supervision, and I have learned from your dedication, leadership and scientific insight. As you always say, LC!

I must also acknowledge the great support of my other scientific mentors, now professors around the world, Prof. Alberto Vomiero and Prof. Haiguang Zhao. My gratitude goes to you for all the precious suggestions, time spent and availability shown in these years.

I would like also to thanks all my colleagues in NanoFemtoLab. Working with you and learning from you has been a privilege. I am sure I will read about the amazing research you will do in the future, and I hope I'll be lucky enough to cross your path again. Special thanks to Yufeng for the long and stimulating discussions.

Thank you also to all the friends I met in Montreal and around the world: Gianluca, Fabrizio, Luca, Marija, Giacomo, Ahlem Z., Azza, Hela, Samira, Lei, Zeyneb and many more. A particular thanks to Artiom and Riccardo: for the time spent together, the many coffee breaks and for your support during the up and down times of this 'PhD journey'.

I am also grateful to my family and friends in Italy, Stefano and Davide, for all the support they gave me during this period.

Last but not least, thank you Ahlem for the time, patience and precious support you always give me.

RÉSUMÉ

Pour réduire notre dépendance de combustibles fossiles et contrôler les émissions de gaz à effet de serre, il est nécessaire de passer à des sources d'énergie plus durables. Ce défi peut être relevé par les cellules solaires dites de troisième génération. Au cours de la dernière décennie, ces dispositifs se sont rapidement améliorés en matière d'efficacité de photoconversion et sont devenus l'une des alternatives les plus rentables par rapport aux cellules de silicium disponibles sur le marché, grâce à la disponibilité des matériaux et des processus de fabrication simples et peu coûteux.

Cette thèse explore principalement les interactions entre les matériaux semi-conducteurs et comment leurs propriétés peuvent être contrôlées, en appliquant des modulations appropriées des interfaces des nanomatériaux. Plus précisément, ce travail se focalise sur l'étude de trois types de cellules solaires : à colorant (DSSC), à points quantiques (QDSC) et celles à perovskite (PSC) allons des études fondamentales de l'alignement énergétique de la bande et de la dynamique des porteurs dans les points quantiques de chalcogénure métallique composite (QD) jusqu'à la réalisation de dispositifs pleinement opérationnels, avec des couches d'interface modifiées afin de réduire la recombinaison porteuse et améliorer la collecte et donc le rendement final et la stabilité. Une nouvelle photo anode pour DSSC est présentée. Un composite de nanotubes de carbone fonctionnalisés à parois multiples (F-MWCNTs) et de TiO_2 est utilisé comme photo anodes et le rôle du F-MWCNTS dans le transfert de charge sont étudiés. De l'autre côté, le film mince commun coûteux en Pt CE en DSSC est remplacé par un CE nanostructuré à faible coût fait de nanofibres creuses en Pt/Pd d'alliage sont proposées. Là CE produite est non seulement moins chère, mais aussi plus performante. En QDSC, la modulation de l'injection de charge peut être réalisée en choisissant correctement la composition des QDs. Cependant, on manque encore d'études sur la dynamique de charge et la structure locale de la bande électronique dans les objets à l'échelle quantique nanométrique directement développée sur des substrats. Pour cette raison, dans ce travail, nous étudions les propriétés électriques de chaque QD de chalcogénure métallique de tailles différentes sur un matériau semblable au graphème en utilisant une technique avancée telle que la microscopie à force de sonde Kelvin (KPFM). Les PSC avec structure p-i-n inversée sont également fabriqués. Le PEDOT: PSS HTL commun est remplacé par un HTL hybride basé sur un composite d'oxyde de graphène (OG) et de points de carbone (Cdots). La présence de Cdots résout le problème d'OG comme goulot d'étranglement pour l'extraction des trous de la couche de pérovskite. La contribution des Cdots pour améliorer la performance finale a été étudiée.

Mots-clés : Recombinaison de charge ; Collecte de charge ; Cellules solaires sensibilisées aux colorants (DSSC); Cellules solaires à points quantiques (QDSC); Cellules solaires à perovskite (PSC); Microscopie à force de sonde Kelvin (KPFM); Spectroscopie d'impédance électrochimique (EIS); Points de carbone; couche de transport de charges

ABSTRACT

To reduce our dependence on fossil fuels and control the greenhouse emissions, it is necessary to transit to more sustainable sources of energy. This challenge may be addressed by the so-called 3rd generation solar cells. In the last decade, these devices have rapidly improved in terms of photoconversion efficiency and became one of the most cost-effective alternatives to the commercial available silicon cells, due to simple, low-cost materials and fabrication process. This thesis explores how semiconducting materials interact with each other and how, by applying suitable modulations of the interfaces of nanomaterials, we can control proprieties, such as charge injection and light management, in order to improve the final performances of the device. Specifically, this work focuses on Dye Sensitized Solar Cells (DSSCs), Quantum Dots Solar Cells (QDSCs) and Perovskite Solar Cells (PSCs) starting from fundamental studies of band energy alignment and carrier dynamics in composite metal chalcogenide quantum dots (QDs) up to realizing full operational devices, with modified interface layers in order to reduce the carrier recombination and improving the charge collection and thus the final efficiency and stability.

A new photoanode for DSSC is presented. A composite of functionalized multi-wall carbon nanotubes (F-MWCNTs) and TiO_2 is used as photoanodes and the role of F-MWCNTS in the charge transfer is investigated. On the other side, the common expensive Pt thin film CE in DSSC is replaced with a low-cost nanostructured CE made of hollow nanofibers of an alloy Pt/Pd is proposed. The CE produced is not only cheaper but also shows improved performance.

In QDSC, the modulation of charge injection can be realized by properly choosing the composition of the QDs. However, there is still a lack of studies on the charge dynamics and the local electronic band structure in quantum-confined nanoscale objects directly grown on substrates. For this reason in this work it is investigated the electrical properties of individual metal chalcogenide QDs with different size on graphene-like material by using an advanced technique such as Kelvin Probe Force Microscopy (KPFM).

PSC with inverted p-i-n structure are also fabricated. The common PEDOT:PSS HTL is replaced with an hybrid HTL based on a composite of Graphene Oxide (GO) and carbon dots. The presence of carbon dots addresses the issue of GO acting as bottleneck for the extraction of holes from the perovskite layer. The contribution of Cdots to the enhancement of the final performance is investigated.

Keywords :Charge recombination ; Charge collection ; Dye Sensitized Solar Cells (DSSCs); Quantum Dots Solar Cells (QDSCs); Perovskite Solar Cells (PSCs); Kelvin Probe Force Microscopy (KPFM); Electrochemical Impedance Spectroscopy (EIS); Carbon Dots; Charge transport layer

SOMMAIRE RÉCAPITULATIF

1. Introduction

La consommation mondiale d'énergie augmente chaque année et les ressources limitées en combustibles fossiles nécessitent le développement de ressources énergétiques renouvelables. Actuellement, plus de 85 % des besoins énergétiques mondiaux sont couverts par les combustibles fossiles, ce qui accélère le réchauffement climatique et entraîne des effets délétères sur notre environnement.[1] Même si les réserves estimées de combustibles fossiles varient de 150 à 400 ans de production mondiale au rythme actuel pour le charbon, de 40 à 80 ans pour le pétrole et de 60 à 160 ans pour le gaz naturel, leur impact sur l'environnement est très préoccupant.[2] En particulier, la principale préoccupation concerne l'émission de gaz à effet de serre, tels que le dioxyde de carbone (CO2), et sa contribution au réchauffement climatique.

Au cours des 60 dernières années, la concentration de CO_2 dans l'atmosphère est passée d'environ 280 parties par million (ppm) à 404 ppm en 2018.[1] Depuis 1920, les émissions provenant des combustibles fossiles représentent la principale source d'émissions anthropiques dans l'atmosphère et leur part relative n'a cessé d'augmenter jusqu'à présent. Selon l'International Panel on Climate Change (IPCC), il y a 50 % de chances de stabiliser la température moyenne de la planète à une augmentation de 2 °C par rapport à la période préindustrielle si les concentrations de CO_2 sont maintenues en dessous de 450 ppm.[1] Si le changement de température peut être limité à moins de 2 °C, il y a de bonnes chances que la société puisse s'adapter.

Les décisions économiques et politiques qui seront prises au cours des 20 prochaines années quant à l'énergie seront cruciales pour maintenir le niveau de CO_2 en dessous du seuil critique de 450 ppm. En fait, pour réduire notre dépendance à l'égard des combustibles fossiles et contrôler les émissions de gaz à effet de serre, il est nécessaire de passer d'une production d'énergie à base de combustibles fossiles à des sources d'énergie plus durables. Jusqu'à présent, l'adoption de ressources nouvelles et respectueuses de l'environnement a été principalement déterminée par des considérations économiques plutôt que par des obstacles technologiques. C'est pourquoi il est important, en tant que scientifiques et ingénieurs, de développer de nouvelles technologies dont le coût et l'impact environnemental seront pris en compte, afin d'offrir des solutions à la fois économiques et écologiques et ainsi, ouvrir la voie à une adoption rapide de celles-ci.

Parmi toutes les énergies renouvelables vertes (éolienne, biomasse, chaleur et hydroélectricité), l'énergie solaire est la seule source ayant le potentiel de satisfaire tous nos besoins énergétiques. Chaque heure, le rayonnement provenant du soleil serait suffisant pour alimenter la planète entière pendant un an. Il a été

estimé que couvrir 0,1% de la surface de la terre avec des cellules solaires d'une efficacité de 10%, correspondant à 1% des zones désertiques ou 20% de la surface des bâtiments et des routes, permettrait de couvrir la consommation mondiale en électricité. Évidemment, ce modèle n'est pas durable, mais les futures infrastructures énergétiques seront plutôt une combinaison de différentes sources d'énergie, au sein desquelles le PV jouera certes un rôle majeur mais ne sera pas le seul contributeur.

Depuis 2008, le marché du photovoltaïque (PV) connaît une croissance exponentielle : en 2008, la capacité globale du PV était d'environ 15GW, aujourd'hui celle-ci atteint plus de 500GW. [2] Le marché des cellules solaires est aujourd'hui l'un des marchés ayant la croissance la plus rapide et il est clair qu'il ne s'agit plus seulement d'un marché de niche mais constitue bel et bien une part de la production énergétique mondiale.

Cependant, l'énergie électrique produite par le PV n'est toujours pas en mesure de concurrencer le prix de l'électricité produite par des systèmes plus conventionnels et, jusqu'à présent, elle a été subventionnée par des incitations gouvernementales afin de rendre ses coûts plus compétitifs. Dans ce cadre, la recherche de dispositifs PV plus efficaces et moins coûteux joue un rôle essentiel pour ouvrir la voie à leur distribution mondiale.

Afin d'être compétitives sur le marché avec un prix par watt similaire à celui des appareils en silicium, les cellules solaires dites de troisième génération doivent encore être améliorées sur le plan des performances et de la stabilité. Indépendamment de l'architecture, toutes les cellules solaires nanostructurées sont confrontées au problème de la recombinaison des charges et des collectes. En général, pour tout dispositif dans lequel se produit la génération de photocopieurs, il est nécessaire que ces charges (excitons) atteignent, par dérive, par diffusion ou par combinaison des deux mécanismes, l'interface de séparation des charges sans recombinaison.

Afin d'avoir des cellules solaires à haut rendement, l'un des points clés est de supprimer (ou de réduire autant que possible) les voies de recombinaison et d'améliorer l'injection et le transport de la charge du matériau absorbant vers les électrodes. En effet, même s'il est possible de concevoir des matériaux organiques ou inorganiques avec une plage d'absorption qui s’étend vers de plus grandes longueurs d'onde, si le dispositif solaire présente des voies de recombinaison élevées, l'efficacité s’en trouvera limitée. De plus, dans la plupart des cas, l'appareil présente également une stabilité réduite due par exemple à la photo oxydation de l'absorbeur.

Différentes stratégies peuvent être mises en œuvre afin d’améliorer ces interfaces, résoudre la question de la recombinaison des charges et améliorer la collecte des charges. En particulier, les couches de transport de charge (CTL), telles que la couche de transport d'électrons (ETL) et la couche de transport de trous

(HTL), peuvent jouer un rôle fondamental dans le transfert de charge de l'absorbeur à l'électrode et agir comme contacts sélectifs des porteurs.

2. Objectifs

Dans ce travail, ces questions seront abordées sous différents angles, en partant des études fondamentales sur l'alignement de la bande d'énergie et de la dynamique des porteurs dans les points quantiques (QDs) d'un composite de chalcogénure métallique jusqu'à la réalisation de dispositifs opérationnels complets, tels que DSSC et PSC, avec des couches d'interface modifiées afin de réduire la recombinaison des porteurs et améliorer la collecte de charge et donc le rendement final et la stabilité.

Sur le DSSC, j'ai concentré mon attention sur deux différents composants du DSSC : la photoanode et la contre-électrode (CE). Ce dernier constitue l'un des composants les plus chers du DSSC car il est généralement fabriqué à base de platine (Pt). Afin de réduire la quantité de Pt utilisée tout en améliorant l'efficacité finale de la cellule, nous envions un CE nanostructuré fait de nanofibres creuses déposées par une méthode simple et économique comme l'électrofilage. Ces résultats peuvent aider à adapter la structure générale de la CE dans les systèmes photoélectrochimiques afin de renforcer leurs propriétés fonctionnelles, et ce, grâce aux avantages offerts par cette morphologie.

En ce qui concerne l'autre composant principal du DSSC, en l'occurrence, la photoanode, l'incorporation de nanostructures de carbone à faible dimension telles que les nanotubes de carbone (CNT) et les feuilles de graphène dans les électrodes semi-conductrices a récemment été proposée pour améliorer la collecte et la performance des charges des DSSC. Toutefois, la contribution de ces matériaux quant à l'amélioration de l'PCE n'est pas encore bien comprise. C'est pourquoi j'ai décidé d'étudier systématiquement le rôle des nanotubes de carbone multi-parois fonctionnalisés (F-MWCNTs) dans une photoanode TiO_2.

Les QD de chalcogénure de métal comptent parmi les matériaux les plus prometteurs en tant que récolteurs de lumière dans les systèmes entièrement inorganiques utilisés dans le cadre d'applications dans les cellules solaires et la production de combustibles solaires. Cependant, peu d'études ont été conduites sur la dynamique de charge et la structure locale de la bande électronique dans les objets à l'échelle nanométrique quantique directement cultivés sur des substrats. J'ai donc décidé d'étudier les propriétés électriques de chaque QD de chalcogénure métallique de taille et de composition différentes, cultivées par absorption et réaction de couches ioniques successives (SILAR) sur un matériau de type graphène en utilisant une technique avancée comme la microscopie à force de sonde Kelvin (KPFM). Les résultats obtenus aideront à concevoir des dispositifs solaires à base de QDs avec injection et collecte de charge améliorées.

Tout en travaillant sur les nanotubes de carbone et les matériaux à base de graphène pour développer des photoanodes composites, je me suis également intéressé, comme dernière contribution, à la famille des

nano-allotropes de carbone : les points de carbone (Cdots). Bien que les Cdots aient été principalement utilisés dans des applications biomédicales, dans le cadre de cette étude, je suis en train de développer de nouveaux points de carbone en mettant l'accent sur des applications tournant autour l'énergie solaire. En particulier, j'étudie leur mécanisme de transfert de charge pour les utiliser comme CTL ou absorbeur dans les cellules solaires. Grâce à une bourse du Conseil de recherches en sciences naturelles et en génie du Canada (CRSNG), j'ai pu collaborer en 2017 avec le professeur Diau à la National Chiao Tung University (NCTU) de Taiwan. Avec son groupe, je me suis concentré sur le développement d'un nouveau HTL à faible coût, à haut rendement et vert pour les cellules solaires en pérovskite à base de Cdots.

3. Améliorer la collecte des charges et leur transport dans les photoanodes DSSC

Bien que les photo-anodes mésoporeuses offrent de bonnes performances, en grande partie grâce à la récolte de la lumière du film nanocristallin sensibilisé au colorant, celles-ci présentent toutefois quelques inconvénients : tout en offrant une surface spécifique extrêmement élevée pour la charge de colorant, les réseaux méso-poreux souffrent d'une densité élevée des limites des grains, ce qui favorise la recombinaison de charge dans les dispositifs opérationnels.

Différentes stratégies ont été proposées pour accroître la collecte des charges, telles que l'utilisation de divers semi-conducteurs d'oxyde métallique, en particulier des nanostructures unidimensionnelles (1D) comme les nanorods (NR),[163, 164] nanofils (NWs)[165-167] et nanotubes (NTs)[168-171] à électrodes basées. Parmi ces différentes nanostructures 1D, celles à base de carbone sont particulièrement intéressantes. Depuis leur découverte en 1991,[172] les NTC ont joué un rôle important dans le développement de technologies énergétiques alternatives propres et durables, [173] en raison de leurs extraordinaires propriétés électroniques et mécaniques.[174] L'incorporation de nanostructures de carbone de faible dimension telles que les NTC [56, 175, 176]et les feuilles de graphène[177,178, 179] dans les électrodes semi-conductrices a récemment été proposée pour améliorer la collecte de charge et la performance PV des DSSCs. Il a été prouvé que les NTC 1D peuvent améliorer le transport des électrons à l'intérieur des DSSC à base de TiO_2.[55] Ils peuvent être utilisés en combinaison avec le TiO_2 grâce au bon alignement de la bande électronique avec le TiO_2 et le verre conducteur FTO (**voir Figure 3.1**), offrant une voie plus efficace pour le prélèvement et le transport des électrons photo-générés. Cependant, en raison de leur grande surface spécifique, les NTC ont tendance à s'agglomérer en faisceaux, ce qui réduit la solubilité dans la plupart des solvants, et par conséquent pourrait réduire la capacité de dispersion lorsqu'ils sont mélangés avec du TiO_2.[180] Une dispersion non homogène des NTC dans la pâte de TiO_2 pourrait annuler leurs effets bénéfiques. Par conséquent, la capacité à disperser les NTC de façon homogène à l'intérieur de la matrice TiO_2, ainsi que la capacité à produire une

forte interaction interfaciale, sont des défis clés pour maximiser la contribution des NTC à leur application dans les DSSC. [176]

Afin d'améliorer l'interaction interfaciale avec l'oxyde métallique, l'une des méthodes possibles consiste à introduire des groupes fonctionnels à la surface des matériaux carbonés par un traitement acide. Un des inconvénients est la possibilité d'introduire des défauts à la surface du graphène ou des NTC. C'est la principale raison pour laquelle il n'a pas été possible de traiter les plaquettes de graphène sans les dégrader, alors que les NTC, nanostructures multi-parois, ne sont que peu affectées (**Figure 3.1 d-g**). Par conséquent, la quantité de matière qui peut être introduite dans la photoanode avant d'avoir une dégradation mécanique et électrique peut être fortement augmentée dans le cas des nanotubes à parois multiples fonctionnalisés (F-MWCTNs).

En particulier, l'introduction de groupes carboxyliques à la surface des NTC pourrait intensifier les interactions avec le TiO_2 en augmentant leur dispersibilité dans la matrice d'oxyde de titane, évitant ainsi la formation de fissures même à des charges élevées (les fissures commencent à apparaître autour de 3,5 % en poids). De cette façon, nous avons pu étudier les effets des F-MWCNT dans une large gamme de concentrations, jusqu'à 4 % en poids. À titre de comparaison, dans des études antérieures, la plage de concentration n'était que de 0,2 à 0,3 % en poids (% en poids) en raison de la dispersibilité moindre des NTC non fonctionnalisés qui cause des fissures dans le TiO_2 à partir de 0,25 % en poids.

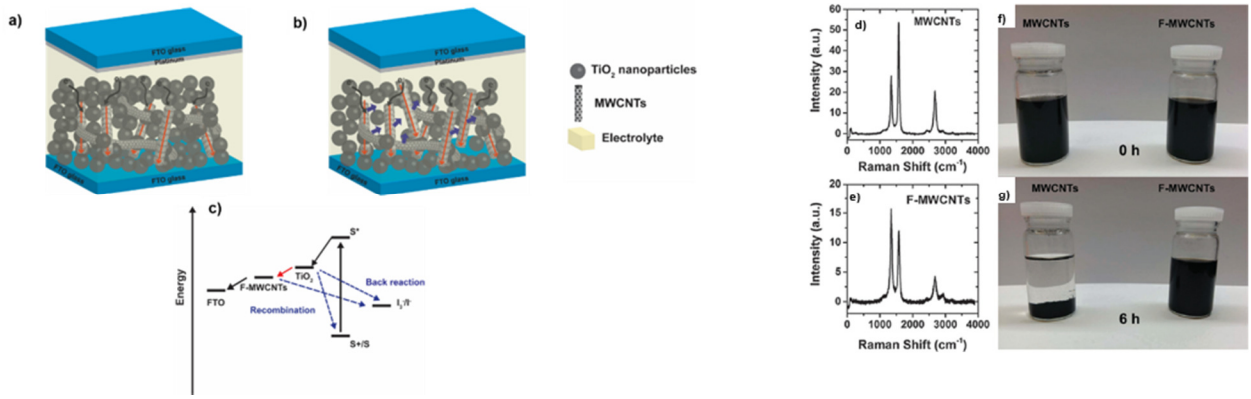

Figure 3.1a) Illustration schématique du concept d'amélioration de la collecte des charges dans une photo-anode basée sur un système composite avec des NTC intégrés dans une structure mésoporeuse en TiO2. (b) À une concentration élevée de F-MWCNT, l'agglomération de F-MWCNT permet un contact direct entre les F-MWCNT et l'électrolyte, ajoutant ainsi une nouvelle voie de recombinaison (flèches bleues) (c) Schéma du diagramme en bande électronique du DSSC fonctionnalisé avec les CNT.Spectre Raman des (a) MWCNT et (b) F-MWCNT. Aux points (c) et (d), on signale une dispersion des MWCNT et des F-MWCNT dans une solution d'éthanol à 0 h et après 6 h, respectivement.

Propriétés fonctionnelles des DSSC

Nous avons étudié l'effet des différentes charges de F-MWCNT sur les propriétés fonctionnelles des DSSC. Les courbes de tension de densité de courant (J-V) de certaines cellules sous la lumière solaire simulée AM 1.5G et l'efficacité quantique externe (EQE) sont présentées à la **figure 3.2** a et b.

Les DSSC à base de F-MWCNTs/TiO_2 avec une concentration allant jusqu'à 2 % en poids montrent une PCE supérieure à celle du TiO_2 nu. À la concentration optimale de 2 % en poids, nous avons obtenu une augmentation maximale résultant en une PCE aussi élevée que 7,95 %, avec une augmentation d'environ 30 % par rapport au TiO_2 pur (6,05 %). La présence de F-MWCNTs dans la plage de concentration allant jusqu'à 2 % en poids augmente significativement Jsc par rapport aux photoanodes en TiO_2 pur, alors que les autres paramètres cellulaires (Voc, FF) ne jouent pas un rôle majeur dans la modification de PCE.

Afin d'étudier et de mieux comprendre les changements induits par la présence de F-MWCNT sur les processus physiques et chimiques qui ont lieu dans l'appareil de commande, l'EIS a été réalisée. En particulier, pour les dispositifs DSSC, il est important de se concentrer sur la résistance de recombinaison R_{rec} et la capacité chimique C_{μ}, qui peuvent donner une indication des processus de recombinaison se produisant dans le film. Afin de mieux comprendre la résistance de recombinaison, R_{rec} peut être analysé en fonction de la tension de polarisation.[193,195,196] Dans la **figure 3.2 d**, dans la région des faibles potentiels (jusqu'à 550 mV), où la principale contribution provient du transfert de charge du substrat FTO non couvert au fond du film poreux (également appelé couche arrière)[44], la résistance suit la même tendance que l'efficacité : R_{rec} augmente de 0 % à 2 % en poids, alors qu'il diminue de nouveau à des concentrations plus élevées de F-MWCNT. L'augmentation de la quantité de F-MWCNT entraîne une diminution de R_{rec} associée à la réaction inverse. Ce type de comportement peut être dû à des agglomérations locales de F-MWCNT qui peuvent, à leur tour, créer des pièges et des défauts de surface. En outre, à des concentrations élevées de F-MWCNT, lorsque des agglomérations se forment, un contact direct entre les F-MWCNT et l'électrolyte peut se produire, ce qui augmente la perte d'électrons directement des F-MWCNT à l'électrolyte, réduisant encore plus R_{rec}.

Une confirmation de la présence de défauts de surface est présentée à la **Figure 3.2 e**, qui illustre la capacité chimique en fonction du biais appliqué. Les échantillons présentant des concentrations élevées de F-MWCNT (3 % en poids et 4 % en poids) présentent un pic autour de 750 mV. Ce pic est associé à des états sous-localisés en raison de défauts à la surface, ce qui entraîne une diminution de l'efficacité de la cellule.[198,199]

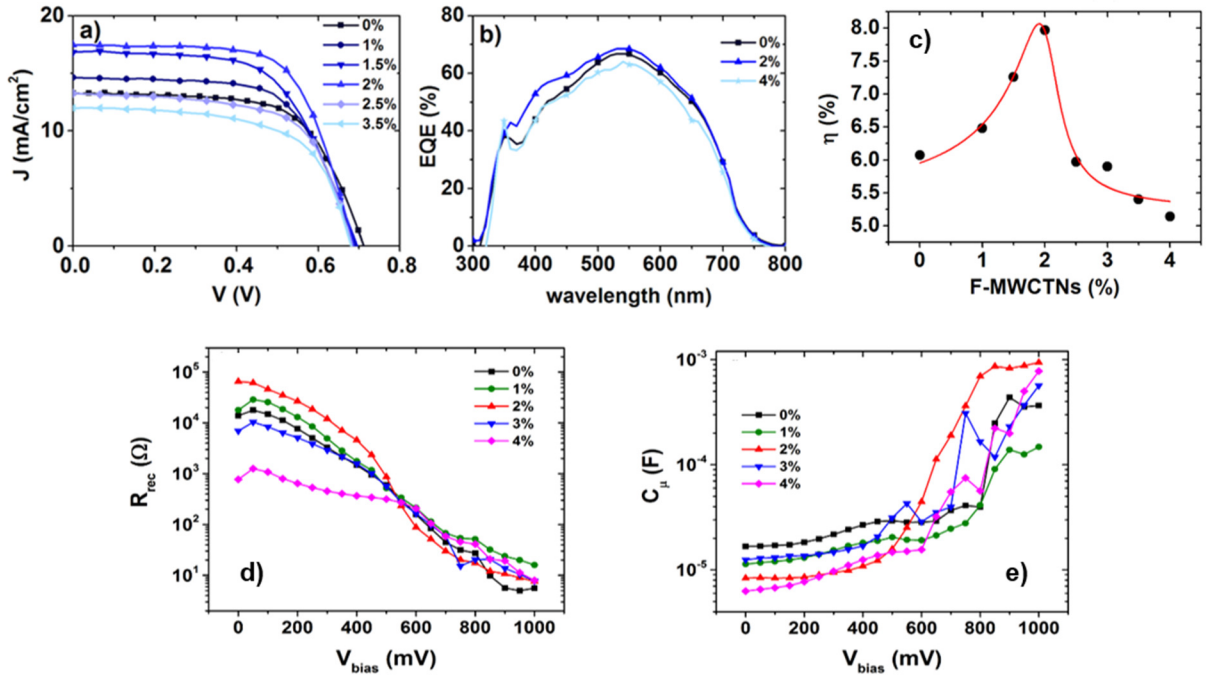

Figure 3.2(a) Courbes J-V des DSSCS à six pourcentages différents de F-MWCNT sous lumière solaire simulée (AM 1,5G, 100 mW cm2). b) EQE des échantillons les plus représentatifs. c) Variation des PCE en fonction de la charge du F-MWCNT. La ligne rouge est un guide pour l'œil. d) Résistance à la recombinaison et e) Capacité chimique mesurée dans l'obscurité.

En conclusion, suite à mes travaux, j'ai pu démontrer une méthodologie rapide et hautement reproductible qui vise à améliorer la collecte et le transport des charges sur les DSSC par l'ajout de F-MWCNTs dans une pâte commerciale de TiO_2. Les résultats montrent que l'incorporation de F-MWCNTs dans une électrode de travail TiO_2 pendant la synthèse améliore efficacement les propriétés physico-chimiques de la cellule, atteignant un PCE de 7,95%, ce qui représente une augmentation de plus de 30% par rapport au TiO_2 nu. Le rôle principal des F-MWCNT est de stimuler l'injection d'électrons depuis la photoanode jusqu'au contact frontal, en augmentant considérablement la collecte des charges photo-générées et en réduisant la recombinaison des charges. L'efficacité accrue est également due à l'amélioration de l'absorption du colorant.

4. Amélioration du transfert de charge en DSSC par modulation des propriétés de la contre-électrode

Différentes approches ont été proposées pour améliorer le rendement des DSSC: Amélioration de la captation de la lumière par le colorant en augmentant son coefficient d'extinction molaire ou en étendant l'absorption du spectre solaire à la région proche infrarouge (NIR); électrolyte amélioré; et dispositif conçu pour augmenter la collecte de charge et réduire la recombinaison. Ce dernier peut être appliqué sur différents éléments du DSSC, en particulier sur la photoanode ou sur la CE.

Le platine (Pt) demeure le matériau préféré dès CE dans ce type de cellules en raison de ses propriétés catalytiques et de sa stabilité chimique et électrochimique supérieure.[202-204] Cependant, le coût élevé du platine peut être un facteur préjudiciable à la commercialisation des DSSC à haute performance et aux systèmes photoélectrochimiques en général. Par conséquent, la nécessité de mettre au point une CE rentable, sans pour autant réduire son activité électrocatalytique et sa stabilité, est un facteur clé pour l'application commerciale des DSSC.

Dans le cadre de ces présents travaux, nous utilisons un procédé de fabrication simple et efficace pour la nanostructuration dès CE pour les DSSC à activité catalytique accrue en utilisant la pulvérisation magnétron pour revêtir les nanofibres de polymère électro-filées, qui servent de gabarits sacrificiels, avec un alliage bimétallique Pt/Pd. En accordant la morphologie et la composition des nanofibres, nous démontrons que la quantité de métal précieux peut être réduite jusqu'à un facteur de quatre.

Les CE nanostructurés ont été testés dans des DSSC pour fournir une étude complète de leur performance PEC en faisant varier l'épaisseur du revêtement par pulvérisation cathodique Pt/Pd (20, 40 et 80 nm) et la densité des nanofibres sur des substrats en verre FTO (temps de filage électrique : 40 ou 120 s). Cela nous a permis de déterminer l'architecture optimale d'CE pour améliorer l'PCE, et grâce à une étude détaillée des processus de transfert de charge qui se produisent dans les CE, nous avons pu attribuer cette augmentation à l'amélioration des performances électro catalytiques.

La **figure 4.1** illustre la morphologie des fibres fabriquées à différentes épaisseurs de revêtements. Lorsque l'épaisseur du revêtement est faible en Pt/Pd, la formation de grains fins de nanoparticules connectées est clairement visible dans l'insert à haute résolution, et quand l'épaisseur augmente, la taille des grains augmente. Cependant, on a également constaté que, selon l'épaisseur du catalyseur pulvérisé, les fibres étaient sujettes à la rupture après l'élimination du polymère.

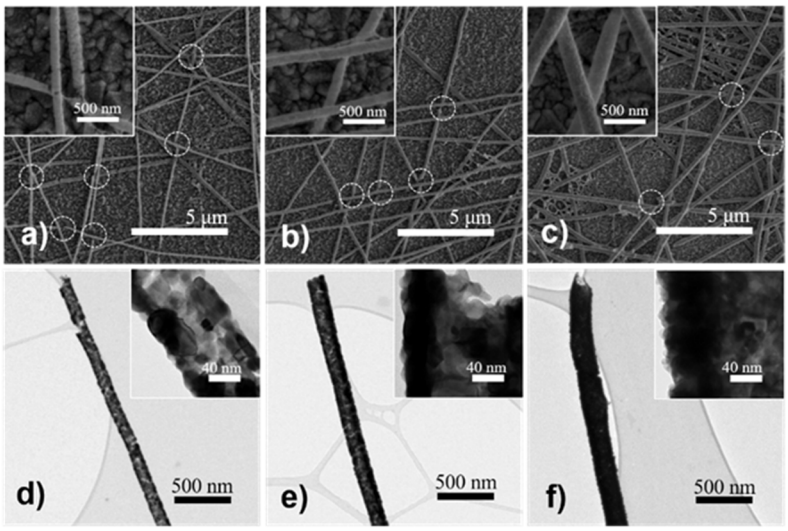

Figure 4.1 Images SEM et TEM des nanofibres creuses obtenues à différents revêtements par pulvérisation Pt/Pd. a) et d) 20 nm, b) et e) 40 nm et c) et f) 80 nm.

Quant aux propriétés fonctionnelles des DSSC assemblés avec différents EC, la **figure 4.2** a-c montre que pour un dépôt de nanofibres de 40 s, l'PCE augmente pour toutes les épaisseurs du film en Pt/Pd, comparativement aux EC plats. Pour un dépôt de 120 s, l'augmentation est négligeable, voire nulle. À la densité optimale de nanofibres (40 s, **figure 4.2 b**), l'effet principal pour toutes les épaisseurs Pt / Pd est d'augmenter la densité de courant de court-circuit (Jsc). De plus, Comparé au CE plat, le CE réalisé avec un dépôt de 40 s du gabarit de nanofibre polymère et pulvérisée avec 80 nm de Pt/Pd (40NF80nm), a montré une augmentation Jsc de 13% pour un PCE maximal égal à 7,50%. Globalement, l'PCE a augmenté de 15 % par rapport à l'CE plat.

Nous avons aussi observé que pour les mêmes conditions d'éclairage, la tension en circuit ouvert (Voc) et le facteur de remplissage (FF) sont très similaires pour toutes les cellules et ne jouent pas un rôle majeur dans l'augmentation du PCE. L'amélioration obtenue dans ce travail (15%), est plus élevée que celle rapportée dans les travaux précédents (8%) dans lesquels une méthode similaire de gabarit/pulvérisation de polymères a été utilisée. [204]

Par la suite, afin de mieux comprendre les mécanismes catalytiques des différents EC, nous avons réalisé l'EIS en utilisant une configuration de cellules symétriques, pour éliminer la contribution de la photoanode TiO_2. Les courbes de Nyquist obtenues sont illustrées dans la **figure 4.2 d**, y compris le circuit équivalent utilisé pour le montage.

Toutes les courbes présentent deux demi-cercles. Un arc à haute fréquence, qui est attribué au processus de transfert de charge à l'interface électrode/électrolyte, et un l'arc à basse fréquence (demi-cercle le plus à droite) qui est alloué à l'impédance de diffusion Nernst des ions dans l'électrolyte.[224-226] La **figure 4.2 d** montre clairement que la cellule la plus performante (40NF20nm) présente l'arc à basse fréquence le plus

petit par rapport à l'EC plat et à celui avec une densité accrue de la nanofibre (120NF20nm), indiquant un taux de diffusion ionique plus rapide sur cet échantillon.

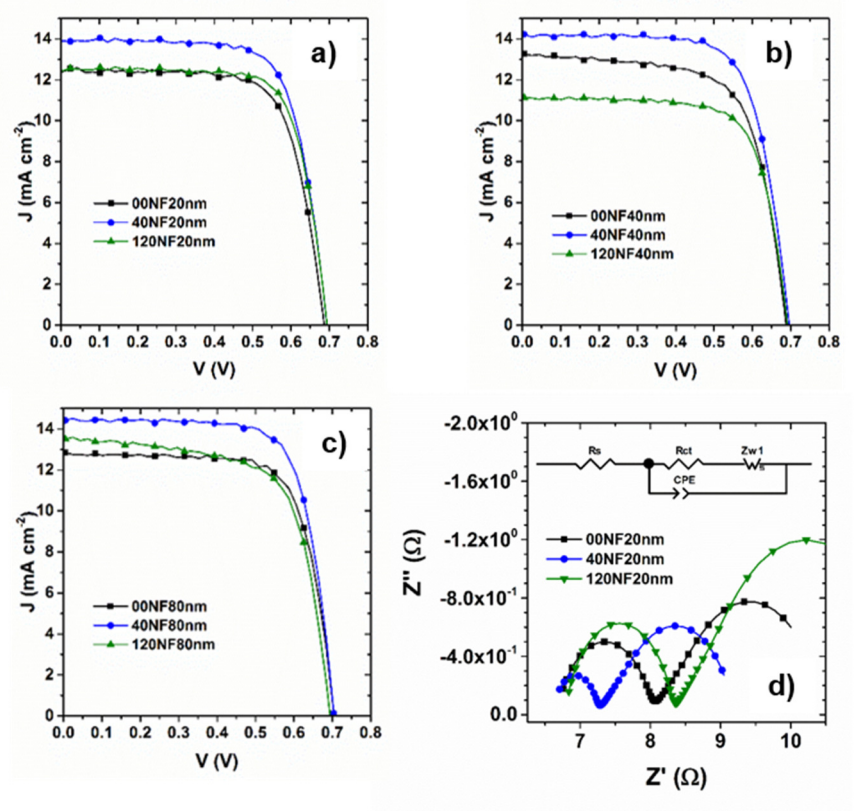

Figure 4.2 a-c) Courbes J-V de cellules solaires utilisant différents CE. d) Diagramme de Nyquist à partir de mesures d'impédance de cellules symétriques. Le circuit Randles utilisé pour l'adaptation des données est illustré dans l'encadré, il comprend une résistance série Rs, une résistance de transfert de charge Rct, un élément CPE à phase constante pour la prise en compte de la capacité double couche et un élément Warburg impédance W1. Les lignes pleines sont les courbes ajustées.

Les CE nanostructurés ont été fabriqués en revêtant des gabarits de polymères sacrificiels 1D d'un film mince en Pt/Pd, produisant des nanofibres creuses. La morphologie et la quantité de catalyse ont été optimisées pour leur application dans les DSSC. Une amélioration de 15% de PCE a été obtenue dans les nanofibres creuses CE à partir d'un temps d'électrofilage de 40 s et d'un film Pt/Pd de 80 nm d'épaisseur. De plus, nous avons montré que la quantité de Pt/Pd pulvérisé peut être réduite à 20 nm, sans réduire significativement l'efficacité globale. L'amélioration de la fonctionnalité résulte de l'augmentation de la durée de vie des électrons dans les DSSC assemblés, attribuée à l'augmentation de la surface spécifique de l'architecture des nanofibres creuses et à l'amélioration des performances électro-catalytiques, comme le montre la double diminution de la valeur du R_{ct}.

5. Réglage de la structure de la bande électronique du chalcogénure métallique unique Quantum Dots

Les points de Quantum (QDs) sont très prometteurs. Ce sont des nano cristaux semi-conducteurs d'une taille typiquement comprise entre 1 et 20 nm. Ils présentent un confinement quantique des états électroniques en raison de leur petite taille,[70] en particulier, la quantification électronique produit des niveaux d'énergie discrets, déplaçant également la position de l'état fondamental et le premier état excité. Ces caractéristiques sont très utiles dans plusieurs systèmes composites, dans lesquels les QDs sont physiquement greffés sur différents échafaudages.[96] La modulation de la structure globale de la bande électronique des systèmes composites permet l'exploitation de plusieurs processus physiques/chimiques, qui sont critiques dans les applications les plus avancées. L'injection de charge et la dynamique des électrons, l'exploitation des électrons chauds et la génération multiple d'excitons pour les photons à absorption unique sont parmi les exemples les plus importants. [232-234] dans de nombreuses applications optoélectroniques, telles que les dispositifs émetteurs de lumière (LED),[235, 236] la photocatalyse, [237] et les cellules solaires.[238] Les QDs sont greffés sur des semi-conducteurs d'oxyde métallique (MOS) (principalement sous forme de couches mésoporeuses ou fines, par exemple TiO_2, ZnO, et SnO_2 entre autres). Dans le cas des cellules solaires, un exciton se forme dans les QDs photoexcités, qui doit ensuite être rapidement divisé en une paire électron-trou à l'interface entre le MOS et les QDs pour éviter la recombinaison de charge. Si le processus de dissociation de l'exciton et d'injection de charge à l'interface QD/MOS est lent, les électrons photogénérés se recombineront avec les trous, réduisant ainsi l'efficacité globale du dispositif. Par conséquent, l'interface entre les QDs et le MOS est d'une importance critique et plusieurs facteurs doivent être pris en compte pour obtenir un transfert de charge efficace à travers cette interface. En particulier : (1) les niveaux d'énergie des MOS et des QDs doivent être alignés pour garantir une injection de charge rapide ;[63, 64] (2) les QDs à bande interdite directe sont préférables en raison de leur absorption optique élevée ;[65, 66] (3) la distance entre les QD/MOS (principalement déterminée par la longueur du ligand qui greffe le QD du MOS) doit être contrôlée pour améliorer le couplage électronique.[67]

Jusqu'à présent, aucune étude n'a été menée sur les QDs sans ligands simples des composites à base de chalcogénure métallique. Dans ce travail, la microscopie à force atomique (AFM) et la microscopie à force de sonde Kelvin (KPFM) sont utilisées pour étudier des QDs uniques composés de PbS, CdS et PbS/CdS développés par SILAR sur du graphite pyrolytique hautement ordonnées (HOPG). Il s'agit d'un système modèle qui permet d'étudier les propriétés des QDs individuels en minimisant tout autre effet collectif (p. ex. élargissement de l'absorption excitonique/des pics d'émission dus à la distribution de la taille des QDs) et/ou interaction QD-QD. Dans ce chapitre, nous rapportons la variation de la différence de potentiel de

contact (DPC) d'un seul SILAR-QD via KPFM, en étudiant l'évolution de leur structure de bande électronique en fonction de la taille et de la composition du QD.

Sur la **figure 5.1**, la topographie et les images de différence relative de potentiel de contact (CPD) des trois systèmes : CdS QDs, PbS QDs et PbS/CdS QDs déposés sur HOPG (le substrat a été mis à la terre avec la pointe à 0 V), sont présentées. Le profil de la hauteur des QDs représentatifs (**figure 5.1 g, h, i**) est en accord avec la distribution des tailles mesurée par TEM et AFM, montrant des variations entre 3 et 11 nm. Dans les images CPD (**Figure 5.1 d, e, f**), la surface HOPG est électriquement homogène, avec une faible oscillation de 10 mV, environ 0 V sur la zone balayée. Les QDs sont représentés sous forme de pics positifs par rapport au substrat HOPG (comme indiqué dans la section expérimentale, la valeur DPC réelle est négative). Les valeurs négatives de DPC indiquent que la fonction de travail des QDs est supérieure à celle du substrat HOPG. En comparant le profil de hauteur et la DPC, plus les DQ sont grands, plus la DPC est négative. Des observations similaires s'appliquent à tous les échantillons. Dans tous les cas, la DPC des QDs varie en fonction de leur taille et indépendamment de leur type. Le DPC devient monotone et plus négatif (avec une tendance presque linéaire) lorsque la taille du QD augmente.

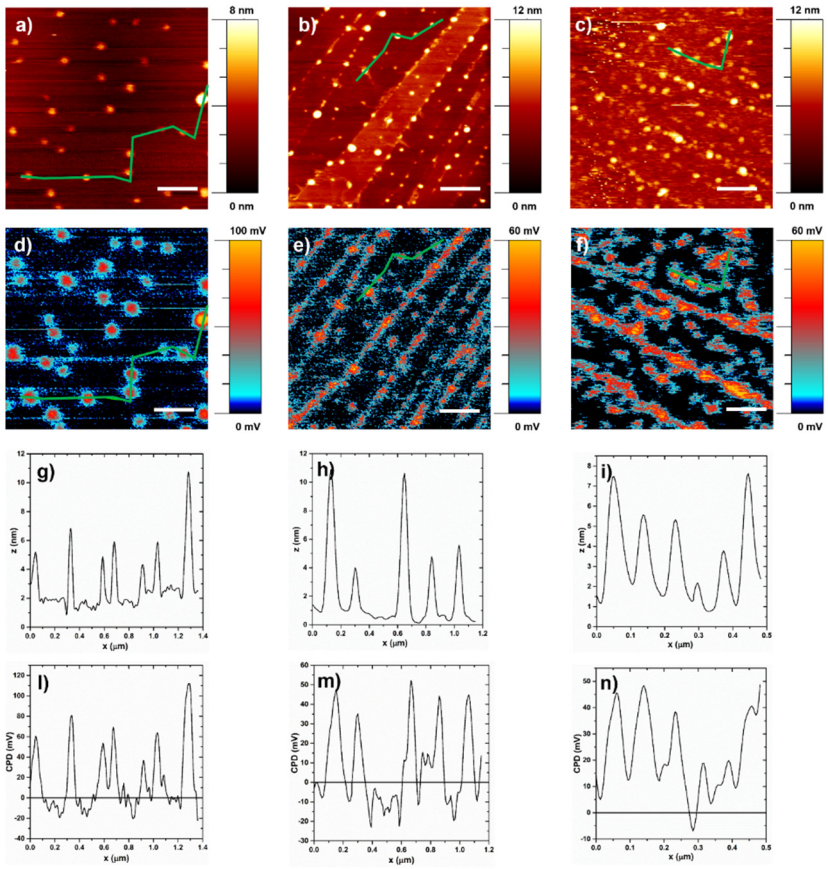

Figure 5.1 Mesure AFM et KPFM simultanée des CD, PbS et PbS/CdS QDs. a-c) Morphologie des CdS, PbS et PbS/CDs QDs sur une surface de 1 µm1 µm, respectivement. d-f) Image simultanée CPD des QDs. La barre d'échelle est de 200 nm. g-i) Profil en coupe de la ligne en a-c. l-n) Profil en coupe des valeurs KPFM de la même ligne en d-f.

En général, la variation de la DPC dépend principalement, comme prévu, des propriétés électroniques des différents matériaux, plutôt que de leurs caractéristiques géométriques. Nous nous attendons alors à ce que les électrons passent de CdS à PbS lorsqu'une jonction PbS/CdS est formée, jusqu'à ce qu'un nouvel équilibre soit atteint, dans lequel le niveau de Fermi (E_F) des deux matériaux est égal. Le nouveau niveau E_F doit être situé entre le niveau E_F des matériaux individuels, PbS et CdS, avant le contact.

A partir des valeurs relatives du E_F, il est également possible de déterminer la position relative de la bande de Valence (VB) et celle de la bande de conduction (CB). Les résultats des calculs, basés sur les données expérimentales, sont présentés aux **figures 5.2**. La position de la CB dans les QD CdS est beaucoup plus élevée que celle dans les QD PbS, comme prévu, permettant une injection de charge efficace dans MOS comme TiO_2 et ZnO (pour des raisons de clarté, nous rapportons en pointillé rouge la valeur de la littérature de la position CB relative de TiO_2 par rapport à HOPG). Cependant, nous devons être prudents lorsque nous comparons la position des bandes électroniques dans les semi-conducteurs et les données de la littérature. En raison de l'interférence des conditions atmosphériques pendant les mesures, nous pouvons avoir des espèces adsorbées, telles que des molécules d'eau, sur les différentes surfaces, ce qui peut induire un

déplacement du CPD et ainsi influencer les valeurs absolues des potentiels mesurés.[264] Pour cette raison, si la mesure des positions relatives de la CB et de la VB des QD PbS et CdS est raisonnablement précise, leur position absolue ne peut pas être déterminée avec la même précision. Un comportement similaire a été observé précédemment et les valeurs réelles de la position absolue des états électroniques/bandes peuvent être récupérées en décalant les données d'une valeur constante, en fonction de l'amplitude de la fonction de travail de référence.[262]

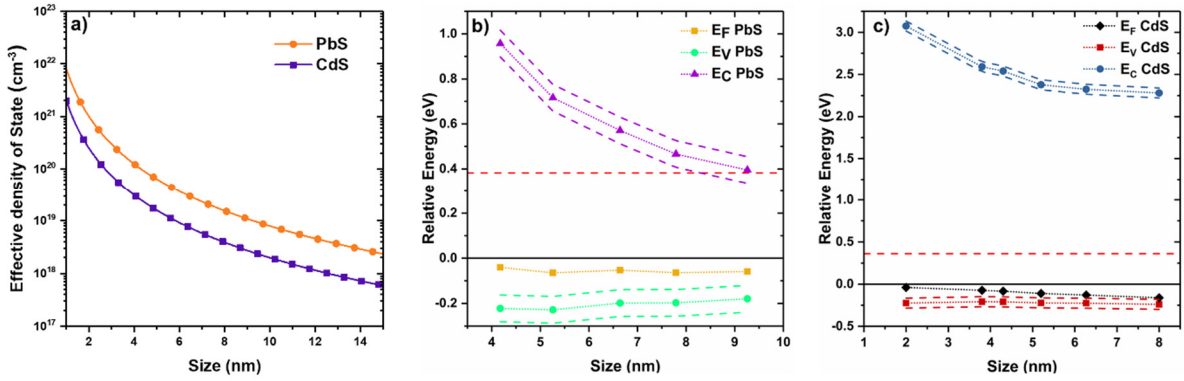

Figure 5.2 Densité effective de l'état calculée comme décrit dans le manuscrit pour les QDs PbS et CdS (a). Positions de niveau VB, CB et Fermi par rapport au substrat HOPG pour les QDs PbS (b) et CdS (c) de tailles différentes. La ligne pointillée rouge représente la bande de conduction de TiO_2 ajustée pour la fonction de travail de référence du HOPG.

En résumé, KPFM a été utilisé pour étudier pour la première fois les propriétés électriques locales des QDs individuels de chalcogénure de métal, optiquement actifs dans la région spectrale NIR, de taille et composition différentes, développés par une approche SILAR. La variation du potentiel de surface d'un QD individuel en fonction de sa taille et de sa composition a été mesurée. Comme prévu, KPFFM a été sensible à la composition des différents matériaux et à leur structure de bande électronique.

6. Amélioration de l'extraction des trous dans les cellules solaires en pérovskite planaire inversée

Ce travail est basé sur un stage que j'ai effectué à l'été 2017 à l'Université Nationale Chao Tung de Taiwan sous la direction du Professeur Eric Diau. Je me suis concentré sur l'ingénierie de l'interface des cellules solaires en pérovskite afin de faciliter le transfert électron/trou de la couche de pérovskite vers l'électrode. Dans ce cadre, j'ai prévu d'augmenter l'efficacité des cellules solaires en ajoutant à l'interface entre le verre

conducteur et la perovskite, une couche hybride formée d'oxyde de graphène (GO) et de points de carbone (Cdots).

Les Cdots sont des nanoparticules discrètes, quasi-sphériques, de taille inférieure à 10 nm. Ils sont exclusivement composés d'éléments non toxiques et abondants sur terre (C, N, H et O) et peuvent être synthétisés en grandes quantités par une simple approche hydrothermale ou par micro-ondes.[52] Par rapport aux QDs semi-conducteurs conventionnels, leurs avantages incluent le fait d'être non toxiques, bon marché, chimiquement stables et simplement préparés à partir de matières premières riches en carbone.[270] Pour montrer leur polyvalence, nous exploiterons dans ce travail les propriétés optoélectroniques des Cdots pour modifier la couche de transport des trous (HTL) d'une PSC.

Bien qu'il ait été démontré que GO est un matériau efficace pour l'extraction des trous, la propagation des trous sur les groupes d'oxygène limite le transfert des trous extraits et provoque la recombinaison des charges. Pour surmonter ces limites, nous avons introduit les Cdots pour former un HTL GO/Cdots homogène afin de développer des PSC inversés à haute efficacité. Ce travail démontre qu'une quantité optimale de Cdots en proportion optimisée dans un composite avec des nanosheets GO peut améliorer significativement l'extraction des trous du film de perovskite à l'interface GO/ITO(Indium Tin Oxide) .De plus, nous concevons également des Cdots spécifiques pour augmenter la stabilité de la PSC. La stabilité à long terme est l'un des paramètres les plus critiques pour les cellules solaires en général (également parce qu'elle influe sur le coût global), et constitue un défi majeur pour les PSC spécifiquement. En particulier, la stabilité du PSC sous la lumière ultraviolette reste un problème majeur.[275, 276] Pour résoudre ce problème, nous avons préparé des Cdots absorbant les UV et les avons noyés dans une matrice polymère pour servir de couche de rétrogradation sur la cellule solaire.

Une approche solvothermale a été utilisée pour former des Cdots avec des groupes fonctionnels abondants, y compris des groupes hydroxyle, carboxyle et amide. Ces groupes fonctionnels confèrent une grande dispersibilité dans les solvants polaires, tels que l'eau et le méthanol. (**figure 6.1 a)** En présence de GO dans la solution de Cdots préparés, l'intensité photoluminescente (PL) diminue considérablement avec l'augmentation de la concentration de GO, alors que la position et la forme des lignes d'absorption ne sont pas affectées. Comme déjà signalé dans des systèmes similaires, cette interaction peut être attribuée au transfert de charge des porteurs de charge photo induits dans les Cdots à GO. (**figure 6.1 b-c**)

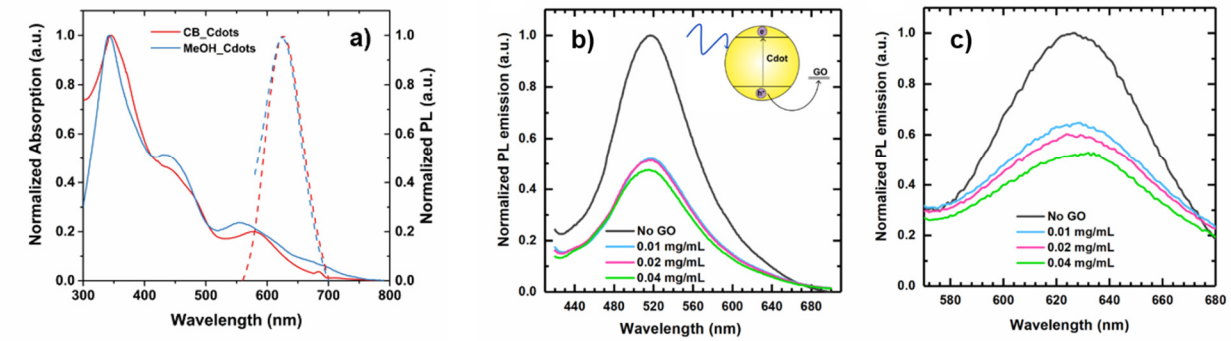

Figure 6.1 a) Absorption et émission (λex= 540 nm) de Cdots après purification (MeOH_Cdots, solvant est du méthanol) et après échange de ligands (CB_CDots, solvant chlorobenzène) ; spectres de fluorescence des Cdots en solution chlorobenzène à concentration variable de GO. b) λex = 400 nm, c) λex = 540 nm.

Le HTL Cdots/GO HTL a été préparé à l'aide d'une technique de revêtement par rotation la solution de dispersion Cdots_CB de concentrations variées (0,025, 0,05 et 0,1 mg /mL) sur la couche GO. La couche GO/Cdots préparée a été utilisée comme HTL dans un PSC inversé basé sur la configuration du dispositif ITO/GO /Cdots /MAPbI3 /PCBM /BCP /Ag. Dans la configuration inversée, il est indispensable d'avoir un HTL transparent afin de ne pas perdre la lumière incidente et le photocourant. L'ajout de Cdots n'augmente pas l'absorption dans la gamme 400-500 nm, sans effet néfaste sur l'absorption de la couche de perovskite. Par conséquent, nous pouvons conclure que l'amélioration des performances des dispositifs résulte des changements des propriétés optiques et électroniques à l'interface, comme nous le verrons plus loin.

L'effet de diverses charges de Cdots sur les propriétés fonctionnelles des PSCs a été étudié. Les courbes J – V des meilleures cellules avec des concentrations variées de Cdots dans la couche GO / Cdots sous forme de HTL sous une lumière solaire simulée AM 1.5G, et l'efficacité des photons incidents au courant (IPCE) sont reportées dans la **figure 6.2**. Pour l'appareil GO, un PCE de 14,7% a été obtenu, une valeur plus élevée que celle rapportée par Wu et al. (PCE = 12,4%) pour un appareil similaire.[21] En général, tous les appareils champions avec GO / Cdots comme HTL ont montré des performances PV bien supérieures : 15,6%, 16,2% et 15,4% pour les Cdots se chargeant à 0,025, 0,05 et 0,1 mg / mL, respectivement. Les performances améliorées de GO / Cdots sont principalement dues à leur augmentation de JSC. Des densités de courant de court-circuit plus élevées dans les dispositifs GO / Cdots ont été confirmées par les spectres IPCE (**figure 6.2 b**)

A partir de ces observations, nous avons déduit que l'ajout de Cdots en quantité optimale sur les nano-feuilles GO augmente la capacité d'extraction des trous d'une couche GO. Pour élucider la dynamique des processus de transfert de charge au niveau de la couche composite GO/Cdot, nous avons appliqué des désintégrations PL en équilibre et en régime transitoire avec des techniques de comptage monophotonique corrélé dans le temps (TCSPC).

Lorsque GO ou GO/Cdots ont été introduits à l'interface de la couche PSK, on a observé une forte trempe (quenching) au PL, maximisée à 0,05 mg mL^{-1} de Cdots et avec des intensités de PL qui suivent l'ordre ITO/PSK > ITO/GO/PSK > ITO/GO/0,025Cdot/PSK > ITO/GO/0,025Cdot/PSK > ITO/GO/0,05Cdot/PSK (**figure 6.2 c**). La trempe PL à l'état d'équilibre indique une contribution substantielle des Cdots à l'extraction des trous du film de pérovskite. Une tendance similaire à la PL à l'état d'équilibre est observée dans les mesures de durée de vie, en associant la décroissance la plus courte à l'échantillon avec GO / Cdots à 0,05 mg mL^{-1}. Tous les PL transitoires ont été équipés d'un modèle de décroissance bi-exponentielle. Cela soutient l'hypothèse d'un transfert de charge amélioré en présence d'une quantité optimale de Cdots (**figure 6.2 d).**

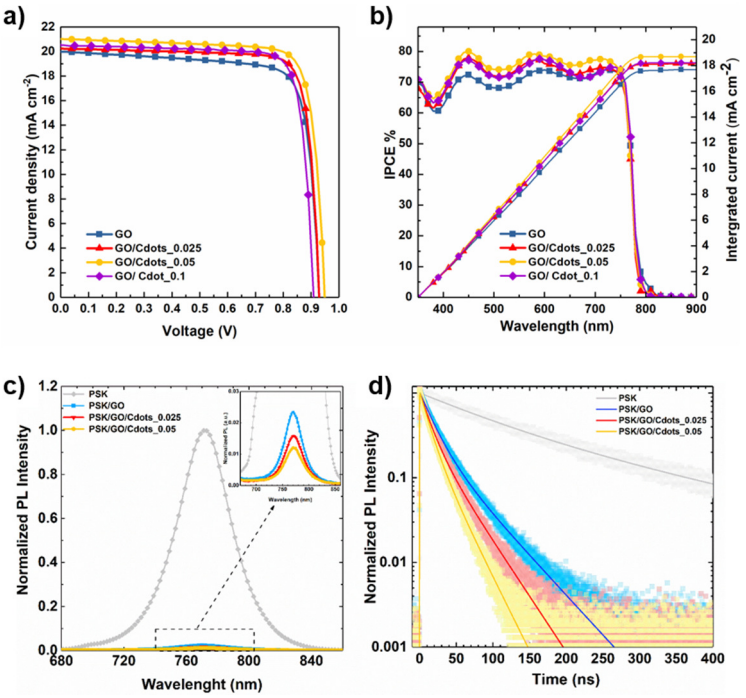

Figure 6.2 a) Courbes J-V pour les meilleurs échantillons dans des conditions optométriques, b) IPCE et densités de courant intégrées. c) Spectres de photoluminescence de couches minces de pérovskite déposées sur des ITO, sur des GO et sur des GO/Cdots à charge variable, recueillis avec une excitation de 635 nm, d) décroissances transitoires de PL obtenues par la technique TCSPC avec excitation à 635 nm et sonde à 770 nm.

Les résultats de la photovoltage transitoire (TPV) suggèrent qu'un alignement plus favorable du niveau d'énergie et une bonne capacité de blocage des électrons de la couche hybride de transport de trous GO/Cdots 0.05 pourraient efficacement supprimer le processus de recombinaison de charge (**figure 6.3 a**). Les spectres d'impédance électrochimique (EIS) ont servi à élucider les propriétés électroniques et la recombinaison inter-faciale dans la cellule solaire avec des Cdots en quantités variables (**figure 6.3 b**). Pour tous les échantillons, un seul grand demi-cercle est visible dans la courbe de Nyquist ; cet arc, généralement observé à des fréquences moyennes, est lié à la recombinaison des charges à l'intérieur de la cellule

solaire.[288, 289] La caractéristique la plus remarquable des parcelles de Nyquist est que la cellule traitée avec des Cdots à 0,05 mg/mL conduit à un arc plus grand indiquant un phénomène de recombinaison réduit. Une autre confirmation du phénomène de recombinaison réduite pour la quantité optimale de Cdots, provient de l'analyse de R_{rec} lors de la variation de la polarisation de tension (**figure 6.3 c**). Dans toute la gamme des V_{bias}, la valeur de R_{rec} pour la meilleure cellule (avec 0,05mg/mL Cdots) est supérieure aux autres.

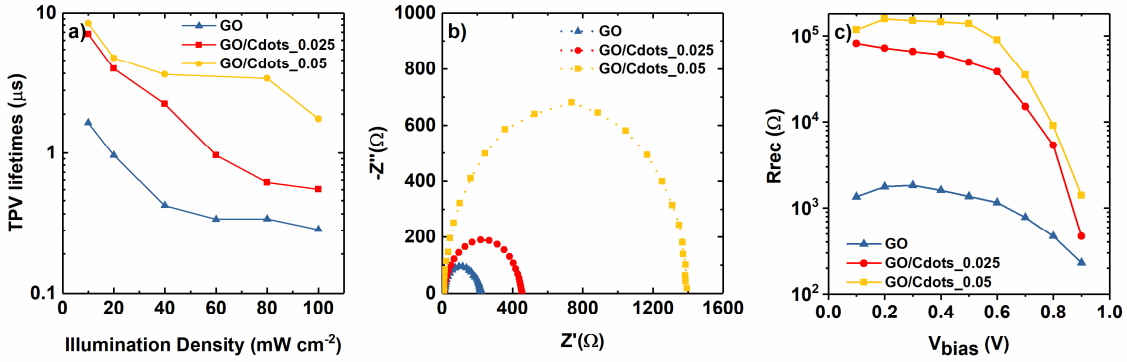

Figure 6.3 a) Mesure de la tension photovoltaïque transitoire d'échantillons représentatifs à des densités d'éclairement variées ; b) Diagramme de Nyquist à 900 mV dans l'obscurité de trois échantillons représentatifs avec des HTL variés : GO, GO/Cdots 0,025 et GO/Cdots 0,05 ; (c) résistance de recombinaison des trois échantillons représentatifs.

Un autre défi lié à la stabilité des PSCs est la stabilité de la perovskite à la lumière ultraviolette. Pour résoudre ce problème et augmenter la stabilité à long terme de nos appareils, nous avons préparé un autre type de Cdots qui absorbent dans la région UV et une émettent autour de 450 nm. Les Cdots dispersés dans l'isopropanol ont ensuite été mélangés avec de la polyvinylpyrrolidone (PVP) et enrobés par centrifugation sur le côté en verre des dispositifs PSC. L'ajout de la couche protectrice de Cdots, a non seulement amélioré la stabilité de l'appareil (+20%), mais a également augmenté l'PCE de la cellule (16.8%) : le film à base de Cdots a éliminé la partie UV du spectre et l'a décalée vers une gamme de longueurs d'onde plus appropriée qui peut être absorbée par le film en perovskite.

En résumé, une méthode rapide et hautement reproductible pour préparer un HTL efficace et stable pour les PSC à hétérojonction planaire basée sur Cdots/GO a été démontré. Ces résultats montrent que l'utilisation de Cdots en quantité optimale a amélioré l'PCE de l'appareil à 16,2 %. De plus, l'utilisation de Cdots absorbant les UV appropriés comme film protecteur sur le côté extérieur du PSC a amélioré la stabilité contre le rayonnement UV de plus de 20% tout en augmentant le PCE jusqu'à 16,8%. Le présent travail fournit des indications importantes pour la poursuite des recherches sur l'exploitation des propriétés des nanomatériaux carbonés en tant qu'alternatives aux CTL à haute conductivité pour améliorer l'efficacité des PSC planaires.

7. CONCLUSION ET PERSPECTIVES

Conclusion

La dynamique de charge et la gestion de la lumière de différentes architectures, telles que DSSC, QDSC et PSC, ont été explorées dans cette thèse. Au cours des 5 prochaines années, il est d'une importance fondamentale de disposer d'une technologie à faible empreinte de carbone afin de réduire les émissions de gaz à effet de serre et de limiter le changement climatique. En vertu de ces prémisses, le DSSCs, le QDSC et la PSC peuvent jouer un rôle majeur dans la transition vers des technologies plus vertes. Il est donc urgent, bien qu'il s'agisse encore d'un défi de taille, d'explorer une méthode simple et robuste pour réaliser un contrôle puissant des processus de rechargement et de recombinaison des charges, et donc de réduire significativement les pertes d'énergie pendant les processus de transfert et de transport des charges.

Au cours des travaux présentés dans ce manuscrit, les effets de l'incorporation de différentes concentrations de groupes carboxyle (COOH)- F-MWCNTs, dans des couches actives de TiO_2 pour les DSSCs ont été explorés. Il a été démontré que la présence d'une quantité optimale de F-MWCNT dans les photoanodes augmente l'PCE jusqu'à 7,95% et le Jsc jusqu'à 17,5 mA cm^{-2}. L'amélioration des performances a été établie par l'augmentation de la charge de colorant, la réduction de la recombinaison des charges (comme le montrent les mesures de la charge de colorant et de l'EIS), et grâce à la couverture conforme des F-MWCNT, qui permet une collecte rapide et efficace des charges dans les cellules solaires en fonctionnement. Ces résultats peuvent aider à améliorer l'PCE dans les DSSC d'une manière élégante et simple, en minimisant le besoin d'étapes supplémentaires (par exemple, pré et post-traitement avec $TiCl_4$) pour la préparation des photoanodes.

Par la suite, une nouvelle contre-électrode pour DSSC à base de nanofibres creuses en Pt/Pd a été proposée. En effet, nous avons constaté que le CE optimisé peut augmenter la densité de courant de court-circuit et conduire à une augmentation de PCE d'environ 15 % par rapport au CE plat. Ces résultats suggèrent une stratégie simple et directe pour augmenter l'PCE dans les DSSC, minimiser l'utilisation de métaux précieux utilisés dans ce type d'appareils et, plus généralement, adapter la structure de la CE dans les systèmes photoélectrochimiques afin d'augmenter leurs propriétés fonctionnelles, grâce aux avantages offerts par cette morphologie complexe.

Puis, la microscopie à force de sonde Kelvin a été utilisée pour étudier les propriétés électriques de chaque QD de chalcogénure métallique de taille et de composition différentes développés par absorption et réaction successives de couche ionique (SILAR) sur un matériau de type graphène. En utilisant KPFM, on a pu observer la variation locale du FE à l'intérieur d'un QD individuel et de distinguer les différents matériaux

d'un point de vue électronique, sans interférence avec la morphologie de l'échantillon. Cette étude est pertinente pour les processus liés à la dynamique d'excitation, qui sont déterminés par l'environnement local à l'interface des systèmes composites.

Finalement, l'effet de l'intégration des Cdots dans des cellules solaires à haute performance à hétérojonction planaire inversée en perovskite a été étudié. Des Cdots ont été utilisés pour modifier la couche de transport des trous dans les dispositifs PSC planaires. En introduisant des Cdots sur l'oxyde de graphène (GO) en tant que HTL, l'efficacité du PSC s'est considérablement améliorée, passant de 14,7% dans le cas du GO nu à 16,2% du meilleur appareil avec une teneur en Cdots optimisée. Lors de l'application de Cdots avec une absorption conçue dans la gamme UV comme couche de rétrogradation, les performances du dispositif ont été encore améliorées, atteignant un PCE maximum de 16,8% (+14%) ; la stabilité du dispositif a été également améliorée de plus de 20%. Ce travail révèle une amélioration efficace des extractions de charge et donc des performances des PSC planaires en utilisant les Cdots/GO comme matériau de transport des trous.

Perspectives

La réduction des processus de recombinaison est essentielle pour obtenir une efficacité élevée et une stabilité à long terme. La couverture complète des ETL est d'une importance fondamentale pour améliorer la capacité d'absorption de la lumière et réduire la surface découverte de l'oxyde métallique afin de minimiser l'interface oxyde du métal/électrolyte. Le revêtement de l'électrode d'oxyde méso-poreux avec un matériau mince à large bande interdite peut encore être amélioré. Des techniques avancées, telles que le dépôt de couche atomique (ALD), donnent des résultats prometteurs dans cette direction, permettant un meilleur contrôle de l'épaisseur et de l'uniformité du film.

Une meilleure compréhension des mécanismes de la dynamique des charges est encore nécessaire. En raison de la grande complexité (physique et chimique) des systèmes tels que DSSC, QDSC et PSC, il n'est toujours pas possible jusqu'à présent de prévoir avec précision comment une petite modification du système, c'est-à-dire le remplacement d'une composante, affectera la performance. La future orientation de la recherche est de comprendre et de maîtriser les mécanismes qui se produisent en particulier à l'interface oxyde/teinture/électrolyte (HTM).

Il convient de noter que les progrès de la technique solaire et de l'efficacité de conversion de l'énergie doivent aller de pair avec la progression des techniques de stockage. En effet, jusqu'à présent, il n'existe pas de solution satisfaisante pour stocker efficacement l'énergie générée par le PV. Des approches perturbatrices des technologies de stockage sont nécessaires pour compenser l'intermittence de la lumière solaire et permettre le développement d'un système complet d'énergie propre. L'une des solutions prometteuses est la

conversion de la lumière solaire en combustibles solaires, tels que l'hydrogène. La technologie des combustibles solaires offre de nombreuses possibilités de découverte de nouveaux matériaux et systèmes qui permettront des voies déployables et rentables pour la production directe de combustibles à partir du soleil.

TABLE OF CONTENTS

LIST OF FIGURES

LIST OF TABLES

ABBREVIATIONS

Abbreviation	Meaning
1D	One dimensional
AFM	Atomic Force Microscopy
AM 1.5G	Air Mass 1.5G
a-Si	Amorphous-Si
CB	Conduction Band
CBD	Chemical bath deposition
Cdots	Carbon dots
CE	Counter-electrode
CED	Cumulative energy demand
CNTs	Carbon nanotubes
CO_2	Carbon dioxide
CPD	Contact Potential Difference
CTL	Charge transport layers
DMF	Dimethylformamide
DMSO	Dimethyl sulfoxide
DRIFT	Diffuse reflectance infrared Fourier transform spectroscopy
DSSCs	Dye-sensitized solar cells
E_F	Fermi level
E_g	Band gap
EIS	Electrochemical Impedance Spectroscopy
EPBT	Energy payback time
ETL	Electron transport layer
FF	Fill Factor
F-MWCNTs	Functionalized multi-wall carbon nanotubes
FTO	Fluorine tin oxide
G1	First Generation
G2	Second Generation
G3	Third generation
GBL	γ-butyrolactone
GDP	Gross domestic product per capita
GHG ER	Greenhouse gases emissions rate
GHI	Global horizontal irradiation
GIXRD	grazing incidence X-ray diffraction
HOMO	Highest occupied molecular orbital
HOPG	Highly oriented pyrolytic graphite
HTL	Hole transport layer
I	Current
I_M	Maximum current
IPCC	International Panel on Climate Change

IPCE	Efficiencies of incident photons to current
I_{SC}	Short Circuit Current
ITO	Indium tin oxide
J	Current Density
J_{SC}	Short Circuit Current Density
KPFM	Kelvin Probe Force Microscopy
LCA	Life Cycle Assessment
LUMO	Lowest unoccupied molecular orbital
$MAPbI_3$	Methylammonium lead-iodide
MOS	Metal oxide semiconductor
MSC	Mesoporous single-crystal
NRs	Nanorods
NSERC	Natural Sciences and Engineering Research Council of Canada
NTs	Nanotubes
NWs	Nanowires
PCBM	[6,6]-phenyl C61-butyric acid methyl ester
PCE, η	Power conversion efficiency
PEDOT:PSS	Poly(3,4-ethylenedioxythiophene) poly(styrene-sulfonate)
PHJ	Planar heterojunction
PL	Photoluminescent
P_{MAX}	Power generated by the cell
ppm	Parts per million
PPP	Purchasing power parity
PSC	Perovskite solar cell
PSK	Perovskites
PTAA	Poly (triarylamine)
PV	Photovoltaic
QDs	Quantum Dots
QDSC	Quantum Dots Sensitized Solar Cells
rGO	Reduced graphene oxide
SEM	Scanning Electron Microscopy
SILAR	Successive ionic layer absorption and reaction
SWCNTs	Single wall carbon nanotubes
TCO	Transparent conductive oxide
TEM	Transmission Electron Microscopy
TPV	transient open-circuit photovoltage
TSCPC	Time-Correlated Single Photon Counting
V	Voltage
VB	Valence band
V_M	Maximum potential
V_{OC}	Open Circuit Voltage
XPS	X-ray Photoelectron Spectroscopy
XRD	X-ray powder Diffraction

1 INTRODUCTION

1.1 The energy crisis and challenge

The world energy consumption is growing every year and the limited fossil fuels resources require the development of renewable energy resources. Currently more than 85% of the world's energy requirement is being supplied by fossil fuels which increases global warming and has deleterious effects on our environment.[1] Even if the estimated reserves of fossil fuels range from 150 to 400 years for coal, 40–80 years for oil, and 60–160 years for natural gas, there is a serious concern on their impact on the environment.[2] In particular the main concern is related to the emission of greenhouses, such as carbon dioxide (CO_2), and how they contribute to the global warming.

In the last 60 years, the concentration of CO_2 in the atmosphere has increased from approximately 280 parts per million (ppm), to 411 ppm in 2019 (**Figure 1.1 a**).[1] Since 1920 the emission from fossil fuel is the dominant source of anthropogenic emissions to the atmosphere and its relative share has continued to increase until present. Accordingly to the International Panel on Climate Change (IPCC), there is a 50% chance of stabilizing the average global temperature at a 2 °C increase over the pre-industrial period if we are able to keep the concentrations of CO_2 under 450 ppm.[1] If the temperature change can be limited to less than 2 °C, there is a good chance that society can adapt. In the last 5 years, a slowdown in the growth rate of the global fossil CO_2 emissions can be observed. In particular, after an increased growth rate of 3% per year in the 2000s, a slower growth rate below 1% per year can be seen starting from 2010, with a more pronounced slowdown from 2014. (**Figure 1.1 b**)[3]

Taking in account the type of fossil fuels, in the last year, around 40% of fossil CO_2 emissions were from coal, 34% from oil, 19% from natural gas, and the remaining 7% from cement and other smaller sources (**Figure 1.1 c**). Since 2005, China became the largest emitter of CO_2, with in the last year emission nearly 10 $GtCO_2$, 27% of the total global emissions. USA is the second largest country that emit more CO_2, with a share of 18%. Europe (represented as the 28 countries of the European Union together) accounts for less than 9% (**Figure 1.1 d**).

Although in recent years some climate policies started to have some effect , the global fossil CO_2 emissions continue to growth.[4] Current national policies still put the world on a pathway of increasing greenhouse gas emissions through to 2030.[4] One of the main reasons is that current directives are leading to a higher adoption of cleaner energy but they do not favor in parallel the phase out of fossil fuels.

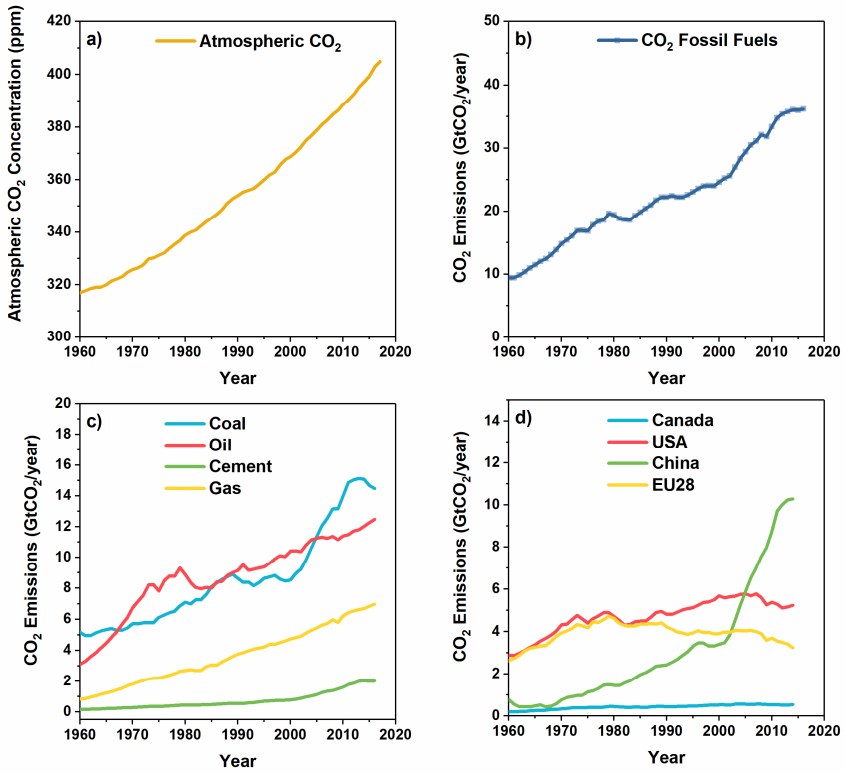

Figure 1.1. a) Concentration of CO_2 in the atmosphere since 1960. b) Global CO_2 fossil fuel emitted per year since 1960. c) Share of CO_2 per type of fossil fuel and d) per representative countries.

The economic and political decision on energy in the next 20 years will be crucial to maintain the level of CO_2 below the critical point of 450 ppm. In fact, to reduce our dependence on fossil fuels and control the greenhouses emissions, it will be necessary to transit from a fossil-fuel based energy conversion to more sustainable sources of energy (**Figure 1.2**). Until now the adoption of new and environmental friendly resources is mainly determined by economic considerations, rather than technological impediments. That's why it is important, as scientists and engineers, to develop new technologies in which the price and environmental impact is taken in account, in order to offer low-cost and eco-friendly solutions to pave the way for their adoption.

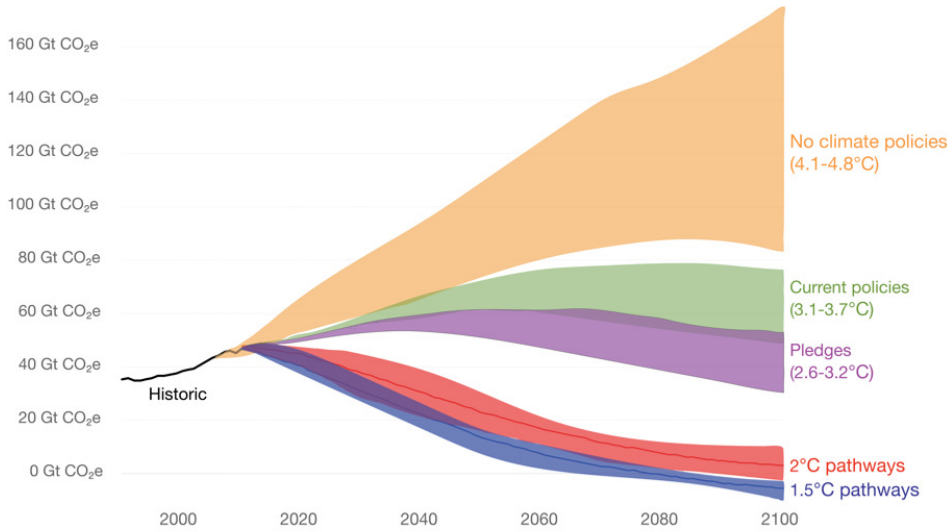

Figure 1.2. Potential future emissions pathways of global greenhouses gases in the case of different climate polices. Reprinted with permission.[5]

1.2 Capture, converting and exploiting the sun light: the energy challenge of the next years

Looking at the share of global final energy consumption at the end of 2018, renewable energies provided an estimated 19.3%. Of this total share, traditional biomass, used primarily for cooking and heating in remote and rural areas of developing countries, accounted for about 9.1%, and modern renewables for 10.2%. Among them, hydropower accounted for an estimated 3.6% of total final energy consumption, while other renewable power sources (photovoltaic included) comprised less than 1.6%. [2]

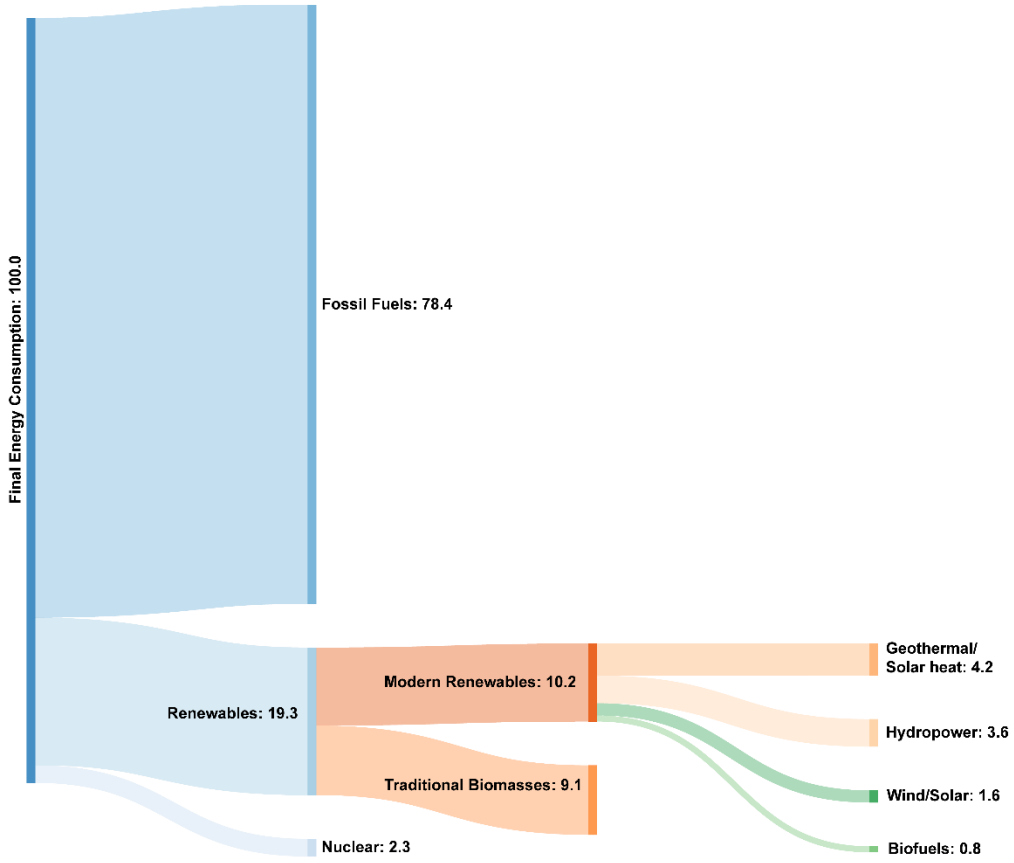

Figure 1.3. Share of global final energy consumption at the end of 2018. Data taken from REN21. Renewables 2019 Global Status Report.[2]

Among all the green renewable energies (wind, biomass, heat and hydropower), the solar energy is the only source that has the potential to meet all our energy needs. Every hour, radiation impinging from the sun would be sufficient to power the whole planet for one year. It has been calculated that covering 0.1% of the earth's surface area with solar cells of 10% efficiency, corresponding to 1% of desert areas or 20% of the area of buildings and roads, would provide for global electricity consumption. Of course this model is not sustainable, but any future energy infrastructures will be more a mix of different energy sources, in which solar energy will play a major role but will not be the sole one.

Since 2008, the photovoltaic (PV) market exhibits an exponential growth: in 2008 the global capacity of PV was around 15GW, nowadays we reached more than 500GW. The solar cells market is one of today's fastest growing markets and it is clear that it is not anymore only a niche market but part of the global electricity production.[2]

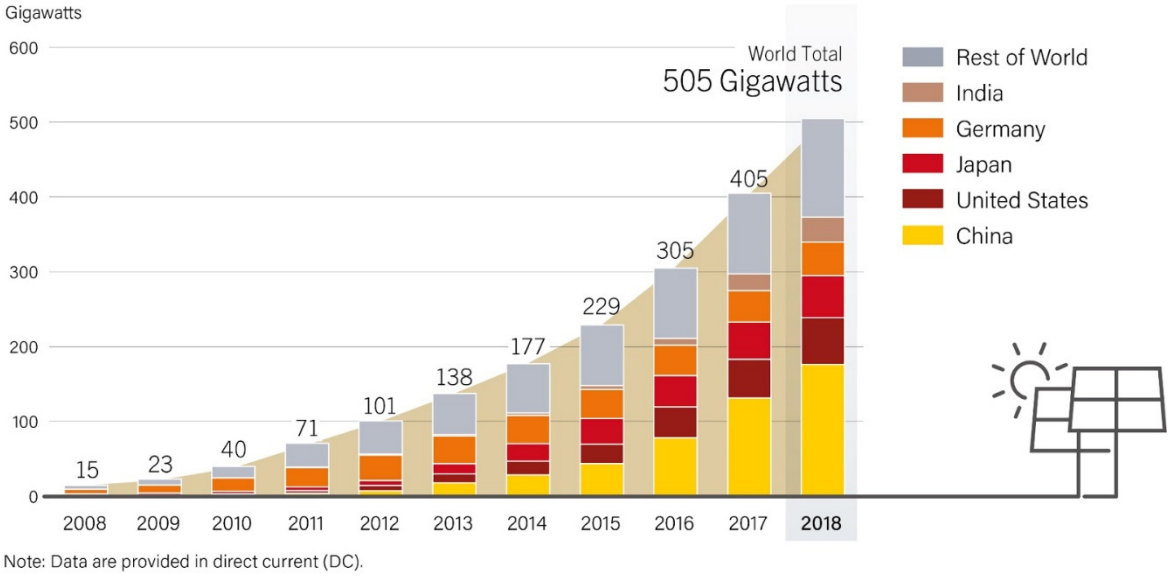

Figure 1.4. Solar PV global Capacity, by country and region in the last decade (2008-2018). Reproduced from Ref [2].

However, the electrical power generated by PV is still not able to compete with the price of electricity generated by more conventional systems and until now it has been subsidized with government incentives in order to make more competitive the costs. In this framework, the research for more efficient and low cost PV devices assumes a critical role to pave the way to their global distribution.

One of the main advantages of the solar energy is that, despite its temporal and geographical variability, it remains one of the most equitably distributed energy resources: no location in the world lacks direct local access to sunlight. If we observe the worldwide average global horizontal irradiation (GHI) (**Figure 1.5**) interestingly, except few regions, the highest irradiance can be found in countries that are considered poor.[6] In fact, for example, if we take the 30 highest gross domestic product per capita (GDP) countries and 30 lowest ones and correlate them with the yearly average GHI, it is clearly visible that the countries with most insolation have a GDP lower than 3000 Purchasing power parity (PPP) dollars.[6] Excluding Australia, the other exception are 6 out 7 countries of the Arabic peninsula. However, in this latter case, it is necessary to consider that sometimes the GDP cannot correctly interpret the condition of a nation. In particular, in this case, it can hide the poverty disparities: in these countries, in average, the top 1% of the population has an income around 200 times higher than the bottom 90% of the population. [6]

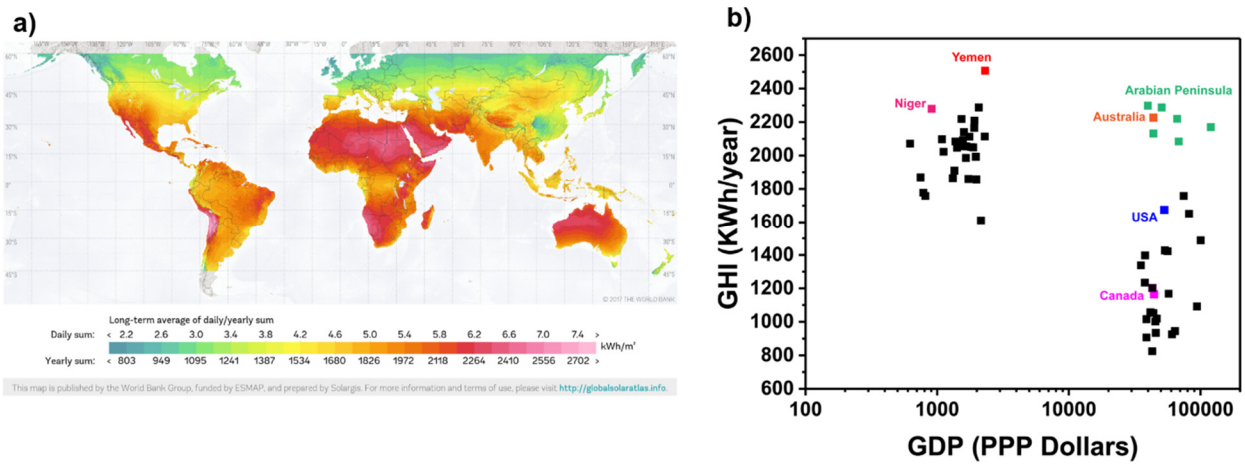

Figure 1.5. a) Worldwide average global horizontal irradiation and b) correlation between GHI and GDP of the 30 richest and the 30 poorest countries. Data from World Bank, Global Solar Atlas, GDP per capita based on purchasing power parity (PPP).

The situation depicted in **Figure 1.5 b**, clearly show that poor countries have the highest amount of insolation but they do not have the resources to exploit it. In fact, in order to have an efficient system, it is necessary to create a smart power-grid that integrates small and large scale production of electricity based on PV. This process of integration is still expensive and require high amount of energy.[7] Growth in energy use and emissions will be dominated by developing countries, as they try to close the large disparity with the developed countries, thus the use of cleaner energies, such as solar and wind in those regions would be beneficial. Even if silicon solar cells can be a good choice, less energy-intensive production of PV technologies could be a way to help development countries in the adoption of clean sources.

1.2.1 Solar Cell Classification

The most widely used classification scheme today focuses on efficiency and area cost. With these two metrics it is possible to obtain three different categories: first (G1), second (G2) and third generation (G3) (**Figure 1.6**).

Silicon (Si) solar cells belong to the G1 generation, and are till now, the most common PV device, with a market share of more than 85%. In the past decades, they have been widely explored and commercialized due to their relatively high power conversion efficiency (PCE) and long-term stability (more than 20 years). However, the fabrication of Si and thin film solar cells is complicated, it is energy intensive and requires high-qualified people and expensive equipment.

In the G2 generation are included all the solar cells based on thin films of semiconductor material deposited on a transparent conductive substrate and covered with a metal counter electrode (market share of 14%).

The most common semiconductors for these kind of devices are amorphous-Si (a-Si), CdTe, $CuInS_2$, $CuInSe_2$ and $CuInGaSe_2$. The maximum theoretical efficiency in the G1 and G2 devices with single p-n junction, corresponds to the thermodynamic limit and it is equal to 33.7%. This value, also known as the Shockley-Queisser limit, is due to the fact that photons with energy lower than the band gap (E_g) are not absorbed while photons with energies higher than E_g are not completely exploited as the additional energy is lost as heat.[8] The G3 generation is based on similar thin film technology but it is based on more 'novel' concept and it includes unique thin-film devices, such as dye-sensitized solar cells (DSSCs), organic solar cells (OPV), quantum dot sensitized solar cells (QDSCs), and perovskite solar cells (PSCs) along with a variety of "exotic" concepts, including multi-junction cells (tandem), hot-carrier collection, carrier multiplication, and thermos-photovoltaics. **Figure 1.6** reports the three generation on a plot of efficiency vs. cost. As visible, the G3 generation, in theory, would allow the possibility to overcome the Shockley-Queisser limit reaching high efficiency for a tenth of the cost of the current silicon-based PV.

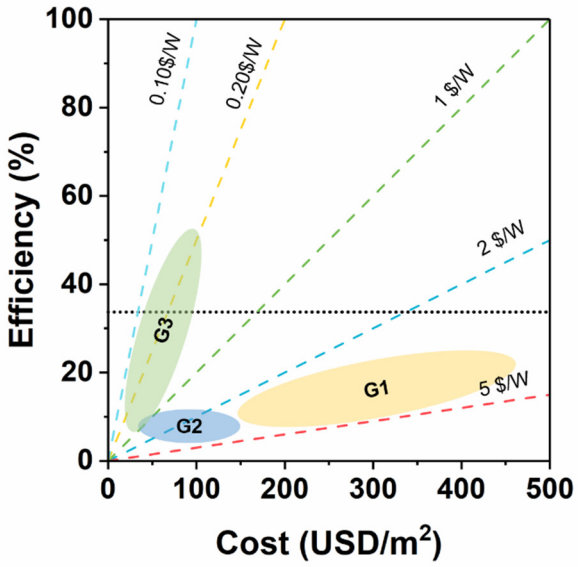

Figure 1.6. Classification of PV based on price and power.

Even if this categorization is still been widely used among the researchers, in the last years it has been observed that it may not adequately describe the modern PV technology landscape. For example, Jean et al., have observed that current PV devices do not fall in the marked zones: nearly all modern G1 and G2 technologies appear close to the zone designated G2, and up to now, no third-generation technology has approached the zone marked G3 (**Figure 1.7**). [9]

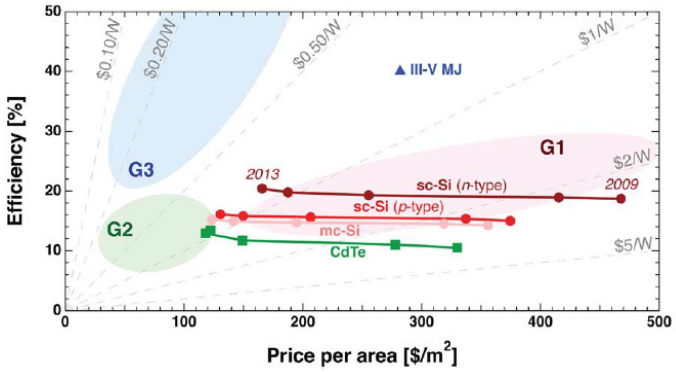

Figure 1.7. Classification of PV based on price and power with superimpose the real actual price of some PV technologies. Reproduced from Ref. [9] with permission from the Royal Society of Chemistry.

1.2.2 Taking in account the environmental-impact of PV technologies

The recent Paris Agreement of COP21 confirmed the goal of limiting global temperature increase well below 2 °C and acknowledged the need to reduce the greenhouse gases emission. In this framework, the choice of PV technologies should not be relegated only to its cost, but it should be taken in account along with its environmental impact.

To evaluate the environmental impact of a technology it is necessary to resort to some kind of indexes. In this particular case three main parameters will be used: the cumulative energy demand (CED), the energy payback time (EPBT) and greenhouse gases emissions rate (GHG CO_2 ER).[10]

Briefly, the CED refers to the amount of primary energy used within the entire life cycle of the product from raw materials extraction until end-of life stage including installation, transportation and energy-mix used. The EPBT is defined as the time required for the solar PV system to generate the same amount of energy used in its entire life cycle starting from raw materials extraction up to construction and decommissioning phase. The CO_2 ER, equals the carbon footprint per kWh electricity generated. All these factors can be estimated theoretically by Life Cycle Assessment (LCA) methodology. In general, LCA allows to estimate and assess the environmental impacts attributable to the life cycle of a product. [10] In recent years various works used LCA to estimate the environmental performance of different kind of PV technologies. As the results of LCA depends by many factors, from the geolocation of the PV up to the PCE at the time of the study, in this specific case the CED, EPBT and GHG CO_2 ER are estimated considering a best, worst and average case scenario, in which the best and worse values are the single values found in recent literature while the average values is obtained by averaging different recent studies. [11-15]

The comparison among representative PV modules is shown in **Figure 1.8**. Compared to thin films and DSSC, QDSC and PSC technologies, mono- and poly-crystalline Silicon solar cells show the worst performances, with highest amount of energy necessary for their production (CED), highest EPBT and GHG. This is mainly due to the energy intensive process of crystalline silicon production that involves several steps, including silicon purification, wafer production, cell/module processing, module encapsulation, equipment manufacturing, and framing. Regarding the EPBT, it has to be noted that it decreases with the efficiency of the PV system, thus the worst case of Silicon PV can be also related to old efficiency data. Furthermore, the silicon production process creates a large amount of waste materials increasing its environmental impact, reflected in the high values of GHG. GHG emissions data for wind power and hydropower are in average around 26 g $CO_{2\text{-eq}}$/kWh and 38 $CO_{2\text{-eq}}$/kWh, respectively.[16] Wind in this context is the cleanest energy, however is highly geo and time dependent. The higher impact of solar PV is mainly due to module manufacturing process, however it still resulting better environmental impacts in comparison to hard coal plant that has an emission range of 750–1050 g $CO_{2\text{-eq}}$/kWh.[17]

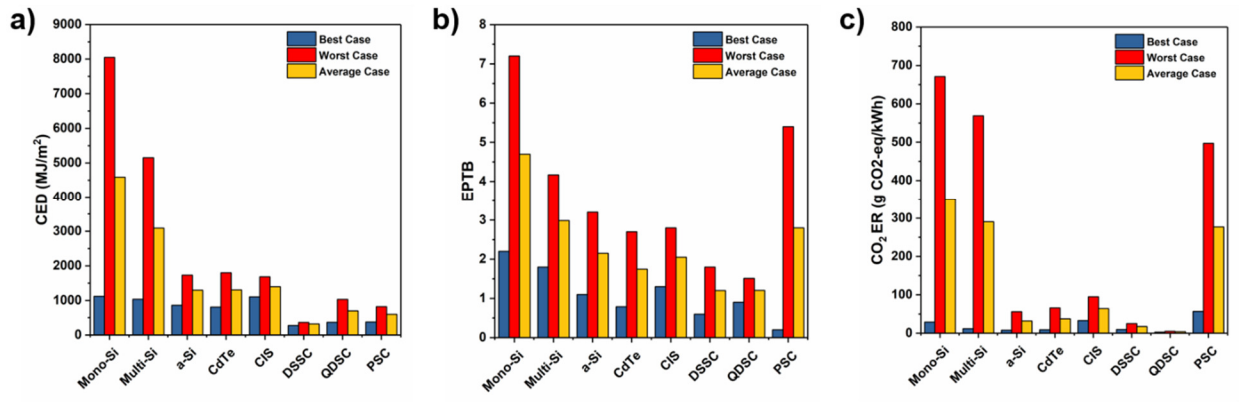

Figure 1.8. Comparison among representative PV modules of a) CED, b) EPTB and c) GHG CO_2 ER

From these data, it is clear that different PV technologies, at similar price per Watt, have very different environmental impact. In particular the CED and GHG indexes give an idea of how much energy is required and how much pollution is emitted for the production of a particular solar cell. In this context, 3rd generation solar cells can be compared to other low impact green renewable resources, such as wind and hydropower. New technologies, such as DSSCs, QDSC clearly shows low values, while PSC still presents high GHG emission. However, it should be noted that PSC method of fabrication and performance are still at lab-scale and are in constant improvement. In particular, in GHG emission, the lifetime of the cell significantly impacts its value, emphasizing the role of device stability in order to develop more environmentally sustainable perovskite solar modules. As PSC are already close to more than 24% in PCE, with an ambitious

step to over 20% module efficiency in a durable device, they could be considered in all effects one of the clean PV technologies.

At similar price points, compared to classical Silicon based PV, thin-film based solar cells, are more environmentally friendly, while c-Si and m-Si can be classified as high energy intensive and GHG emission. The lower environmental impact of thin films solar cells is mainly due to the fabrication process, as it can use 10 to 1000 times less material than c-Si, reducing cell weight per unit area and increasing power output per unit weight.

In the near future, aside considering the price per watt of a PV technologies, the energy and CO_2 emission required for their production and distribution should be also taken into consideration.

1.3 Basic Definition for Solar Cells

A standard technique to measure the solar cells performance is a current-voltage (I-V) or current density – voltage (J-V) curve. In order to obtain such curves, it is necessary to sweep the voltage with a device able to control the load, such as a potentiostat. Considering the multitude of working principles of different solar cells, only the general parameters of the I-V(J-V) curves will be introduced. Generally, these parameters are employed to compare results from different laboratories.

- ***Air Mass 1.5G (AM 1.5G):*** it is the standard solar spectrum utilized to compare solar modules. In general, while passing through the atmosphere, the sunlight is attenuated by scattering and absorption phenomena: the more atmosphere through which it passes, the greater the attenuation will be. The spectrum after travelling through the atmosphere to sea level with the sun vertical is referred as AM 1. In general solar panels do not operate under this condition but they usually are at certain angle respect to the sun. For this reason, and for commercial ones as well, as standard a value of AM 1.5 has been chosen. AM 1.5 means the light irradiated on the earth after passing through an atmosphere 1.5 times thicker than the real one. This value correspond to a zenith angle of 48.2°. This spectrum represents the average solar spectrum along the year for the country at temperate latitudes (USA, Europe, China, Japan).

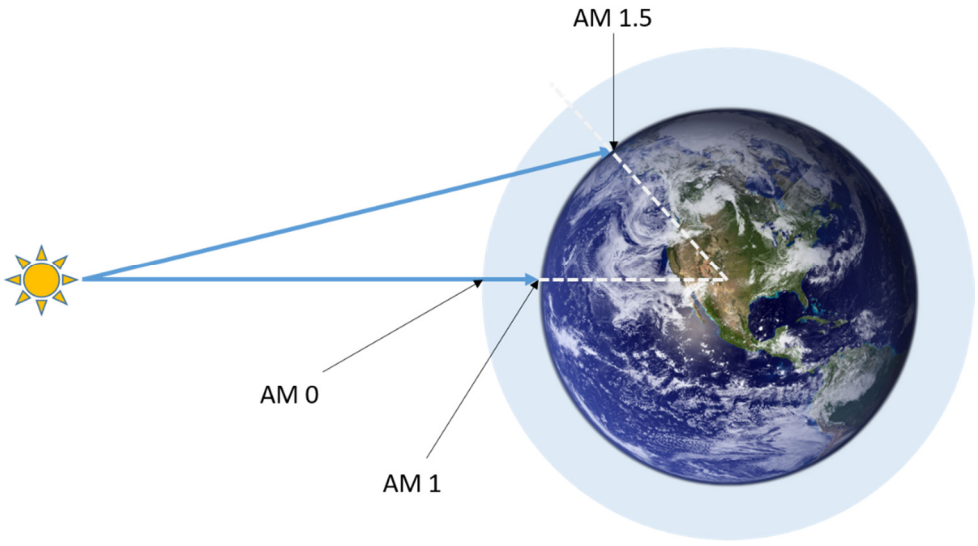

Figure 1.9. Schematic for the definition of Air Mass

- ***Short Circuit Current (I_{SC}) and Short Circuit Current Density (J_{SC}):*** I_{SC} represents the current produced through the cell when no external load is applied (e.g. the two electrodes are connected, V=0 and the resistance tends to zero) while the short density current it is the current value averaged over the area.

- ***Open Circuit Voltage(V_{OC}):*** it is the potential difference generated by a solar cell under illumination when there is no supply of current (e.g. the two electrodes are not connected to anything, I=0 and the resistance tends to infinite)

- ***Fill Factor (FF):*** it is the ratio between the maximum power generated by the cell (P_{MAX}) and the theoretical maximum given by the product of V_{OC} and I_{SC}. P_{MAX} is obtained by the product of the maximum current (I_M) and maximum potential (V_M).

$$FF = \frac{V_M I_M}{V_{OC} I_{SC}}$$

- ***Power Conversion Efficiency (η, PCE):*** it is defined as the ratio between the P_{MAX} and the optical incident power (P_{in}).

$$\eta = \frac{P_{MAX}}{P_{in}} = \frac{FFV_{OC}I_{SC}}{P_{in}}$$

In **Figure 1.10** is reported a typical I-V curve of a solar cell. Under dark conditions, the curve presents a strong asymmetry and shows a typical diode behaviour. Under light conditions, the curve shifts towards the IV quarter due to the generation of a photocurrent.

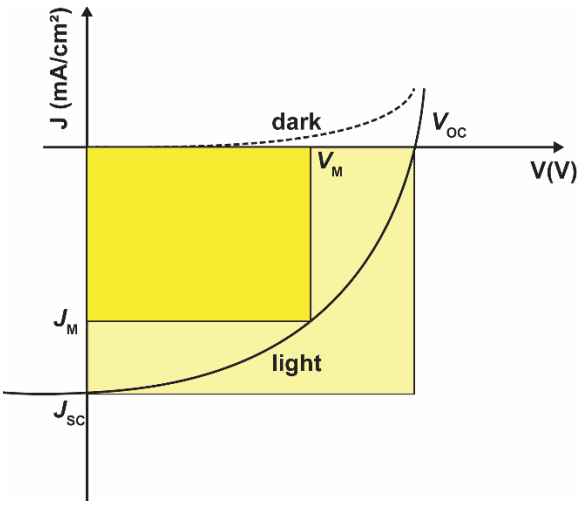

Figure 1.10. Typical J-V curve of a PV device.

1.4 Overview on Photoelectrochemistry Systems

In this section it will be given an overview on semiconductors and electrolytes and the kind of junctions formed when they are in contact with each other. This section focuses on bulk materials but the basic ideas can also be applied to mesoporous systems, such as DSSCs and QDSCs. The first investigation of a semiconductor-liquid interface was undertaken by E. Becquerel in 1839, motivated by photography. He took a solutions containing a silver halide salt (AgCl) and noted that, under illumination, a current was produced between two platinum electrodes immersed in the electrolyte.[18] This result, termed the "Becquerel effect", represented the first reported photovoltaic device. Only in the '60s, led by the great progresses in the field of semiconductor solid state physics, the explanation of this phenomena was given thanks to the work of Brattain and Garret and subsequently Gerischer, who undertook the first detailed electrochemical and photoelectrochemical studies of the semiconductor–electrolyte interface.[19, 20]

In the 1972, the seminal work of Fujishima and Honda showed the potential application of photoelectrochemical systems for solar energy conversion and storage.[21] In their work, an n-type semiconducting metal oxide, TiO_2, was used as photoanode; under illumination it showed that the oxidation of water to oxygen could be achieved at significantly more negative potentials compared to the standard redox potential of the H_2O/O_2 redox couple. This result showed that it might be possible to use sunlight to split water into hydrogen and oxygen. Today, this process is generally known as photoelectrolysis.

1.5 Semiconductor materials

The quantum theory of solids presents a complete description of the energy levels in a semiconductor, its charge carriers and how they move.[22, 23] In general, in a single atom, there is a very rigid structure for the energy levels of electrons. Instead, when a solid material forms, a certain number of atoms merge together and, in particular, in a crystalline solids the atoms assembled together in periodic arrangement in order to minimize the energy of the system. The separation between the single atoms becomes comparable to their atomic size, and their atomic orbitals combine to form molecular orbitals, with a spacing between the discrete energy levels that decreases with increasing number of atoms. When the number of atoms is large enough, the energy levels are so closely spaced that they appear continuous, forming an energy band. The filled energy states correspond to the valence band (VB, its upper edge is denoted as E_V) and the empty states correspond to the conduction band (CB, its lower edge is identify as E_C). The cut-off between the occupied and unoccupied states takes the name of *Fermi level* (E_F).

In a metal the bands are partly filled or they are overlapping, in this case one band is filled and the other empty. The electrons can easily move as there are plenty of states available within the band at (almost) the same energy (i.e. E_F is inside the conduction band). Instead, in a semiconductor or insulator, there is a

forbidden energy range in which allowed states cannot exist. Energy bands are permitted above and below this energy gap. The separation between E_C and E_V is called the bandgap or energy gap (E_g) (**Figure 1.11**) and E_F is between the two bands. In general we can identify as insulator all the materials with a bandgap higher than 4 eV, otherwise, for E_g lower than 4 eV the material is considered a semiconductor. Thanks to their narrow bandgap, some electrons can cross from the valence band into the conduction band after for example thermal activation. In a semiconductor thermal activation is noticeable already at room temperature or even below.

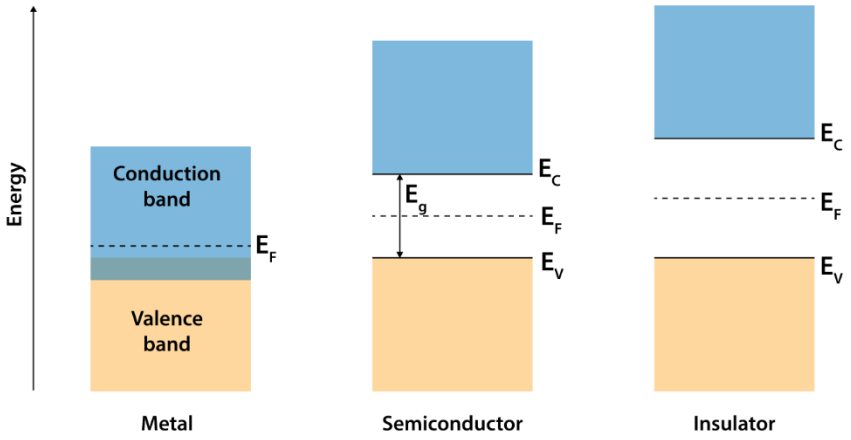

Figure 1.11. Band diagram for metal, semiconductor and insulator.

One of the most important properties of a semiconductor is the possibility to vary its resistivity by introducing different impurities. This process is known as doping and there are two kinds: if the introduced doping atoms have more valence electrons than the atoms in the material, the excess electrons will be donated to the CB and the material is n-doped. Conversely, if the doping atoms have fewer valence electrons than do the atoms in the material, the material is p-doped. The origin of the names n- and p-type is due to the first experiments in which it was found that if a metal element was pressed against a p-type material, a positive bias was required on the semiconductor to produce a noticeable current. Equally, a negative bias was required on an n-type material to produce a large current.

The density of energy states for the conduction band is given by:

$$N_C = \frac{8\sqrt{2\pi}}{h^3}(m_e^*)^{\frac{3}{2}}(E - E_C)^{\frac{1}{2}} \qquad (1)$$

While for the valence band:

$$N_V = \frac{8\sqrt{2\pi}}{h^3}(m_h^*)^{\frac{3}{2}}(E - E_V)^{\frac{1}{2}} \qquad (2)$$

where h is constant of Planck and m_e^* and m_h^* are the effective masses of electrons and holes, respectively.

In a nondegenerate semiconductor, i.e. without added impurities, the density of electrons in the band is given by:

$$\boldsymbol{n = N_C e^{-(\frac{E_C - E_F}{kT})}} \quad \textbf{(3)}$$

While the hole density can be calculated as:

$$\boldsymbol{p = N_V e^{-(\frac{E_F - E_V}{kT})}} \quad \textbf{(4)}$$

In an intrinsic semiconductor (that by definition is nondegenerate as well), the two density are equals:

$$\boldsymbol{n = p = n_i} \quad \textbf{(5)}$$

where n_i is the intrinsic carrier density.

This is because at temperature above 0 K, thermal agitation occurs and as a result, there is a continuous excitation of electrons from the VB to the CB, leaving an equal number of holes in the valence band. This process is balanced by recombination of the electrons in the CB with holes in the valence band. By equating (3) and (4) we can then calculate E_F as:

$$\boldsymbol{E_F = \frac{E_C + E_V}{2} + \frac{kT}{2} \ln(\frac{N_V}{N_C})} \quad \textbf{(6)}$$

From this equation we can derive that the Fermi level of an intrinsic semiconductor generally lies very close to, but not exactly at, the middle of the bandgap.

It also follows that for a nondegenerate semiconductor, the product of the majority carriers with the minority carriers is fixed and decreases exponentially with increasing band gap, in fact it is equal to:

$$\boldsymbol{np = N_C N_V e^{\left(-\frac{E_C - E_V}{kT}\right)} = N_C N_V e^{\left(-\frac{E_g}{kT}\right)} = n_i^2} \quad \textbf{(7)}$$

By introducing a n-type or p-type doping, the Fermi Level of the semiconductor can be shifted. The relative position of E_F depends on the electron and hole concentration, i.e., on the doping of the semiconductor. In general, for n-type doping the Fermi Level shifts towards the CB while for p-type doping, the Fermi level will be found closer to the valence band (**Figure 1.12**).

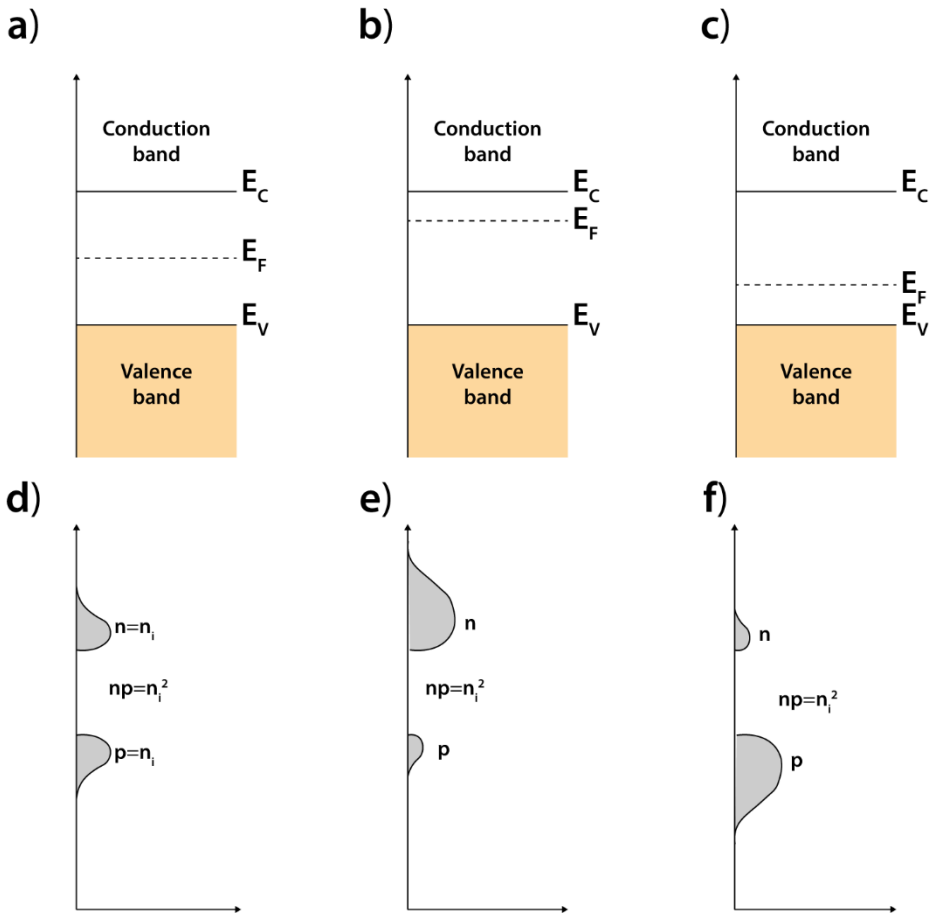

Figure 1.12. Schematic band diagram for (a) intrinsic, (b) n-type, and (c) p-type semiconductors at thermal equilibrium and corresponding carrier concentrations (d, e and f respectively).

Even if a semiconductor is nondegenerate, it can presents n- or p-type characteristics due to the presence of crystalline defects, vacancies, dangling bonds, etc. . For example TiO_2, one of the most common metal oxide semiconductor used in DSSC and QDSC, is an intrinsic semiconductor with n-type behaviour due the presence of oxygen vacancies.[24]

When a semiconductor is excited optically or by carrier injection, the thermal-equilibrium condition of a semiconductor system is disturbed ($np = n_i^2$) and processes exist to restore the system to equilibrium ($p \neq n_i^2$). If $np > n_i^2$ these processes are recombinations, while if $np < n_i^2$ we have thermal generation.

A transition in which an electron jumps from a high energy to a low energy state, is called recombination. Electron vacancies, in this case, can be thought as trapped holes. Thus, the transition can be seen as an electron-hole recombination, in which both 'particles' disappear and energy is released, for example in the form of photons of phonons.[25] Transitions within a band are not normally considered as recombination events as they take place very quickly.

In general a recombination can be radiative if there is emission of photons or non-radiative if no photons are emitted. The band-to-band recombination is an unavoidable process because it simply depends on the existence of energy bands. If the energy of an electron from the conduction band to the valence band is conserved by emission of a photon, we have a radiative recombination. In some cases the energy is conserved by transfer of the energy to another free electron or hole (Auger process). If no photons are involved, we have a non-radiative multi-phonon process. (**Figure 1.13 a**) Band-to-band transitions are more probable for direct-bandgap semiconductors which are more common among III-V compounds.

In indirect bandgap semiconductors, the dominant transitions are indirect recombination/generation via bulk traps present within the bandgap (**Figure 1.13 b**). In addition to foreign cation and anion dopants, the presence native point defects in the crystal, such as vacancies and interstitial defects creates traps for the carriers at shallow and deep levels. If the energy difference between the trap and the band is in the order of the thermal energy k_BT, the trap is considered shallow. Alternatively, if the difference is larger than the thermal energy, it is called a deep trap. The presence of traps is in general described as a band tails of a density N_t, which decreases exponentially with respect to the distance E from the band edge:

$$\boldsymbol{N_t}(\mathrm{E}) = N_C e^{\frac{E}{kT_0}} \qquad \textbf{(8)}$$

The trap-assisted recombination is described in the Shockley-Read-Hall (SRH) model of the net generation rate:

$$U = \frac{\sigma_n \sigma_p v_{th} N_t \left(pn - n_i^2\right)}{\sigma_n \left(n + n_i e^{\left(\frac{E_t - E_i}{kT}\right)}\right) + \sigma_p \left(p + n_i e^{\left(\frac{E_i - E_t}{kT}\right)}\right)}$$

Where σ_n and σ_p are the capture cross sections of electrons and holes, respectively and E_t is the trap energy. Interestingly, the net transition rate U is maximized when E_t=E_i indicating that for an energy spectrum of bulk traps, only those near the mid-gap are effective recombination/generation centers.[23]

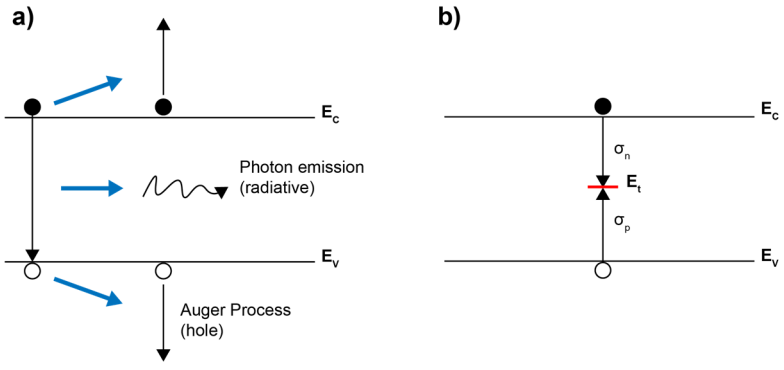

Figure 1.13. Recombination processes: (a) Band-to-band recombination (b) Recombination through single-level traps (non-radiative). Adapted from Ref 23.

1.6 Electrolytes

An electrolyte is in general a salt that dissociates in solution in the form of ions, and can behave as a conducting medium. Dissimilar from a degenerate semiconductor, in which the conductivity is dominated by one type of carrier (electrons for n-type and holes for p-type), in an electrolyte both positive and negative charges are present in equal concentration.

Considering the case of a simple one-electron redox couple, the electrochemical potential of electrons is given by:

$$\boldsymbol{\mu_{e,redox} = \mu^{0}_{redox} + kTln\left(\frac{c_{ox}}{c_{red}}\right)} \quad \textbf{(8)}$$

in which μ^0_{redox} is the formal redox energy including non-ideality effects, while c_{ox} and c_{red} are the concentrations of the oxidized and reduced species of the redox system, respectively.

In order to bridge the gap between the terminology of solid state physics and electrochemistry it should be emphasized that the Fermi level is actually the electrochemical potential of electrons in the solid. Normally, in solid-state physics, it is used the energy scale with vacuum as reference, while in electrochemistry, the potential is scaled with the standard hydrogen electrode (SHE) or normal hydrogen electrode (NHE) as reference. The electrochemical potential of electrons in a redox system is equivalent to the Fermi level $E_{F,redox}$ on the absolute scale:

$$\boldsymbol{E_{F,redox} = \mu_{e,redox}} \quad \textbf{(9)}$$

In this case, the energy of a redox couple is given by:

$$\boldsymbol{E_{F,redox} = E_{ref} - eU_{redox}} \quad \textbf{(10)}$$

in which U_{redox} is the redox potential vs NHE, e is the elementary charge and E_{ref} is the energy of the reference electrode versus the vacuum level. Even if the difference of the potential of the NHE versus an electron in vacuum cannot be precisely measured,[26, 27] it is possible to give an estimation of E_{ref}. In this thesis, we will use the value recommended by IUPAC, a reference of -4.44 eV [28] and we can rewrite the equation (10) as:

$$\boldsymbol{E_{F,redox} = -4.44\,eV - eU_{redox}} \quad \textbf{(11)}$$

Besides the Fermi level of the redox system, an electrolyte has energy states that can be empty or occupied by electrons. These energy states correspond to the oxidized and the reduced species of the redox system, respectively.

Based on the fluctuating energy level model developed by Marcus,[29] and successively applied by Gerischer to describe the solid/liquid interface between a semiconductor and an electrolyte,[30] the electronic states of a redox system can be described by Gaussian distributions, in particular:

$$D_{ox} = e^{\left[-\left(\frac{\left(E-E_{F,redox}-\lambda\right)^2}{4kT\lambda}\right)\right]} \quad (12)$$

and

$$D_{red} = e^{\left[-\left(\frac{\left(E-E_{F,redox}+\lambda\right)^2}{4kT\lambda}\right)\right]} \quad (13)$$

in which λ is the reorganization energy of electron transfer theory.[26] Briefly, the reorganization energy takes in account the energy in two relaxation processes: the one involved in the solvation shell around the reduced species following transfer of an electron to the vacuum level and the one for the reverse process, that is, electron transfer from vacuum to the oxidized species. It is normally assumed that λ is equal for both processes. Due to fluctuations in the solvation shell surrounding the molecule, the electron states of a redox system are not discrete energy levels but are distributed over a certain energy range (**Figure 1.14**).

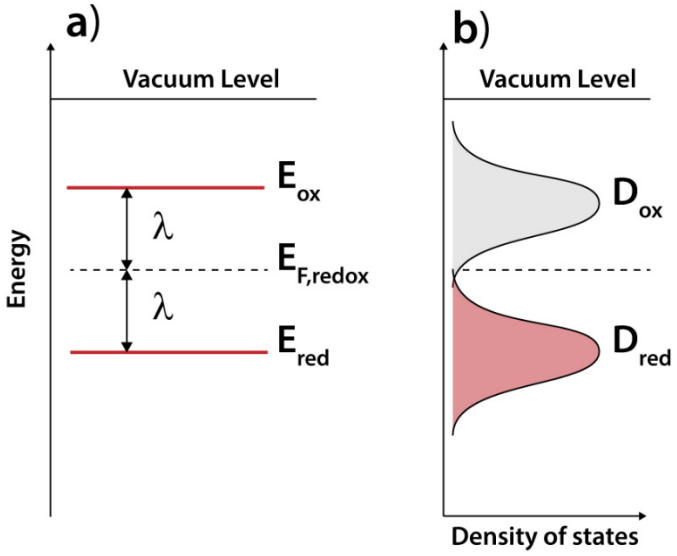

Figure 1.14. Electron energies of a redox system using vacuum as a reference level. E_{red} correspond to the occupied states, while E_{ox} to the empty states. (b) Corresponding distribution functions.

1.7 The semiconductor-electrolyte interface

When a semiconductor is brought into contact with an electrolyte containing a redox system, electrons will flow at the interface till equilibrium is achieved. In particular, at the equilibrium, the Fermi levels of the semiconductor and the redox system must be equal on both sides of the interface:

$$\boldsymbol{E_F = E_{F,redox}} \quad \textbf{(14)}$$

We can have two distinct cases: if E_F is larger than $E_{F,redox}$, electrons will flow from the semiconductor to the electrolyte creating a depletion layer, while if E_F is smaller than $E_{F,redox}$, electrons will flow in the opposite direction, from the electrolyte to the semiconductor and they will accumulate at the semiconductor interface, forming an accumulation layer. These layers affect the band structures of the semiconductor, as at equilibrium, at the interface, a potential difference occurs and the energy bands are bent upward or downward. The transfer of electric charge produces a region on each side of the junction where the charge distribution differs from the bulk material; in the semiconductor this region is known as the space-charge layer. In the electrolyte, near the interface, a double layer is formed.[31] The inner layer, known as Helmholtz layer, can be formed by adsorption of ions or molecules, by oriented dipoles, or by the formation of surface bonds between the solid and the species in solution. The outer layer, the Gouy-Chapman layer, is presented only for low ion concentration.[31] In general, for sufficiently high ion concentration, the capacitance of an electrolyte can be approximated with the Helmholtz layer (C_H).

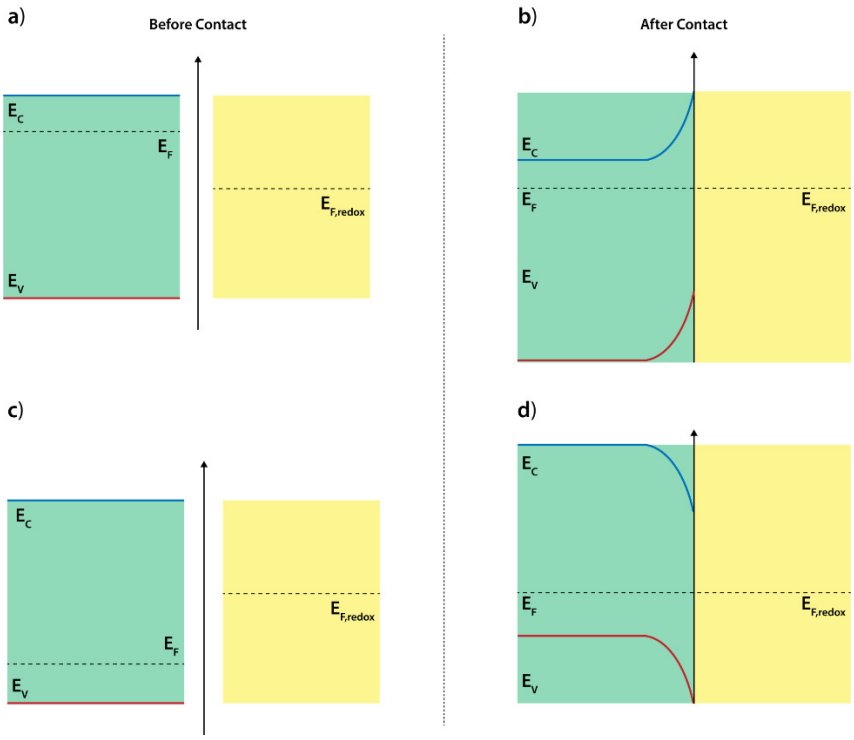

Figure 1.15. Band banding at the interface semiconductor/electrolyte. Case of E_F larger than $E_{F,redox}$: before (a) and after (b) contact E_F smaller than $E_{F,redox}$: before (c) and after (d) contact

The flat band potential (V_{FB}) is a very useful quantity as it expresses the location of the valence and conduction band edge of the semiconductor respect to the redox potential. Practically, this is the potential that needs to be applied to the semiconductor to reduce the band bending to zero. Several techniques can be used to determine V_{FB} of a semiconductor. The most common one is the so-called Mott–Schottky analysis that contemplates the measurement of the capacity of the semiconductor–electrolyte junction.[32] It is important to note that the space charge capacity of the semiconductor (C_{sc}) is in series with that of the Helmholtz layer (C_H) present at the electrolyte side of the interface. If the capacitance at the interface is measured under depletion condition, we have that $C_H >> C_{sc}$, so the effective measured capacity is that of the space-charge layer and so of the semiconductor side.[32]

In particular we can calculate quantitatively C_{SC} of the semiconductor by solving the Poisson equation. We obtain:

$$\frac{1}{C_{SC}^2} = \frac{2}{\varepsilon_0 \varepsilon_r e N_D A^2}\left(\boldsymbol{\phi_{SC}} - \frac{kT}{e}\right) \qquad \textbf{(15)}$$

Where ϕ_{SC} is the potential across the space charge layer, A is the area of the semiconductor, ε_0 is the vacuum permittivity and ε_r is the dielectric constant of the semiconductor material. The potential ϕ_{SC} can be written in function of the applied potential, ϕ_A, obtaining:

$$\phi_{SC} = \phi_A - V_{FB} \quad (16)$$

Thus, we obtain that:

$$\frac{1}{C_{SC}^2} = \frac{2}{\varepsilon_0 \varepsilon_r e N_D A^2}\left(\phi_A - V_{FB} - \frac{kT}{e}\right) \quad (17)$$

By plotting $1/C^2_{SC}$ as a function of the applied potential ϕ_A, the value of V_{FB} potential can be found as the intercept on the x-axis.

In aqueous solution the flat band potentials of most oxide semiconductors shifts by 0.059 V when the pH is changed by one unit, due to the protonation and deprotonation of surface hydroxyl groups.[27]

The energy positions at the surface for several semiconductors in contact with aqueous solutions is reported in **Figure 1.16**. It is very useful to know the band edge positions of a semiconductor, as it determines the maximum reduction and oxidation potentials of the photogenerated electrons and holes.

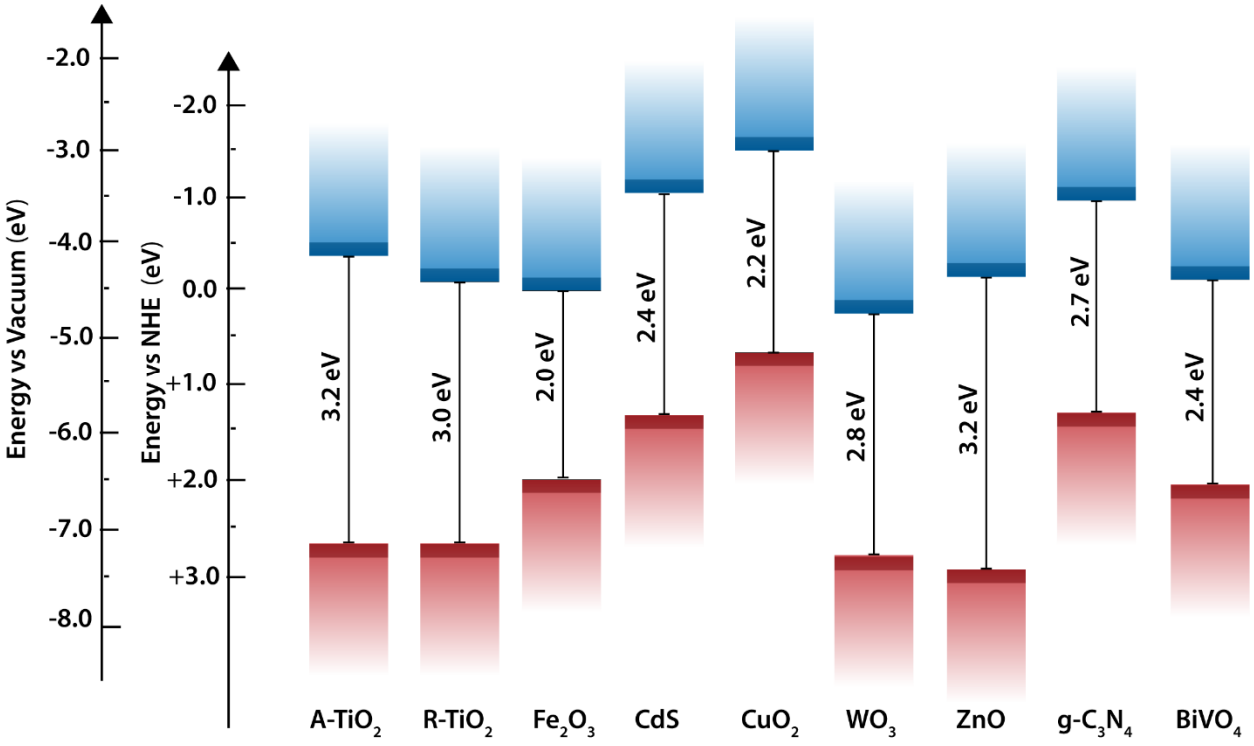

Figure 1.16. Band structures of common semiconductors used in PEC applications. The diagram is valid for a pH of 7. The valence and conduction bands are represented as thick lines as there is an uncertainty of few tenths of eV in the band edge positions.

2 THE KEY CHALLENGE TO HIGH EFFICIENCY: THE ROLE OF CHARGE TRANSPORT LAYERS IN CHARGE INJECTION AND TRANSPORT

As seen in Chapter 1, in order to be competitive on the market with price per watt similar to the silicon devices, the so-called 3rd generation solar cells still need further improvement on the performance and stability sides.

Independently of the architecture, all nanostructured solar cells face the problem of charge recombination and collections. In general, in any device in which photocarrier generation occurs, there is the necessity that these charges (excitons) reach, by drift, diffusion or both mechanisms, the charge-separating interface without recombining.

In order to have high efficiency solar cells, one of the key point is to suppress (or reduce as much as possible) the recombination pathways and improve the charge injection and transport from the absorber material towards the electrodes. In fact, even if it is possible to design organic or inorganic materials with an extended absorption range towards longer wavelengths, if the solar device presents high recombination pathways the efficiency will be limited. Furthermore, in most cases, the device will present also a reduced stability due to for example, photo oxidation of the absorber.

To control the charge collection while reducing the recombination, there are two main parameters that it is necessary to optimize:

(i) *Minimization of the energy barriers required for charge extraction.* During the transport from the absorber to the contact, the loss of energy due to discontinuities of the valence band (VB) or the conduction band (CB) should be minimized. The amount of charge injected from the absorber to the electrode is mainly determinate by the energy barrier at the interface between the two materials. This difference can be controlled by engineering the interface contacts, to increase charge transport and maximize the open circuit voltage.

(ii) *Selective extraction of charges.* The contacts should show some selectivity for charge collection, such that there is a selective extraction of a carrier type while blocking the opposite one. Charge transport layers can be used to improve the selectivity of the contacts. These layers should have wide band gap and suitable energy levels respect to the absorber material and the electrodes.

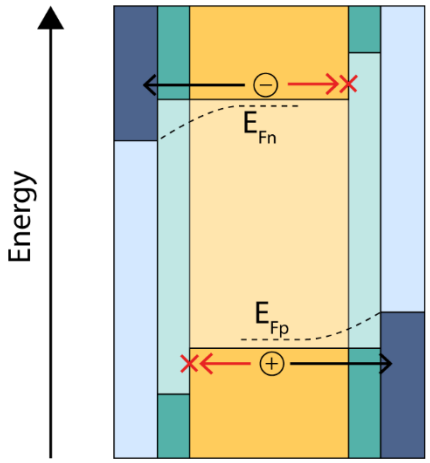

Figure 2.1. A driving force is required (shown by a gradient in the quasi-Fermi levels E_{Fn},E_{Fp}) to transport the photogenerated charges to an external contact. Electron will travel to the photoanode (left contact) while the holes has to reach the cathode (right contact). The contacts have to be selective to one type of charge carrier, to prevent positive and negative charges from reaching the opposite contact.

Different strategies can be implemented to improve these interfaces and address the issue of charge recombination and improve the charge collection. In particular, charge transport layers (CTL), such as electron transport layer (ETL) and hole transport layer (HTL), can play a fundamental role in the charge transfer from the absorber to the electrode and act as selective contacts for the carriers.

As the specific recombination pathways and charge injection mechanism can differ for each type of solar cells, in this chapter, the different architectures of DSSC, QDSC and PSC will be introduced and their recombination mechanisms will be analyzed. Furthermore a brief overview of different strategies to modify the CTLs for reducing the recombination will be presented.

2.1 Dye Sensitized Solar Cells

Dye-sensitized solar cells have taken up broad interest as a promising low-cost solar cell technology since they were first reported in 1991. DSSCs employ specific materials which their scope is optimized for specific cell functions such as photon absorption, charge separation, and charge transport.

The proof of concepts of the possibility of using dye molecules as light harvester for generating photocurrent started to appear in literature at the end of the '80s.[33, 34] However, these devices were showing a very limited photoconversion efficiency, mainly due to the poor optical density of the layer, determined by the low specific surface area of the investigated materials. In 1991, M. Graeztel and O'Regan proposed a revolutionary concept in the field, introducing a mesoporous film composed by small nanoparticles (size smaller than 20 nm) as scaffold for the light-harvester. The as-realized device showed efficiency up to 7%.[35-37] Since then, over the last 20 years, devices based on DSSC architecture have attracted a massive

increase in research effort, leading to significant advances in PCE, reproducibility and stability. In the past few years, renewed interest for this kind of devices has emerged, thanks to discoveries in the design of new dyes and electrolytes, boosting the PCE up to 14% [38-40].

The general structure of a DSSC (**Figure 2.2 a**) comprises three main parts: the photoanode, the cathode and the electrolyte. The photoanode consists of a transparent conductive electrode, usually a glass substrate coated with a transparent conductive oxide (TCO) such as fluorine tin oxide (FTO) or indium tin oxide (ITO); a mesoporous metal oxide semiconductor (MOS, such as TiO_2) film sensitized by a monolayer of dye molecules grafted on oxide surface. The electrolyte usually is an iodide/triiodide redox couple dissolved in acetonitrile and the cathode consists of a platinum-coated FTO.

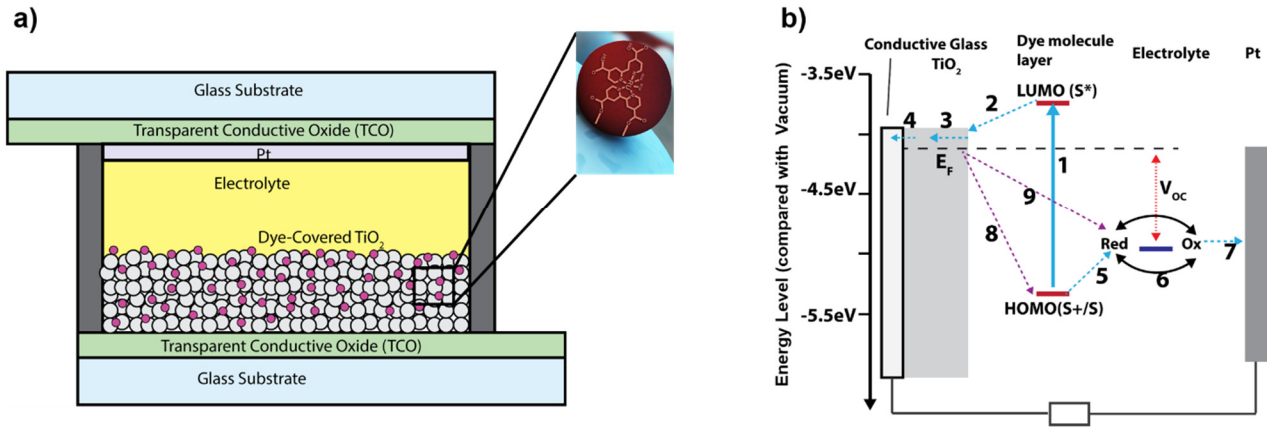

Figure 2.2. a) Schematic of the components of a DSSC. b) Basic working principle of a DSSC.

Compared to a traditional silicon solar cell based on a classical p-n junction, in DSSCs the absorption of light and separation of the charges are two separated phenomena, occurring in different regions of the cell. The basic working principle of a DSSC is illustrated in **Figure 2.2 b**. Upon light absorption by the dye molecule (process 1), electron injection into the CB of TiO_2 (process 2) occurs. The electrons in the TiO_2 CB electrons diffuse towards the electrode and are subsequently collected by FTO substrate (process 3-4). On the other side, the oxidized dye is regenerated by the hole injection into the electrolyte (process 5) and by diffusion the holes reach the counter electrode (process 6), where they are reduced (process 7), fulfilling an electronic circuit. This process does not always take place, in fact, the electrons before reaching the FTO could also recombine with the oxidized dye molecules in the highest occupied molecular orbital (HOMO) level (process 8) or recombine with the oxidized species of the electrolyte that have not been reduced by the platinized cathode (process 9). In order to achieve high efficiency, successful suppression of these two recombination pathways is necessary.

The performance of the DSSC is mainly based on the energy band alignment of its four main components: the excited state (LUMO, lowest unoccupied molecular orbital) and ground state (HOMO) of the dye, the Fermi level (E_F) of the metal oxide semiconductor (usually a n-type material, with E_F localized close to the CB) and the redox potential of the electrolyte.

In theory, excluding any possible recombination, the amount of electron injected in the CB of the metal oxide semiconductor, and so the photocurrent, is mainly defined by the difference (band gap, E_g) between the HOMO and LUMO orbitals of the dye. Smaller E_g will give higher photocurrents due to a broader absorption of wavelengths of the sun spectrum. Of course there is a limitations: it is necessary that the LUMO is higher (less negative) than the CB of the MOS in order to have charge injection. Moreover, in order to guarantee that the dye accepts electrons from the redox couple (oxidation process), it is necessary that its HOMO level is below (more negative) of the redox potential of the electrolyte. The photovoltage in DSSCs is limited by the energy difference between the CB edge of the electron-conducting nanostructure metal oxide and the redox potential of the electrolyte (V_{OC} in **Figure 2.2 b**).

As mentioned before, compared to a traditional p-n junction based solar cell that converts light in electricity exploiting the photoelectric effect happening at the semiconductor interface, the DSSC working mechanism do not involve the charge recombination between hole and electrons, since the latter are injected from the dye into the MOS and so there is no generation of holes in the MOS valence band. Moreover, the charge transport happens in the mesoporous layer of the MOS, a layer completely separated from where the photoelectron are generated. Thus, a medium only transports a certain type of carriers, consequently decreasing recombination and allowing the high standards for the quality of materials to be relaxed and therefore manufacturing costs to be reduced.

2.1.1 Control of the recombination pathways in DSSC

Considering the kinetics of the processes occurring in the DSSC (**Figure 2.3**), it is possible to note that the time constants of the extraction of the photogenerated electrons in the FTO have similar timescale of the recombination pathways.[41] This makes the photoanode interface one of the crucial layer of the DSSC. In general, the photoanode is made by a mesoporous semiconductor material; in most cases it is a n-type wide bandgap metal oxide, such as TiO_2, that acts as ETL.

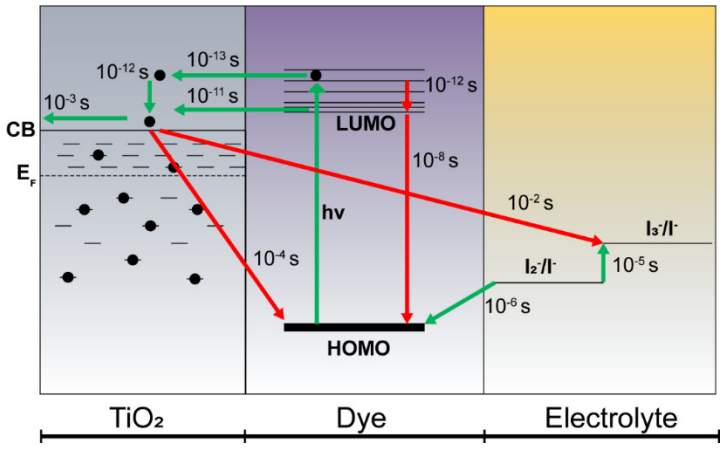

Figure 2.3. Time constant of charge injection and transport phenomena in a DSSC. Data readapted with permission.[41] Copyright 2009 American Chemical Society.

At this interface, different losses can occurs due to: differences in energy level between the dye LUMO and the semiconductor E_F; the intrinsic resistance of the semiconducting layer; and the recombination of injected electrons with the dye or with oxidized species of the redox couple. Many strategies have been applied in order to minimize these recombination paths and optimize the PCE. In particular, we will focus on the methods for increasing the charge collection, and thus the photocurrent of the DSSC by modification of the photoanode to reduce the recombination.

Due to the intrinsic morphology of this layer, made by a network of nanometer size particles (around 20 nm), the electrons move by a hopping process and grain boundaries between them play a critical role in the recombination phenomena.[42, 43] A typical thickness of the TiO_2 photoanode is around 15 µm, thus, assuming a random walk, the distance that the photogenerated electrons have to travel is in the order of 100 µm. Two main strategies can be used: reducing the path that the electrons have to travel or improving the electron transport in the TiO_2.

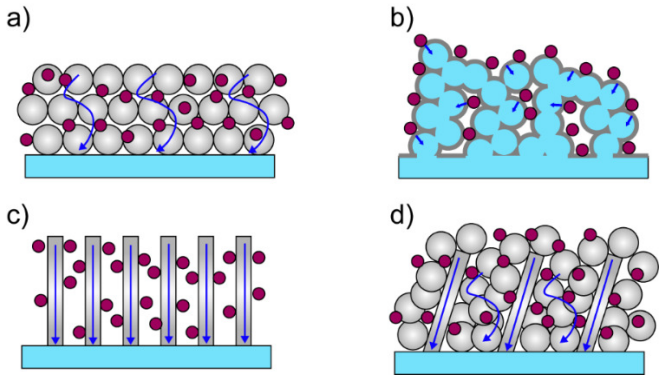

Figure 2.4. Structures of different photoanodes for DSSCs. a) mesoporous nanoparticles b) Nanostructured FTO, covered by a thin layer of the ETL. c) 1D-nanostructured photoanode. d) 1D/nanoparticles hybrid structure based film.

In order to decrease the path of the electrons, nanostructuring the photoanode or the TCO is among the most promising options. For example, the FTO can be grown as nanowires or as a nanoporous matrix on which a thin layer of TiO_2 is deposited. In these kind of architectures the transparent electrode is extended deep within the semiconductor framework.[44-46] Even though this approach showed enhanced charge collection and improved the efficiency, the absolute performance are still quite limited due to the reduced surface area and the poor crystallinity of the TiO_2 layer. Furthermore this approach requires complicated methods to grown the photoanode that hinder the possibility of a future commercial application (**Figure 2.5**).[44]

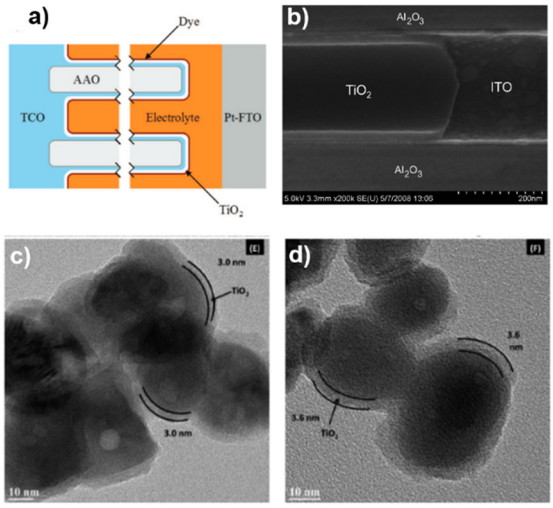

Figure 2.5. (a) Concentric nanotube DSSC photoanode with ITO lining the pores; (b) Cross-sectional SEM image of a TiO_2 tube cleaved to reveal the i-ITO tube beneath. Adapted with permission.[46] 2008 Copyright American Chemical Society. (c,d) TEM of TiO_2 layers deposited by ALD on nanoITO cores. Adapted with permission.[44] 2014 Copyright American Chemical Society.

Structure disorder is generally considered to lead to a charge trapping–detrapping transport, thereby greatly slowing the charge transport. Thus, many researchers focused on the growth of one dimensional (1D) nanostructure of the metal oxide interface. The application of single crystalline nanowires and nanotubes can in fact, fasten charge transport compared to the mesoporous network.[47] For example, in an anatase TiO_2 nanoparticle film, the electron diffusion coefficient is more than two orders of magnitude lower than in single crystals.[48] 1D nanostructures such as nanotubes (NTs), nanowires (NWs), nanorods (NRs), and nanofibers have been proposed. In the case of 1D nanostructures the morphology and the crystallinity of the TiO_2 play an important role in the charge transport and recombination. For example, polycrystalline TiO_2 NTs used as photoanode in DSSC have shown to improve the efficiency mainly due to an increased collection efficiency while the charge transport is similar to nanoparticles matrix (**Figure 2.6 a**).[49] Decreasing the disorder inside the nanotube can lead to a further improvement of the final PCE, due to the

simultaneous improvement of the charge transport along with the reduction of recombination **Figure 2.6 b-f**).[50, 51]

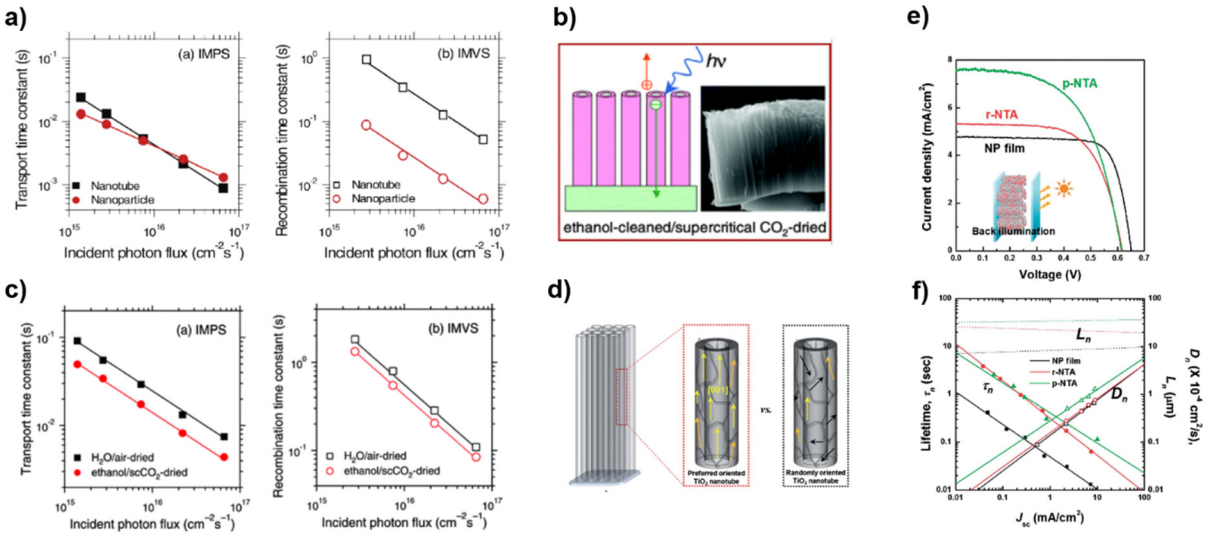

Figure 2.6. Comparison of (a) transport and recombination time constants for NT- and nanoparticle-based DSSCs as a function of the incident photon flux for 680 nm laser illumination. The NTs based DSSCs shows an increased collection efficiency while the charge transport is similar to nanoparticles matrix. ***Reproduced with permission.*** **[49]** ***Copyright 2007, American Chemical Society*** **b) Bundle-free and crack-free nanotube arrays after supercritical CO_2 drying treatment. c) Comparison of the transport time constant and recombination time constant as a function of the incident photon flux for NTs-based photoanode treated with CO_2 and without. The CO_2 treatment improves the charge transport along with the reduction of recombination.** ***Reproduced with permission.*** **[51]** ***Copyright 2007, American Chemical Society*** **d) Schematic diagrams of the preferentially oriented TiO_2 nanotube arrays (P-NTA) and the randomly oriented TiO_2 nanotubes (R-NTA). e) J-V curve and f) Charge dynamic properties of P-NTA and R-NTA.** ***Reproduced with permission.*** **[50]** ***Copyright 2012, Royal Society of Chemistry.***

Based on these results, a further improvement in the performance can be obtained by employing NWs arrays in which each individual nanowire is a single crystal with a highly oriented crystallographic structure (**Figure 2.7**).[47, 52]

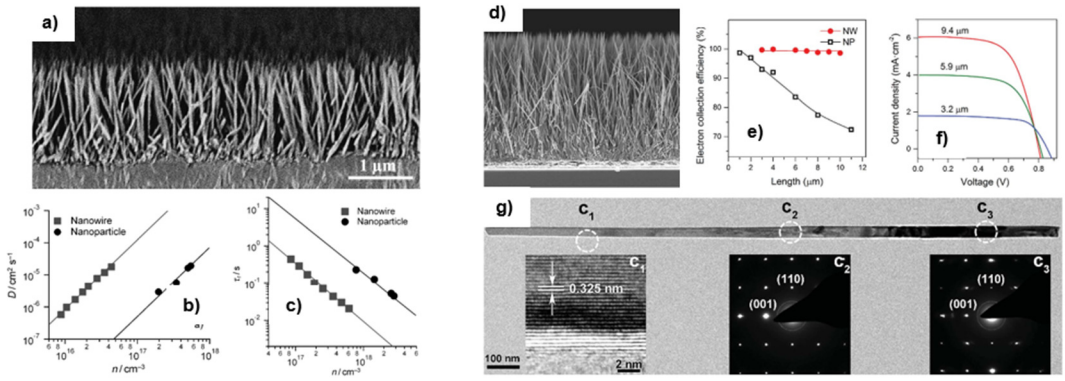

Figure 2.7. a) FE-SEM cross-sectional images of NW arrays on FTO-coated glass; b) electron diffusion coefficients (*D*) as a function of the photoelectron density (*n*); c) Comparison of recombination lifetimes for rutile NW- and NP-based DSSCs

as a function of the photoelectron density with laser illumination at 680 nm; *Reproduced with permission*.[47] *Copyright 2011 John Wiley and Sons* d) Microstructure characterization of the long and well-separated TiO_2 NWs. e) Dependence of the electron collection efficiency on the NW length and NP-film thickness. (f) Comparison of the current density–voltage characteristics of the NW-based cells. g) TEM images of part of a single NW. *Reproduced with permission*.[52] *Copyright 2018 Royal Society of Chemistry*

While the application of 1D materials can lead to an increased transport of the electrons, they have a main drawback: their low surface area to volume ratio due to their relatively large diameter (ca. 100 nm) and/or free space between them, significantly limit the possibility of dye loading. A possible solution is the use of hyper branched arrays, composed of a combination of nanowire (NW)-nanosheet (NS)-nanorod (NR). Optimized structures showed two-fold increase of the dye-loading capacity compared with the single nanowires counterpart, reaching a remarkable PCE of 9.09%.[53] However, the main contribution to the enhanced PCE comes from a larger dye loading and reflectance of the photoanode. In fact, due to the presence of a high number of interfaces the charge recombination is highly increased. [53] An elegant solution is the use of a porous network combined with 1D crystalline nanowires. This architecture can combine the high specific surface of mesoporous nanoparticle films, and the fast electron transport and the light scattering effect of single-crystalline nanowires.[54, 55] A recent evolution of this idea has been reported by Snaith et al. with the synthesis of a mesoporous single-crystal (MSC) TiO_2 anatase film. These high-surface-area anatase single crystals showed remarkable improvement in charge transport compared to nanoparticles and they were employed to fabricate all-solid-state, low-temperature sensitized solar cells with a PCE of 3%[56] (**Figure 2.8**).

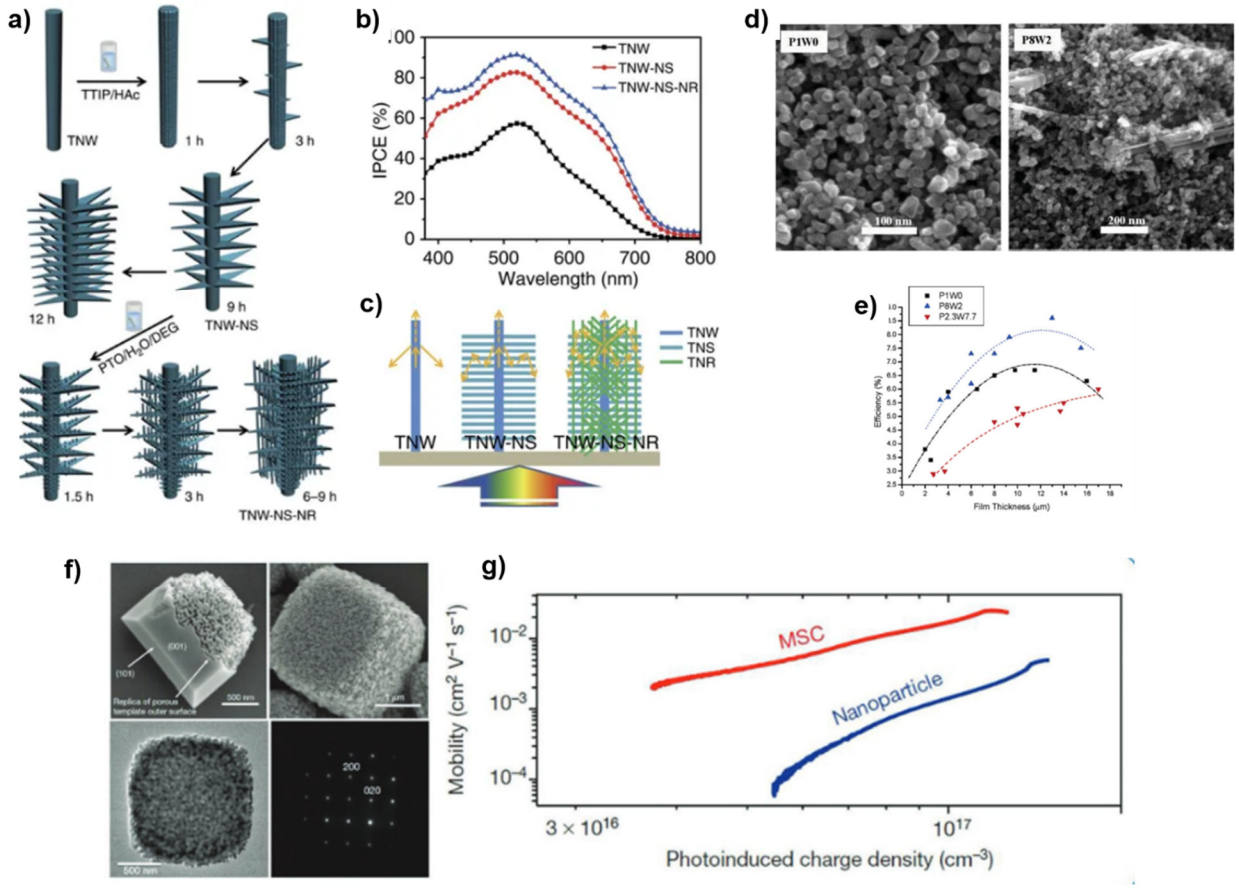

Figure 2.8. a) Schematic diagram showing the growth process of hierarchical TiO_2 structures. b) IPCE spectra of DSSCs based on TNW, TNW–NS and TNW–NS–NR array photoanodes with similar film thickness. c) Schematic illustrations of light reflecting and scattering. *Reproduced with permission*. [53] *Copyright 2014 Nature Publishing Group.* d) Cross-section SEM images for photoanodes of pure NPs (left) and NPs/NWs (right). e) Efficiency as a function of photoanode thickness for different NP/NW ratios. *Reproduced with permission.* [54] *Copyright 2006, American Chemical Society.* f) SEM and TEM images of mesoporous TiO_2 single crystals with diameters of ≈1 μm. c) Comparison of charge mobility between photoelectrodes composed of mesoporous TiO_2 single crystals (red curve) and nanoparticles (blue curve). *Reproduced with permission*. [56] *Copyright 2013 Nature Publishing Group.*

Although, ideally 1D hierarchical TiO_2 structures could be perfect photoanodes, they are still far from reaching high performance. Their synthesis also require complicated process that, as there is not enough increase in the performance, it does not justify the increment in the cost.

A particularly interesting approach for increasing the charge transport and collection in the photoanodes is the formation of an energy gradient that directs the electrons toward the substrate. In this method, by using composite materials that differ by their CB potential, it is possible to tune the band alignment inside the photoanode and enhance the charge collection properties, thus reducing the recombination pathways. This approach requires a very specific electrode design which ensures that the electrons will not encounter energy barriers (the more negative material) while diffusing to the FTO.

Core/shell metal oxide structures can create a favorable path for the electrons by tuning the band alignment inside the nanoparticles. In this approach, it is fundamental to have a correct coverage of the photoanode, without creating barriers between the TiO_2 nanoparticles. By coating the nanoparticles of TiO_2 with wide band gap oxides, such as MgO or Nb_2O_5, the surface resistance of TiO_2 can be increased, thus reducing the electron-hole recombination and the back electron transfer to the electrolyte. Furthermore, in some cases, the high specific surface area of the nanoporous coating layer can promote the adsorption of dye molecules and enhances the cell performance. For example, Nb_2O_5 has a CB 100mV higher than TiO_2 and this potential difference forms an energy barrier at the electrode–electrolyte interface, which can reduce the rate of recombination processes of the photoinjected electrons.[57] Interestingly, Bisquert et al, found that the improvement in PCE by coating with Nb_2O_5 of TiO_2 nanorods does not come from a decrease in the rate of recombination or a shift of CB of TiO_2, but it is due to an increased charge injection efficiency of the dye into the rutile nanorods, facilitated by the presence of niobium oxide coating.[58] (**Figure 2.9**)

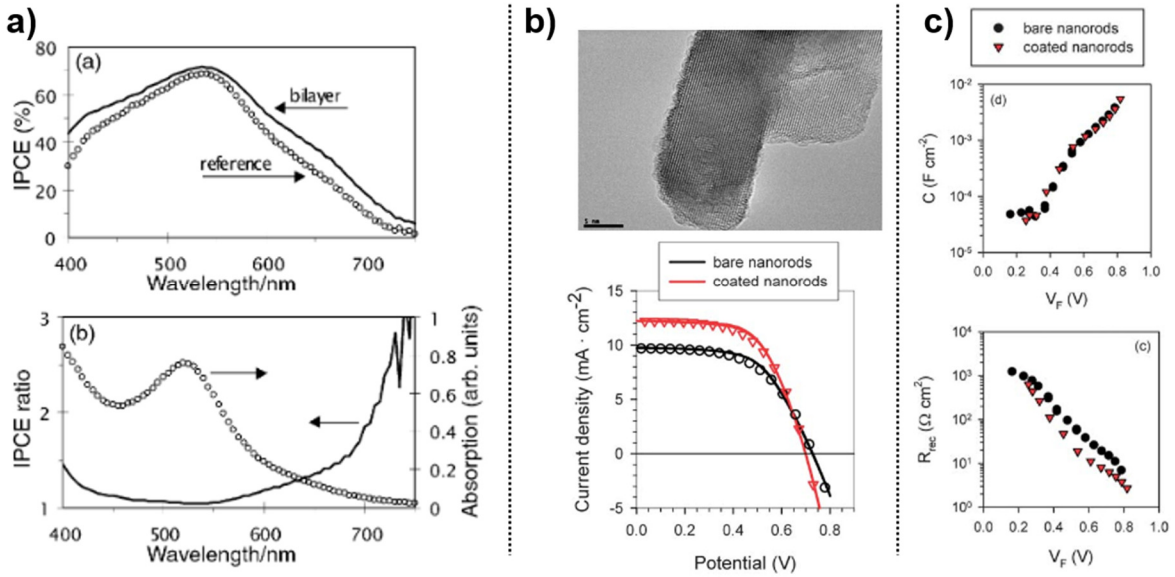

Figure 2.9. a) IPCE curves of the reference dye sensitized solar cell and the cell containing the bilayer electrode (Nb_2O_5 coated TiO_2 nanoparticles) and the ratio between the IPCE values of the two solar cells as a function of the illumination wavelength revealing its wavelength dependence. *Reproduced with permission.*[57] *Copyright 2000 Royal Society of Chemistry.* b) TEM image (top image) of the end of Nb_2O_5 coated TiO_2 nanorod presenting the rutile crystal surrounded by an amorphous border which includes Nb_2O_5; J-V curve of the DSSC with and without Nb_2O_5 coating. c) Recombination resistance and chemical capacitance obtained from impedance analysis at 1 sun illumination of bare and Nb_2O_5 coatedTiO_2 nanorod. The metal oxide coating does not influence the recombination resistance. *Reproduced with permission*[58] *Copyright 2008 Royal Society of Chemistry*

Besides the use of wide band gap materials, the most common coating strategy for TiO_2 photoanodes is to use a $TiCl_4$ treatment. The $TiCl_4$ treatment has been in use since 1993, where it was used to improve the photocurrent of Degussa P25 TiO_2 nanoparticles.[59] In general, with this treatment, a coating of crystalline

TiO_2 is formed and the main effects of this treatment are downward shift in the TiO_2 CB potential and a 20-fold decrease in the electron/electrolyte recombination rate constant (**Figure 2.10 a**). The overall result is a boost in photocurrent that improve the final PCE.[60] It may be noted that a downward shift in the CB should give a lower V_{OC} (**Figure 2.2 b**). This does not occur due to the simultaneously reduction in the recombination rate that allow the build-up of a higher density of charge in the TiO_2. This effect compensates for the downward movement of the band edge. [61]

In order to improve the selectivity of the ETL, it is possible to grow a compact layer of TiO_2 between the FTO and the mesoporous TiO_2 layer. This compact layer is much denser than the TiO_2 layer; therefore, it can reduce the contact surface area between bare FTO sites and the redox electrolyte. In this case, the improvement of PCE depends also from the dye employed. In fact, it has been observed that in the case of N719 (the most common dye for DSSCs), the PCE improves of no more than 10% while for less bulky dyes the improvement is more pronounced (**Figure 2.10 b**). This is because the Ru-sensitizer blocks the dark current at the FTO/electrolyte interface and itself is an effective ‘‘blocking layer’’ on FTO.[62] On the other side, for planar organic dyes anchored on TiO_2, it is essential the use of a compact TiO_2 layer between the FTO and the mesoporous layer in order to reduce charge recombination losses. In this latter case an improvement of 160% in PCE has been observed. This is due to the fact that the dye's orientation and its structure influence the proximity of the I_3^- from the FTO surface directly influencing the final PCE. The overall dye mono-layer thickness affects the recombination kinetics across the FTO/dye/electrolyte interface[63] (**Figure 2.10 c and d**). In general TiO_2 blocking layer can be an effective way to improve the efficiency by reducing the recombination at the FTO/mesoporous TiO_2/electrolyte interface; however it is necessary to control its thickness, as it introduces a non-negligible internal series resistance, which hinders the use of thick blocking layers, and, finally, limits the outcomes of this approach for TiO_2 –DSSCs.[64, 65]

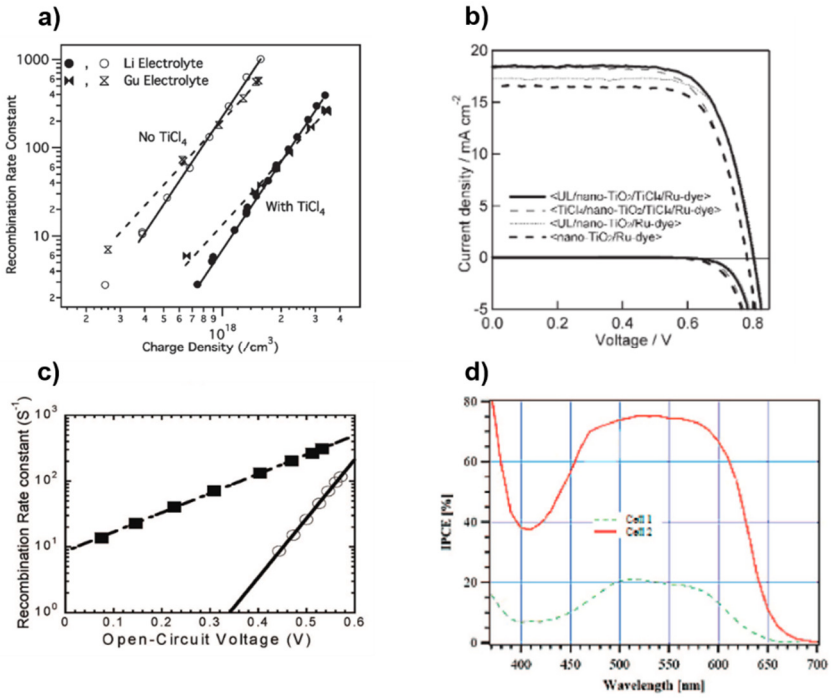

Figure 2.10. a) Recombination rate constant at V_{OC} vs charge density for cells with and without $TiCl_4$ treatment. Reproduced with permission.[60] Copyright 2007 Royal Society of Chemistry. b) Photovoltage–current characteristics curves of DSSCs by using four types of electrodes under a solar simulator, dye N719. Reproduced with permission.[62] Copyright 2005 Royal Society of Chemistry. c) Charge recombination rate constant derived from transient open-circuit voltage decay, for a DSSC with a blocking layer (open circles, solid line) and without a blocking layer (solid squares, dot-dashed line). d) Importance of the blocking layer. IPCE of two solar cells sensitized with a planar dye (Mc2). With the addition of the blocking layer, the light-harvesting efficiencies are increased (red line). Reproduced with permission.[63] Copyright 2008 American Chemical Society.

A recent clever design of Graeztel et al. eliminates the spacer between the photoanode and counter-electrode. Based on the premise that an efficient CTL has to be selective towards one of the charges (electrons or holes), this new design replaces the traditional platinum electrode with a p-type polymer semiconductor that serves as hole-selective electron-blocking layer. Contrary to the use of metal electrodes, this configuration does not electronically shunt the device. This architecture attenuates the Warburg resistance and improves the PCE up to 13.1%.[66] (**Figure 2.11**)

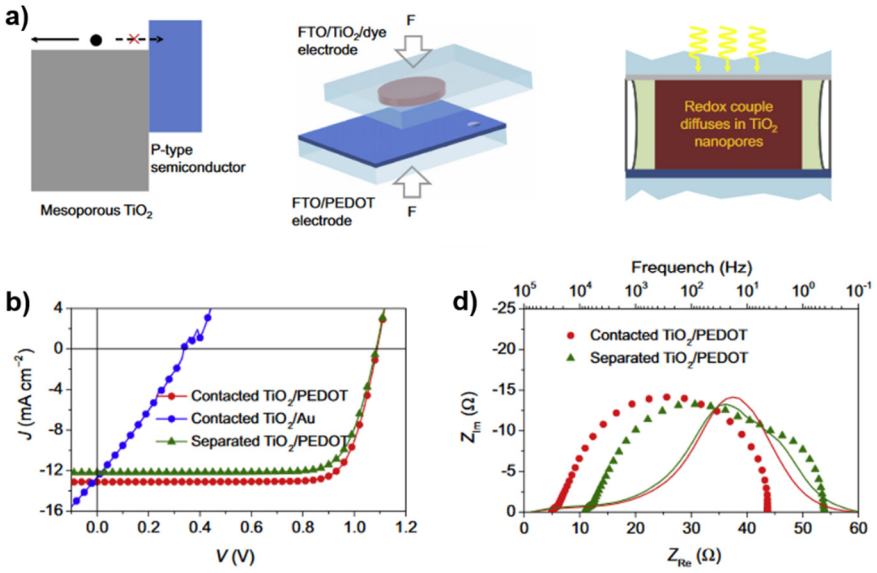

Figure 2.11. a) Type II junction alignment of the band edges for the mesoporous TiO_2 film and a p-type semiconductor layer. The p-type semiconductor serves as an electron-blocking hole-selective charge collection layer. In the DSSC with the contacted electrodes, the redox couple diffuses merely through the mesoscopic TiO_2 film. b) Current density-voltage (J-V) curves of the DSCs based on the n-p contact of TiO_2 and PEDOT, direct contact of TiO_2 and Au, and the separated TiO_2 and PEDOT collector electrodes. c) Nyquist (symbols) and Bode (solid lines) type plots of solar cells from electrical impedance spectroscopy measurement under white light. Reproduced with permission.[66] ***Copyright 2018 Cell Press.***

Researches have also tried to boost electron transport rate by controlled addition of small quantities of carbon nanotubes (CNTs) or graphene nanosheets. For a more in-depth look to the structure of CNTs and graphene, more accurate review on this topic is suggested.[67] In this paragraph it will be analyzed briefly the role of these carbon allotropes in improving the charge dynamics inside the photoanode of a DSSC. The idea behind is to create a 'bridge' to fasten charge collection in the photoanode after exciton separation and electron injection from dye to oxide (**Figure 2.12 a)**. The first appearance of CNTs in the semiconducting layer of DSSCs was reported in the work of Jang et al., in which single wall CNTs (SWCNTs) were incorporated into nanocrystalline TiO_2 films.[68] The SWCNTs addition improved the PCE of 25% due to the fact that CNTs significantly reduced the resistance of the films and facilitate electron transport within the cell. It was also observed an increased light scattering that could contribute to the improvement of the performance (**Figure 2.12 b**).

The role of CNTs was quite debated in literature, with studies, such as of Kamat et al arguing their beneficial roles. In fact, the addition of carbonaceous material in TiO_2 downshifts its CB, thus decreasing the photovoltage nullifying the benefit obtained in the boost of the photocurrent (**Figure 2.12 d**).[69] Since then, many studies optimized the CNTs loading and an improved PCE as high as 40% was obtained compared to samples without CNTs (**Figure 2.12 e**).[70, 71] The main effect of introducing CNTs is a boost of the

photocurrent due to the increased electron transport, enhanced light-harvesting efficiency, and/or high dye loading. The effect on the dye loading, up to now, is still not clear, with studies showing conflicting results.[72]

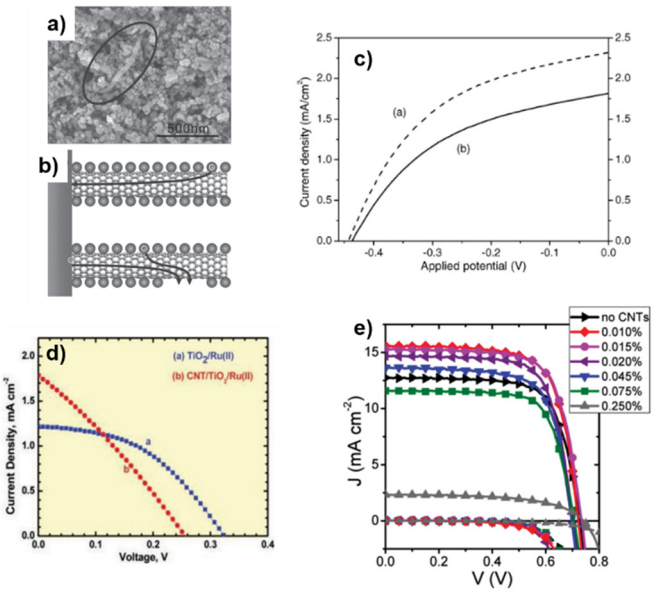

Figure 2.12. a) SEM of CNT/TiO_2 composite film indicating the part of CNTs not covered by TiO_2 nanoparticles. b) Schematic illustration for the loss of photogenerated electrons by the naked part of CNTs. ***Reproduced with permission.***[72] ***Copyright 2012 American Chemical Society.*** **c) J-V curves of DSSCs prepared with and without a-SWCNs in the TiO_2 films** ***Reproduced with permission.*** [68] ***Copyright 2004 Royal Society of Chemistry. d)*** **Single walled carbon nanotube-TiO_2 nanoparticle composite system and J–V curve under simulated sunlight.** ***Reproduced with permission.***[69] ***Copyright 2008, American Chemical Society.*** **e) Current density−voltage curves of solar cells fabricated using films with different CNT content (solid lines, AM1.5G irradiation (100 mW cm^{-2}); dashed lines, dark).** ***Reproduced with permission.***[70] ***Copyright 2013, American Chemical Society***

Similar approach was used for the introduction of graphene in the TiO_2 matrix. Yang et al. used graphene as an electron bridge in the photoanode. In that work graphene was found to act as a shuttle for electrons to the current collector, lowering recombination in the device and boosting the efficiency up to 7%. In a previous work of our group, we have shown the role of graphene in enhancing the PCE of DSSCs, by using low concentration of graphene, below the limit of percolation.[73] The use of low concentration (0.01~0.02 wt%) of graphene significantly boosts the current density compared to pure TiO_2 photoanodes, while the other cell parameters (V_{OC} and FF) do not play a major role in altering PCE. The use of electrochemical impedance spectroscopy (EIS) showed that the main role of graphene is to boost electron injection from the photoanode to the front contact, thereby significantly increasing the collection of photogenerated charges and reducing charge recombination. An excess of graphene might reduce the V_{OC}, increasing dramatically the charge recombination through direct charge transfer from the photoanode to the electrolyte (**Figure 2.13 a-c**). In other works the graphene not only was used in the mesoporous TiO_2 but also in other layers of the cell. For example, Chen et al. placed reduced graphene oxide (rGO) in both the blocking layer and in the

TiO_2 scaffold layer,[74] while Tang et al. incorporated rGO in the blocking, scaffold, and scattering layer leading to a more efficient device (η = 8.7% compared to 6. 5% for a device with just a TiO_2 layer) (**Figure 2.13 d and e**).[75] In general, in the case of graphene as for CNTs, not only an improvement of the charge transport is observed, but increased dye absorption and scattering contribute to the improved performance.

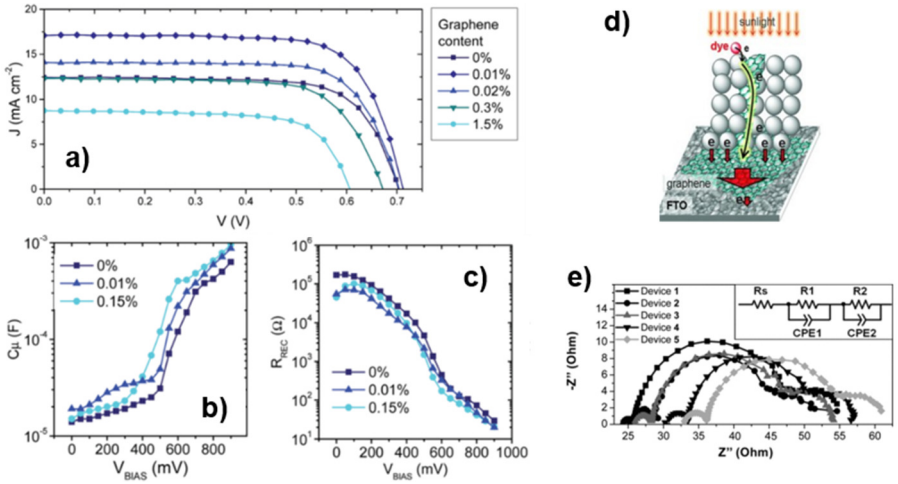

Figure 2.13. a) J-V curves of DSSCs with different content of graphene. The maximum is reached for 0.01%wt with an efficiency of 8%. Chemical Capacitance (b) and recombination resistance (c) of representative DSSCs with different load of graphene. ***Reproduced with permission.***[73] ***Copyright 2015 Royal Society of Chemistry.*** **d) DSSC with graphene as an interlayer of FTO/TiO_2 and in TiO_2 nanoparticle network. e) Electrochemical impedance spectra of device 1, 2, 3, 4, and 5 (the inset shows the equivalent circuit). Cell 1 is without graphene, Cells 2 to 5 contain different amount of graphene.** ***Reproduced with permission.***[74] ***Copyright 2011 John Wiley and Sons***

2.2 Quantum Dots Sensitized Solar Cells

The architecture of a QDSC is directly derived from DSSC. The main difference lies in the type of sensitizer used for harvesting the light: in QDSCs, the organic dye molecules are, in fact, replaced by inorganic semiconducting QDs. The other components of the cell are similar to DSSCs: the photoanode is composed by a wide-band gap MOS (also in this case, usually it is TiO_2) deposited on a conductive glass (FTO or ITO). As for the DSSC, it is necessary to add a cathode and an electrolyte or hole transport material.

In theory, the basic idea of substituting the dye with semiconductor QDs is quite trivial: as we have seen, the architecture of the two devices is very similar. This strict analogy made initially think and use exactly the same components of DSSC to realize QDSC. But this turned out to be more complicated than expected: in fact, the use of QDs instead of dyes forces the entire photoelectrochemical system to change profoundly due to reasons linked, on one hand, to the chemical compatibility between the various constituents, and on the other to the search for an optimal alignment of the bands. It was therefore necessary to study new materials. The first works on QDSCs were realized in 1990 by the group of Weller in which mesoporous TiO_2 photoanodes were sensitized by CdS QDs grown *in-situ*.[76] Up to 2007, QDSCs didn't draw much attention since their efficiency was much lower compared to their analog DSSCs due mainly to the limited compatibility of the QDs with the I^-/I_3^- electrolyte. Since then, with the introduction of polysulfide electrolyte or solid hole transport materials and the development of both materials and mechanisms following intense investigations, the highest PCE of QDSCs has been improved from 5% to nearly 13%, making them one of the more competitive emerging solar cells.[77]

The working principle (shown in **Figure 2.14**) of a QDSC is essentially similar to a DSSC. Upon illumination, the QDs absorb solar energy and electrons in the VB of the QDs are promoted to the CB, generating electron-hole couples (the so-called exciton). The excitons move towards the interface TiO_2/QDs where dissociation of the charges happens: electrons in the CB of the QDs are quickly injected into the CB of the metal oxide under the driving force of the energetic difference in the CB between the QDs and metal oxide. Successively, the electrons transfer through the TiO_2 mesoporous film to the TCO substrate and then to the counter electrode through an external load. Meanwhile, the oxidized QDs are regenerated by reduced species of the redox couple in the electrolyte, while the oxidized species of the redox couple are reduced by the electrons from the external circuit under the catalysis of CE. As for DSSC, the electron transfer process is always in competition with electron recombination paths. As shown in **Figure 2.14** in red arrows, there are four main recombination pathways in QDSCs: (a)the electrons can recombine inside the QD due to the presence of defect states, (b) the electrons in the TiO_2 CB can recombine with the holes (back transfer) of the QD at the TiO_2/QD interface, (c) recombination at the TiO_2/electrolyte interface of electrons in TiO_2 with the electrolyte, and (d) recombination at the QD/electrolyte interface of excited electron in the QD

with oxidized species in the electrolyte. Compared to the DSSCs, the presence of defects in the QDs (and also due to the fact that the QDs coverage of the TiO_2 is less efficient) aggravate the charge recombination processes. In recent years, considerable efforts have been made to address the recombination issues.

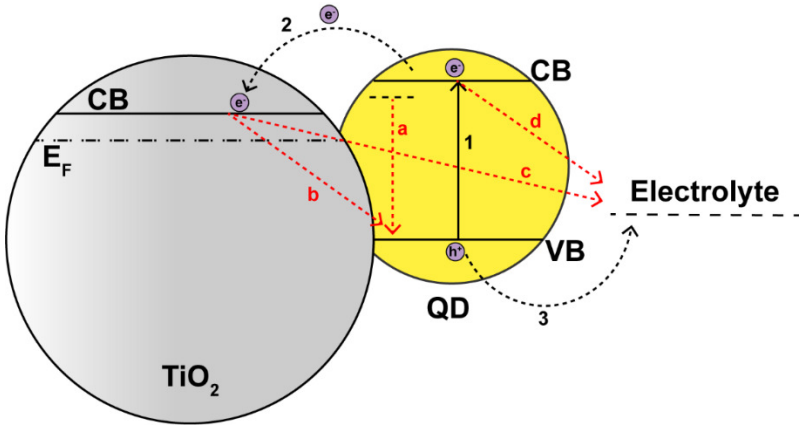

Figure 2.14. Schematic of the working principle of a QDDSC showing the four different types of recombination paths.

2.2.1 Controlling the recombination in QDSC

If the process of exciton dissociation and charge injection at the QD/MOS interface is slow, the photo-generated electrons will recombine with holes, reducing the overall efficiency of the device. Thus, controlling the charge dynamics at the QD/MOS interface is of critical importance to achieve high efficiencies. To obtain efficient charge transfer across this interface several factors should be considered: (1) the energy levels of the MOS and QDs should be aligned, to guarantee fast charge injection;[78, 79] (2) direct band gap QDs are preferable, due to their high optical absorption;[80, 81] (3) the distance between the QD/MOS (mainly determined by the length of the ligand that grafts the QD on the MOS) should be controlled to improve electron coupling. [82]

QD material engineering

One of the major charge-recombination process takes place inside QDs through defect states. In fact for nanometer-sized QDs, there is a very high proportion of surface to interior atoms. Such surface atoms have a low coordination number and high defect concentration so that the charges can be easily trapped at the surface.[83, 84] Thus, high-quality QDs have become a prerequisite for high-efficiency solar cells. One of the main advantages of QDs over organic dyes is that, due to the quantum confinement effect, it is possible to easily tune their optoelectronic properties by changing their size and composition.[83, 85] (**Figure 2.15**) Furthermore, by creating core/shell structure it is possible to finely tune the position of the energy bands

and control the charge transfer inside the QDs. Thus, in QDSCs, it is possible to control the charge dynamics and improve the charge collection, not only by engineering the photoanode material, but also by tuning the semiconductor QD itself.

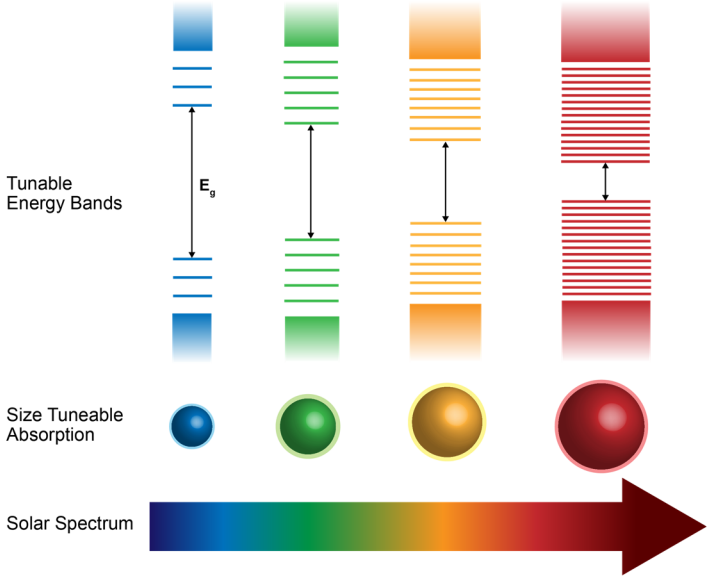

Figure 2.15. Size-dependent absorption and energy bands of QDs

There are mainly two strategies to prepare QDs: *ex-situ* and *in-situ*.(**Figure 2.16**) In the *ex-situ* method, the QDs are pre-synthesized following usually a wet-chemistry approach that forms colloidal QDs. Colloidal QDs have the advantage of presenting a very narrow size distribution, which results in well-defined optical and electronic properties in terms of absorption excitonic peaks and photoluminescence.[86] On the other hand, in the *in-situ* approach, QDs are directly grown on a surface and they present a much broader size distribution, yet they are in closer contact with surface atoms, compared to colloidal QDs. This leads to the creation of a very sharp interface that is favorable for processes such as exciton dissociation and charge injection, since they are critically dependent on the QD-surface distance.[82] Colloidal QDs can be easily loaded into the host matrix from solution,[87, 88] while direct nucleation and growth of the QDs at the surface of the scaffold can be obtained with different techniques, such as chemical bath deposition (CBD) or successive ionic layer absorption and reaction (SILAR). [89, 90]

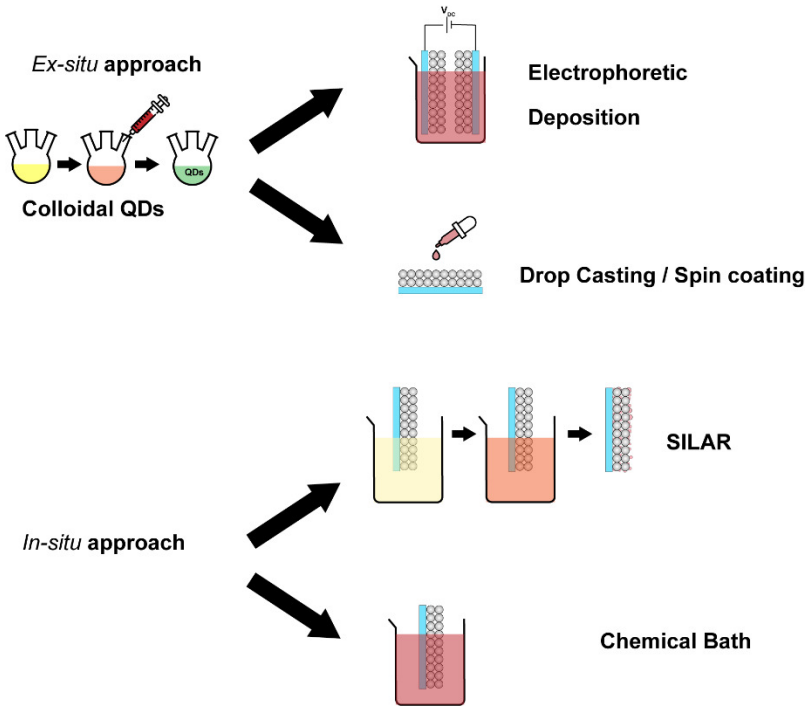

Figure 2.16. In-situ and ex-situ fabrication methods of QDs.

Regardless of the synthetic method, hetero-structured QDs in core/shell configuration are among the most attractive material to use in recombination design since their photoelectric properties can be tailored through the shell materials. In general, based on the relative energy offsets of bulk CB and VB edges of the component materials, the band alignment of semiconductor hetero-structures can be classified as type I, quasi-type II and type II (**Figure 2.17**). In type I structures, both the CB and VB of the core are confined within the band gap of the shell material, therefore electrons and holes are confined in the material with the lowest band gap (the core). Type II QDs present a staggered band alignment with the CB and VB of the core lower (or higher) than the band edges of the shell. In this way the carriers are localized in different materials across the heterostructure.[91] In the quasi-type II regime the leakage of the electrons from the core to shell is permitted, but the holes are confined in the core, leading to a reduction in the recombination.[92, 93] It has been shown that core/shell QDs can be tuned from type I to type II by changing either the core size or the shell thickness.[94] In particular, growing a thick shell can form a quasi-type II band alignment.[95]

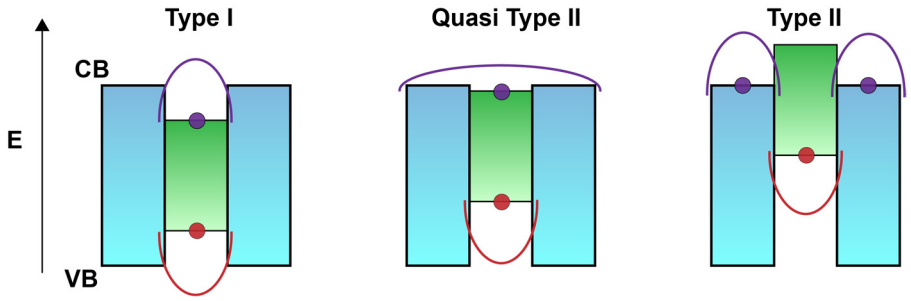

Figure 2.17. Schematic band alignments at the hetero-interface between two semiconductors of core/shell QDs.

Clearly, the type II architecture is the most advantageous to reduce the recombination inside the QDs as fast electron transfer from the QD sensitizer to the oxide matrix can happen due to the spatially separation of electron and hole in the QDs. Based on this design, many QDSCs have been fabricated and a record PCE of 7.17% has been achieved for ZnTe/CdSe-based QDSCs. In particular, Zhong et al, showed that the type-II core/shell QDs improved not only the light-absorption range of the solar cells, but also increased the electron-injection and suppress charge-recombination processes.[96]

The type I architecture has been used as well successfully to control the recombination and improved the PCE.[97-99] In this case, as the shell has both CB and VB higher/lower compared to the core, it is important to control its thickness. In fact, if too thick, the shell can act as a barrier and prevents electron injection from the QD to the metal oxide. Instead, if the shell is thin enough, around 1-2 nm, there are two main benefits: 1) the shell acts as a barrier between the electron and the electrolyte, preventing the recombination of the photo-charges; 2) the shell passivates the surface of the core reducing the recombination inside the QD and electron back transfer from TiO_2 to the trap states of QDs is also retarded. For example, Zhong et al. showed that by growing a ZnS shell around $CuInS_2$ QDs the PCE of the cells can be improved from 5% up to 7.04%. This enhancement can be attributed to a passivation effect of the shell, as shown by the improved photoluminescent (PL) emission. The passivation with ZnS improved the electron lifetime and reduced the recombination.[100] (**Figure 2.18**)

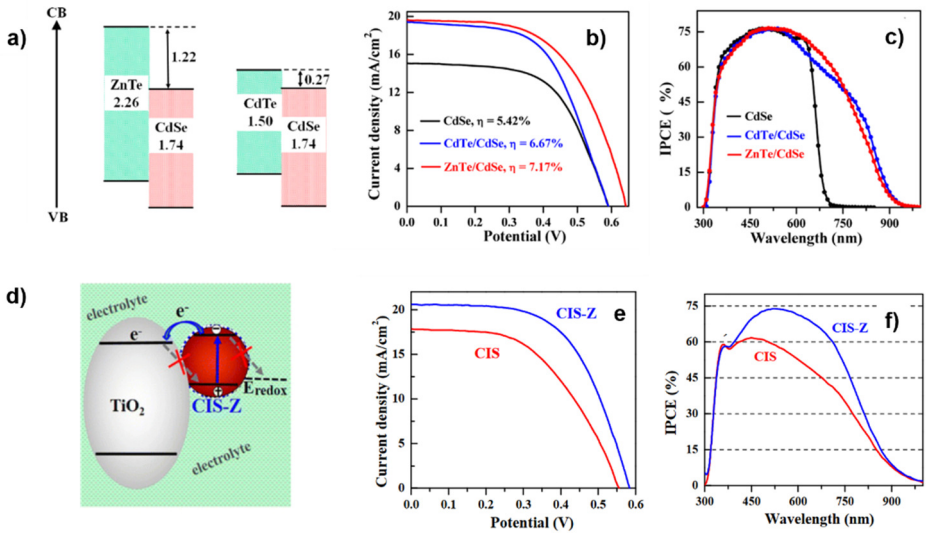

Figure 2.18. a)Band gap and band offsets (in eV) for type II interfaces ZnTe/CdSe and CdTe/CdSe. J-V curves (b) and IPCE (c) of type II QDs based solar cells. ***Reproduced with permission.[96] Copyright 2015, American Chemical Society.*** **d) Mechanism of QDSC based on core/shell $CuInS_2$/ZnS QDs. J-V curves (e) and IPCE (f) of $CuInS_2$/ZnS QDs compared to only core $CuInS_2$ QDs.** ***Reproduced with permission.[100] Copyright 2014, American Chemical Society.***

The core/shell structure can be also altered by increasing the size of the shell, creating a so-called 'giant' QDs. In this architecture, as the thickness of the shell increases and the composition ratio is adjusted, the electronic band structure of the core/shell QDs changes, leading to the formation of a quasi-type II core/shell structure.[101] To alleviate the stress induced by the lattice mismatch between the shell and the core, a gradient inside the shell can be introduced. This gradient layer can strongly suppress Auger recombination.[102] Furthermore, by adding the alloyed interface layer, the band structure formed can significantly accelerate the charge carrier transition, leading to reduce charge recombination. QDSCs based on this gradient structures have been realized with efficiencies up to 6.86%.[103]

Nonetheless, the best performing QDSC are not based on core/shell architecture but on alloyed QDs in which a wide band material is alloyed into the core of the QD. This strategy has been shown to be better in reducing the density of trap. In fact, while the shell strategy can passivate the defects only on the surface, by alloying it is possible to reduce the density of trap defects both at the surface and inside the QD due to the hardened lattice structure and decreased atomic intradiffusion. Furthermore due to the upshift of the CB edge, electron injection can be improved. Based on this strategy, PCE record of 11.66% have been reached with Zn-CuInSe QDs and more recently a certified 12.98% have been recorded by a co-sensitization method with Zn-CuInSe QDs and Zn-CuInS QDs.[104-106]

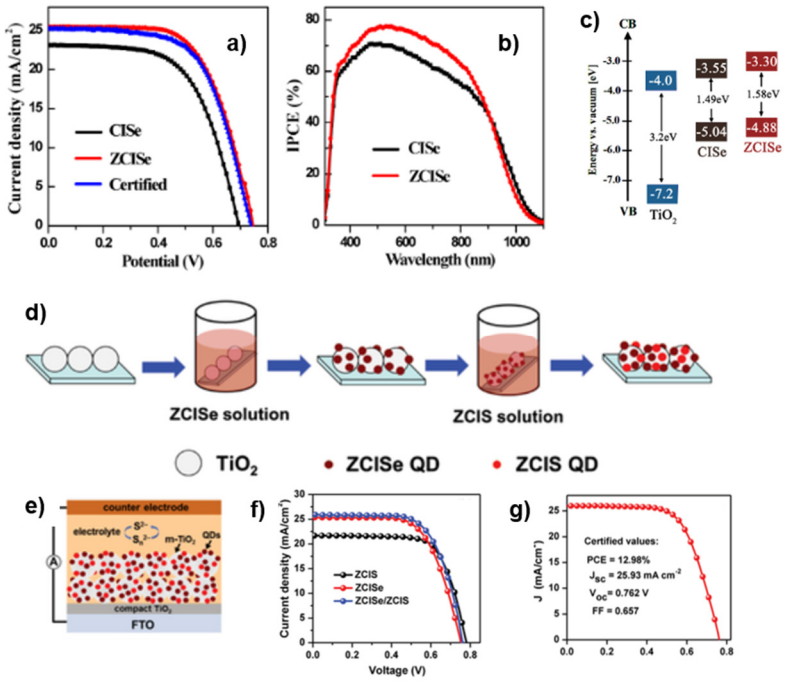

Figure 2.19. a,b)Photovoltaic performances of QDSCs sensitized with ZCISe and CISe QDs. (a)J−V curves for the champion cells (b) Corresponding IPCE spectra. c) Schematic energy level diagrams of TiO_2, CISe, and ZCISe QDs. *Reproduced with permission.[106] Copyright 2016, American Chemical Society.* d) Schematic illustration of the preparation of ZCISe/ZCIS cosensitized TiO_2 film electrode. e) Schematic illustration of the cell device. f) J–V, of ZCIS, ZCISe, and ZCISe/ZCIS QD-sensitized TiO_2 film electrodes. g) Certified results of ZCISe/ZCIS QDSCs. *Reproduced with permission.[105] Copyright 2019, John Wiley and Sons.*

Interface engineering in QDSCs

Due to the similarities in the architecture, to engineer the interface MOS/QDs many solutions have been borrowed from the DSSC field. As seen in the chapter 2.1.1, the design of novel nanostructures of MOS is an effective approach for improving light harvesting and electron transport. For example, 1D-nanostructured metal oxide materials, such as NTs, NRs, and NWs, have been explored as ETL in QDSCs to facilitate faster electron transfer.[107-110]As in the case of DSSCs, the main disadvantage of these structures is the smaller surface area that reduce the loading of QDs and thus the amount of light absorbed. The first example of TiO_2 NRs photoanode applied in QDSCs was presented by Kamat et al., showing superior electron-transport capacity compared to the counterpart of mesoporous nanoparticles film.[108, 111] Branch hierarchical structures, formed by TiO_2/ZnO nanowires, have shown remarkable improvement in efficiency and scattering of light, with efficiency of 5.2%.[112] To improve the loading of the QDs, a three-dimensional (3D) hierarchically branched hollow sphere-nanowire hybrid TiO_2 photoanode has been proposed. This architecture combines the advantage of the high surface area of the NPs TiO_2 combined with higher electron transports offered by 1D structure, reaching efficiency of more than 6%.[113] Another elegant solution to increase the loading of QDs, while maintaining the 1D structure, has been proposed by Cao et al, in which

the surface of ZnO NRs was chemically treated to increase the loading of QDs by making the surface of NR rougher.[114] (**Figure 2.20**)

Overall, the PCEs of 1D-nanostructured photoanode QDSCs still lag far behind those of more traditional nanoparticles TiO_2-based ones. However, 1D-structures possess great potential to realize high-efficiency QDSCs due to their unique properties, especially higher electron transport. Thus, it is necessary and meaningful to further improve the PCE of 1D-based QDSCs through optimizing the QD sensitizers and interface characteristics.

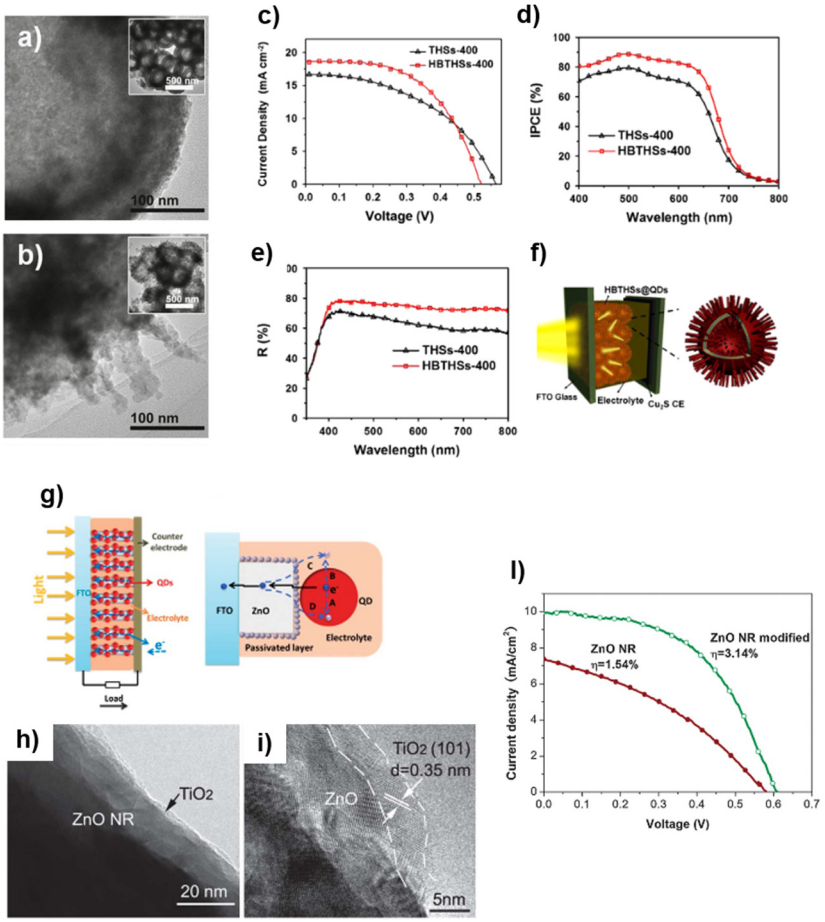

Figure 2.20. TEM images of (a) hollow TiO_2 (THS) nanosphere@QDs and (b) hyperbranched hollow TiO_2 (HBTHS) nanosphere @QDs. c)J-V curves and (d) IPCE spectra of QDSSCs based on THSs-TiO_2 and HBTHSs-TiO_2. (e) UV–vis diffused reflectance spectra. (f) Schematic diagrams of HBTHSs@QDs and the solar cell. *Reproduced with permission.*[113] *Copyright 2015, Elsevier.* Schemes of the (g) ZnO nanorods coated with TiO_2 based QDSC structure and charge recombination pathways. h) TEM and (i) HRTEM images of the modified ZnO NR, showing the ZnO NR coated with TiO_2 nanoparticles with a size of 4–5 nm. h) J–V curves of the modified and unmodified ZnO NR array photoanode based QDSC. *Reproduced with permission.*[114] *Copyright 2013 Royal Society of Chemistry*

Similarly to DSSCs, in QDSCs both QDs and bare TiO_2 are in direct contact with the electrolyte. This create a further recombination channel for the electrons that can be captured by the oxidized species in the electrolyte. Contrary to DSSC, in the QDSCs it is possible to use a post-treatment coating strategy for the full photoanode, in which a wide-band gap material can be coated on the surface of the mesoporous film already sensitized with QDs. By doing this, the direct contact with the electrolyte can be avoid thus reducing the electron recombination due to the oxidized electrolyte.

One of the most widely used post-treatment consists on the deposition of ZnS over the sensitized electrode, taking advantage of the straightforward preparation. This treatment was first used by Yang et al in 2002, and proved that a ZnS layer grown by SILAR over a QDs sensitized TiO_2 electrode, in that case PbS/CdS QDs can increase the photostability and PCE.[115] Due to the overall low efficiency achieved this strategy was ignored till 2008, when Toyoda et al, employed it on CdSe colloidal QDs sensitized TiO_2 photoanodes and achieved an impressive PCE improvement of more than 74%.[116, 117] Subsequent studies demonstrated that the ZnS layer covers the QDs and passivates their surface states, reducing as well the recombination with the electrolyte. ZnS covers as well the TiO_2 layer avoiding direct recombination of TiO_2 electrons with the electrolyte (**Figure 2.21**).[118]

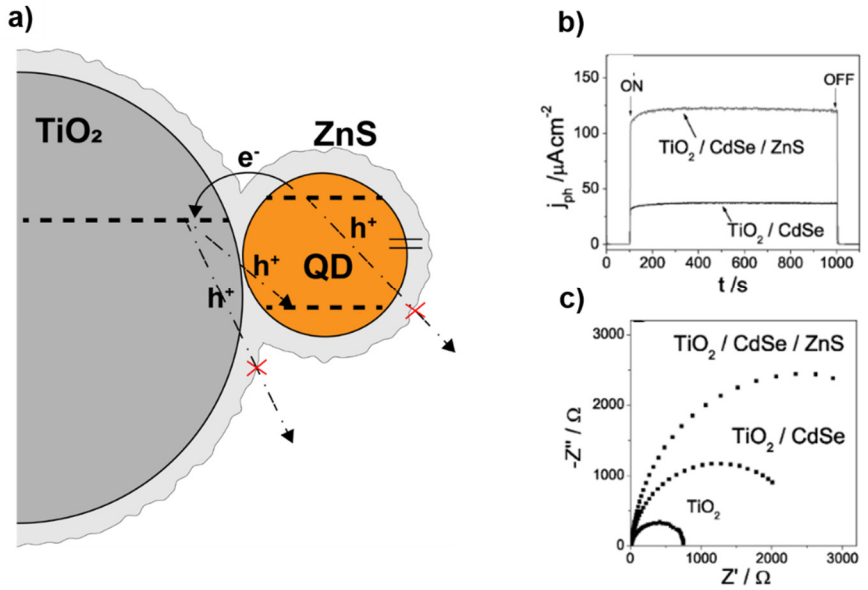

Figure 2.21. a) Possible recombination and trapping in surface/interfacial states, in TiO_2/CdSe/ZnS photoanodes. b) Photocurrent experiments for TiO_2/CdSe and TiO_2/CdSe/ZnS electrodes. c) Electrochemical impedance spectra for TiO_2 electrodes sequentially modified with CdSe QDs and ZnS. *Reproduced with permission.*[118] *Copyright 2011 Royal Society of Chemistry*

Recently, it has been proved that ZnSe could be a better passivation material for QDSC. Works of Cao et al have demonstrated that when ZnSe is used as a passivation layer, compared with solar cells without

passivation layer and even with the ZnS passivation layer, it presented ~90% and ~30% improvement in PCE.[119-121]

Metal oxides have been used as passivating layers for QDSC. MgO, Al_2O_3 and SiO_2 have been all employed successfully as coating layers.[99, 122-125] A remarkable result in PCE has been obtained with silica coating, in which QDSCs based on type-I CdSeTe/CdS core/shell QDs with optimized CdS shell thickness and additional coating of amorphous TiO_2 and SiO_2 exhibited a maximum PCE of 9.48% under one sun illumination, significantly higher than the PCE of the QDSCs based on uncoated CdSeTe QDs. This improvement is mainly attributed to suppressed charge recombination within the QDs and at the QDs/TiO_2/electrolyte interface with the CdS shell grown over the CdSeTe QD.[99] In general, the main function of these inorganic overcoating layers is as energy barriers to prevent interaction (and thus recombination) between the photogenerated electrons in QDs/metal oxide films, and the electrolyte.

2.3 Perovskite solar cells

In the research of the best material suitable as sensitizer for the DSSC a relatively old family of materials has emerged in the last years as a serious contender for utility scale solar power. [126]

Metal halide perovskites (PSK) are a particular class of materials with a stoichiometry ABX_3, in which A is an organic cation with a charge +1, B is an inorganic cation with charge +1 and X is an halide ion with charge -1 (**Figure 2.22**). By varying the stoichiometry between them, it is possible to vary the band gap of metal halide perovskites. The structure of the perovskite crystal and the charge are balanced by the organic cations.

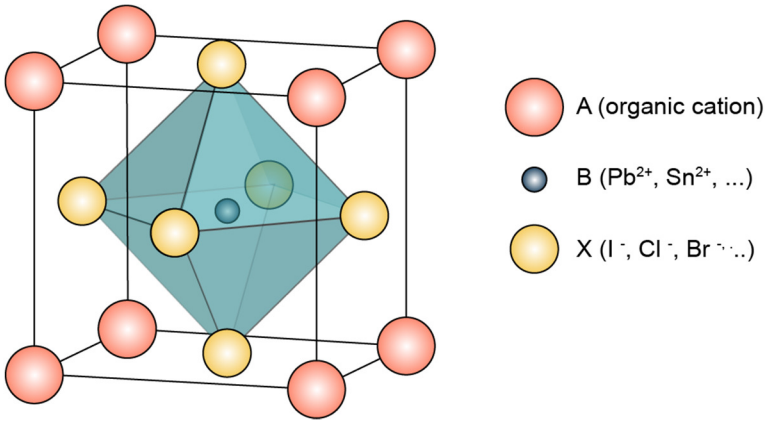

Figure 2.22. Crystal structure of a perovskite with stoichiometry ABX_3

The history of this material is quite old, with the first paper on metal halide perovskite published in 1892 by Prof. H.L. Wells.[127] However, the first application of this material in solar devices was published only in 2009 by Prof. Miyasaka's group. In this work the authors replaced the sensitizer of a DSSC, the organic dye, with a methylammonium lead-iodide ($CH_3NH_3PbI_3$, $MAPbI_3$) perovskite.[128] The efficiency of their best cell was around 2.2% however the main issue was the stability. In fact, due to the presence of the liquid electrolyte, the perovskite was degrading over only few hours.[128] Only in late 2012, efficiencies close to 10% were first achieved in solid state cells, in which the liquid electrolyte was replaced by a solid HTL.[129, 130] Since then, organic/inorganic halides with the PSK structure have start to gather interested in the scientific community. The excellent optical properties and the easy fabrication offered by these materials has resulted in a rapid increase in publications and research on this topic enhancing the PCE of these devices up to a certified 24 %.[131, 132]

$MAPbI_3$ perovskite have been the most studied material has it showed excellent light-harvesting abilities, with a bandgap of 1.55eV, and ambipolar charge transport.[133] In general, any PSC device is composed of three main parts: a light absorber (the perovskite materials) is sandwiched between an ETL, and a HTL.

Depending on whether electrons or holes are collected by the bottom of the conducting substrate, the PSC can be classified in n-i-p or p-i-n respectively. The latter configuration is also called inverted structure. Based on these properties two main configuration of solar cells have been developed: mesoscopic perovskites solar cells and planar heterojunction (PHJ) PSC.[134, 135]

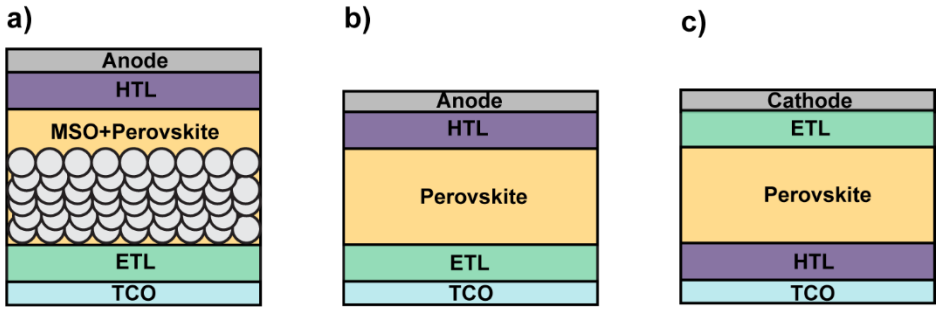

Figure 2.23. Different architectures of a perovskite solar cell. a) Mesoporous configuration, b) planar n-i-p configuration, c) planar inverted p-i-n configuration.

Compared to the more traditional mesoscopic configuration, the PHJ architecture offers the advantages of a simplified device configuration and fabrication procedure. In particular, these structures do not present the problem of pore filling of the mesoporous layer and can be fabricated via simple solution-based method at low temperature (<150 ˚C), enabling flexible photovoltaic application. [136]

The conventional mesoscopic configuration is based on the architecture of a solid state DSSC in which the ETL is made by mesoporous layer of TiO_2 deposited on a compact layer of titania. The perovskite film is then spin-coated on the mesoporous TiO_2 layer from a solution using a solvent such as dimethylformamide (DMF), γ-butyrolactone (GBL) or dimethyl sulfoxide (DMSO), followed by the deposition of the HTL. On top of that, a metal electrode, such as gold (Au) or silver (Ag), is thermally evaporated.

In the PHJ configuration, the ambipolar charge transport property of the PSK is exploited and the mesoporous oxide is removed. In this architecture, the perovskite thin film is deposited on top of an HTL, such as poly(3,4-ethylenedioxythiophene) poly(styrene-sulfonate) (PEDOT:PSS) or inorganic material such as NiO. An electron acceptor, the ETL, such as [6,6]-phenyl C61-butyric acid methyl ester (PCBM), is then deposited on top of the perovskite layer. Au or Ag metal contacts are evaporated on top of the ETL.

The simplified working mechanism of this architecture is similar to DSSC and QDSC: upon photoexcitation, an exciton is formed. Due to the high dielectric constant of the perovskite, the exciton can easily be dissociated in electrons and holes.[137] From the CB of the PSK, electrons are then injected into the ETL, while holes are transferred to HTL from the VB of the perovskite. These photogenerated charge

carriers are subsequently collected as photocurrent at the front and back contacts of the solar cell. The observation of long PL lifetimes, large diffusion lengths that can exceed 1µm and ambipolar transport led to the realization that there is no explicit need of a mesoscopic structure such as TiO_2 and perovskite solar cells can be highly efficient even in a conventional planar thin-film structure.[138, 139]

After photogeneration, the charges encour in possible recombination paths (**Figure 2.24**). During the transport in the perovskite film, bulk recombination of the charge carrier occurs: charge carriers can be trapped by bulk traps and then recombine with the opposite free charge carriers or electroncs can also recombine with the free holes (path (a) in **Figure 2.24**). The first recombination dominates at low charge carriers densities while the latter is prevalent in high charge carriers density condition.[140] Once the electrons (holes) reaches the interface with the ETL (HTL) interfacial recombinatio can take place due to traps and or energy barriers causing accumulation of charges (b and c recombination paths in **Figure 2.24**). The ETL and HTL interfaces in PSC plays a fundamental role as they do not only control the charge collection but also they affect the stability of the PSC and the hysteresis (contrary to QDSCs and DSCs, PSCs still suffer of hysteresis phenomena).

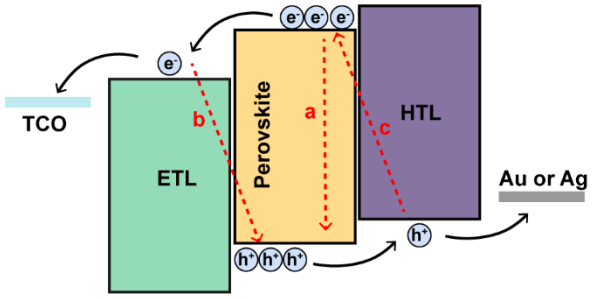

Figure 2.24. Schematic of recombination process in perovskite solar cell.

In the following sections we will focus on the PHJ configuration and in particular on the inverted p-i-n configuration. As in this thesis work has been done on the enginerization of the HTL in inverted PSC, due to the extremily wide literature on PSC, it will be only analyzed the control of the recombination at the TCO/HTL/PSK interface for this kind of architecture.

2.3.1 Control of recombination processes by interface engineering

The first reported inverted PHJ PSC showed a maximum PCE =3.9%. The architecture was based on the ITO/PEDOT:PSS/MAPbI3/PCBM/BCP/Al configuration.[141] Although the PCE was much lower compared to mesoscopic PSC at that time, this work highlighted the possibility of designing a PSC that could be processed at low temperature (below 150 ˚C).

As in the case of the other configurations, also in the inverted PHJ PSCs the main body of research focused on controlling the quality of the perovskite layer to achive high PCE. In fact, the grain boundaries and pinholes play an important role in the performance and stability. It has been observed that the presence of a large number of grain boundaries in the polycrystalline perovskite film has multitude of deterimental effects: it increases the recombinations, reduces the charge transport, with impact on the V_{OC}, light soaking effect and hysterirs.[142, 143] Pin-holes can cause short circuit paths and increase the degradation effect of moisture om the PSC.

It has to be noted that the actual role of grain boundaries in the recombination process is still not completely understood and appears to depend on the fabrication method.[143] Conflicting results have been reported in literature, with also beneficial effect of grain boundaries.[144] However, it is well established that grain boundaries have a strong effect on the long-term stability of the cells and its hysteresis.[143]

For example, by using an interdiffusion method which involves the stacking of PbI_2 and MAI in a sequence by spin-coating it is possible to form a free pin-holes film of $MAPbI_3$ layer . The optimizied device yield a PCE of 15.3%.[145]As an alternative strategy, it is possible to replace the lead halide precursors in the simple "one-step" deposition process. In particular, by replacing the common lead halide with lead acetate ($Pb(Ac)_2$) precursor, it is possible to obtain a smooth pin-hole free PSK layer (**Figure 2.25**).[146] The addition of additives to the lead acetate precursor can yields efficiency up to 18%.[147, 148]

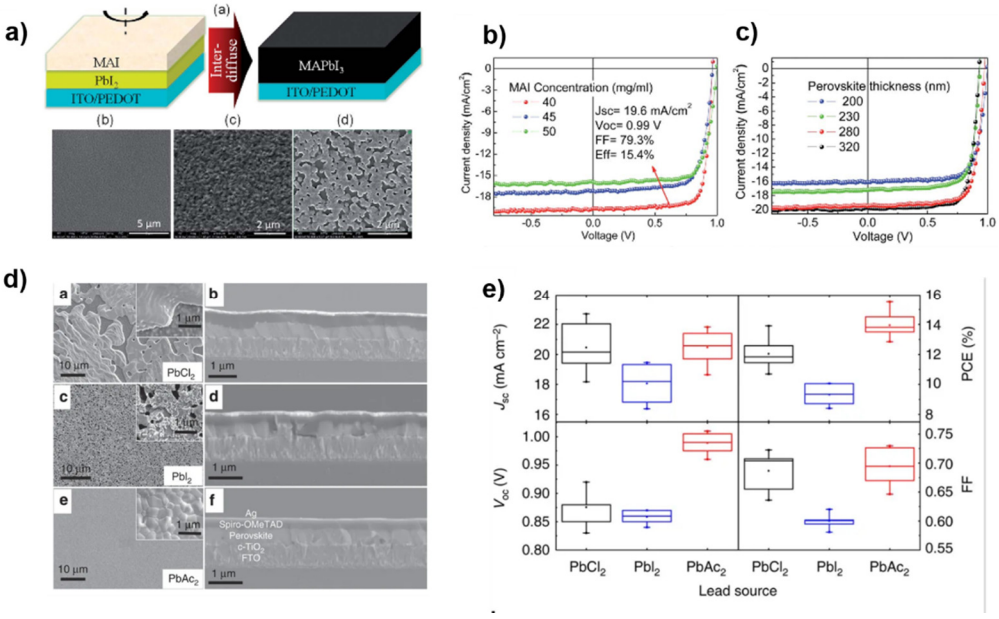

Figure 2.25. a) Schematics of spin coating of PbI and MAI using orthogonal solvents and the conversion of the stacking layer into a perovskite layer upon annealing. (b) Photocurrents of the device with a varied MAI concentrations and (c) Photocurrents of the devices with perovskite films of different thickness. ***Reproduced with permission.*** **[145]** ***Copyright 2015 Royal Society of Chemistry.*** **d) SEM images of perovskite film deposited with different lead sources e) Device performance at optimized conditions using different lead sources.** ***Reproduced with permission.*** **[146]*Copyright 2015 Nature Group.***

In order to increase the grain size and crystallinity of perovskite light absorbers, one common method is the solvent-annealing method in which the $MAPbI_3$ film is exposed to dimethylformamide (DMF) during thermal-annealing. With this treatment, the grain size of the solvent-annealed perovskite increased to 1 μm, much larger than only thermal-annealed perovskite grain (260 nm).[149]

Combining the use of addictive and solven treatment, it is possible to furhter increase the performance. For example, the cooperation of lead thiocyanate additive and a solvent annealing process lead to PCE over 17% due to increase grain size.[150] Interestingly, the presence of a small quantity of water could improve the PCE of the inverted structure. By exploiting a synergistic effect of a H_2O additive and DMF vapor treatment *via* a two-step spin coating method, Graeztel et al developed an inverted PSC with a high PCE of 20.1%. The cell shows no current hysteresis and was stable in inert and ambient atmospheres with appropriate encapsulation. The increased PCE was attributed to the formation of grains with a horizontal size up to 3 μm and a lateral size equal to the film thickness.[151]

Although fewer studies have considered interfacial layer engineering than perovskite layer engineering for optimizing the performance, the charge transfer layers plays a fundamental role in the final PCE of the solar cells.[152] In particular, in the inverted PHJ configuration, the HTL is one of the key components to prepare highly efficient and stable PSCs. In fact, in this configuration, as the light enters from the HTL side, it is the first layer interacting with the light, and in which a charge injection happen.[152, 153] Furthermore as the perovskite layer is deposited on top of it, the HTL can play a role in the morphology of the PSK layer.

In general, to have high efficient inverted PSC, an ideal HTM should fulfil some general requirements: the HOMO of the HTM should be compatible with the VB of the PSK layer, sufficient hole mobility, high thermal and photochemical stability, high transparency in the visible region and a low cost of fabrication.[153] A great number of HTMs have been developed and incorporated in PSCs, which are composed of organic and inorganic hole-conductors. So far, the majority of inverted PSC use PEDOT:PSS as HTL. The use of PEDOT:PSS has its benefits such as good reproducibility, good performance and no hysteresis, however severe charge injection losses at the interface can limit the V_{oc} of the PSC.[152, 154] Furthermore, PEDOT:PSS has several problems including high acidity, hygroscopic properties, and inhomogeneous electrical properties, resulting in poor long-term stability. [152, 154]

To improve the charge injection, energy-level alignment at the interfaces has been shown to play an important role. Poly (triarylamine) (PTAA) with proper energy level alignment, efficient carrier transport and mitigation of bulk defect activities can be used as HTM to replace PEDOT:PSS.[155] Devices based on it show improved performance and a larger V_{OC}.[152, 156] On the other side, due to the high hydrophobicity of

PTAA, the perovskite films presents an increase number of defects that cause a lower fill factor and reduce the reproducibility of the film. [157-159]

To increase the wettability, treatment of the surface of the HTL can be applied. It has been observed that the interaction of the surface groups on the HTL with the perovskite layer can also influence the crystallization and the perovskite film morphology (thus affecting the pin-holes and gran boundaries as well). Lee at al. have shown that by functionalizing the PTAA layer with the interface compatibilizer poly[(9,9-bis(30-((N,N-dimethyl)-N-ethylammonium)-propyl)-2,7-fluorene)-alt-2,7-(9,9-dioctylfluorene)] dibromide (PFN-P2), the wettability can be improved thus enhancing the reproducibility thanks to a free pinhole formation of the perovsksite layer.[157] Recently, an impressive PCE of 20.1% was achieved for inverted planar PSC by surface modification of the PTAA HTL with an efficient hydrophilic group (C–O & C=O) grafted buffer layer (HGGBL). This approach lead to a decrease in the surface potential and surface tension force of the non-wetting HTM, facilitating the nucleation and growth of perovskite crystals (**Figure 2.26**).[160] Interestingly, other reports highlighted an opposite trend, in which the nonwetting surface of the HTL is favorable for forming compact, pin-hole free, and large grains perovskite film. These differences seems to depend on the fabrication method. [159, 161]

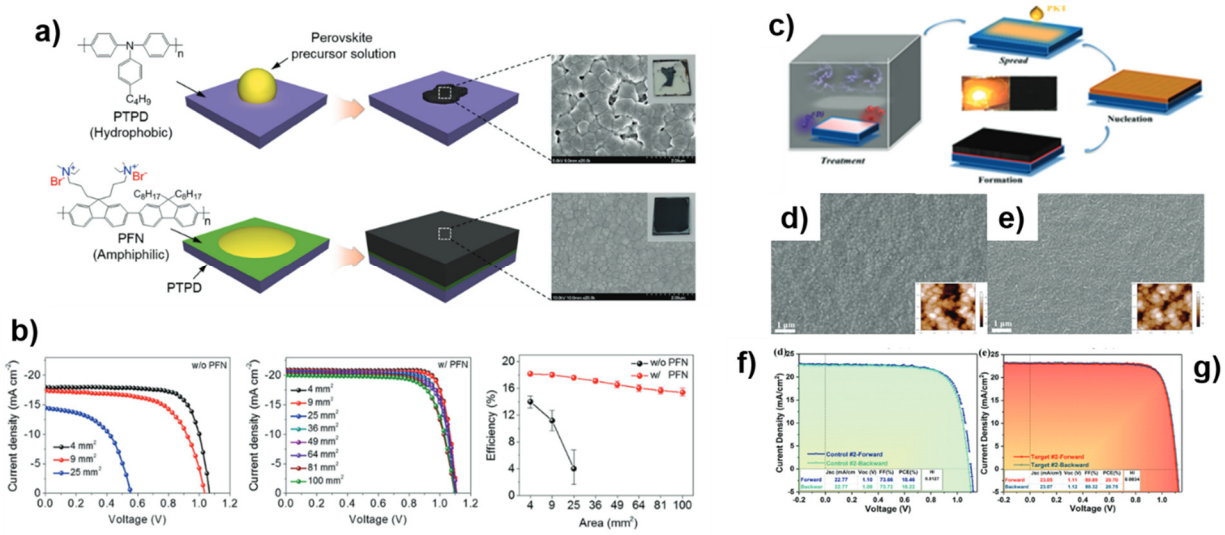

Figure 2.26. a) Schematic illustrations of perovskite film formation on organic HTLs with and without PFN. b) J–V characteristics of devices without and with the PFN as a function of the active device area. ***Reproduced with permission.*** **[157]** ***Copyright 2017 John Wiley and Sons.*** **c) Schematic representation of the fabrication procedure. d) SEM images of device with a buffer layer without HGG and (e) with HGG. J–V curves of (f) the device with a buffer layer without HGG and (f) with HGG.** ***Reproduced with permission.*** **[160]** ***Copyright 2019 Royal Society of Chemistry.***

Inorganic materials such as NiO_x,[162-164] and copper based ones, such as CuO_x,[165] CuSCN,[166] CuI,[167] have been explored as HTL for inverted PSC. Compared to organic hole conductors, inorganic p-type materials usually possess high chemical stability, hole mobility and low cost starting materials.

Thin organic interlayers or self-assembled monolayers (SAMs) have been applied on metal oxides HTL to improve their transport properties. By controlling the dipole orientation it is possible to tune the work function of NiO: it can be either lowered (negative dipole) or increased (positive dipole), leading to a change in energy level alignment with the subsequently deposited perovskite film.[168]

Once the charges are injected in the HTL, they should be transported to the contact, thus the conductivity of the interface should be considered. A low conductivity or mobility of the interfacial materials determines high series resistance, impeding charge carriers to arrive at the electrodes within their lifetime. Intrinsic p-type doped HTL can present high mobility, such as CuSCN. Ye et al. reported the CuSCN-based inverted PSCs with the PCEs ranging from about 11% to 16% depending on preparation procedure of MAPbI3 film,[166] however CuSCN based PSC presents issues of instability.[169]

In order to increase the charge mobility of the HTL, doping can be applied. For example, Cu-doping has been used successfully in NiO-based HTL for inverted planar PSC. The HTL showed and improved electrical conductivity and favorable perovskite crystallization, thus improving the final PCE with values up to 15.4%.[163] Further improvement on the deposition method, such as by combustion route, can lead to PCE of 17%.[170] Cesium has been used as well as successful dopant for increasing the conductivity of NiO, leading to an impressive PCE of 19.35%.[171]

An alternative HTL based on carbonaceous materials has recently been proposed. Carbon-based HTL can offers an improved stability of the PSC but up to now the device efficiency seems to be not yet comparable to the small molecules and inorganic HTLs.

The firsts report of PSC made of graphene oxide (GO) deliver an efficiency over 12%.[172] GO in nature should be an insulator, however it has been observed that compared to graphene, graphene oxide's electrical conductivity and optical transparency dramatically depends on the level of oxidation.[173] As the properties of rGO can be influenced by the choice of the reducing agents,[174] to further improve the conductivity, GO can be reduced by different reducing agents such as p-hydrazinobenzenesulfonic acid hemihydrate, sodium borohydride and hydrazine. Yeo et al. reported the first rGO-based PHJ inverted PSC showing that devices based on rGO have three times longer half-lifetime than devices with PEDOT:PSS under ambient conditions.[175] In fact, due to the presence of few surface oxygen functionalities, rGO has inherent passivation ability against moisture and oxygen. Device based on rGO achieved also higher PCE than devices with PEDOT:PSS. The explanation of the enhanced efficiency was found in the superior charge

transport ability due to higher conductivity of rGO and better-aligned energy levels between rGO and the anode than PEDOT:PSS.

For example Diau et al, showed an excellent performance of GO-based PSC, with efficeincy close to 13%. By using appropriate reducing agent, the as-prepared rGO-based PSC displayed a further improve in efficiency, with a remarkable value of 16%.[176] Interestingly, compared to rGO, GO showed better extraction properties from the PSK layer, but a slower kinetic of the hole transport once injected in the HTL. The reason is attributed to the presence of oxygen groups on the GO surface that act as hole-extraction sites but also as traps for the holes, increasing overall the recombination. Delocalized holes on the rGO surface, instead, favour the charge transfer and thus better performance.

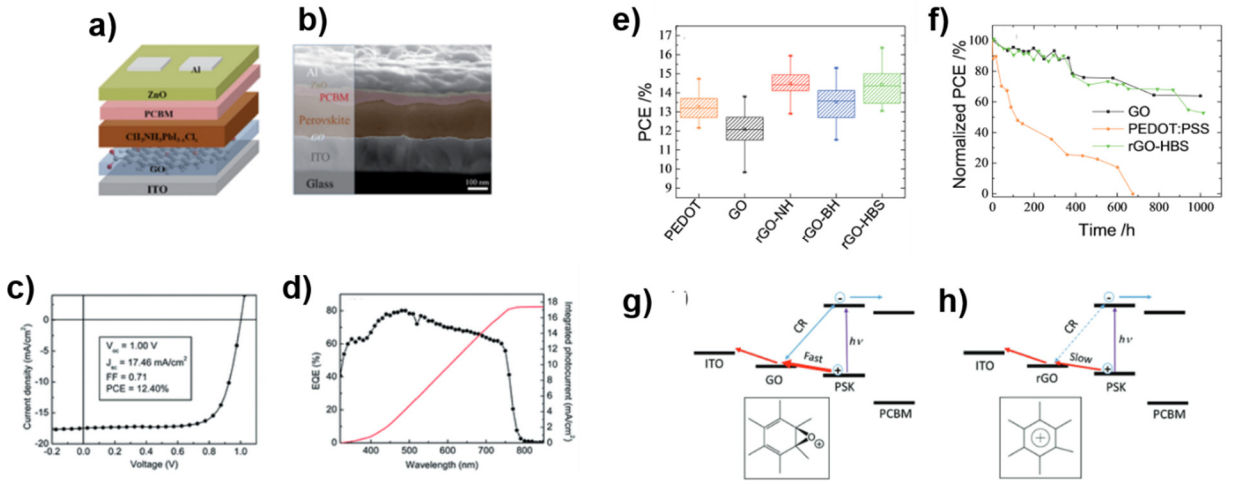

Figure 2.27. a) Schematic and SEM image (b) of the inverted photovoltaic device configuration with GO as HTL. C) J–V curve and (d) IPCE of champion device employing 2 nm GO as hole conductor. ***Reproduced with permission.*** **[172]** ***Copyright 2014 Royal Society of Chemistry.*** **e) Device performance for PSC devices made of varied GO and rGO HEL. f) Profiles of efficiency stability. Schematic illustration of a mechanism of charge transfer for g) GO and h) rGO.** ***Reproduced with permission.*** **[176]** ***Copyright 2018 John Wiley and Sons.***

3 Thesis objectives

As described in Chapter 2, independently of the architecture, controlling the charge injection and the recombination is essential to fabricate high efficiency solar cells. In this work, these issues will be tackle from different perspectives starting from fundamental studies of band energy alignment and carrier dynamics in composite metal chalcogenide quantum dots (QDs) up to realizing full operational devices, such as DSSC and PSC, with modified interface layers in order to reduce the carrier recombination and improving the charge collection and thus the final efficiency and stability.

The thesis is based on 4 main different objectives.

Regarding the DSSC, I focused my attention onto two different interfaces of the DSSC: the photoanode and the counter-electrode (CE).

1. ***Modification of the DSSC photoanode.*** As seen in chapter 2.1, the incorporation of low-dimensional carbon nanostructures such as CNTs and graphene sheets into semiconductor electrodes was recently proposed to improve the charge collection and performance of DSSCs. However, the role of these materials in improving the PCE is still not well understood. For this reason I decided to systematically investigate the role of functionalized multi-wall carbon nanotubes (F-MWCNTs) in a TiO_2 photoanode.
   This project is based on four tasks:
   - (i) *Integration of F-MWCTNs in TiO_2 photoanode*. Different amount of F-MWCNTs are blended with TiO_2 paste.
   - (ii) *Characterization of the composite structure.* The morphology and optical properties of the different photoanodes is investigated.
   - (iii) *Device fabrication and evaluation of the performance*
   - (iv) *Charge transfer investigation.* Electrochemical Impedance Spectroscopy (EIS) is used to investigate the role of F-MWCNTs in the charge kinetics in the photoanode.

2. ***Modification of the Counter Electrode.*** The CE is one of the most expensive component of the DSSC as commonly is made of platinum (Pt). In order to reduce the amount of Pt used while improving the final efficiency of the cell, a nanostructured CE made by hollow nanofibers deposited by a facile and low cost method such as electrospinning is designed. These results can help to tailor the general CE structure in photoelectrochemical systems to boost their functional properties, thanks to the advantages afforded by this morphology. This project is based on four tasks:

- (i) *Preparation of the CE by electrospinning.* By controlling the time of sputtering and electrospinning deposition, different morphologies of nanofibers-based CE are prepared.
- (ii) *Characterization of the composite structure.* The morphology and optical properties of the different CE is investigated.
- (iii) *Device fabrication and evaluation of the performance.*
- (iv) *Investigation of the catalytic activity of the different CE.* Open-circuit voltage decay and EIS are employed to investigate the charge transfer dynamics.

As seen in chapter 2.2, metal chalcogenide QDs are among the most promising materials as light harvesters in all-inorganic systems for applications in solar cells and production of solar fuels. In this framework, the third objective of this PhD work is:

3. ***Investigation of the electrical properties of individual metal chalcogenide QDs.*** There is still a lack of studies on the charge dynamics and the local electronic band structure in quantum-confined nanoscale objects directly grown on substrates. Therefore I decided to investigate the electrical properties of individual metal chalcogenide QDs with different size and composition grown via a successive ionic layer absorption and reaction (SILAR) on graphene-like material by using an advanced technique such as Kelvin Probe Force Microscopy (KPFM). These results will help in designing QDs-based solar devices with improved charge injection and collection. This project is based on four tasks:
    - (i) *Deposition of metal chalcogenide QDs on Highly Oriented Pyrolytic Graphite (HOPG).* PbS, CdS and PbS/CdS QDs will be deposited by SILAR method on HOPG.
    - (ii) *Characterization of the QDs.* The morphology and composition of the different QDs is investigated.
    - (iii) *KPFM study of the local variation of the surface potential.* The variation of the surface potential of individual QDs is measured by KPFM.
    - (iv) *Reconstruction of the band alignment of single QDs.* The evolution of the electronic band structure as a function of QD size and composition is investigated

For the last part of my work, I focused on PSC, and in particular on the investigation of the interface of planar inverted structure. The objective for this section is:

4. ***Modification of the hole transport layer in inverted PSC.*** Thanks to a fellowship from the Natural Sciences and Engineering Research Council of Canada (NSERC), in 2017 I could collaborate with Prof. Diau at the National Chiao Tung University (NCTU) in Taiwan. With his group, I focused on

the developing of a novel low cost, high efficient and green HTL for perovskite solar cells based on carbon dots (Cdots). This project is based on six tasks:

- (i) *Surface functionalization of Cdots.* The Cdots are functionalized to allow their integration in the PSC fabrication process.
- (ii) *Characterization of the Cdots.* The morphology and optical properties of the Cdots are investigated.
- (iv) *Preparation of the HTL based on Graphene Oxide (GO) and Cdots*
- (v) *Device fabrication and evaluation of the performance.*
- (vi) *Investigation of charge transfer and band alignment of the Cdots/GO hybrid.* Photoluminescence (PL), transient PL decays and transient photovoltage (TPV) decays investigated the charge-transfer kinetics. KPFM and cyclic voltammetry (CV) are employed to analyze the electronic band alignment at the interface between GO/Cdots and the perovskite film.
- *(vii) Integration of a downshifting layer (DSL) based on UV Cdots.* A DSL is integrated on the outside of the PSC in order to improve their stability

3.1 Thesis Organization

This thesis is divided in eight parts and organized as follows:

In *Chapter 1* the energy crisis problem is introduced and the motivation of this work are presented

In *Chapter 2* is presented an overview of the recombination processes in DSSCs, QDSC and PSC system.

In *Chapter 3* the objective of the thesis are presented.

In *Chapter 4*, a composite photoanode to improve the charge collection of DSSC is introduced. In specific, the fabrication of DSSCs with a composite photoanode based on TiO_2/MWCNTs is presented and the effects of different loading of MWCNTs on the final performance of the device are investigate.

In *Chapter 5* the role of the counter electrode in DSSC is investigated by replacing the common thin film of Pt with a nanostructured CE made by hollow nanofibers of an alloy of Pt/Pd deposited by electrospinning.

In *Chapter 6* composite of metal chalcogenide QDs are deposited by SILAR method on a highly oriented pyrolytic graphite (HOPG) substrate and their energy band alignment is investigated by KPFM technique.

In *Chapter 7* perovskite solar cells with inverted p-i-n structure are fabricated. The common PEDOT:PSS HTL is replaced with an hybrid HTL based on a composite of GO and carbon dots. The presence of carbon

dots address the issue of GO acting as bottleneck for the extraction of holes from the perovskite layer. The contribution of Cdots to the enhancement of the final performance is investigated and revealed. Furthermore, the issue of stability of the PSC is addressed by fabricating and using a downshifting layer based on carbon dots as a protective layer for the solar cell.

In *Chapter 8* are reported the conclusion and outlook on possible future works based on the results obtained in this thesis.

4 Improving charge collection and transport in DSSC photoanodes

This chapter is based on the paper "*Functionalized multi-wall carbon nanotubes/TiO_2 composites as efficient photoanodes for dye sensitized solar cells*" published on *Journal of Materials Chemistry C 4, 16 (2016): 3555-3562.*

Although mesoporous photoanodes offer good performances, largely due to light harvesting of the dye-sensitized nanocrystalline film, there are some drawbacks: while offering extremely high specific surface for dye loading, mesoporous networks suffer from a high density of grain boundaries, which promote charge recombination in operating devices.[177]

As seen in the chapter 2, different strategies have been proposed to increase charge collection, such as the use of various metal oxide semiconductors, particularly 1D nanostructures like nanorods (NRs),[178, 179] nanowires (NWs)[180-182] and nanotubes (NTs)[183-186] based electrodes. Among these various 1D nanostructures, the carbon-based ones are particularly interesting. Since their discovery in 1991,[187] carbon nanotubes (CNTs) have played a significant role in the development of alternative clean and sustainable energy technologies,[188] due to their extraordinary electronic and mechanical properties.[189] The incorporation of low-dimensional carbon nanostructures such as CNTs [71, 190, 191] and graphene sheets[192,193, 194] into semiconductor electrodes was recently proposed to improve the charge collection and PV performance of DSSCs (see Chapter 2.1 for details). The 1D CNTs have been proven to be able to enhance the electron transport inside TiO_2 based DSSC.[70] They are suitable to be used in combination with TiO_2 thanks to the good electron band alignment with the TiO_2 and the FTO conducting glass (see **Figure 4.1**), offering a more efficient pathway for the collection and transport of photo-generated electrons. However, due to their high surface area, CNTs tend to agglomerate in bundles, thereby reducing the solubility in most solvents, which could reduce the ability to be dispersed, when mixed with TiO_2.[195] A non-homogenous dispersion of CNTs into TiO_2 paste could cancel their beneficial effects. Therefore, the ability to homogeneously disperse CNTs inside the TiO_2 matrix, as well as the ability to produce a strong interfacial interaction, are key challenges in maximizing the contribution of CNTs for their application in DSSCs. [191]

In this chapter, I explore the possibility to use functionalized multi-wall carbon nanotubes (F-MWCNTs) to overcome the issue of inhomogeneous dispersion of the CNTs in the TiO_2 and improve the final efficiency of the DSSSCs. In particular, a systematic investigation of the role of F-MWCNTs in a TiO_2 photoanode is carried out. CNTs have been modified by an acid treatment to achieve F-MWCNTs, to improve their stability in polar solution and hence increase their homogenous dispersibility in the TiO_2 matrix.[196] In addition, the functionalization introduces chemical groups (e.g. carboxylic groups) that can

increase the interaction with the TiO_2 nanoparticles and enables a better coverage of F-MWCNTs with titania.

Low-dimensional carbon nanostructures incorporated into the photoanode have shown increased PCE but their contribution to the final efficiency of the solar cell is not well understood. For this reason, in this chapter, the role of the F-MWCNTs in the charge transfer in operating DSSC devices will be investigated by EIS, helping us to identify the physical-chemical mechanism that underpins the increase in PCE.

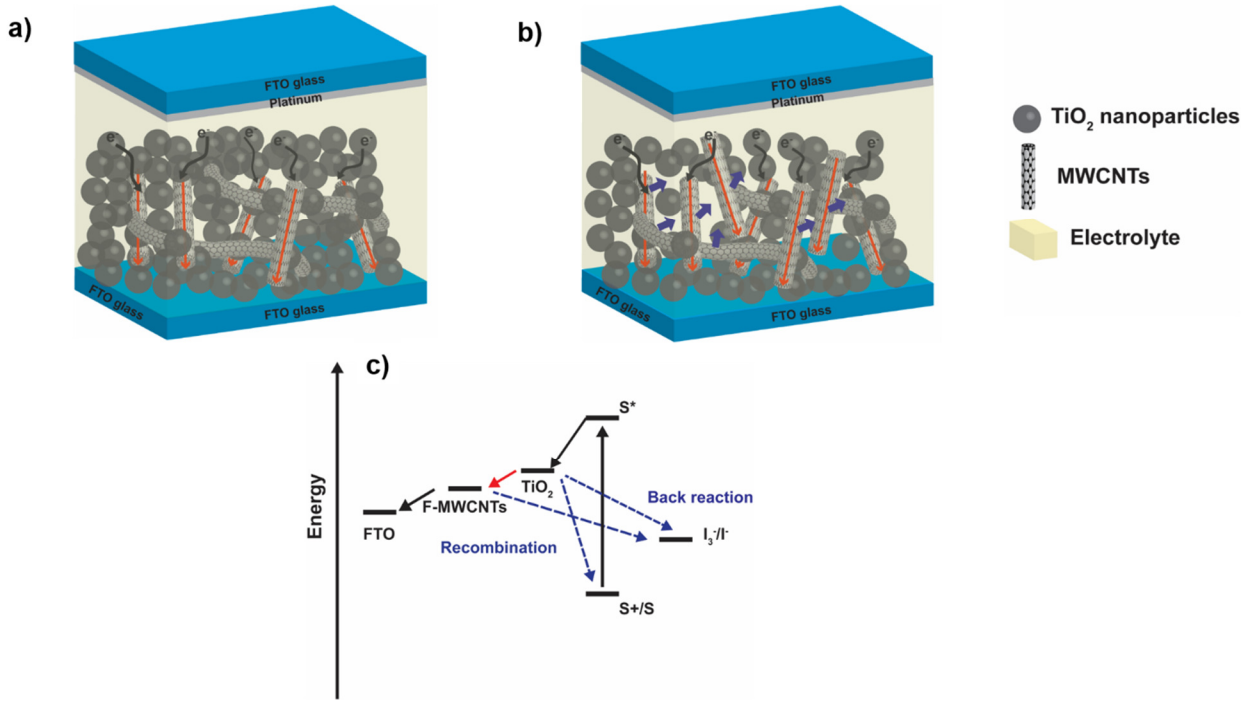

Figure 4.1. (a) Schematic illustration of the concept of improved charge collection in a photoanode based on a composite system with CNTs embedded in a TiO_2 mesoporous structure. (b) At high F-MWCNT concentration, F-MWCNT agglomeration enables direct contact between the F-MWCNTs and the electrolyte, adding a new recombination pathway (blue arrows) (c) Schematic of the electronic band diagram of the DSSC functionalized with CNTs.

4.1 Results and discussion

4.1.1 Morphological and optical characterization

Raman spectra of the MWCNTs before and after the acid treatment are shown in **Figure 4.2 a** and **b**. The D and G bands characteristic of CNTs, are clearly observed at 1330 cm^{-1} and 1580 cm^{-1}, respectively. They can be attributed to CNTs' defects (band at 1330 cm^{-1}), a disorder-induced mode, and to an in-plane E_{2g} zone-center mode.[197] As expected, after functionalization, the ratio between the intensities of these two

bands increases, due to the formation of surface defects in CNTs as a consequence of the insertion of chemical groups and bond breaking. [196, 198]

In **Figure 4.2 c** and **d** a comparison of MWCNTs and F-MWCNTs dispersion in ethanol at different times is shown. MWCNTs undergo strong precipitation, while no optical difference can be appreciated for F-MWCNTs in solution. The presence of hydroxyl and carboxylic groups keep the MWCNTs stable in solution up to 6 months (not shown here).

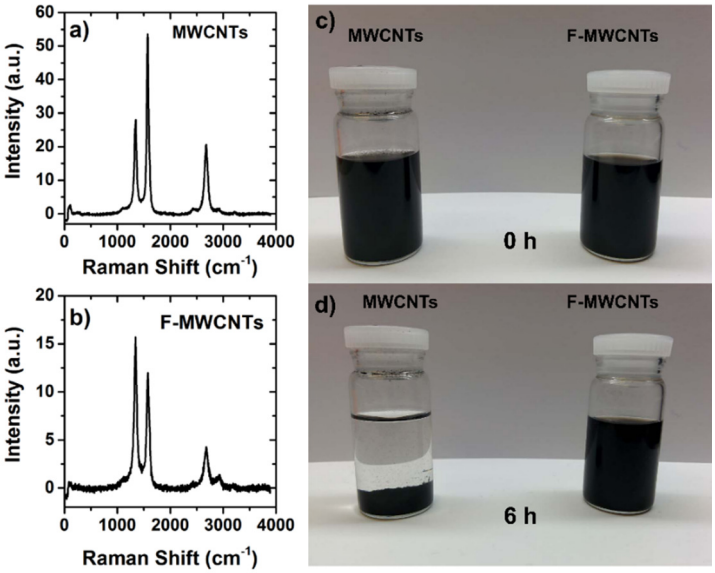

Figure 4.2. Raman Spectra of the (a) MWCNTs and (b) F-MWCNTs. In (c) and (d) is reported a dispersion of MWCNTs and F-MWCNTs in ethanol solution at 0h and after 6h, respectively.

In **Figure 4.3** atomic force microscopy (AFM) images of the MWCNTs are shown. The samples were prepared by spin-coating a diluted solution of a mixture of TiO_2 and F-MWCNTs (or MWCNTs) on FTO, to obtain a thin film in which the CNTs were visible. In both cases (**Figure 4.3 b** and **c**) the CNTs were conformally covered by TiO_2 nanoparticles.

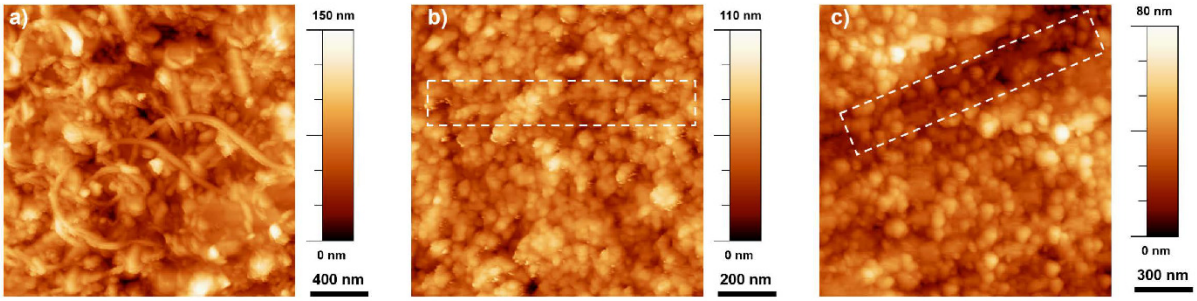

Figure 4.3. AFM images of a) F-MWCNTs on FTO, (b) F-MWCNTs/TiO_2 and (c) MWCNTs/TiO_2. The dashed squares highlight the presence of the CNTs.

Scanning Electron Microscopy (SEM) images of the F-MWCNTs/TiO_2 composite photoanode films are shown in **Figure 4.4**. Typically, F-MWCNT concentrations up to 2% wt are not visible by SEM imaging (**Figure 4.4 a** and **b**) due to conformal coverage and absence of cracks. [190]

From our analyses the coverage of F-MWCNTs by TiO_2 NPs is similar to what is reported in the literature for analogous systems: [70, 199] the TiO_2 NPs conformally cover the CNTs (and graphene sheets in case of graphene addition), making them almost invisible to SEM observation. High resolution TEM applied to similar systems was unable to identify any difference in the grafting of TiO_2 NPs to CNT/graphene structure. The main difference induced by the presence of MWCNTs (or graphene) in the composite is the variation of density/porosity (as demonstrated below through AFM) and the formation of deep cracks at high F-MWCNTs concentration. We were able to detect F-MWCNT only in the 4 wt% sample. A high F-MWCNTs load leads to a less compact TiO_2 layer and can induce some cracks in the film, as visible in **Figure 4.4 c** to **f**. At this high percentage, it is possible to observe MWCNTs aggregates conformally covered by TiO_2 nanoparticles. **Figure 4.4 c** and **Figure 4.4 d** show some F-MWCTNs, covered by TiO_2 nanoparticles, confirming their presence inside the metal oxide scaffold after high-temperature annealing.

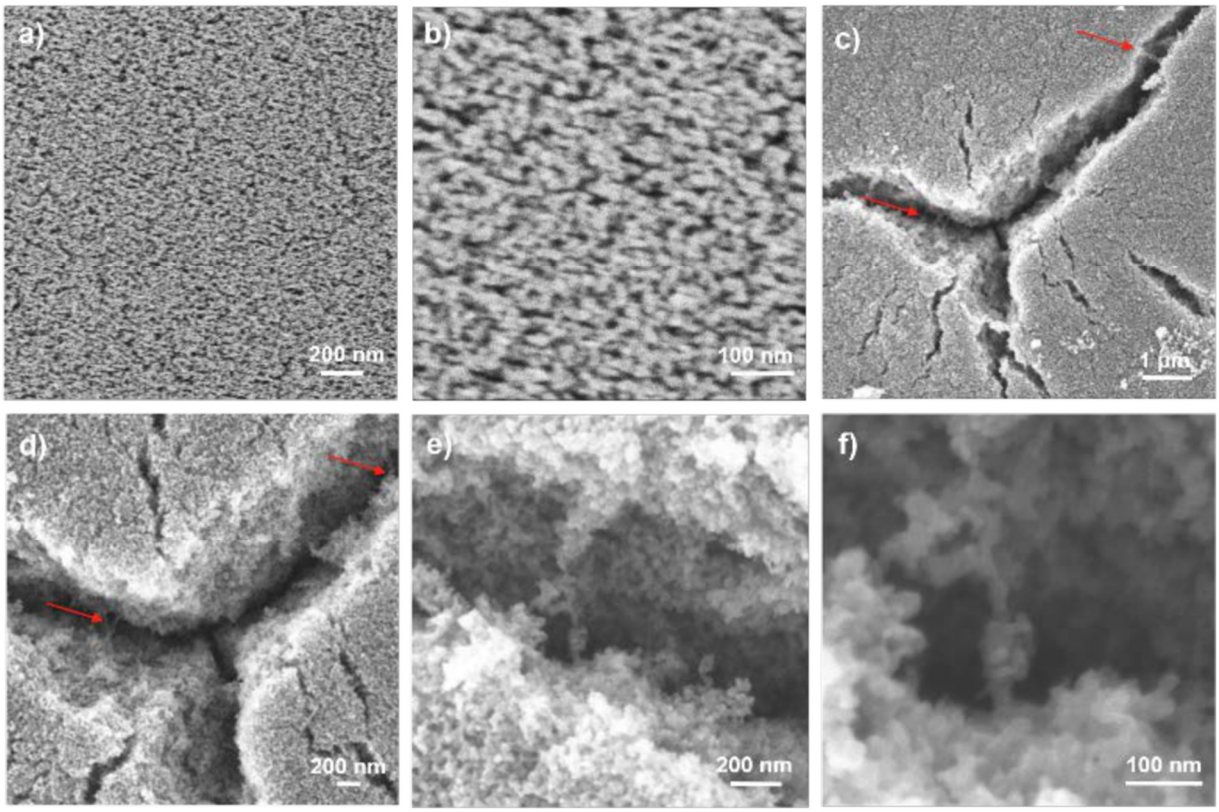

Figure 4.4. SEM images at different magnifications of 2 wt% F-MWCNTs/TiO_2 photoanode (a,b), and 4 wt% F-MWCNTs/TiO_2 photoanode (c-f). Red arrows indicate the F-MWCNTs, partially covered by TiO_2 NPs.

To investigate the effects of F-MWCNTs on the absorbance in the visible range, UV-Visible absorption spectroscopy was performed on samples containing various percentages of F-MWCNTs. The results in **Figure 4.5** suggest a slight increase in absorbance from 0 to 4 wt% F-MWCNTs. Absorbance from F-MWCNTs is in competition with absorbance from the dye for charge photogeneration, as photons absorbed by F-MWCNTs do not contribute to the photocurrent and are lost, thus affecting the performance of the cell. However, the slight increase of absorbance even in the sample with higher F-MWCNT concentration calls for a minor contribution of this effect in impairing PCE (otherwise we would expect a proportionality between F-MWCNT loading and PCE reduction). The UV-Vis reports the photoanodes with only the active layer of TiO_2/F-MWCNTs and not the complete one (with scattering layer and dye) used in the device. In fact, for high scattering thin film this measurement is not suitable.

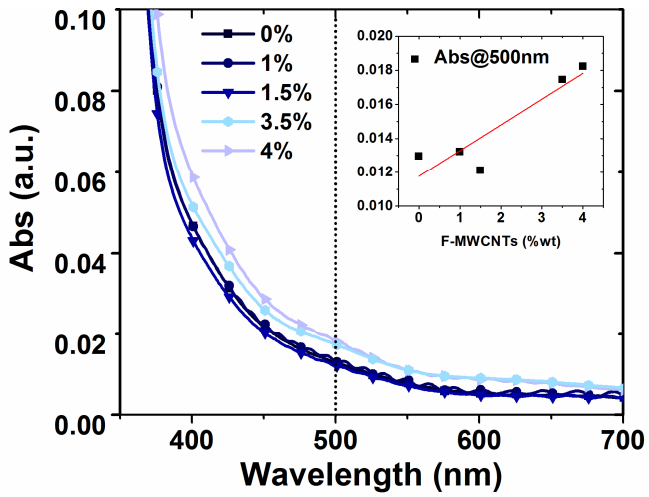

Figure 4.5. Absorbance spectra of various samples containing different percentage of F-MWCNTs. The increase in absorbance is highlighted in the inset that reports the change in absorbance at 500 nm for different F-MWCNTs concentrations.

Further confirmation of the presence of F-MWCNTs inside the TiO_2 matrix after the annealing process was obtained from diffuse reflectance Fourier-transform infrared (DRIFT) and Raman spectroscopies. Similar results are obtained independent of F-MWCNTs concentration. The Raman spectrum of a typical TiO_2/F-MWCNTs nanocomposite is showed in **Figure 4.6 a**. The three intense bands at 394.7, 514.5 and 637.2 cm^{-1} are ascribed to the B_{1g}, $A_{1g} + B_{2g}$ and E_g modes of anatase TiO_2, respectively. [200]

The D (disordered carbon induced) and G (graphite carbon related) bands are represented respectively at 1200 cm^{-1}, 1650 cm^{-1}, indicating the co-existence of TiO_2 and F-MWCNTs in the nanocomposite. These bands can be attributed to CNT defects and a disorder-induced mode as well as in-plane E_{2g} zone-center mode.[197]

The DRIFT spectrum (4000-400 cm^{-1}) of a typical photoanode containing F-MWCNTs is shown in **Figure 4.6 b**. The stretching modes of C-H bonds are clearly visible in the region 3000-2800 cm^{-1}, where asymmetrical and symmetrical stretching vibrations of $–CH_2$ and $–CH_3$ groups can be observed. The region from 3500 to 3000 cm^{-1} is dominated by the stretching vibration of –OH groups: the associated band is relatively sharp and the typical, very broad shoulder usually associated with the stretching vibration of hydroxyls in carboxylic acids is absent. This suggests that the –COOH groups generated in the functionalization process of MWCNTs are no longer present while the carbon materials are inserted in the TiO_2 scaffold. This hypothesis is also confirmed by the analysis of the fingerprint region (inset in **Figure 4.6 b**), where, together with the stretching mode of C=O (1649 cm^{-1}), symmetrical and asymmetrical stretching vibration of O-C-O groups are recorded (1488 cm^{-1} and 1405 cm^{-1}, respectively).

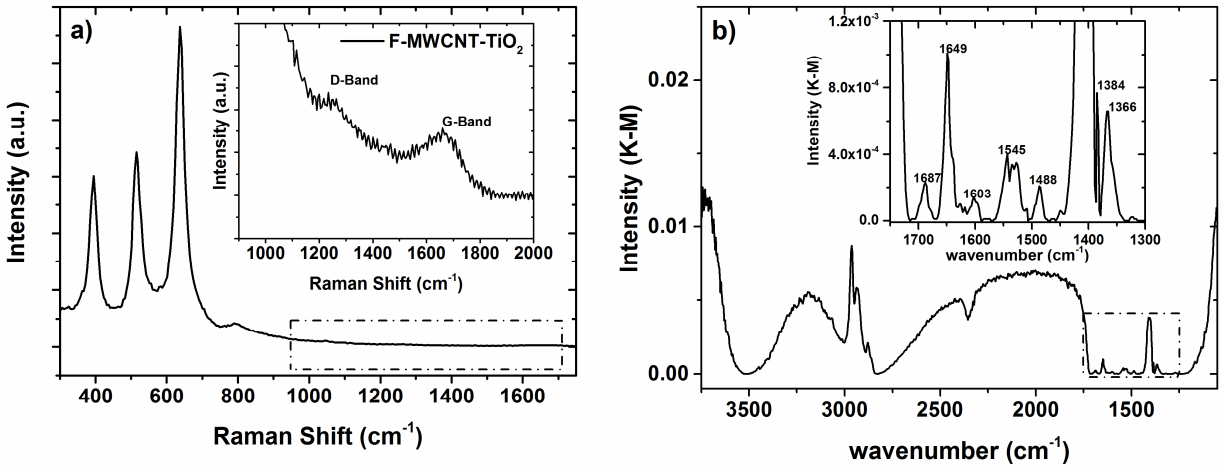

Figure 4.6. a) Raman spectrum and b) DRIFT spectrum of a typical F-MWCNTs-TiO_2 photoanode.

To further analyze the effect of the addition of F-MWCNTs, the surface morphology of the samples was investigated by AFM. A variation in film roughness is clearly visible from the AFM images reported in **Figure 4.7**, in which three samples at different F-MWCNTs concentrations are analyzed: 0, 2 and 4 wt%, respectively. A different dimension of the pores visible at the surface of the TiO_2 film is apparent, and it is observed to increase with the increasing of the percentage of F-MWCNTs. Previous work reported that the introduction of F-MWCNTs into a TiO_2 matrix generally induces better separation of TiO_2 particles, consequently resulting in a structure with higher porosity and surface area. [190, 195, 201]

The addition of F-MWCNTs up to medium load (2% wt) enlarges the network of the TiO_2, thus leading to larger surface pores. It is likely that increased porosity does not reflect only at the surface of the film, but also in its bulk, leading to larger surface area, as also confirmed from the dye loading quantification reported below. Further increase of the amount of CNTs leads to the formation of agglomerations resulting in

irregular and large pore sizes that can affect the roughness of the photoanode and reduce the specific surface area (decreasing consequently the dye loading).

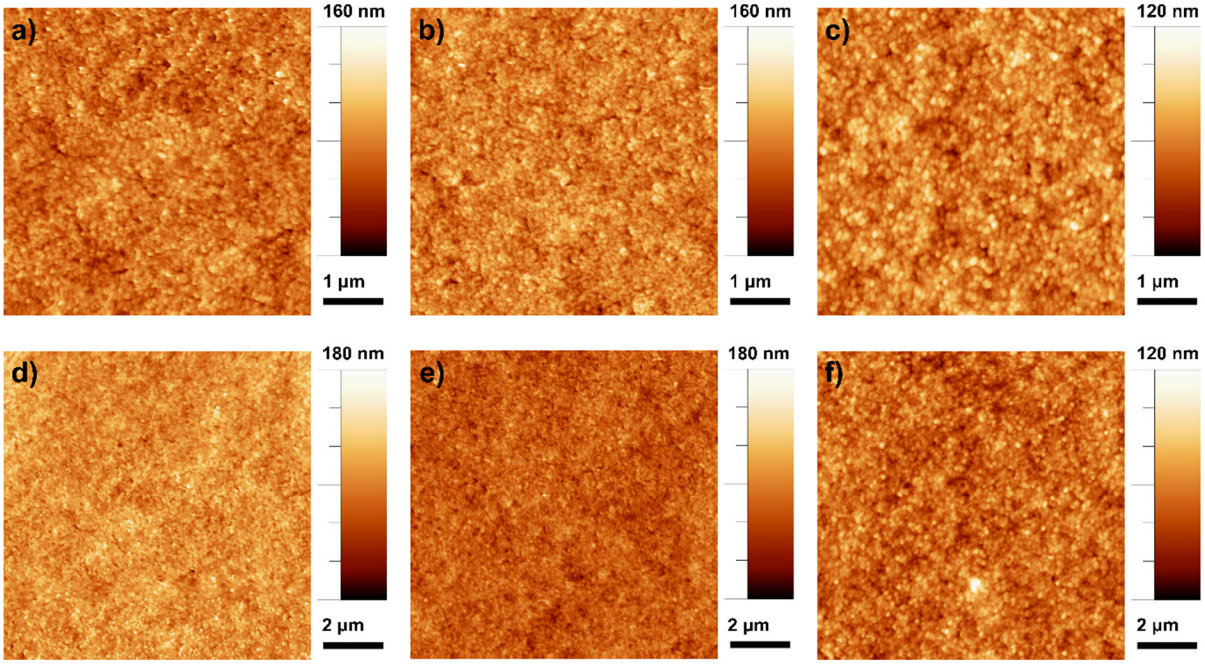

Figure 4.7. AFM images of sample with different concentration of F-MWCNTs: a,b,c) 0 wt%, 2 wt %, 4 wt% on 5 µm*5 µm; d,e,f) 0 wt%, 2 wt %, 4 wt% on 10 µm*10 µm.

A further confirmation of this phenomenon comes from the analysis of dye loading (**Figure 4.8 a**). Both dye loading and volume density increase with the increasing of F-MWCNTs amount (up to 2 wt%) and then start to decrease again at further F-MWCNT addition. The data indicate that at optimum F-MWCNTs loading (2 wt%) an electrode with maximum porosity and specific surface area is formed, which maximize the dye loading and optical density of the photoanode. The quantitative parameter to estimate the available surface for a certain photoanode is the so-called roughness factor, which is defined as the total available surface per sample area. It can be calculated by taking into account the measured dye loading and film thickness, under the hypothesis of monolayer dye absorption on the TiO_2 surface. **Figure 4.8 b** displays the values of the roughness factor as a function of F-MWCNTs concentration for samples with the same thickness (mandatory for fair comparison of different samples). A value of 1.6 nm^2/dye molecule was used to estimate the roughness factor. [202] This estimation indicates that the photoanode surface roughness increases with the incorporation of F-MWCNTs up to 2 wt %, while it decreases for higher loads.

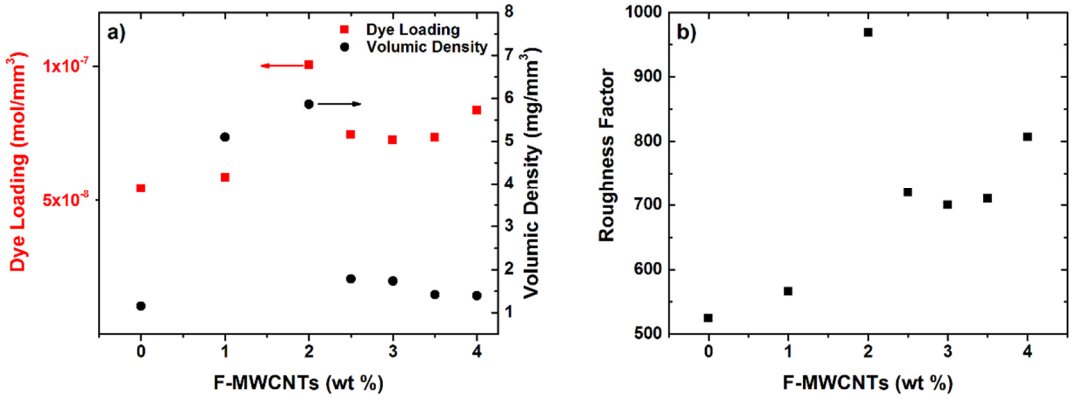

Figure 4.8. a) Dye loading (left) and Volume Density (right) of samples at different load of F-MWCNTs. At the optimum value of F-MWCNTs (2 wt%) corresponds the maximum in dye loading and volume density. b) Roughness factor calculated for different load of F-MWCNTs.

4.1.2 Functional properties of DSSCs based on F-MWCNTs

We investigated the effect of different F-MWCNT loading on the functional properties of DSSCs. The J-V curves of selected cells under AM 1.5G simulated sunlight and the External Quantum Efficiency (EQE) are reported in **Figure 4.9 a** and **b**. Table 1 reports the PV parameters (V_{oc}, J_{sc}, FF and PCE). The trend of PV parameters as a function of F-MWCNT loading is reported in **Figure 4.9 c** to **Figure 4.9 f**.

Compared with bare TiO_2, the F-MWCNTs/TiO_2-based DSSC with concentration up to 2 wt% showed higher PCE. At the optimum concentration of 2 wt% we obtained a maximum increase resulting in PCE as high as 7.95%, with an enhancement of around 30% with respect to pure TiO_2 (6.05%).

The presence of F-MWCNTs in the concentration range up to 2 wt% significantly boosts J_{sc} compared to pure TiO_2 photoanodes, while the other cell parameters (V_{oc}, FF) do not play a major role in altering PCE.

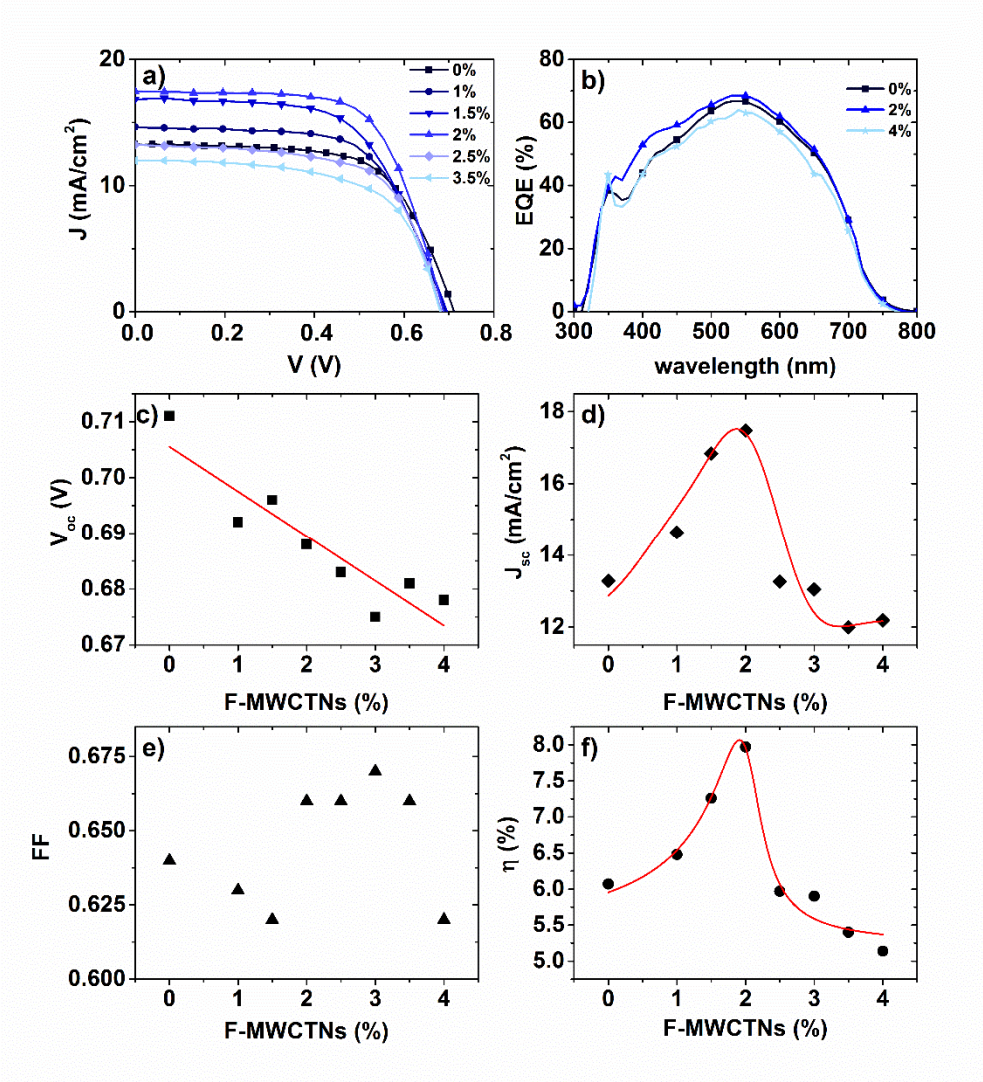

Figure 4.9. a) J-V curves of DSSCSs at six different percentages of F-MWCNTs under simulated sunlight (AM 1.5G, 100 mW·cm^{-2}). b) EQE of the most representative samples. (c to f) Variation of functional parameters (V_{oc}, J_{sc}, FF, and PCE) as a function of F-MWCNTs loading. Red lines are a guide for the eye.

Table 4.1 Functional characteristics of the DSSCs

[F-MWCNTs] (wt%)	V_{oc} (V)	J_{sc} (mA cm^{-2})	FF	PCE (%)
0	0.71±0.01	12.9±0.4	0.65±0.02	**6.05±0.05**
1	0.69±0.01	14.8±0.6	0.63±0.01	**6.55±0.05**
1.5	0.69±0.01	16.85±0.01	0.62±0.01	**7.15±0.15**
2	0.69±0.01	17.50±0.05	0.66±0.01	**7.85±0.10**
2.5	0.680±0.005	13.2±0.1	0.66±0.01	**5.95±0.05**
3	0.670±0.005	12.8±0.4	0.66±0.01	**5.70±0.20**
3.5	0.680±0.005	12.00±0.05	0.67±0.01	**5.50±0.20**
4	0.670±0.005	12.15±0.05	0.64±0.05	**5.30±0.20**

The J_{SC} reaches its maximum in the 2 wt% sample and then suddenly decreases at higher F-MWCNTs concentrations: 2.5 wt% of MWCNTs results in a J_{SC} almost equal to the sample of pure TiO_2. The EQE on selected samples (0 wt%, 2 wt% and 4 wt%) confirms the trend with higher values for the samples at 2 wt%.

V_{oc} is slightly but systematically affected by the presence of MWCNTs. As pointed out by several recent studies, [70, 192, 193, 203] the addition of carbonaceous materials results in a V_{oc} decrease, most probably due to the downshift of the CB in the composite system, compared to pure TiO_2, [192] as the V_{oc} is determined by the difference between the redox potential of the electrolyte and the Fermi level of TiO_2. [204, 205] The larger the F-MWCNT concentration, the larger the expected V_{oc} decrease, as found in our cells. The decrease is of the order of a few tens of mV (32 mV between the pure TiO_2 and the 4 %wt sample), which does not significantly affect the increase in PCE which is prompted by current density increase. This result is in contrast to what Kamat observed in 2008. [206] In that case, however, CNT concentration was much larger, as the photoanode was essentially composed of CNTs covered by TiO_2 nanoparticles. Therefore the V_{oc} decrease was much more pronounced and led to a strong decrease of PCE. Another possible concurring reason for this behaviour at high F-MWCNT concentration could be the partial coverage of the surface of the F-MWCNTs by the TiO_2 nanoparticles, which leave them in direct contact with the electrolyte. [194, 207] This creates a preferential path for charge recombination, which results in charge loss and decrease in V_{oc}.

4.1.3 Electrochemical Impedance Spectroscopy

We applied EIS to gain insight on changes induced by the presence of F-MWCNTs on the physical and chemical processes which take place in the operating device. In particular, we focused on the recombination resistance R_{rec} and the chemical capacitance C_{μ}. We could not observe the transport resistance due to the large conductivity of the samples. [208,209]

Figure 4.10 a compares the Nyquist plots of three different cells (bare TiO_2, 2% wt and 4% wt) at bias voltage equal to Voc. Three semicircles are clearly observable in the measured frequency range from 100 mHz to 300 kHz and located in the high, intermediate and low frequency regimes, from left to right respectively. The arc at high frequency is assigned to the impedance of the electron transfer at the Pt CE, the one at intermediate frequency corresponds to recombination at the TiO_2 surface, and the last one at low frequencies represents the ionic diffusion process inside the electrolyte. [208,210,211] The most remarkable feature is that the 2% wt cell leads to the smallest arcs at mid frequencies, related to recombination at the TiO_2 surface. The medium arc takes into account the recombination resistance of the mesoporous layer: for the cell exploiting 2 %wt F-MWCNTs this feature is much smaller compared to the others. This behaviour indicates that the presence of an optimum amount of F-MWCNTs promotes efficient electron transport, increasing the overall conductivity of the TiO_2 matrix.

The peak frequency of the central arc (ω_{max}) in a Nyquist plot gives a simple relationship with the reaction rate constant for recombination. [211] A lower value indicates a lower recombination rate. By extrapolating the ω_{max} value of the central arc for the three cells, we observe that the smallest one corresponds again to the 2% wt cell, while the others exhibit values that are 3-4 times higher: 15 Hz (2% wt) versus 60 Hz (4% wt) and 75 Hz (0% wt). This means that the recombination rate constant for the cell at 2% wt is smaller than the other cell. The slower recombination rate indicates a larger recombination resistance within the photoanode, resulting in much slower back-reaction, confirming the beneficial effect of the addition of MWCNTs.

A further confirmation of this behaviour is visible in **Figure 4.10 b** and **c**, which reports the R_{rec} of five samples at different F-MWCNTs concentrations. **Figure 4.10 9 b** displays the Nyquist plots of three cells at low voltage bias (250 mV): only a high resistance arc due to the charge recombination and capacitance of the back layer can be appreciated, while the counter electrode contribution is hidden. The increase in recombination resistance in this range is attributed to the reduction of the back reaction between the FTO, the TiO_2/F-MWCNTs composite and the electrolyte. [44] In **Figure 4.10 c** in the region at low potentials (up to 550 mV), where the main contribution comes from the charge transfer from the uncovered FTO substrate at the bottom of the porous film (also called back layer),[212] the resistance follows the same trend as the efficiency: R_{rec} increases from 0% to 2 wt%, while it decreases again at higher F-MWCNT concentrations.

Increasing further the amount of F-MWCNTs leads to a decrease of R_{rec} associated with the back reaction. This kind of behaviour can be due to local agglomerations of F-MWCNTs that can create traps and surface defects.

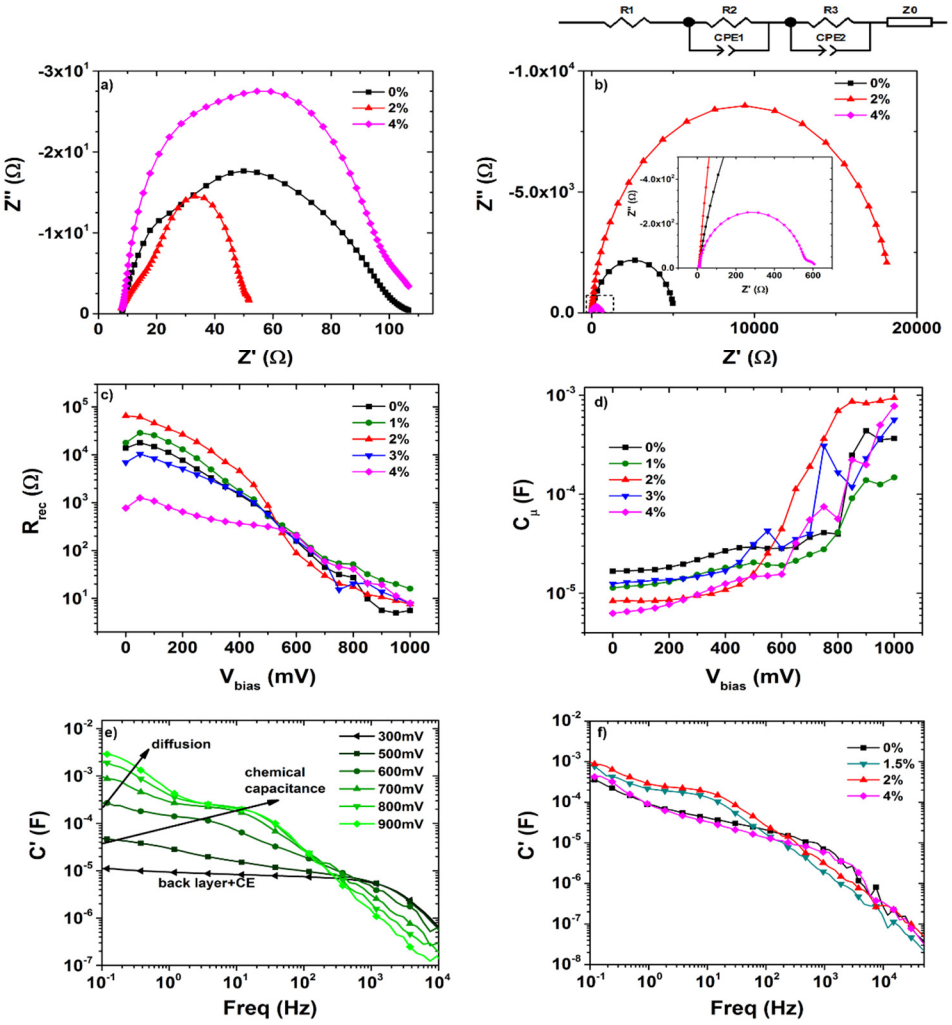

Figure 4.10. EIS analysis of DSSCs at different F-MWCNTs concentrations. (a) Nyquist plot in dark at bias equal to Voc; (b) Nyquist plot in dark at low bias (V_{bias} = 250 mV) and equivalent circuit used for fitting the data. The inset is a zoom on the Nyquist plot of the sample at 4 wt%; (c) Recombination resistance and (d) Chemical capacitance from EIS measurements in dark; (e) Real part of the capacitance at several applied potentials for the cell with 2 wt% of F-MWCNTs (f) Real part of the capacitance at V_{bias} = Voc for 4 different concentrations of F-MWCNTs: 0 wt%, 1.5 wt%, 2 wt%, 4 wt%.

In addition, at high F-MWCNTs concentrations, when agglomerations are formed, a direct contact between F-MWCNTs and electrolyte can occur, which boosts electron loss directly from F-MWCNTs to electrolyte, further reducing R_{rec}. A confirmation of the presence of surface defects can be seen in **Figure 4.10 d** that reports the chemical capacitance as a function of the applied bias. The samples with high F-MWCNTs

concentrations (3 wt% and 4 wt%) exhibit a peak around 750 mV. This peak is assigned to sub-bandgap-localized states due to defects in the surface, causing a decrease in the efficiency of the cell. [213,214]

Figure 4.10 e shows the real part of the capacitance versus frequency in the 2 %wt cell for several values of applied bias. The different contributions to the overall capacitance are clearly observable. At low bias the low frequency limit of the capacitance is due to the contribution of the back layer and the counter electrode. When the bias is increased, the contribution of the chemical capacitance becomes dominant and the contribution from the diffusion in the electrolyte appears at higher bias. The dominant contribution of the chemical capacitance to the overall capacitance is clearly visible for the cell with 1.5 wt% and 2 wt% of F-MWCNTs as shown in **Figure 4.10 f**, while for lower/higher concentrations it is not as prevalent as for the others.

Optimum concentration of F-MWCNTs (2 wt%) exists that maximizes PCE. At higher F-MWCNTs loads, nanotube agglomeration tends to be prevalent, compared to the phenomenon of increasing surface area, resulting in a net decrease in PCE. In fact, as highlighted by AFM and dye loading measurements, the presence of conglomerates leads to formation of large pore sizes above 2wt% of F-MWCNTs that can reduce the specific surface area. This pores' enlargement can bring in direct contact the F-MWCNTs agglomerates with the electrolyte, increasing the recombination of the photo-generated electrons (as shown by the EIS analysis), which causes a reduction in the overall efficiency of the cell.

4.2 Conclusions

In conclusion, in this work I was able to demonstrate a fast and highly reproducible methodology to improve the charge collection and transport on DSSCs by addition of F-MWCNTs into a commercial TiO_2 paste. These results show that incorporating F-MWCNTs into a TiO_2 working electrode during the synthesis efficiently improves the physical/chemical properties of the cell, achieving a PCE of 7.95%, which represents more than a 30% increase compared to the bare TiO_2 sample. The main role of F-MWCNTs is to boost electron injection from the photoanode to the front contact, significantly increasing the collection of photogenerated charges and reducing charge recombination. The enhanced efficiency is also due to the improvement in dye uptake: the presence of F-MWCNTs influences the morphology of the titania matrix, increasing, for optimal loading values, the surface area available. An excess of F-MWCNTs reduces the open circuit photovoltage, increasing dramatically the charge recombination through direct charge transfer from the photoanode to the electrolyte as shown by EIS analysis. Finally, the proposed methodology is very fast and avoids any surface treatments, which are typically used to boost PCE in standard fabrication procedures of DSSCs.

4.3 Materials and methods

4.3.1 Photoanode preparation

The TiO_2 anatase nanoparticles paste were purchased from DyeSol and the standard MWCNTs (>95% Carbon, Sigma-Aldrich, cat. no. 698849, 10 μm average length) were functionalized following the method described by Osorio et al.[196] According to the method used in our group [70], a simple mixing approach was chosen for addition of F-MWCNTs to the TiO_2 paste. A precise amount of MWCNTs solution was mixed by mechanical stirring with a known weight of TiO_2 until full incorporation was reached (this process usually takes 5 minutes). The F-MWCNTs/TiO_2 composite and bare TiO_2 were tape casted on FTO glass followed by a drying process in ambient atmosphere and room temperature for 15 minutes and then 6 minutes at 150 ˚C. Afterwards, the photoanodes were annealed at 200 ˚C for 15 minutes, at 400 ˚C for 15 minutes and at 500 ˚C for 30 min. The prepared photoanodes were further sensitized with N719 dye (0.5 mM in ethanol, Sigma Aldrich) for 24 hours.

Different photoanodes containing various percentages of F-MWCNTs from 1 wt% up to 4 wt% were prepared. The final percentage of F-MWCNTs incorporated in the TiO_2 photoanode was estimated taking into account the photoanode weight before and after annealing. From previous work, the weight loss of TiO_2 paste after annealing is 80% of the original net weight. [70]

4.3.1 Device Fabrication

The DSSCs were fabricated by using the I_3^-/I^- redox couple electrolyte (Solaronix, Iodolyte HI-30), platinized FTO glass as the CE (5 nm thin film of Pt sputter-deposited on FTO), with 25 μm thick plastic spacer between the photoanode and the Pt CE.

4.3.1 Characterization of Materials and Devices

The structure and morphology of the photoanodes with or without F-MWCNTs were characterized by Scanning Electron Microscopy (SEM, FE-SEM LEO 1525 microscope) and AFM (Veeco Enviroscope). To investigate the presence of F-MWCNTs after annealing, Raman spectroscopy and DRIFT analysis were performed. DRIFT was carried out in a Bruker Vertex 70v Spectrometer recording 32 scans at 4 cm^{-1} resolution and displayed in Kubelka-Munk units[215,216] KBr was used as a background. Samples with the highest nominal amount of F-MWCNTs were chosen for both analyses.

We investigated the effect of F-MWCNTs on the optical absorbance using UV-Visible spectroscopy. Dye loading was quantitatively evaluated using UV-Vis spectrophotometry after complete removal of the dye from the photoanode. The photoanode was scraped off, weighted and dissolved in a known amount of

ethanol (3 mL). After sonication (30 min) and centrifugation (15 min @ 5000 rpm), the TiO_2 particles were removed and the absorbance of the solution was measured. Using a fitted calibration curve obtained from solutions of known N719 concentration the dye loading was then extrapolated using the 500 nm peak. The volume density was calculated dividing the mass of the photoanode by its volume.

The current−voltage (I−V) characteristics of the fabricated cells were measured by a Keithley 2400 SourceMeter under simulated sunlight using an ABET2000 solar simulator at AM1.5G (100 mW cm^{-2}) calibrated using a reference silicon cell and mechanical filters. The External Quantum Efficiency (EQE) spectra were acquired in dark using an EQE 200 Oriel integrated system. The measurement step was 10 nm and the photocurrent was recorded using a lock-in amplifier.

EIS was recorded in dark using a SOLARTRON 1260 A Impedance/Gain-Phase Analyzer. The AC signal was 10 mV in amplitude, in the frequency range between 100 mHz and 300 kHz. The applied bias during measurements was between 0 and 200 mV above the open-circuit voltage of the solar cell under illumination. All the samples were measured inside a Faraday cage. The obtained spectra were fitted with Z-View software (v3.0, Scribner Associate, Inc.) by applying an appropriate equivalent circuit.

5 Enhancing the charge transfer in DSSC by modulating the morphology of the counter electrode

This chapter is based on the paper "*Platinum/Palladium hollow nanofibers as high-efficiency counter electrodes for enhanced charge transfer*" published on *Journal or Power Sources*, 335, (2016), 138-145.

In this chapter, the focus is moved from the photoanode to another fundamental layer of a DSSC, the counter electrode (CE). The CE is the main component responsible for the regeneration of the dye as it provides the catalytic surface to enable the reduction of the electrolyte. By tuning its morphology and materials it is possible to boost the charge transfer between the CE and the electrolyte. Furthermore by doing so, the dye stays in the oxidized state for shorter time, reducing the possibility of recombination on the photoanode side.

As seen in Chapter 2.1, after photoinduced electron injection from the dye into the CB of TiO_2, the dye is in its oxidized state and must be reduced by an electron donor in the electrolyte for regeneration. The reduction of the oxidized sensitizer (S^+) by iodide follows this possible reaction mechanism:[41]

$$2S^+ + 3I^- \rightarrow 2S + I_3^- \text{ (Regeneration of S)}$$

$$I_3^- + 2e^- \rightarrow 3I^- \text{ (Regeneration of } I^-\text{)}$$

While the regeneration of the dye is done at the dye/electrolyte interface, the reduction of the electrolyte happens on the surface of the CE. As we have seen briefly in Chapter 2.1, the main role of the CE is to transfer electrons arriving from the external circuit back to the redox electrolyte and reduce the redox species used as a mediator in regenerating the dye. Furthermore, as the CE is positioned at the opposite side of where the light enters, it can reflects the unabsorbed light back to the cell to enhance utilization of sunlight. An ideal CE should have good conductivity, thus low over potential, and exhibit high electrocatalytic activity for reduction of the redox couple at the lowest cost possible. A simple FTO coated glass does not provide enough catalytic activity for the reduction of the triiodide. For this reason, in order to minimize the charge transfer resistance, some catalytic materials is coated on conducting substrates, such as FTO or ITO to speed up the reaction. Platinum (Pt) remains the preferred material for CEs in this type of cells due to its catalytic properties and its superior chemical and electrochemical stability. [217-219]

However, the high cost of Pt can be a detrimental factor for the commercialization of high performance DSSCs and photoelectrochemical systems in general. Therefore, the need to develop a cost-effective CE, without reducing its electrocatalytic activity and stability is a key factor for DSSCs commercial application.

Due to the importance of the CE in a DSSC device, a number of studies have been conducted to replace the Pt as the preferred material for CE. Carbon-based and hybrid Pt-free alloys CE showed promising results but still have some unsolved problems: low stability, reduction in DSSC transparency, and long and complicated production processes. [220-224] Rather than completely removing the Pt, another possibility is to reduce its amount in the CE, without sacrificing electrocatalytic activity and stability. Recently, bi-metallic platinum alloys, obtained by alloying Pt with transition metals (such as Ni, Pd, Co) have been proposed as alternatives to the traditional Pt CE. These alloys have higher catalytic activity than pure Pt, and have shown improved performance and stability, when applied as CE for DSSCs.[225-228]

Recently electrospinning, a facile, low cost and scalable technique was used to produce 1D architectures, including Pt-networks obtained by electrospinning composites from polymer/Pt precursors.[229, 230] These studies employed Pt nanofibers to develop transparent CEs for flexible DSSCs, requiring a minimum coating of 80 nm Pt to provide good mechanical flexibility[229, 231] and/or electrospinning times longer than 10 minutes to achieve a performance similar to that of Pt deposited on FTO glass.[229, 230]

By using a similar approach to Wu et al., in which 1D structures have been obtained by sputtering metal coating thicknesses of at least 80 nm,[231] in this work, we use an efficient and simple fabrication process for nanostructuring CEs for DSSCs with enhanced catalytic activity by using magnetron sputtering to coat with a bimetallic Pt/Pd alloy electrospun polymer nanofibers, which act as sacrificial templates. By tuning the morphology and composition of the nanofibers, we demonstrate that the amount of precious metal can be decreased up to a factor of four. The nanostructured CEs were tested in DSSCs to provide a complete study of their PEC performance by varying the Pt/Pd sputter coating thickness (20, 40 and 80 nm) and density of the nanofibers on FTO glass substrates (electrospinning time: 40 s or 120 s). This allowed us to determine the optimal CE architecture to enhance the PCE and, through a detailed study of the charge-transfer processes occurring in the CEs, we were able to attribute this increase to the improved electro-catalytic performance.

5.1 Results and discussion

5.1.1 Morphological and structural characterization

Polyamide-6 (PA6) nanofibers were randomly deposited onto FTO glasses by short electrospinning deposition time. Successively, the nanofiber networks were used as a sacrificial template to deposit Pt/Pd nanoparticles by magnetron-sputtering. By annealing process, the polymer was removed producing of hollow nanofibers. Using this approach, a highly uniform and interconnected nanofiber network was

obtained. As the sputtered film still maintains a certain porosity, the removal of the polymer is possible.[219, 229, 232]

Figure 5.1 displays the morphology of the fibers obtained with different coating thicknesses. At low Pt/Pd coating thickness the formation of connected fine grains of nanoparticles is clearly visible in the high resolution inset; when increasing coating thickness, the grain size increases. This observation is in agreement with narrowing of the XRD (X-ray powder Diffraction) peaks (**Figure 5.2**) ascribed to face-centered cubic (FCC) crystalline Pt (JCPDS card No. 01-087-0646), meaning that the grain size of the sputtered Pt becomes larger at higher Pt/Pd coating. Most of the nanofibers showed a continuous coating over a large length of the Pt/Pd nanofiber. However, it was also found that depending on the thickness of the sputtered catalyst, the fibers were prone to break after polymer removal. The nanofibers with the lowest Pt/Pd coating (20 nm) were the most affected (as shown by the dotted circles in **Figure 5.1 a**) whereas at the highest coating (80 nm) only few nanofibers were broken, especially at the junctions between several fibers. These features favored the removal of the polymer. Consequently, the nanofibers had a better interconnection at their junctions when using a thicker coating. On the other hand, broken nanofibers could allow easier penetration of the liquid electrolyte within the hollow structure, suggesting a possible improvement in the electrochemical activity of these electrodes.

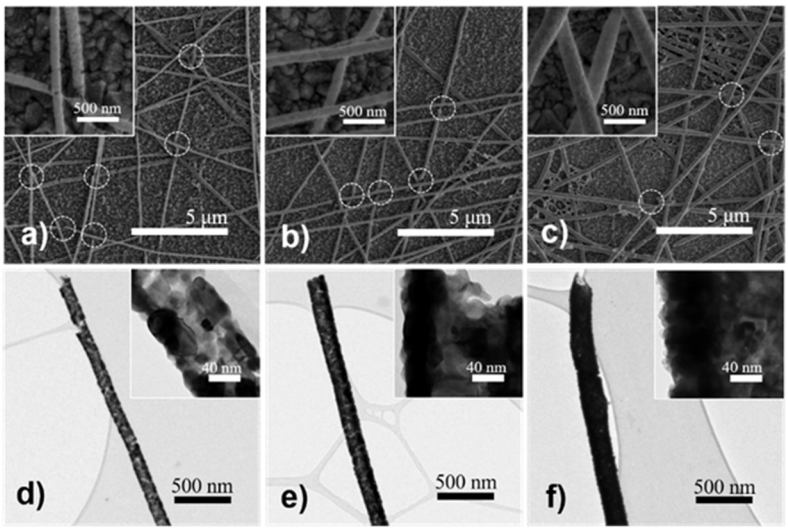

Figure 5.1. SEM and TEM images of the hollow nanofibers obtained at different Pt/Pd sputter coatings. (a) and (d) 20 nm, (b) and (e) 40 nm and (c) and (f) 80 nm.

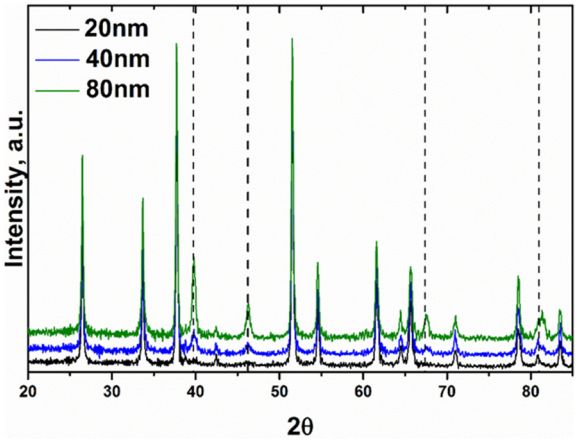

Figure 5.2. XRD patterns of the CEs obtained by varying the Pt/Pd deposition. Dashed lines highlight the peaks corresponding to the cubic Pt (JCPDS card No. 01-087-0646), the rest of the peaks were consistent to the tetragonal SnO_2 (JCPDS card No. 01-088-0287).

The morphology obtained by different thicknesses of the sputtered catalyst is visible in the TEM images **(Figure 5.1 d-f)**. High magnification images show Pt/Pd nanoparticles, 30 to 60 nm in diameter, homogeneously assembled on the surface of the nanofibers. The hollow nanofibers were obtained after polymer removal (confirmed by the brighter central region of the fiber due to lower mass density caused by the empty space).

EDS spectra and semi-quantitative measurements of the chemical composition in the Pt/Pd nanofibers before and after polymer removal are included in **Figure 5.4 a, b**. Carbon was not detected in the EDS confirming the polymer removal after annealing procedure. Additionally, the top view of an individual nanofiber (sputtering direction) is displayed in **Figure 5.4 c** whereas **Figure 5.4 d** includes a nanofiber detached from the substrate after breaking the CE. The bottom part of the nanofiber (side facing the FTO) clearly shows the hollow/concave structure of the nanofiber. The fiber diameter increases at higher Pt/Pd thickness as seen in Table 5.1, with sizes in the range of 120-300 nm.

We compared two different deposition times to increase the CE surface area. Electrospinning deposition time of 120 s yields much higher density of hollow nanofibers, stacked on top of each other (**Figure 5.3 c**).

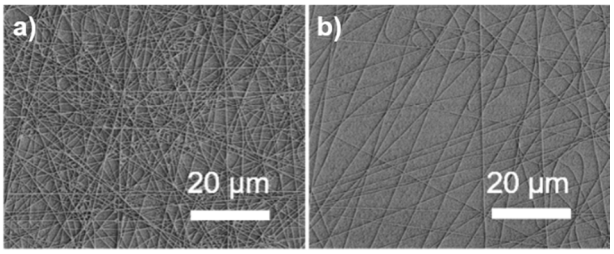

Figure 5.3. SEM images of Pt/Pd hollow nanofibers obtained at (a) 40 s and (b) 120 s electrospinning deposition.

The hollow nanofibers have an average coverage of 16% and 31% for electrospinning deposition times of 40 s and 120 s, respectively. As reported by EDS, the atomic ratio of Pt/Pd to SnO_2 (FTO glass) remains similar at different density of the nanofiber deposited and it increases according to the amount of sputtered catalytic metal from 3, to 6 to 15 when the deposition thickness was increased from 20, to 40, to 80 nm, respectively (Table 5.2).

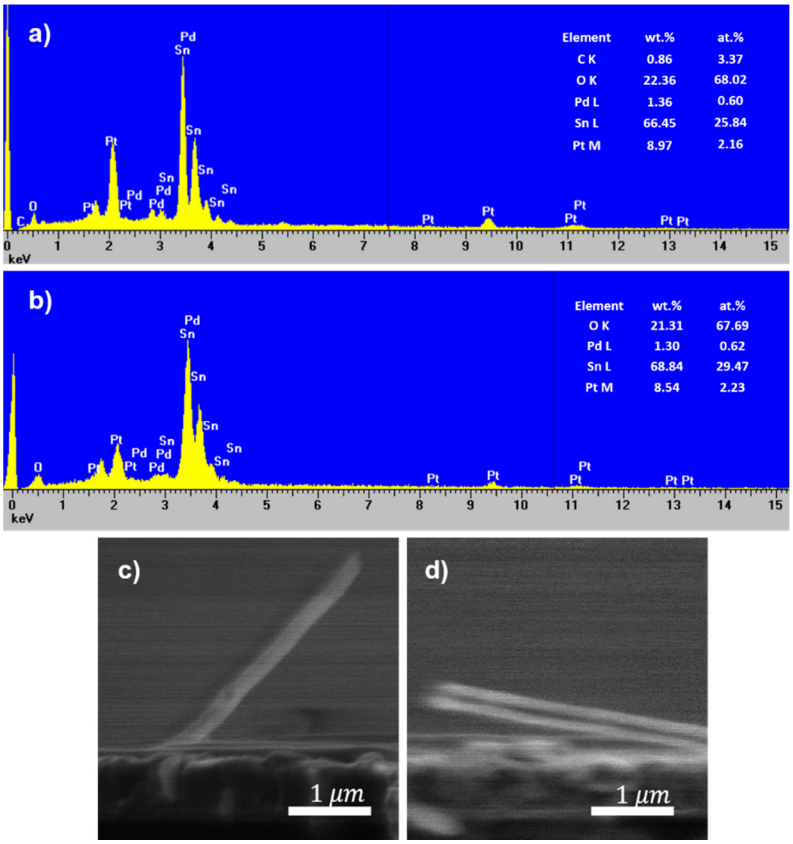

Figure 5.4. EDS spectra and composition of the Pt/Pd hollow nanofibers: (a) before polymer removal (b) after polymer removal. SEM images of the Pt/Pd hollow nanofibers cross-section showing (c) top view of the nanofiber (d) bottom hollow/concave side.

Table 5.1. Physical characteristics of Pt/Pd hollow nanofiber in the CEs.

Sample	Diameter, nm	Area covered, %
40NF20 nm	156 ± 32	12.43
40NF40 nm	182 ± 70.9	16.82
40NF80 nm	193.6 ± 67.7	18.94
120NF20 nm	151.2 ± 42.8	27.15
120NF40 nm	167.4 ± 39.9	29.17
120NF80 nm	215.9 ± 87.6	35.8

Table 5.2. Pt/Pd to SnO_2 (FTO glass) CEs composition obtained by EDS.

	00 NF		40 NF		120 NF	
	wt.%	at.%	wt.%	at.%	wt.%	at.%
20 nm	11.69	2.93	11.36	2.84	13.21	3.85
40 nm	21.15	6.48	19.46	5.60	19.28	5.60
80 nm	43.49	15.21	56.27	16.73	50.44	16.41

Due to how the sputtering procedure works (the sample rotates and tilts while the sputtering is on), some small inhomogeneity in Pt/Pd coverage can be found. They are visible as higher contrast in one side of the edges of the nanofibers, in both TEM (**Figure 5.1**) and AFM images (**Figure 5.5**). The fibers are homogenously deposited onto the FTO substrate forming a randomly distributed network (**Figure 5.5 a**), they feature uniform shape and have an average height size of 200 nm.

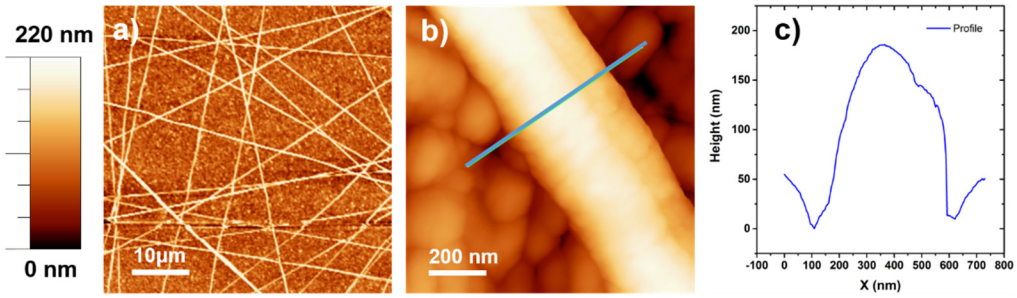

Figure 5.5. AFM scan of 40NF20nm CE. (a) 50x50 µm^2,(b) 1x1 µm^2, (c) profile of the line in (b).

5.1.2 Optical characterization and photovoltaic properties

Due to the lateral dimensions of the hollow nanofibers over 100 nm, they could act as scattering medium in the CE, therefore their light-reflecting ability was studied by diffuse reflectance (**Figure 5.6 a-c**). The lower reflectance ability of the hollow nanofiber CEs compared to the analogous flat CE can be attributed to light trapping within the hollow structures. A systematic decrease of reflectance is observed at increased deposition time (related to fiber density), suggesting the ability of the fibers to trap light, increasing incoherent scattering and decreasing reflectance. In addition, when the Pt/Pd coating is increased, the reflecting behavior becomes similar to that of the flat CE, due to the better coverage of the sacrificial template, as previously shown by SEM images, therefore reducing the amount of light which is trapped within the hollow nanofiber. An increased reflection can be observed in the 700-800 nm region, confirming the incident light-reflecting ability of the Pt CEs. However this enhancement does not contribute significantly to the final increase in PCE of the cell.[233] EQE measurements (**Figure 5.7**) confirm that the light-reflecting properties of the CEs do not contribute to improve the performance of the cells.

Figure 5.6 d-f shows the functional properties of DSSCs assembled with different CEs. For 40 s deposition of nanofibers, the PCE increases for all Pt/Pd film thickness, compared to flat CEs. For 120 s deposition, the PCE change is negligible or even worse than flat CE. At the optimum nanofiber density (40 s, **Figure 5.6 d**), the main effect for all Pt/Pd thicknesses is to boost the J_{sc}. Compared to the flat CE, the CE realized with 40 s deposition of the polymer nanofiber template and sputtered with 80 nm of Pt/Pd (40NF80nm) showed a J_{sc} increase of 13% for maximum PCE equal to 7.50%. Globally, the PCE increased by 15% when compared to the flat CE. The hollow nanofibers remain unaffected after testing in the DSSC (**Figure 5.8**).

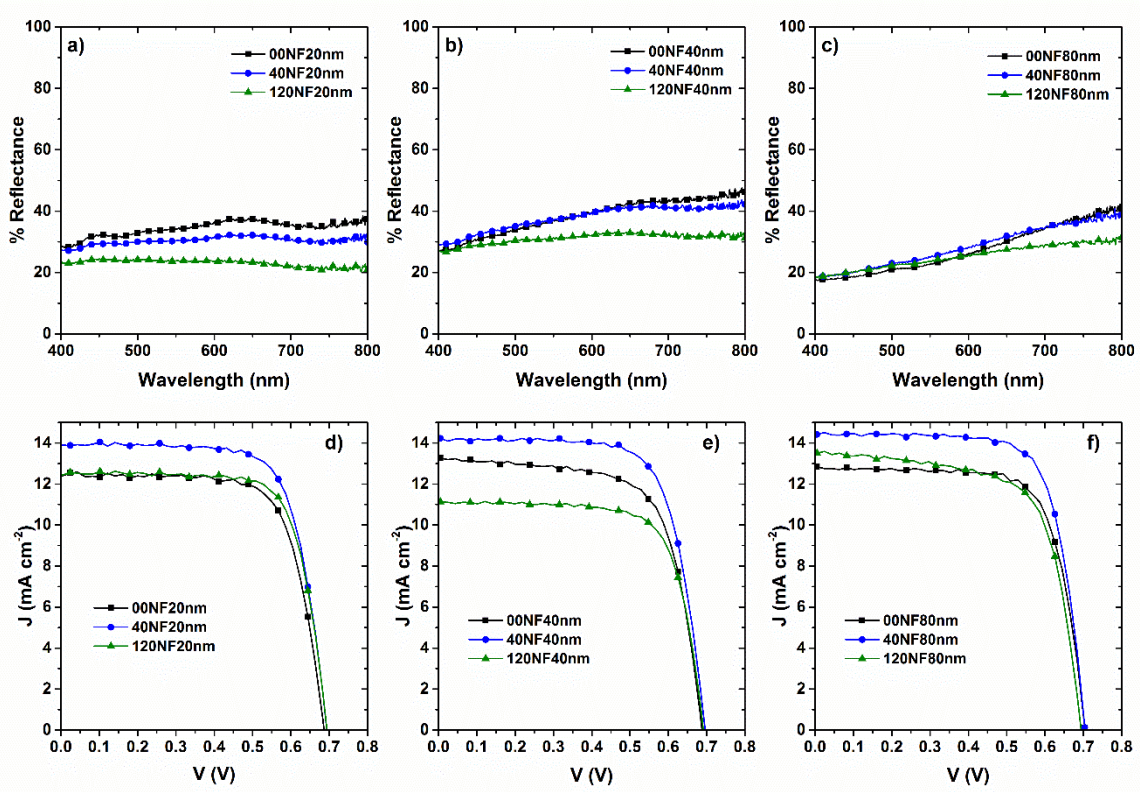

Figure 5.6. Diffuse reflectance measurements of the different counter electrodes (a-c). J-V curves of solar cells using different CEs (d-f).

Under the same illumination conditions, the V_{oc} and the *FF* are very similar for all the cells, and do not play a major role in increasing the PCE. The enhancement obtained here (15%), is higher than the one reported in previous work (8%) in which a similar polymer templating/sputtering method was employed. [219]

Our results are comparable to the performance improvement achieved by similar approach in cells based on a porphyrin sensitizer and Co-based electrolyte. However, in that case time-consuming and hardly scalable processes were used, like ALD deposition and $TiCl_4$ photoanode pre- and post-treatment, making the fabrication of the photoanode and CE expensive and time-consuming.[221] In our approach, we were able to nanostructure the CE by using simple and straightforward steps to improve the PCE.

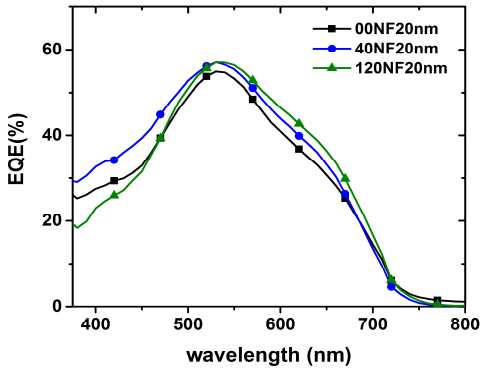

Figure 5.7. EQE of the DSSCs assembled with different nanofiber density.

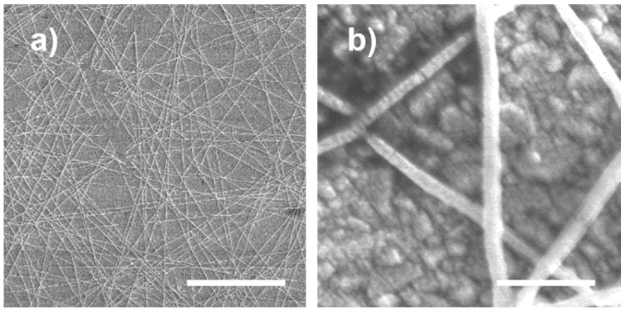

Figure 5.8. SEM images of (a) low (scale bar =20µm) and (b) high magnification (scale bar = 2µm) of 120N80nm CE after testing in DSSC.

Table 5.3 shows the data obtained from current density versus voltage (*J-V*) curves, from which we infer that 40 s nanofiber electrospinning deposition is the optimal condition, independently of Pt/Pd coating thickness. Increasing the Pt/Pd coating on the CEs has minor influence on the PCE. This "plateau" effect is well known: it has been previously found that no significant difference in the charge-transfer resistance at the electrolyte/CE interface was observed for flat CEs with Pt film thicknesses ranging from 25 to 415 nm.[219, 233] Even with the lowest Pt/Pd coating thickness (20 nm) there is a ~15% improvement in PCE using the nanofiber structured CE, when compared to the flat CE with the same coating thickness. To reduce the amount of required Pt, thereby decreasing the total cost of DSSC, we opted to focus on the CEs obtained with the thinnest Pt/Pd coating: 20 nm.

Table 5.3. Functional properties of DSSCs under 1 sun irradiation (AM1.5G, 100 mW cm-2)

Sample	V_{oc} (V)	J_{sc} (mA cm^{-2})	FF	*PCE (%)*

00NF20nm	0.69	12.4	0.72	6.15
40NF20nm	0.69	13.9	0.72	7.00
120NF20nm	0.69	12.5	0.74	6.45
00NF40nm	0.69	13.3	0.72	6.15
40NF40nm	0.70	14.2	0.71	7.05
120NF40nm	0.69	11.1	0.72	6.00
00NF80nm	0.70	12.8	0.72	6.50
40NF80nm	0.70	14.4	0.74	7.50
120NF80nm	0.69	13.5	0.68	6.35

The electron lifetime inside the TiO_2 photoanode plays a major role in determining the PCE.[234, 235] Electron lifetime is affected by many factors, including the photoanode, CE architecture, and materials.[235, 236] In this work the photoanode was the same for all the analyzed devices, and we only modified the CE structure. Thus, the variation of the functional properties can be attributed exclusively to the CE. Specifically, electrons at the CE originating from the external load induce the reduction of the I_3^- species: for this reason, the electron lifetime can be used to evaluate the CE catalytic kinetics.

As seen in Chapter 2.1, in a DSSC, there are mainly two possible recombination reactions: electrons transported within the oxide can recombine either with the oxidized dye or with the oxidized state of the redox couple (I_3^-). For high I_3^- concentrations (more than 30 mM) it has been shown that the electron recombination with the oxidized dye is not a significant loss mechanism and therefore does not limit the performance.[235, 236] Since the recombination with I_3^- is the main recombination mechanism,[237] a fast kinetics of its reduction at the CE is critical for reducing recombination losses. In this way, the availability of I_3^- that can recombine with an injected electron in the TiO_2 will be limited, resulting in a slower V_{oc} decay.

Figure 5.9 displays the V_{oc} decay and the electron lifetime calculated as follows:[236]

$$\tau_e = \frac{k_B T}{e}\left(\frac{dV_{oc}}{dt}\right)^{-1}$$

Where k_B is the Boltzmann constant, T is the absolute temperature and e is the elementary charge. Changing the CE structure affects considerably the V_{oc} decay and consequently the electron lifetime (**Figure 5.9**). Increased electron lifetime is typically attributed to reduced charge losses. The longest lifetime was achieved in the cell with the highest efficiency, confirming that the optimal condition of fiber density can increase the collection of electrons, therefore reducing the recombination. Indeed, the cell with the longest lifetime confirms that a high reduction kinetics of I_3^- at the CE interface limits the recombination of the photogenerated electrons with the triiodide ions, increasing the regeneration of dye and therefore the charge injection from the dye into the CB of TiO_2, decreasing the recombination phenomena. While increased Pt/Pd hollow nanofiber density is expected to provide a higher specific surface for the catalytic process, it is detrimental for the electron lifetime, as inferred from EIS measurements.

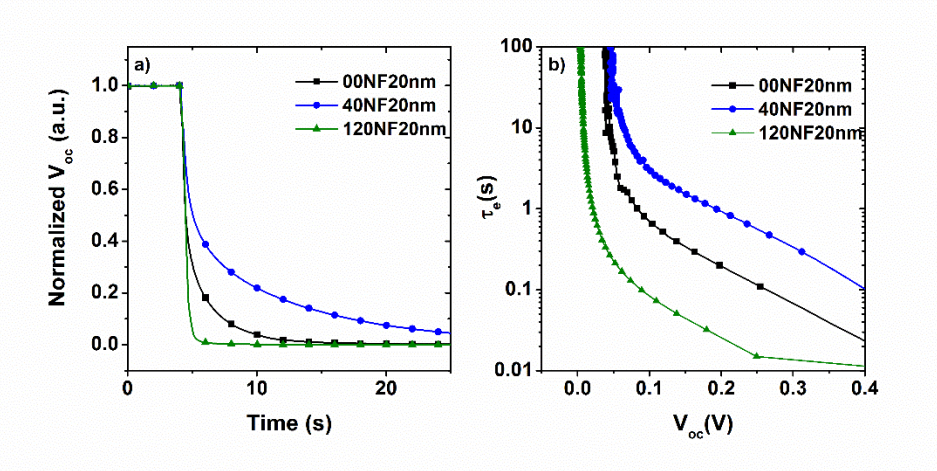

Figure 5.9. (a) V_{OC} decay and (b) corresponding electron lifetime of different CEs configurations.

5.1.3 Electrochemical performance of CEs

CV was carried out in a three-electrode system. **Figure 5.10** reports the cyclic voltammograms of the I^-/I_3^- redox couple on representative CE samples. All the curves exhibit an oxidation and reduction peak in the range -0.5V to 1.1V (vs saturated calomel electrode, SCE). Comparable shapes can be found in literature for system with Pt or Pt/Pd sputtered nanoparticles.[219, 238] The peaks are attributed to the reaction $3I_2+2e^-=2I_3^-$ at the CE interface. As visible in **Figure 5.10 a**, the cathodic and anodic peak current densities of the samples nanopatterned with the fibers are higher than those of the Pt/Pd electrode without fibers, indicating that the presence of hollow nanofibers increase the catalytic activity.

Another important parameter for comparing catalytic activities of different CEs is the peak to peak separation (E_{pp}), which is negatively correlated with the standard electrochemical rate constant of a redox

reaction.[228, 238] The E_{pp} value decreases in the order 40NF20nm (E_{pp}=578 mV) < 120NF20nm (E_{pp}=670 mV)< 00NF20nm (E_{pp}=723 mV), confirming the higher catalytic activity for the best sample (40NF20nm). The electrocatalytic stability of the different samples was tested by measuring 20 cycles of CV **(Figure 5.10 b, c and d)**. As can be observed in **Figure 5.10 b**, the reduction and oxidation peaks remain almost the same suggesting that the nanofiber Pt/Pd CE composite is stable. Moreover, the stability of the best sample with nanofiber is similar to the flat Pt/Pd CE (**Figure 5.10 c**) with a variation of only 11.5% in the cathodic current and a 6.5% in the anodic current. These variations are similar to the one obtain in recent works on Pt nanofiber network deposited on glass and flexible substrates.[229, 230]

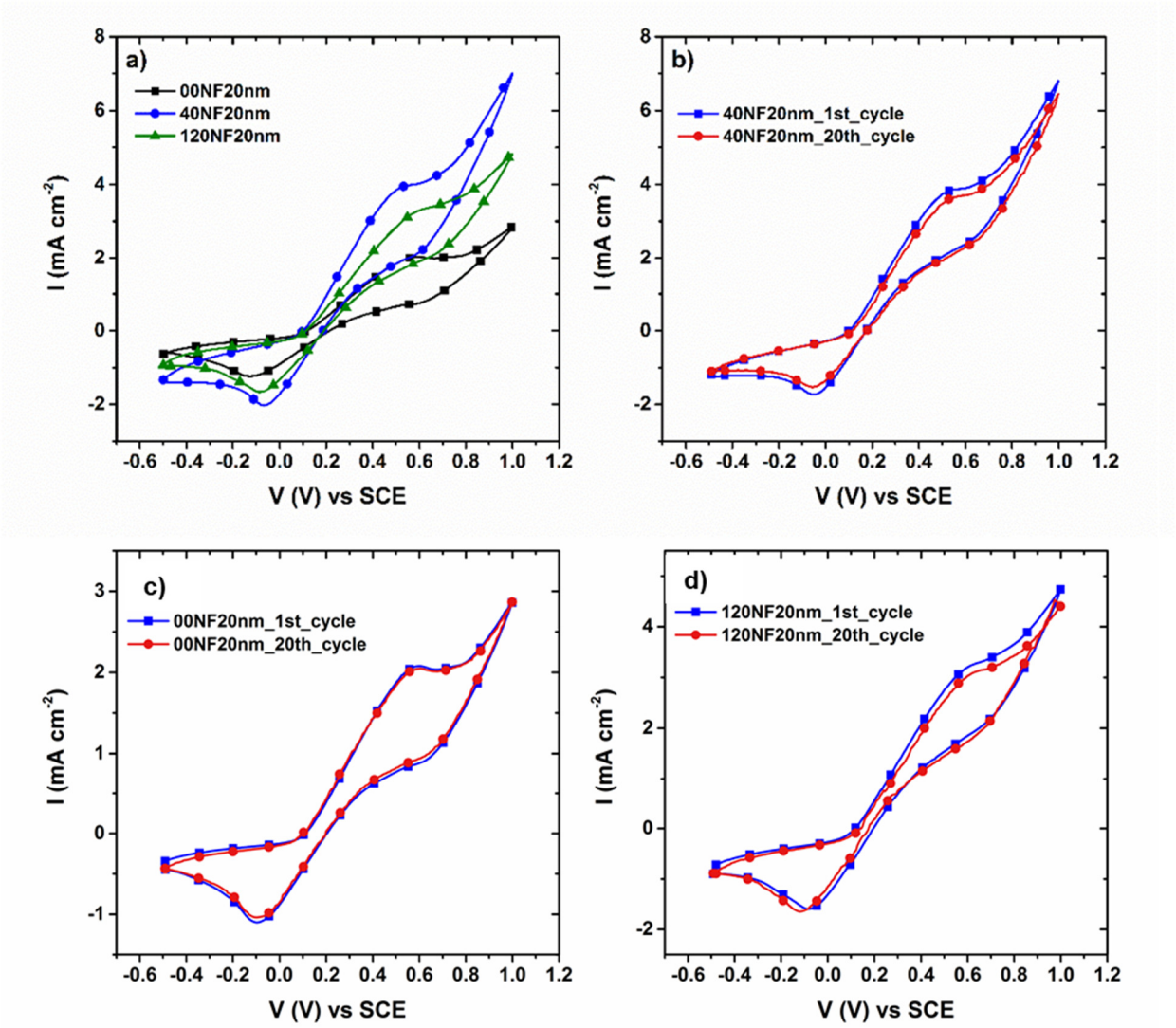

Figure 5.10. a) CV curves of representative Pt/Pd samples. b) CV stability curve of 40NF20nm showing the first and the 20th cycle of CV.

To gain insights on the catalytic mechanisms of the different CEs, we performed EIS using a symmetric cell configuration, to eliminate the contribution of the TiO_2 photoanode. In the symmetric configuration, two identical CEs separated by a 25 μm spacer were filled with the same electrolyte used for all the DSSCs. During the regenerative cycle of DSSCs at the CE, the catalytic reactions are confined to its surface, therefore the charge-transfer resistances in the electrolyte/catalyst is related to the reaction rate on the CEs, which is driven by its surface electro-catalytic activity. The resulting Nyquist plots are displayed in **Figure 5.11**, including the equivalent circuit used for fitting. The extrapolated parameters are reported in Table 5.4. All the plots display two semicircles: the high frequency arc (leftmost semicircle in **Figure 5.11**) is assigned to the charge transfer process at the electrode/electrolyte interface, while the low frequency arc (rightmost semicircle) is attributed to the Nernst diffusion impedance of the ions in the electrolyte.[239-241] From **Figure 5.11**, it is clearly visible that the best performing cell (40NF20nm) has the smallest low frequency arc compared to flat CE and to the one with increased density of the nanofiber (120NF20nm), indicating a faster charge transfer rate on this sample.

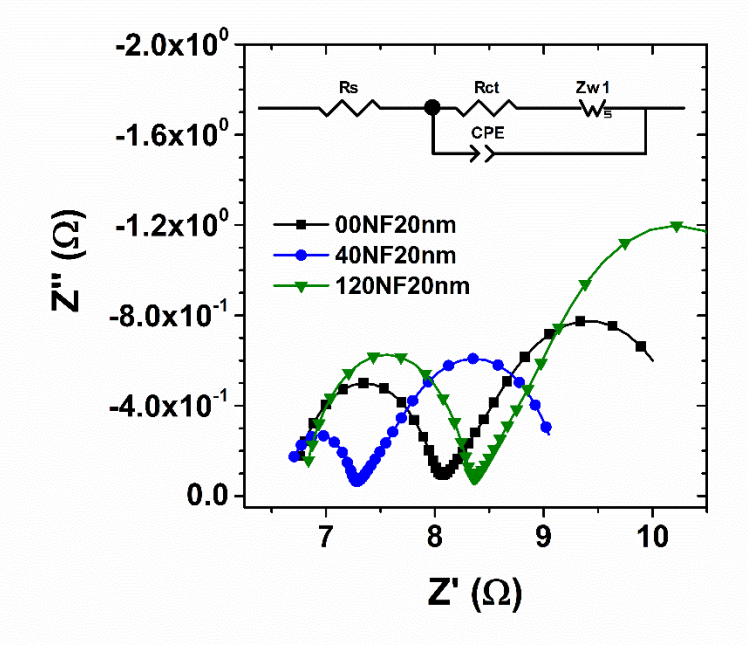

Figure 5.11. a) Nyquist plot from impedance measurements of symmetrical cells. The Randles circuit used for fitting the data is shown in the inset, it includes a series resistance R_s, a charge transfer resistance R_{ct}, a constant phase element CPE for taking into account the double layer capacitance and a Warburg impedance element W1. The solid lines are the fitted curves.

By fitting the data of the high frequency arc we obtain the value of the Nernst diffusion impedance element, Z_{W1}: for the three cells, it increases in the order 40NF20nm < 00NF20nm < 120NF20nm. This means that

the diffusion coefficient (D) of I_3^- ion for the different cells vary in the inverse order, in fact Z_{W1} can be calculated as:[222, 239]

$$Z_{W1} = \frac{kT}{n^2 {e_0}^2 cA\sqrt{i\omega D}} \tanh^{-1}\left(\sqrt{\frac{i\omega}{D}}\delta\right)$$

Where k is the Boltzmann constant, T is the absolute temperature, n is the number of electrons involved in the electrochemical reduction of I_3^- at the electrode (n=2), e_0 is the elementary charge, c is the concentration of I_3^-, A is the electrode area, ω is the angular frequency and δ is the thickness of the diffusion layer. This result indicates that D increases with increasing electrocatalytic activity of the CE, confirming that the 40NF20nm has the highest catalytic activity.

Additionally, by fitting the arc at higher frequency, the value of the charge transfer resistance (R_{ct}) can be extrapolated. The series resistance (R_s) is similar in all the samples because its value is mainly related to the resistance of the FTO substrate and the thickness of the Pt layer, that are kept the same for all the samples.[240] R_{ct} varies inversely with the I_3^- reduction activity of the different CEs (therefore, a lower value indicates a higher catalytic activity).[222, 240, 242] The values are reported in Table 3, showing that the best CE condition has a R_{ct} two times lower than the other samples. The chemical capacitance (C) increases with the insertion of nanofiber, and is maximized for the sample 40NF20 nm. This trend confirms the role of the hollow Pt/Pd nanofibers in increasing the active catalytic surface area of the CE at the optimal condition (40 s nanofibers deposition).

Table 5.4. Fitting parameters from EIS data of CEs

Sample	R_s (Ω)	R_{ct} (Ω cm^2)	Z_{w1} (Ω cm^2)	C (F/cm^2)	β
00NF20nm	6.68	0.33	0.64	$1.99 \cdot 10^{-05}$	0.82
40NF20nm	6.62	0.15	0.48	$2.75 \cdot 10^{-05}$	0.90
120NF20nm	6.79	0.38	0.82	$2.15 \cdot 10^{-05}$	0.87

The sample with the highest amount of nanofiber (120NF20 nm) has lower performance compared to the sample 40NF20 nm, due to the lower electrocatalytic activity confirmed by the higher R_{ct} and the lower diffusion coefficient of the I_3^- compared to the other samples.

A possible explanation of this behavior can be attributed to the increased density of nanofiber-nanofiber contact resistance due to sequential nanofiber stacking and formation of inter-fiber gaps during the process

of polymer removal.[229] Therefore, most electrons are confined in a region close to the FTO substrate, thus limiting electron availability for I_3^- reduction in this sample, which is similar to that on the flat CE.

From the R_{ct} value obtained from the symmetric cells, it is also possible to calculate the exchange current density (J_0), i.e. the current generated at equilibrium (absence of net electrolysis and at zero overpotential) that balances the cathodic and anodic currents, from the following equation:[239, 242]

$$J_0 = \frac{RT}{nFR_{ct}}$$

Where R is the molar gas constant, T the absolute temperature, F the Faraday constant and n the number of electrons involved in the electrochemical reduction of I_3^- at the electrode (n=2). The exchange current density calculated for the 40NF20 nm CE is 81.4 mA/cm^2 while for the standard flat CE is around 38 mA/cm^2. Being J_0 proportional to the I_3^- concentration this further confirms that the electrochemical I_3^- reduction reaction on the CE patterned with nanofiber is enhanced.[238]

5.2 Conclusion and Perspectives

Nanostructured CEs were fabricated by coating 1D sacrificial polymer templates with a Pt/Pd thin film, producing hollow nanofibers. The morphology and amount of catalysis were optimized for their application in DSSCs. 15% PCE improvement was achieved in hollow nanofibers CE obtained from 40 s electrospinning time and 80 nm thick Pt/Pd film. Additionally, we showed that the amount of sputtered Pt/Pd can be decreased to 20 nm, without a significant reduction of the overall efficiency. An improved functionality is the result of the enhanced electron lifetime in the assembled DSSCs, attributed to the increased specific surface area of the hollow nanofiber architecture and to the improved electro-catalytic performance, as shown by the two-fold decrease in the R_{ct}.

A higher amount of hollow nanofibers was found to be detrimental for DSSC PCE, due to the decrease in the electro-catalytic activity, possibly caused by increased nanofiber junction resistances. At optimal conditions, the interconnected network of Pt/Pd hollow nanofibers can enhance charge transfer, leading to high efficiency DSSCs. This is a viable and cost-effective approach to enhance the catalytic surface area in CEs for photoelectrochemical systems with the purpose of boosting the performances through optimization of the electrochemical processes occurring in the operating devices. Additionally, the use of Pt/Pd alloy can decrease the cost compared to a 100% Pt CE. Moreover, the proposed procedure to obtain 1D hollow nanostructures is also a cost-effective solution. The electrospinning technique stands out among other commonly used methods to obtain this kind of nanostructures such as hydrothermal synthesis. Chemical synthesis usually relies on time-consuming and complicated procedures and a large cost for chemicals, disposal of liquid waste, and additional steps for the integration of these nanostructures in the CE.

Such findings represent a promising direction to minimize the use of precious metals and to tailor the CE structure. In addition, the application of this approach for obtaining CEs with improved functional properties can be broadened to different electrochemical systems (i.e. fuel cells and catalytic chemical reactors).

5.3 Materials and methods

5.3.1 CE fabrication

Polymer nanofibers were electrospun onto FTO glasses (sheet resistance 8 Ω/sq) from a 23 wt. % solution of polyamide-6 (PA6, Sigma Aldrich) in formic acid (FA, Sigma Aldrich) kept under stirring for 4 hours. The nanofibers were obtained in a Spraybase, Profector Life Sciences electrospinning unit at 20 kV using a distance of 15 cm and a flow rate of 0.06 ml/h with a 26G needle. CEs were fabricated using two nanofiber deposition times (40 or 120 s). Subsequently, the nanofibers were dried at 70 °C for 15 min followed by sputter coating at the desired thickness using a Pt/Pd alloy (80/20 wt.%) target in a Cressington 208HR high resolution sputter coater, equipped with a thickness controller. The process was conducted under a 0.01 mbar Argon atmosphere, at 80 mA using a rotating disk at a determined angle; the desired thickness was achieved by multilayer coating, depositing 20 nm thick layer each time (up to 4 times). Subsequently, the polymer was removed by heating for 15 min at 500 °C using a 10 °C /min heating ramp.

5.3.1 Device Fabrication

DSSCs were fabricated according to standard procedures. Double layer photoanodes were prepared by tape casting two commercial TiO_2 pastes. The first layer consists of anatase nanoparticles with average size of 20 nm (18 NR-T, Dyesol) and it was first tape casted onto transparent FTO glass substrates (sheet resistance 8 Ω/sq). The thickness of the tape during the casting process was 50 μm. The film was dried for 15 min at ambient temperature and then for 6 min at 120 °C. The procedure was subsequently repeated using a commercial scattering layer consisting of a blend of active anatase TiO_2 particles (~20 nm) and larger anatase TiO_2 scattering particles (diameters up to 450 nm, 18NR-AO, Dyesol). After drying, the bi-layered structure was sintered in ambient atmosphere according to the following steps: 200 °C for 15 min, 400 °C for 15 min and 500 °C for 30 min. Film thickness was measured using a Dektak profilometer and found to be ~18 μm. Subsequently, the photoanodes were sensitized in a 0.5 mM ethanol (Sigma Aldrich) solution of Ru-based complex molecular N719 dye (Dyesol) for 24 hours, and then washed with ethanol to remove any unbound dye molecules. DSSCs were fabricated by using a 25 μm thick Surlyn film (Solaronix) between the photoanode and the Pt/Pd CEs, and they were filled using a triiodide/iodide I_3^-/I^- redox couple electrolyte (Solaronix HI-30).

Table 5.5 shows an example of the labeling system used in this work. The first two digits of the labels are the electrospinning deposition time in seconds, i.e. 40 or 120 s, whereas the second set of digits refers to the coating thickness of the Pt/Pd alloy (20, 40 and 80 nm): a sample labeled 40NF20nm corresponds to a deposition of nanofibers for 40 s and coated with 20 nm of Pt. The samples labeled as 00NF20nm, 00NF40nm and 00NF80nm correspond to the bare FTO (flat CEs) sputtered at different thickness conditions.

Table 5.5 Example of the labelling system for the CE

Pt Thickness (nm)	Nanofiber (NF) Deposition Time (s)	Label
	0	00NF20nm
20	40	40NF20nm
	120	120NF20nm

5.3.1 Characterization of Materials and Devices

The morphology of the nanofibers was characterized by field emission scanning electron microscopy (FE-SEM) using a JEOL JSM7401F FE-SEM equipped with an energy-dispersive X-ray spectrometer (EDS). The physical properties of the nanostructured CEs were obtained by analyzing different SEM micrographs using ImageJ software with DiameterJ plugin, which automatically segments the images converting the fibers into white pixels and the background (substrate) into black pixels. This plugin provides the amount of pixels in the background and this value was used to obtain the fiber area coverage ratio. Nanofibers deposited onto the FTO glasses were sonicated for 10 minutes in ethanol followed by drop casting onto a carbon coated Cu grid and transmission electron microscopy (TEM) images were acquired using a JEOL 2100F TEM. AFM was performed in a Veeco Enviroscope AFM. Pt/Pd hollow nanofiber crystallinity was investigated using grazing incidence X-ray diffraction (GIXRD) in a Bruker D8 Advance X-ray diffractometer equipped with Cu K_{α} radiation. Diffuse reflectance measurements were acquired in a Perkin Elmer, Lambda 750 UV-Vis-NIR spectrophotometer using an integrating sphere setup calibrated with a Spectralon® standard.

The current–voltage characteristics of the fabricated cells were measured by using an Agilent Keysight 2901A under simulated sunlight using an ABET2000 solar simulator at AM 1.5G (100 $mW \cdot cm^{-2}$) calibrated with a silicon reference cell and mechanical filters. External Quantum Efficiency (EQE) spectra were

acquired in dark using an EQE 200 Oriel integrated system. The measurement step was 10 nm and the photocurrent was recorded using a lock-in amplifier.

Cyclic Voltammetry was carried out using a SOLARTRON 1255/1287 in a three-electrode electrochemical system. The cyclic voltammetry (CV) curves were recorded at 50mV s^{-1} using a Pt plate as a CE, an FTO substrate supported Pt/Pd alloy CE with and without nanofiber as a working electrode, and a saturated calomel electrode (SCE) electrode as a reference electrode in a supporting electrolyte (Solaronix HI-30, diluted in acetonitrile).The electrolyte used was Solaronix HI-30. The CEs were investigated from 0.6 V to 1.2 V at a scan rate of 50 mV/s.

EIS was carried out in the dark using a SOLARTRON 1260 A Impedance/Gain-Phase Analyzers, with an AC signal of 10 mV in amplitude, in the frequency range between 100 mHz and 300 kHz. The applied bias during measurements of the dummy-cells in the dark was fixed at 0 V while for the complete DSSCs the bias was between 0 V and 100 mV above the open circuit voltage of the solar cell under illumination. All the samples were measured inside a Faraday cage.

6 Tuning the electronic band structure of single metal chalcogenide Quantum Dots

This chapter is based on the paper "*Direct measurement of electronic band structure in single quantum dots of metal chalcogenide composites*" published on *Small 14 (51), 1801668 (2018)*.

In the previous chapters we have investigated the DSSCs system, and in particular how to improve the charge transfer in the photoanode and cathode by either increasing the catalytic activity of the CE or improving the transport and collection properties. In this chapter, we move the focus on the Quantum Dots system. Instead of analyzing the full functional device, such as a QDSC, a more fundamental approach is followed. In particular the band structure of single QDs of metal chalcogenide is investigated exploiting the Kelvin Probe Force Microscopy (KPFM) technique.

Nanostructured materials have been among the most intensely studied systems in the past two decades due to their size-dependent properties, which are often radically different from those of bulk materials.[83, 243, 244] When the radius of a nanocrystal shrinks close to or below its effective exciton Bohr radius properties change dramatically, and its electronic structure, optical and magnetic attributes can be tuned by varying size and composition. [83, 245, 246] As seen in Chapter 2, among many different classes of nanostructured materials, quantum dots (QDs) are highly promising. QDs are semiconducting nanocrystals with typical size ranging from 1 to 20 nm, which exhibit quantum confinement of the electronic states, due to the size reduction.[85] In particular, electronic quantization yields discrete energy levels, also shifting the position of the ground state and the first excited state. These features are very useful in several composite systems, in which QDs are physically grafted on different scaffolds.[111] Modulating the overall electronic band structure of composite systems enables the exploitation of several physical/chemical processes, which are critical in most advanced applications.[247] Charge injection and electron dynamics, exploitation of hot electrons and multiple exciton generation for single absorbed photons are some of the most important examples. [247-249]

In many optoelectronic applications, such as light-emitting devices (LEDs)[250], photo-catalysis, [251, 252]and solar cells,[253] QDs are grafted on metal oxide semiconductors (MOS) (mainly in the form of mesoporous or thin films, e.g. TiO_2, ZnO, SnO_2 among others). In the case of solar cells, an exciton forms in photoexcited QDs, which then should be rapidly split into an electron-hole pair at the interface between the MOS and QDs to avoid charge recombination.[249] Usually, n-type MOS are used to transport electrons, while holes are regenerated through a specific electrolyte or hole transporting materials. If the process of exciton dissociation and charge injection at the QD/MOS interface is slow, the photo-generated electrons will recombine with holes, reducing the overall efficiency of the device.[254] This is why the interface between

QDs and the MOS is of critical importance and several factors should be considered to obtain efficient charge transfer across this interface (see Chapter 2.2.1 for Details).

The ability to tune QD size and band structure allows to selectively exploit radiation in specific spectral ranges. Some materials, such as Pb chalcogenides, can absorb the near infra-red (NIR) portion of the solar spectrum,[255, 256] which is typically dissipated as heat in commercial silicon-based solar cells. Bulk PbS has a conduction band, which falls below the CB of most used MOS (TiO_2 and ZnO), preventing charge injection from photoexcited bulk PbS to TiO_2 or ZnO. The upward shift of the first excited state in PbS QDs, instead, makes charge injection feasible for very small QDs. However it is necessary to find a compromise between broadening light absorption (by using larger, lower energy gap QDs) and charge injection (by using smaller and higher energy gap QDs).[78, 257] A practical example can be found in QDSCs, which use PbS QDs as sensitizer. Despite presenting extended light absorption in the NIR region, PbS QDs present unfavorable electronic band alignment, which inhibits charge injection from the photoexcited QDs to the MOS (see Scheme in **Figure 6.1**).[78]

A possible approach to overcome this limitation is to use a composite blend (PbS/CdS, for instance). In pure PbS, in fact, a limited band shift exists, when dimensions of QDs shrink, which is ineffective to promote massive charge injection from QD to TiO_2 (**Figure 6.1**), while the addition of CdS makes charge injection effective. It has been recently demonstrated that Pb-based QDs can efficiently transfer charges to the oxide scaffold by producing hot electrons,[258] even though the proposed mechanism is still under debate.[259] The use of a composite system, as mentioned above, e.g. core-shell PbS/CdS QDs, can instead improve the PCE by preserving the broad absorption and favorable electronic band alignment with the MOS. The ability to accurately control the physical/chemical properties of the QDs is essential for any application in which charge injection between the QDs and the MOS plays a major role.

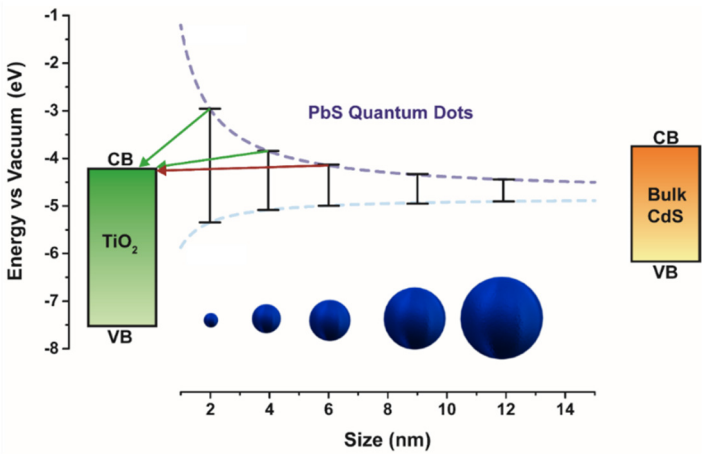

Figure 6.1. (a) Scheme of electronic band structure (with respect to vacuum) of different systems, including bulk TiO_2, bulk CdS and quantum confined PbS. The green arrows from high-energy electronic states in PbS QDs to TiO_2 CB indicate

possible charge injection from QD to oxide, while the red arrow highlights forbidden electron injection, due to unfavorable electronic band alignment. The energy levels for PbS QDs are calculated according to Ref. 81.

Traditional spectroscopic techniques used for surface characterization, when used to study nanometer sized objects are intrinsically limited in spatial resolution, due, for instance, to the finite spot size which cannot resolve individual nanostructures, or to the diffraction limit of light. In recent years, scanning probe microscopy (SPM)-based techniques have been widely used to investigate the electronic properties of individual nanostructures.[260, 261] The most common technique is scanning tunnelling microscopy (STM), which allows for example to investigate individual bulk defects and dopant atoms in semiconductors.[261, 262] However, due to the nature of STM measurements, its application is limited to conductors and highly conductive semiconductors. In addition, the presence of a tunnelling current may cause tip-induced band bending. KPFM can be applied to overcome these disadvantages. [263-265] KPFM is a surface-potential detection method, which determines the contact potential difference (CPD) while scanning with an AFM tip, by compensating the electrostatic forces between tip and sample. KPFM has been successfully used to obtain contact potential (CP) images on a large variety of samples, such as metals, semiconductor surfaces and conducting polymers.[263] In addition, KPFM is effective to measure the contact potential difference with nanometer and sub-millivolt resolution.[266, 267]

Recently KPFM has also been used to characterize heterojunctions formed by QDs on planar semiconductors. However, these studies are limited to self-organized QDs, grown for example by droplet heteroepitaxy (DHE), such as InAs on GaAs, or Ge on Si.[268, 269] Recent studies focused on KPFM measurements of a thin homogeneous film composed of closely packed colloidal QDs, where information on individual nanostructures is not accessible.[270, 271] Up to now no investigation on single ligand-free QDs of metal chalcogenide composites has been done.

In this chapter, AFM and KPFM are applied to investigate single QDs composed of PbS, CdS and PbS/CdS grown by successive ion layer absorption and reaction (SILAR) on highly ordered pyrolytic graphite (HOPG). This is a model system which allows to investigate the properties of individual QDs, minimizing any other collective effect (e.g. broadening in excitonic absorption/emission peaks due to QD size distribution) and/or QD-QD interaction. I report the variation of the CPD of a single SILAR-QD via KPFM, investigating the evolution of their electronic band structure as a function of QD size and composition.

6.1 Results and discussion

6.1.1 Morphological Characterization

Figure 6.2 a-c displays TEM images of the three types of QDs. The QDs present an average size of (4.6±0.9) nm, (4.1±0.6), (5.4±1.2) nm for CdS, PbS and PbS/CdS, respectively, as measured from TEM micrographs. **Table 6.1** compares results on the size distribution obtained from TEM and AFM (**Figure 6.3**), which are in very good agreement.

Table 6.1. Comparison between size distributions obtained from TEM and AFM for the three systems: CdS, PbS, and PbS/CdS.

	QD size from TEM (nm)	***QD size from AFM (nm)***
CdS	4.6±0.9	5.5±1.6
PbS	4.1±0.6	4.5±1.4
PbS/CdS	5.4±1.2	4.7±1.6

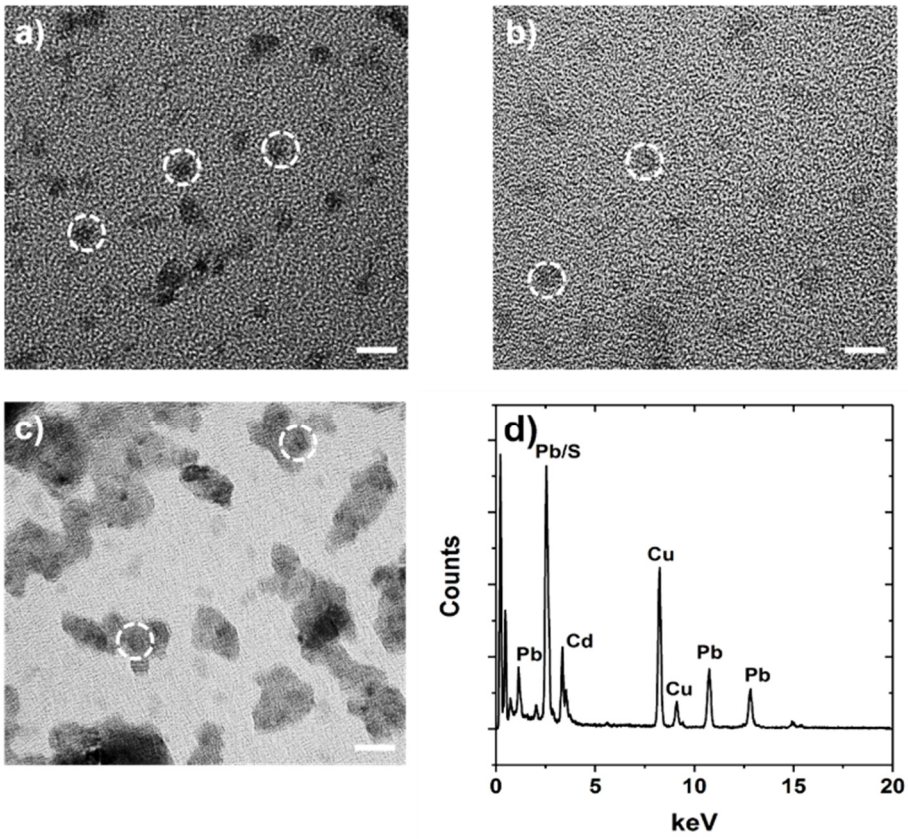

Figure 6.2. High Resolution TEM images of the different QDs a) PbS b) CdS c) PbS/CdS. Scale bare is 10 nm. d) EDX analysis of the PbS/CdS 2/2 composite system, highlighting the presence of Pb, Cd, and S in the sample, as expected.

Energy-dispersive X-ray spectroscopy (EDX) was carried out to verify the presence of the expected elements in the different nanocrystals. The corresponding EDX spectrum of an individual PbS/CdS QD confirms the coexistence of both Pb and Cd (**Figure 6.2d**).

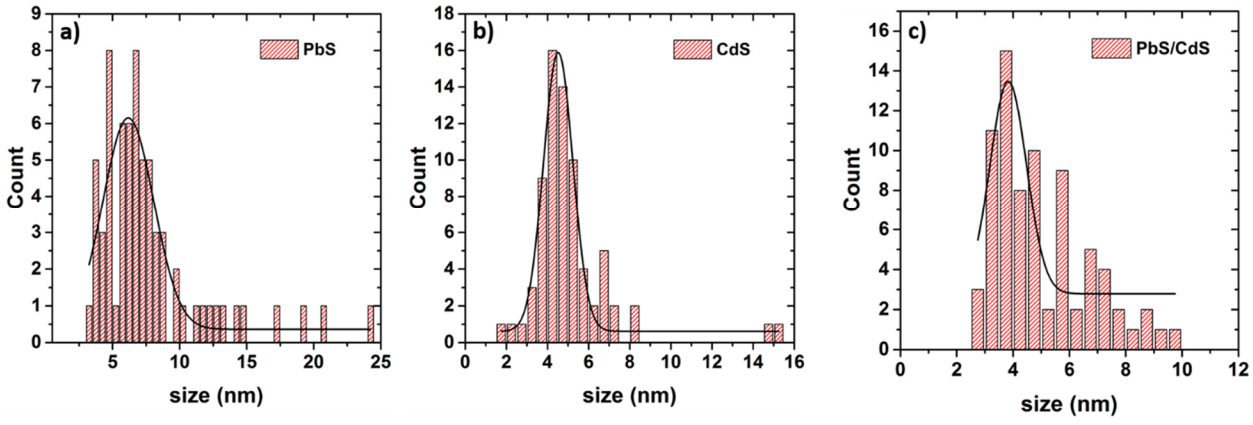

Figure 6.3. Size distribution of the PbS (a), CdS (b) and PbS/CdS (c) QDs obtained with AFM.

6.1.2 Kelvin Probe Force Microscopy

We then proceed with the characterization of the different samples with the KPFM technique. The schematic setup of the KPFM measurement is shown in **Figure 6.4**. In KPFM, the V_{CPD} is obtained through a compensation method, in which a DC-voltage (V_{DC}) is applied to compensate the contact potential difference (V_{CPD}) between the AFM tip and the sample, using the electrostatic force as control parameter.

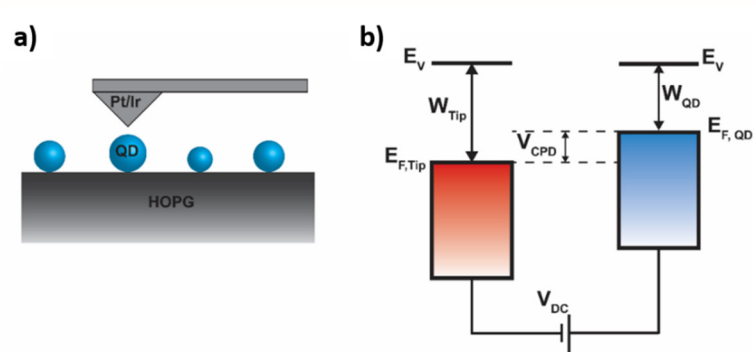

Figure 6.4. (a) Scheme of the experimental set-up for the KPFM measurement on SILAR QDs directly grown on HOPG. (b) Operating principle of KPFM, including the main parameters involved in the measurement.

To measure the electrostatic force independently from the other forces, an AC bias at frequency ω is applied between the tip and the sample, in addition to the tip-sample V_{DC} voltage. The resulting oscillating electrostatic force induces an oscillation of the cantilever at the frequency ω_{AC}.

Considering the tip-sample as a capacitator, it is possible to express the electrostatic force as:[264]

$$F_{el} = -\frac{1}{2}\frac{dC}{dz}[V_{DC} - V_{CPD} + V_{AC}\sin(\omega_{AC}t)]^2$$

Where δC/δz is the capacitance gradient of the tip-sample and the V_{CPD} is the difference in work function (W) between sample and tip:

$$V_{CPD} = \frac{\Delta W}{e} = \frac{W_{sample} - W_{tip}}{e}$$

Where *e* is the elementary charge.

The first harmonic component of the electrostatic force, F_ω, is proportional to V_{CPD}: [264]

$$F_\omega = -\frac{dC}{dz}(V_{DC} - V_{CPD})V_{AC}\sin(\omega_{AC}t)$$

Therefore, F_ω can be cancelled out by a voltage V_{DC} applied by a Kelvin controller through a feedback loop. Hence, the measure of the V_{DC} gives directly the V_{CPD} (the sign of the measured V_{CPD} will be positive (negative) if the nullifying voltage is applied to the sample (tip), respectively) (**Figure 6.4b)**.

Figure 6.5 shows the topography and relative CPD images of the three systems: CdS QDs, PbS QDs and PbS/CdS QDs deposited on HOPG (the substrate was grounded with the tip at 0 V). The height profile of representative QDs (**Figure 6.5** g, h, i) is in good agreement with the size distribution measured by TEM and AFM, showing variations between 3 and 11 nm. In the CPD images (**Figure 6.5** d, e, f) the HOPG surface is electrically homogeneous, with small oscillation of 10 mV around 0 V over the scanned area. The QDs are represented as positive peaks compared to the HOPG substrate (as stated in the experimental section, the real CPD value is negative).

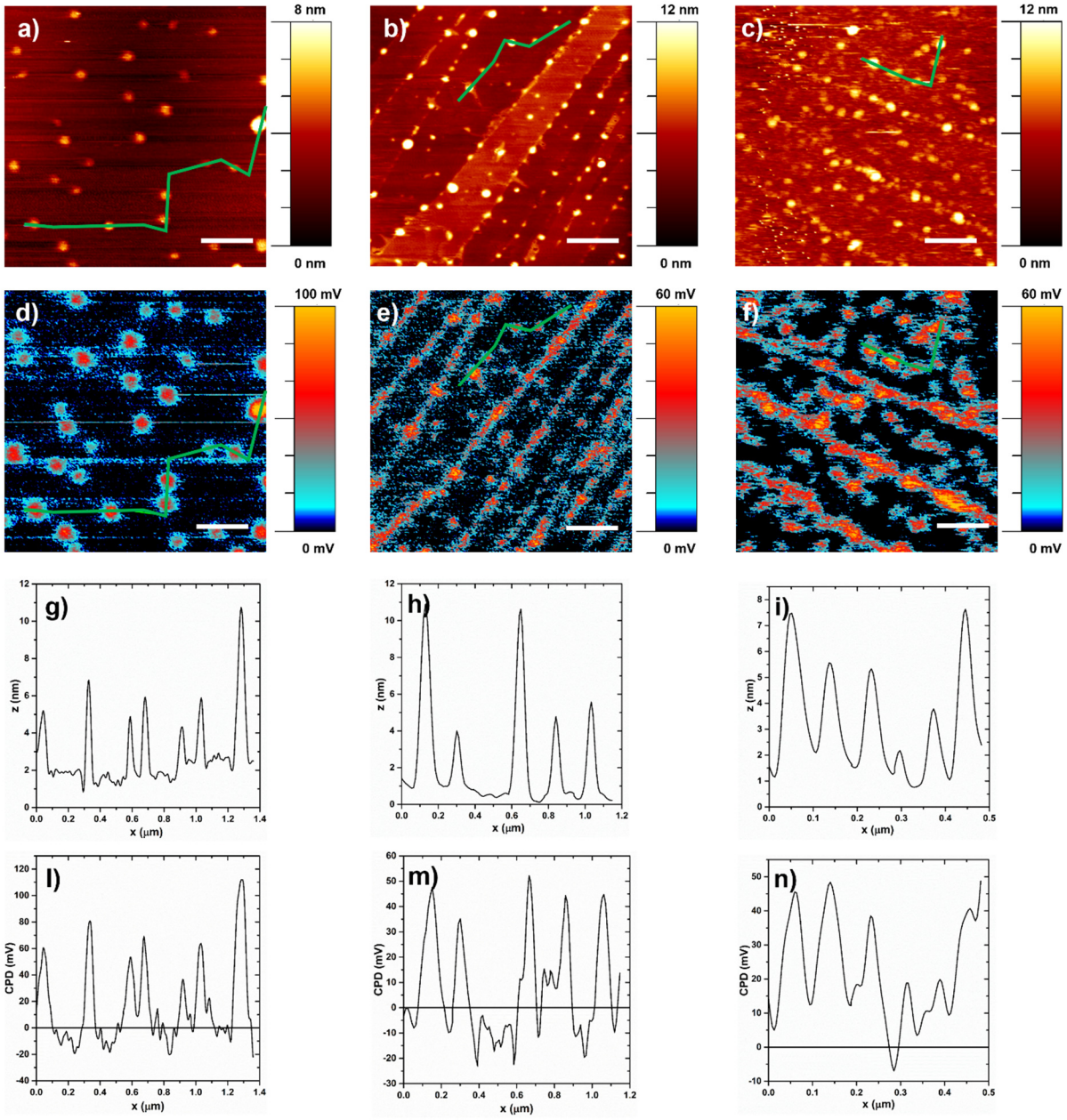

Figure 6.5. Simultaneous AFM and KPFM measurement of CDs, PbS and PbS/CdS QDs. a-c) Morphology of CdS, PbS and PbS/CDs QDs on an area of 1 µm×1 µm, respectively. d-f) Simultaneous CPD image of the QDs. Scale bar is 200 nm. g-i) Cross-section profile of the line in a-c. l-n) Cross-section profile of the KPFM values of the same line in d-f.

A systematic study of the CPD as a function of the QD size was carried out for the three kinds of QDs (**Figure 6.6** a). Due to tip convolution effects, it was not possible to accurately measure the lateral size. We therefore used the so-called "height mode" to determine the size of the nanocrystals. This consists in assuming a hemispherical shape for the QDs and considering the maximum height recorded by the AFM tip as the radius of the sphere. Negative values of CPD denote that the work function of QDs is higher than

that of the HOPG substrate. Comparing the height profile and CPD, the larger the QDs, the more negative the CPD. Similar observations apply to all the samples. In all cases, the CPD of the QDs varies according to their size. Independently from the QD type, the CPD becomes monotonically more negative (with almost linear trend) with increasing QD size.

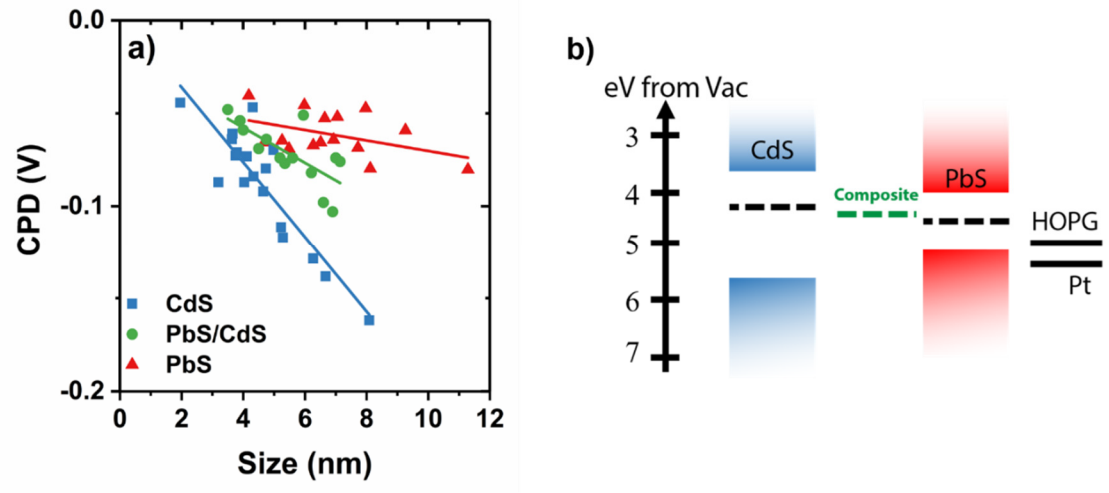

Figure 6.6. a) CPD as a function of the QDs size highlighting that in general the CPD is more negative when the QD size is larger. b) Schematic representation of the band alignment for the three systems considered.

Figure 6.6a shows different slopes for different QD type, indicating that the variation of the CPD is mainly dependent, as expected, on the electronic proprieties of the different materials, rather than on geometrical features. The small fluctuation of the CPD for QDs with the same size and composition can be attributed to variations in particle shape and orientation as well as to the presence of steps on the substrate.[270]

Recently, it has been shown that the Fermi level E_F of PbS QDs changes with size: when the energy band gap (E_G) of the QDs increases, E_F shifts towards the VB of the QDs, while in small bang gap QDs the E_F is closer to the CB.[272] From the CPD trend, it is possible to observe a similar behavior in our samples. In fact, the CPD is strictly dependent on the position of the Fermi level.

In addition, CdS QDs exhibit a more pronounced change in the CPD values (larger slope of the curve), while in PbS QDs the change is smaller. The core/shell QDs present an intermediate behavior and fall between the two core structures **(Table 6.2)**.

Table 6.2. Slope of CPD variation as a function of QD size obtained from linear interpolation of the experimental data in Figure 6.6 a.

	dCPD/d(size) *(mV/nm)*
CdS	-0.020±0.002
PbS	-0.003±0.001
PbS/CdS	-0.0095±0.0025

A possible explanation of this behavior can be the differences in the effective masses of holes and electrons for PbS and CdS QDs.

In general we expect that if the hole and electron effective masses have similar values, the relative shift of the VB and CB will be similar (in opposite direction) and so the Fermi level will not move so much, while in case of different values the shift of either the VB or the CB will be more pronounced and so the Fermi level will be more shifted as well. In our case, the electron and hole effective masses of PbS are almost identical,[273] while the effective mass of holes for CdS is 3.5 times higher compared to $m^*_{e,CdS}$.[274] The differences in the effective masses can justify the low shift of the level of E_F (and therefore of the work function) of the PbS QDs, compared to CdS. Consistently, the core/shell structure, PbS/CdS, exhibits an intermediate behavior, being positioned between the two core structures (**Figure 6.6** a and b).

We expect that the electrons will flow from CdS to PbS when a PbS/CdS junction is formed, until a new equilibrium is reached, in which the Fermi level of the two materials is equal. The new E_F should be located between the E_F of the single materials, PbS and CdS, before contact.

6.1.3 Electronic bands

To obtain an indirect validation of the behavior observed in the CPD for the different QDs, we performed a Mott-Schottky (MS) analysis using a TiO_2/QDs system. We choose TiO_2 as substrate because this is the most commonly applied metal oxide in photoelectrochemical systems, including solar cells and photocatalysts. In general, through the MS analysis, it is possible to determine the flatband potential (V_{fb}) of an electrode through a capacitance measurement of the electrode/electrolyte interface.[275]

The values of V_{fb} corresponding to the intercept of the MS plots are reported in **Figure 6.7** and, after pH correction, they correspond to: + 0.125 V and -0.245 V (vs reversible hydrogen electrode (RHE)) respectively for PbS and CdS. Regarding the composite system PbS/CdS, an intermediate value of – 0.145 V (vs RHE) was estimated. This result supports the previous interpretation that Fermi Level alignment occurs between PbS and CdS. Another qualitative estimation of the positioning of the Fermi level and its shift in the composite system, can be obtained by the Open Circuit Potential (OCP). In fact, when a semiconductor is brought in contact with a redox couple in solution, after reaching electrostatic equilibrium, the Fermi levels of the semiconductor and solution will be the same.[276] If the measure of the OCP is done in dark, its values will be equivalent to the Fermi level at equilibrium. In our case, we obtained the following values: -0.54 V, -0.22 V (vs Ag/AgCl) respectively for TiO_2/PbS and TiO_2/CdS. Again, the composite system TiO_2/PbS/CdS presents an intermediate value of -0.47 V (vs Ag/AgCl), further confirming the shift of the Fermi Level recorded in the CPD data and MS plots.

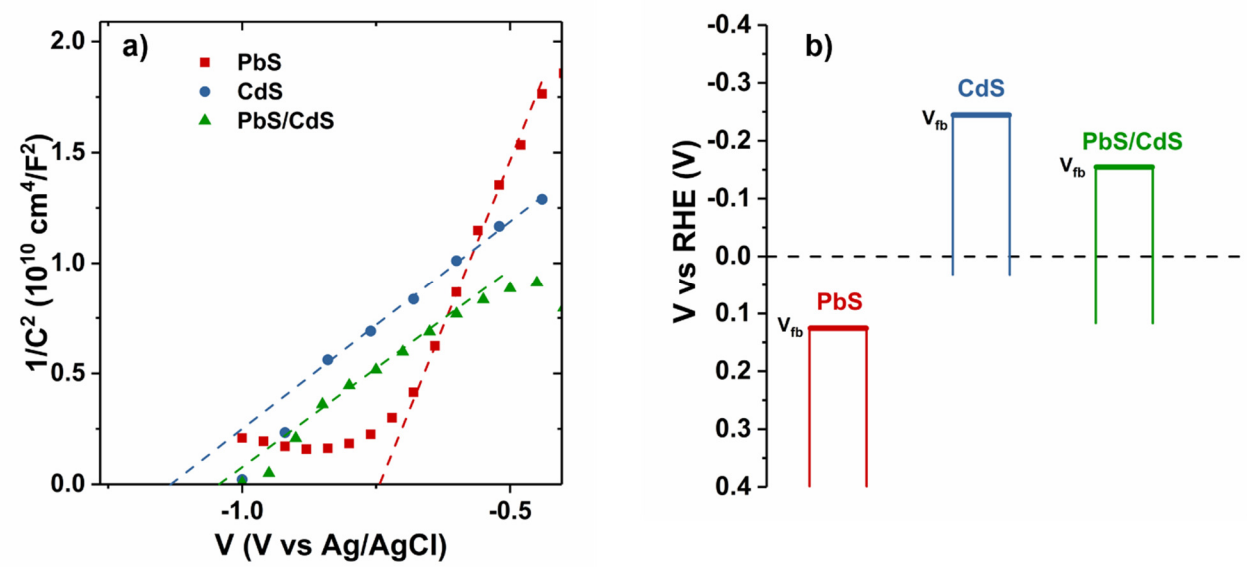

Figure 6.7. Relative Flat Band Potential (V_{fb}) level of PbS, CdS and Pbs/CdS estimated with Mott-Schottky analysis carried out in dark.

From the relative values of the Fermi level, it is also possible to determine the relative position of the VB and CB using the following equation:

$$E_V(QD) = E_F(QD) + kT\ln(\frac{p}{n_v})$$

Where p is the effective hole doping density of the QD, and n_v is the effective density of the valence band state.

The relative conduction band position (E_C), can be estimated by adding the band gap energy to the position of the VB. We can apply this procedure to estimate the relative band positions for different QDs, using the value of CPD as the relative Fermi level of the QDs with respect to the work function of HOPG. To estimate the position of the VB we need to estimate n_v and p for the different QDs. We can estimate the value of n_v as: [277]

$$n_v = \frac{a}{V_{eff}}$$

Where *a* takes in account the degeneration of the band gap in the semiconductor and V_{eff} is the effective volume of the QDs. In our case, the band gap for PbS is 8-fold degenerate (so a=8)[277], while for CdS, the band gap is two-fold degenerate, since CdS is a direct band gap semiconductor. [278] V_{eff} is estimated from the QD volume (V_{QD}):

$$V_{eff} = \frac{V_{QD}}{f}$$

Where f is the fill factor. In our case, we can consider f=0.52 (calculated as the ratio of the volume of a half sphere inscribed in a half cube). The variation of n_v with the QD size is reported in **Figure 6.8 a**. For the core/shell structure an estimate of n_v is currently under investigation, due to the complexity of the composite system. We expect an intermediate value between the PbS and the CdS system, yet a quantitative evaluation is not possible at this time. We therefore limit the comparative analysis to the PbS and CdS systems.

The results of the calculations, based on the experimental data and on the estimate of n_v and p are shown in **Figure 6.8 b** and **c**. Following Ref. 262 we estimated the effective doping level for PbS and CdS equal to $p = 1 \times 10^{17}$ cm^{-3}. In dotted lines we also provide the calculation of CB and VB position for two other values of doping: $p = 1 \times 10^{16}$ cm^{-3} and $p = 1 \times 10^{18}$ cm^{-3}. We observe that the relative values of E_C and E_V follow a similar trend as in the literature, with the Fermi level close to the VB.

The position of CB in CdS QDs is much higher compared to PbS, as expected, enabling an efficient charge injection in MOS like TiO_2 and ZnO (for the sake of clarity, in dotted red line it is reported the literature value of the relative CB position of TiO_2 with respect to HOPG). However, we should be cautious when comparing the position of electronic bands in semiconductors and data in the literature. Due to the interference of the atmospheric conditions during the measurements, we can have adsorbed species, such as water molecules, at the different surfaces, which can induce a shift in the CPD and so influence the absolute values of the measured potentials.[279] For this reason, while the measurement of the relative position of CB and VB for PbS and CdS QDs is reasonably accurate, their absolute position cannot be determined with the same precision. A similar behavior was previously observed and the real values for the absolute

position of the electronic states/bands can be recovered by shifting the data by a constant value, depending on the magnitude of the reference work function.[277]

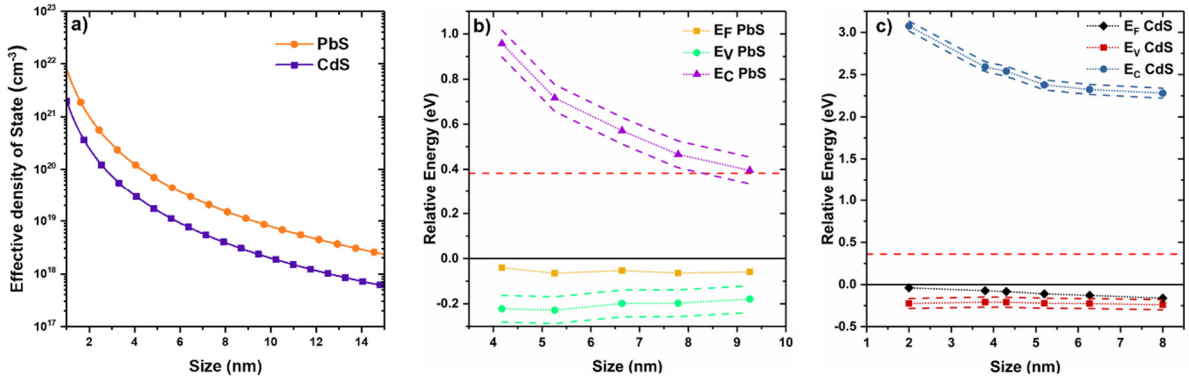

Figure 6.8. Effective density of state calculated as described in the manuscript for PbS and CdS QDs (a). VB, CB and Fermi level positions relative to HOPG substrate for PbS QDs (b) and CdS QDs (c) of different size. The red dashed line represents the conduction band of TiO_2 adjusted for the reference work function of the HOPG (from Ref [280] and Ref [281]). To obtain the CB position, a band gap calculated from Ref 19 for PbS and Ref [282] for CdS was added to the calculated VB.

In the present case, the threshold size for charge injection from PbS QDs to TiO_2 is around 8 nm, which is not in agreement with our previous estimate (5.2 nm), based on measurements of photoluminescence lifetime.[82] The main reason for this discrepancy is that here we take the absolute position of the CB for TiO_2 and the work function of HOPG from the literature (respectively 4.25 eV [280] and 4.6 eV [281]), while it is subject to significant variations, depending on the environmental conditions. For example, it has been shown that the surface potential of HOPG is affected by the relative humidity (RH) and it can shift up to 120 mV (at RH=80%).[279]

6.2 Conclusion and perspectives

In summary, KPFM was used to investigate for the first time the local electrical properties of individual metal chalcogenide QDs, optically active in the NIR spectral region, with different size and composition, grown via a SILAR approach. The variation of the surface potential of an individual QD as a function of size and composition was measured. As expected, KPFM was sensitive to the composition of the different materials and to their electronic band structure.

The Fermi level is found to shift towards more negative values by increasing QD size. The shift is more pronounced in CdS than in PbS, while the composite PbS/CdS exhibits an intermediate behavior. This trend is most likely due to the different relative weight of holes and electrons in the different materials, being

almost the same in PbS, and significantly different in CdS. By assuming standard values for the hole doping density and the effective density of valence band states, we calculated the relative positions of the VB and CB in the pure PbS and pure CdS QDs. In CdS the position of the first excited state as a function of size is much higher than in PbS. This evidence explains the faster charge injection observed in most of the CdS/MOS systems, compared to PbS/MOS.

These results show the possibility of measuring directly the electronic band structure of individual SILAR–grown QDs of metal chalcogenides, tuning their optical and electronic properties according to the desired complex system, in which the QDs are to be integrated. Compared to other techniques, which consider measured values averaged over a population of nanostructures with non-narrow size distribution and compositional variations, our results give an accurate estimate of the electronic band structure of the single QD, and can be use straightforward for predictions on exciton dynamics in composite nanosystems. This kind of direct measurement can represent a solid support in several applications, in which charge dynamics between photoexcited QDs and electron- or hole-transporting materials are critical for maximizing efficiency, like, for instance, in solar cells, photoelectrochemical water splitting and photocatalysis.

6.3 Materials and methods

6.3.1 Sample Preparation

Different QDs were synthetized by SILAR directly on a substrate of HOPG. HOPG substrates were chosen due to their extremely flat surface that enables smooth imaging and characterization of individual QDs via AFM/KPFM. In general the procedure to grow the QDs was conducted as follows: a 0.02 M methanolic solution of Pb-$(NO_3)_2 \cdot 4H_2O$ and a 0.02 M solution of $Na_2S \cdot 9H_2O$ in methanol/water (50/50 V/V) were used as Pb^{2+} and S^{2-} sources, respectively, for PbS QDs. A 0.05 M ethanolic solution of $Cd(NO_3) \cdot 4H_2O$ and a 0.05 M solution of $Na_2S \cdot 9H_2O$ in methanol/water (50/50 V/V) were used as sources of Cd^{2+} and S^{2-}, respectively, for CdS QDs. For each SILAR cycle, 1 min dipping for the HOPG substrate in metallic precursor (Pb^{2+}, Cd^{2+}) was applied. The sample was then washed with the corresponding solvent, to remove unabsorbed chemicals, and dried under N_2 flux. Subsequently, the same process was applied to the sulfide precursor. For growing composite PbS/CdS QDs, the deposition of CdS immediately followed the synthesis of PbS. For this reason, we first expect the nucleation and growth of a PbS core, directly on the HOPG surface, covered by an external CdS shell. The PbS and CdS QDs were grown with two cycles of SILAR while the composite PbS/CdS was grown using first two PbS SILAR cycles followed by two CdS SILAR cycles.

6.3.1 Characterization of Materials and Devices

Transmission Electron Microscopy. A JEOL 2100F microscope, equipped with Oxford Instruments energy-dispersive spectroscopy (EDS), was used at 200 kV to conduct TEM analysis of samples grown on carbon films coated on TEM Cu grids. Average QD sizes were measured using image analysis of 10−15 particles for each condition. Our hypothesis is that QDs grow very similarly on HOPG and on carbon films and with similar sizes. Such hypothesis has been experimentally proven by comparing size distributions obtained from AFM and TEM images.

Atomic Force Microscopy. AFM was performed using Ted Pella Platinum/Iridium tips on QDs directly grown on HOPG substrates. The sample was imaged in several areas of the order of 1 × 1 μm^2. The diameters of the QDs were manually measured using dedicated software from the full width at half maximum (FHWM) of the height of the dots obtained from AFM images, to eliminate tip convolution effects. The cross section of the dots also confirms the same diameter convoluted with the tip diameter.

Kelvin Probe Force Microscopy. KPFM measurements were carried out in a modified atomic force microscope (AFM) using Ted Pella Platinum/Iridium coated tips. The contact potential was measured simultaneously with topographic images using an AC bias (V_{ac} = 50-100 mV) at the second resonance frequency of the cantilever (~ 450 kHz). This set-up allows for an optimal separation from the topography and the CPD channel. Due to the wiring connections used in these experiments, the real CPD values will have the opposite sign of what the images show (in this case the CPD of the QDs will be negative if the plot shows a positive value). For the calculation of the work function, each PtIr-coated Si cantilever was calibrated on HOPG before and after each set of measurements.

Electrochemical characterization. Mott-Schottky and Open Circuit Potential (OCP) analysis were carried out using a SOLARTRON 1255/1287 in a typical three-electrode configuration. The electrolyte was a solution containing 0.35 M Na_2SO_3 and 0.24 M Na_2S (pH =11.5). To remove oxygen before the experiment the solution was purged with Argon. Pt wire and a saturated Ag/AgCl electrode were used as the counter and reference electrodes, respectively. All measurements were carried out with an AC amplitude of 10 mV in the dark and at a frequency of 1 kHz. All potentials measured with respect to Ag/AgCl were converted to the RHE scale taking into account the pH value of the solution.

7 Improving hole extraction in inverted planar perovskite solar cells.

This chapter is based on the paper "*Hole-extraction and photostability enhancement in highly efficient inverted perovskite solar cells through carbon dot-based hybrid material*" published on *Nano Energy*, 62, (2019), 781–790.

In this chapter, the charge extraction in a solar cell is tuned by modifying the charge transport layer, in this case the p-contact of an inverted perovskite solar cell. This work is based on an internship I carried out in the summer of 2017 at National Chao Tung University in Taiwan under the supervision of Prof. Eric Diau. My stage focused on the engineerization of the interface of perovskite solar cells cell in order to facilitate the electron/hole transfer from the perovskite layer to the electrode. In this framework, I planned to increase the efficiency of the solar cells by adding, at the interface between the conductive glass and the perovskite, a hybrid layer formed by Graphene Oxide (GO) and Carbon Dots (Cdots).

From Chapter 2, we have seen that an efficient approach to enhance the performance of third-generation solar cells is to improve charge extraction using a suitable charge- transport layer (CTL). An effective CTL increases the extraction of the photo-generated charge carriers from the absorbing layer while avoiding their recombination. As seen in Chapter 4, we used carbon nanotubes (CNTs) to modify the charge transport properties of a TiO_2 mesoporous layer used as photoanode (thus as ETL) in DSSCs.

In this chapter, we will focus on the latest addition to the carbon nanomaterials family, carbon dots (Cdots).[67] Cdots are discrete, quasi-spherical nanoparticles of size less than 10 nm. They have emerged as prospective competitors to conventional semiconductor quantum dots (QDs) and recently they have been proposed as possible CTL for solar cells.[283, 284] Cdots are exclusively composed of earth abundant elements (C, N, H and O) and can be synthesized in large quantities via a simple hydrothermal or microwave approach.[285] Relative to conventional semiconducting QDs, their advantages include being non-toxic, cheap, chemically stable and simply prepared from abundant carbon-based feedstock.[283]

To show their versatility, we will exploit the opto-electronic properties of the Cdots to modify the HTL of an inverted planar PSC. As seen in Chapter 2.3, the planar inverted configuration is one of the most widely used configurations of PSC. In this architecture, the HTL is critical for achieving high V_{oc} and overall high performance and there is an intense research in finding an alternative to the common HTL PEDOT:PSS. Various promising HTLs, such as NiO_x,[146] CuSCN, [166] and others, have also been explored to fabricate efficient inverted PSK solar cells in the superstrate configuration (see Chapter 2.3 for details). In general, all these HTLs showed good performance at the cost of long and complicated fabrication processes.

Carbon materials have been already employed in PSC, in particular, graphene structures have been shown to be effective CTLs and transparent conductive electrodes in PSCs.[172] As seen in Chapter 2.3.1, GO as a well-known derivative in the graphene family, was applied as a HTL in inverted PHJ PSC and yielded a PCE exceeding 12%.[172, 286] Although GO is an efficient hole-extracting material, hole propagation on the oxygen groups limits the transfer of extracted holes and causes charge recombination. Even if reduced graphene oxide (rGO) can solve this problem, there remain issues that should be addressed: rGO requires protracted and complicated preparation and yields poor surface coverage while in GO-based devices the hole propagation from GO to the InSnO (ITO) substrate is slow.[287]

To overcome these limitations, I decided to employ fluorescent carbon dots (Cdots) to form a homogeneous GO/Cdots HTL to develop high efficiency inverted PHJ PSCs. We could demonstrates that an optimal amount of Cdots in optimized proportion in a composite with GO nanosheets can significantly improve hole extraction from the perovskite film at the interface with GO/ITO.

Furthermore, specific Cdots were design with the scope to increase the stability of the PSC. In fact, long term stability is one of the most critical parameters for solar cells in general (also because it affects overall cost), and is a major challenge for PSCs specifically. In particular, the stability of PSC under ultraviolet light remains a major problem [288, 289]. To address this issue, we prepared UV-absorbing Cdots and embedded them in a polymer matrix to serve as the downshifting layer (DSL) over the perovskite cell. (**Figure 7.1**).

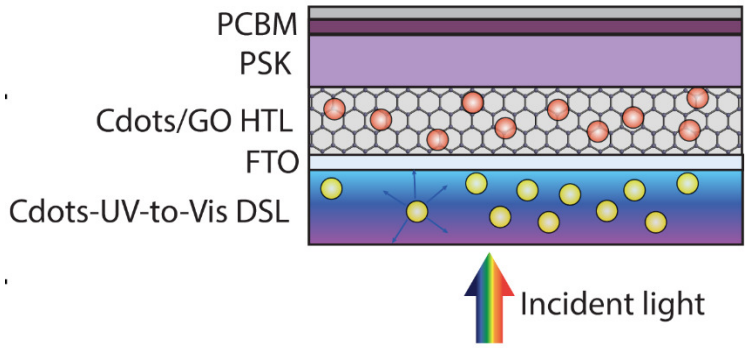

Figure 7.1. a) Schematic of an inverted planar device with Cdots incorporated at the interface between GO and perovskite, and a protective/down-shifting layer made of Cdots/PVP on the exterior side (N.B. the thickness of the layers is not in scale).

7.1 Results and discussion

7.1.1 Synthesis and characterization of Carbon Dots/GO hybrid

A solvothermal approach was employed to form Cdots with abundant functional groups, including hydroxyl, carboxyl and amide groups. These functional groups confer great dispersibility in polar solvents,

such as water and methanol.[290] To integrate the Cdots in the PSC device, however, they must be compatible with the fabrication process; in particular they should be soluble in non-polar solvents such as hexane or slightly polar solvents, such as chlorobenzene and toluene. To obtain a non-polar solubility of the Cdots, the as synthesized Cdots were modified with oleamine (OLA) according to our previous work.[290] In this procedure, an additional step to modify the surface was added to transfer them from a polar solvent to a non-polar solvent. By employing (1-Ethyl-3-(3-dimethylaminopropyl)carbodiimide, EDC), the primary amine from long carbon-chain molecule OLA reacted with the carboxyl group on the surface of the Cdots (**Figure 7.2)**. The obtained OLA-modified Cdots exhibit hydrophobic features due to the long carbon chain, and can be efficiently dispersed in slightly polar solvents, such as chlorobenzene, and even in a non-polar solvent such as hexane.

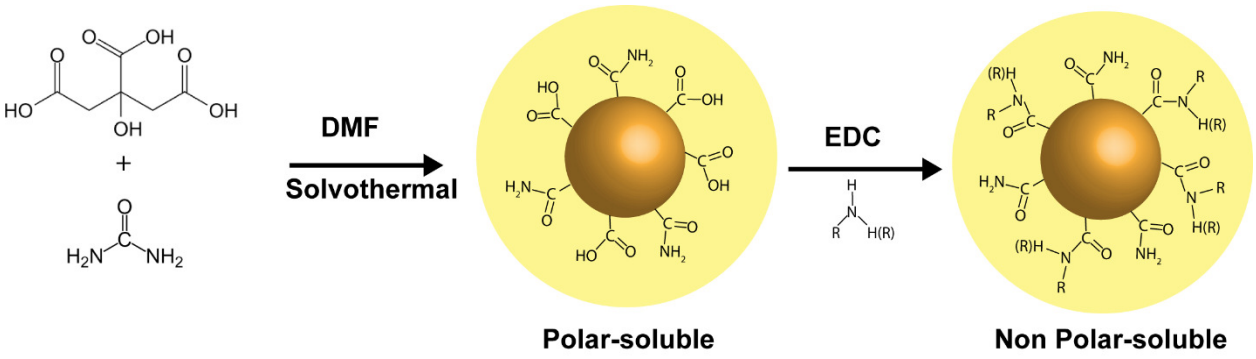

Figure 7.2. Scheme of the Cdots reaction used in this work.

In **Figure 7.3** are reported the absorption and PL spectra of Cdots, before and after surface treatments with OLA (MeOH_Cdots and CB_Cdots respectively). The spectrum acquired from freshly synthesized C-dots exhibits strong absorption extending over the entire window of the visible wavelengths (300-700 nm); **Figure 7.3 b and Figure 7.3 c** report the 2D excitation-emission properties of the Cdots. As expected, the Cdots present wavelength-dependent emissions. The optical properties of the pristine Cdots are mainly preserved upon functionalization with OLA; absorption and emission bands are similar in both samples. The small differences are attributed to the solvents, as Cdots can exhibit a solvent-dependent shift, as previously reported. [291] The functionalization leaves the overall electronic properties of Cdots almost intact, while conferring on them an enhanced solubility in non-polar solvents.

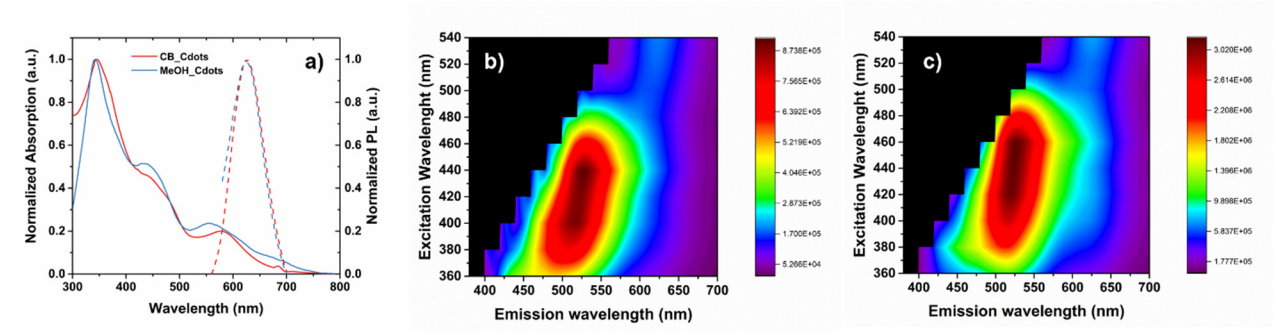

Figure 7.3. a) Absorption and emission (λ_{ex}= 540 nm) of Cdots after purification (MeOH_Cdots, solvent is methanol) and after ligand exchange (CB_CDots, solvent chlorobenzene); b) 2D contour plot showing the wavelength-dependent emission of Cdots as synthesized (MeOH_Cdots); c) after ligand exchange and dispersed in chlorobenzene (CB_Cdots).

X-ray photoelectron spectroscopy (XPS) was carried out to evaluate the chemical composition of the Cdots. The three major elements, C, N and O are identified from the wide scan XPS spectrum (**Figure 7.4**). The high resolution XPS C 1s can be deconvolved into three binding energies (i.e., 284.6 eV (C−C), 287.8 eV (C-N/ C-O), and 288.8 eV (−COOH)). From this analysis the presence of C, N and O is evident. The C 1s spectrum could be fitted with three Gaussian peaks with maxima located at 284.6, 286.8, and 288.1 eV, assigned to C−C (sp_3-hybridized), C−O/C-N, and O=C-O chemical states, respectively. [292] The high resolution N 1s band can be deconvolved into three main peaks corresponding to pyridinic (398.7 eV), pyrrolic (400.6 eV), and graphitic 402.1 eV nitrogen atoms. [293] [294] The O 1s band contains two main peaks at 531.7 and 532.1 eV for C=O and C−O, respectively. [292]

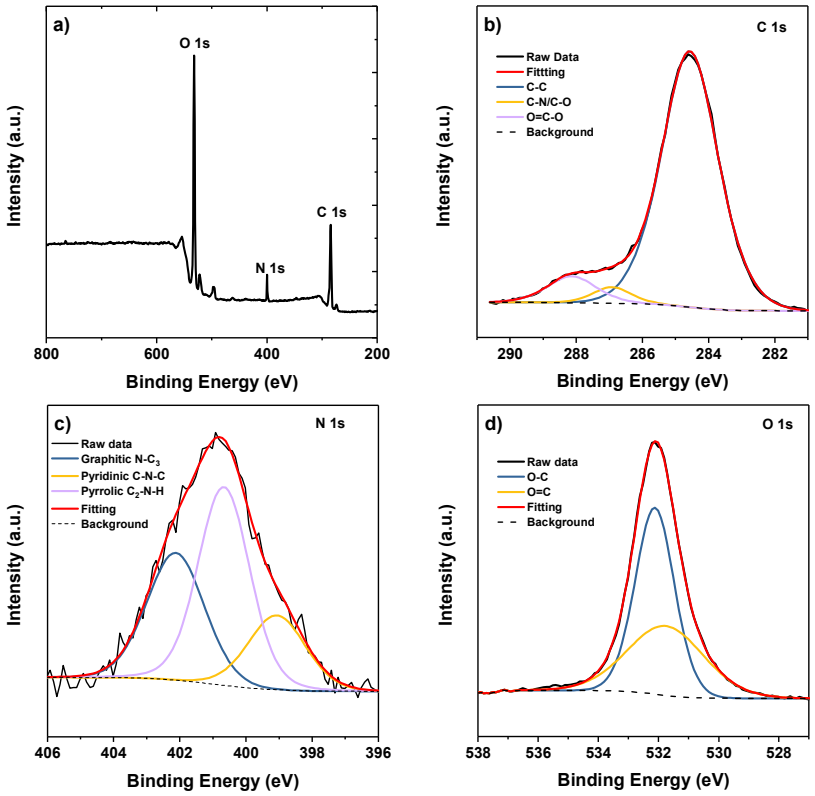

Figure 7.4. a) XPS survey spectrum, (b) C 1s XPS spectrum, (c) N 1s XPS spectrum, (d) and O 1s XPS spectrum of the as-prepared Cdots.

To verify that Cdots can effectively inject holes in the GO, we carried out PL experiments. The solutions of Cdots with varied GO concentration were analyzed and the recorded PL spectra are displayed in **Figure 7.5**. The substantial quenching indicates a strong interaction between Cdots and GO. The PL spectra in **Figure 7.5** show a dominant emission (maxima at 520 nm and 630 nm, when excited at 400 nm and 540 nm, respectively) for pure Cdots, whereas ~60 % of the Cdots PL intensity is quenched by GO. In particular, the PL intensity decreases greatly with increasing concentration of GO in solution, while the position and shape of the absorption lines are unaffected. As already reported in similar systems, this interaction can be ascribed to charge transfer of the photoinduced charge carriers in the Cdots to GO. [291, 295]

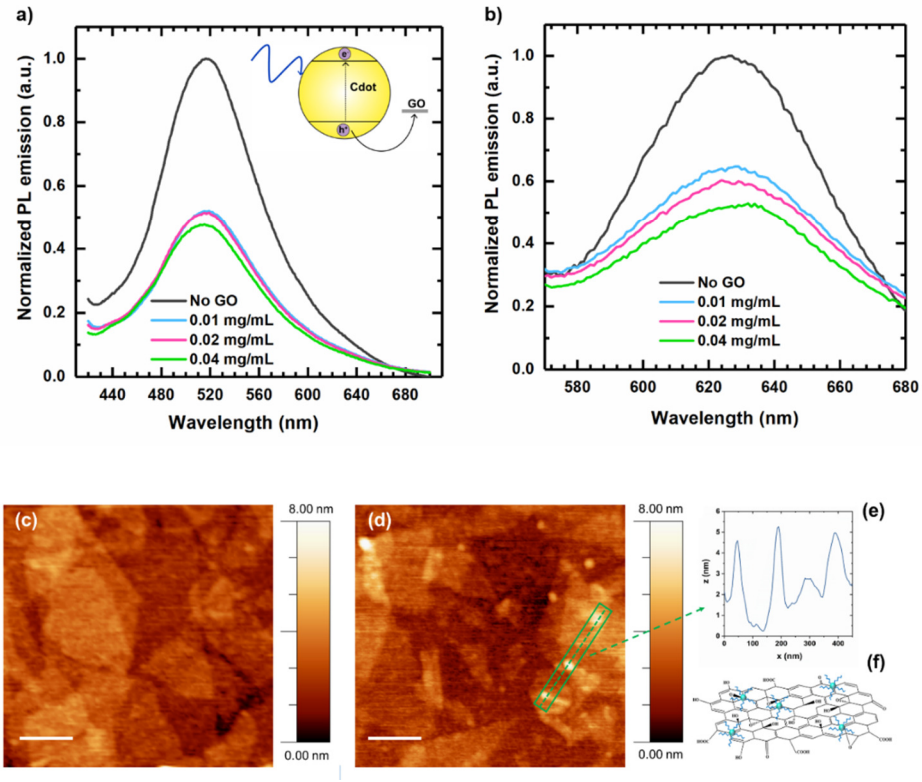

Figure 7.5. Fluorescence spectra of Cdots in chlorobenzene solution at varied concentration of GO. a) λ_{ex} = 400 nm, b) λ_{ex} = 540 nm. Surface morphology of GO film (c), GO/Cdots (d) on area 1 µm x 1 µm. Cdots are clearly visible on the surface of the GO nanosheets. The scale bar is 200 nm. (e) depth profile of an assigned part and (f) schematic of graphene oxide nanosheets with Cdots deposited on top.

The Cdots/GO HTL was prepared by spin-coating the Cdots_CB dispersion solution of varied concentration (0.025, 0.05 and 0.1 mg /mL) over the GO layer. The surface morphology of the GO film with and without Cdots was analyzed by AFM. The GO film (**Figure 7.5c**) exhibits a nano-sheet feature with 1-3 layers; the thickness is estimated to be ~2-3 nm. Cdots on the surface of GO are clearly observed (**Figure 7.5d**), their size is in the range 4-6 nm and their presence does not alter significantly the RMS roughness (RMS ~1 nm vs 0.89 nm for the pure GO film).

7.1.2 Characterization of perovskite solar cell based on Cdots/GO hybrid

The prepared GO/Cdots layer was used as HTL in an inverted PSC based on device configuration ITO/GO /Cdots /$MAPbI_3$ /PCBM /BCP /Ag. The cross sectional and top view scanning electron microscope (SEM) images for all perovskite films grown on ITO/GO and ITO/GO/Cdots substrates are shown in **Figure 7.6**. Pin-hole-free, close-packed and uniform perovskite films were formed, which are an essential condition for a high-performance solar cell in a planar structure.[296]

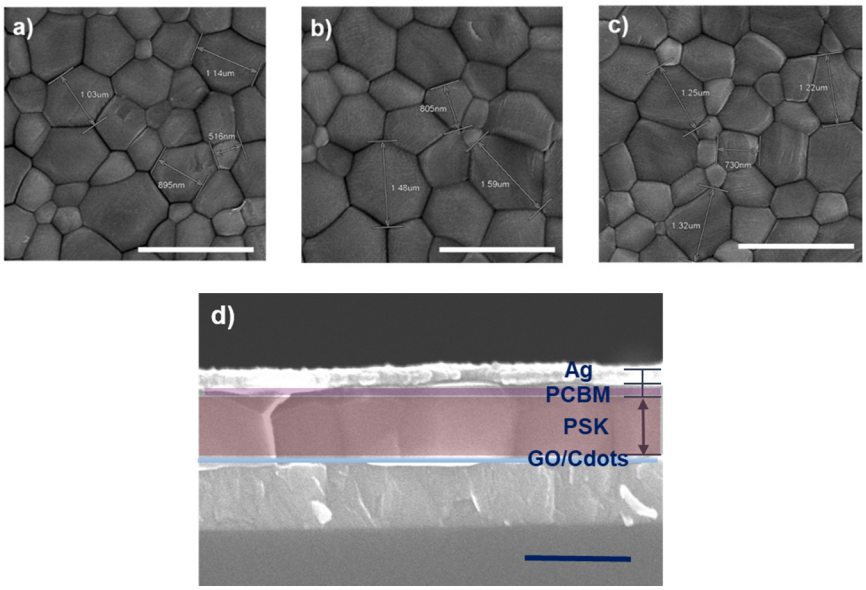

Figure 7.6. SEM top view images of a) perovskite on GO b) perovskite on GO/Cdots 0.025 and c) perovskite on GO/Cdots 0.05. The scale bar is 1 µm. (d) SEM cross section of the device. The scale bar is 500 nm.

The crystal structure of the perovskite film for all samples, ITO/GO and ITO /GO /Cdots, was analyzed using XRD; no significant variation of crystallinity of the perovskite was observed (**Figure 7.7**). The XRD shows the typical crystallinity of the perovskite films MAPbI3 film with tetragonal I4/mcm phase structure, consistence with previous literatures.[297, 298]

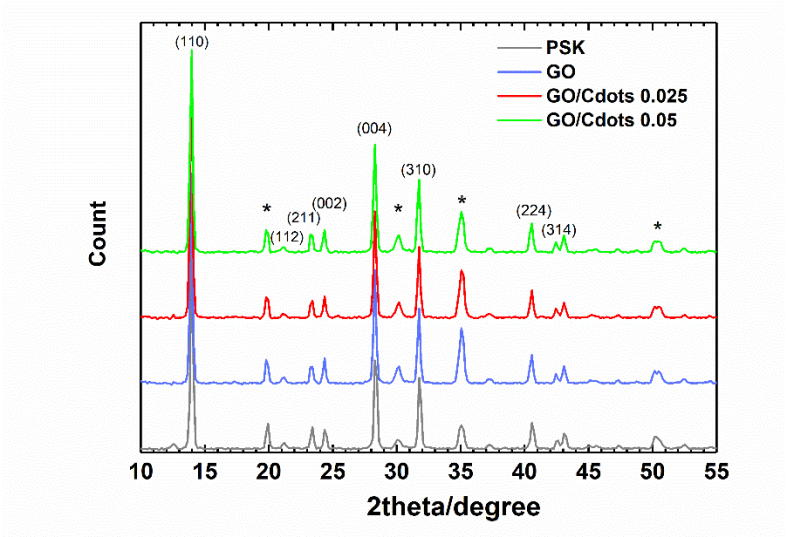

Figure 7.7. XRD of the different samples. The diffraction signals from the ITO substrate are marked with *.

In the inverted configuration, it is essential to have a transparent HTL so as not to lose the incident light and photocurrent. As shown in **Figure 7.8**, the addition of Cdots does not increase the absorption in the 400-500 nm range, with no detrimental effect on the absorption of the perovskite layer. Hence, we can conclude that the improved performance of the devices arises from the changes of the optical and electronic properties at interface, as discussed below.

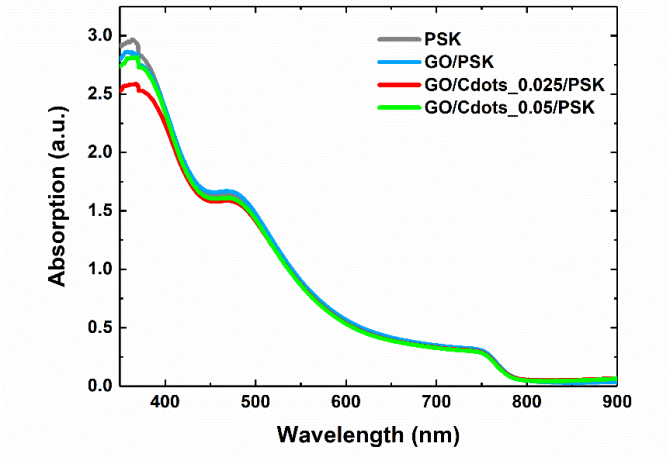

Figure 7.8. Absorption spectra of most representative samples: FTO/PSK, FTO/GO/PSK, FTO/GO/Cdots_0.025/ PSK and FTO/GO/Cdots_0.05/ PSK

7.1.3 Effect of varied Cdots loadings on the functional properties of the solar cells

The effect of varied Cdots loadings on the functional properties of PSCs was investigated. The *J–V* curves of the best cells with varied concentration of Cdots in the GO/Cdots layer as HTL under AM 1.5G simulated sunlight and the efficiencies of incident photons to current (IPCE) are reported in **Figure 7.9. Table 7.1** reports the photovoltaic (PV) performance parameters (V_{OC}, J_{SC}, FF and PCE).

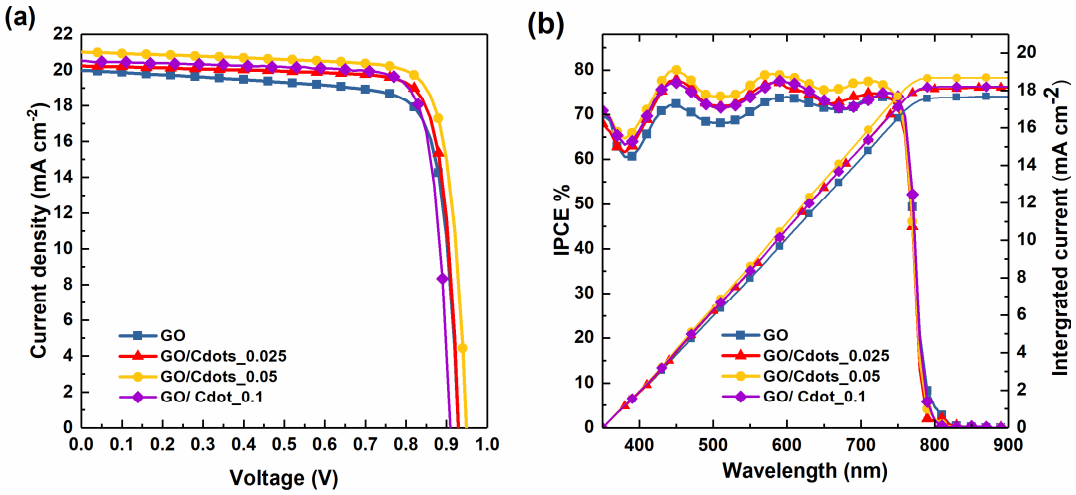

Figure 7.9. a) *J-V* curves for the best samples under optmized conditions, b) IPCE and integrated current densities.

For the GO device, a PCE of 14.7 % was obtained, a higher value compared to the one reported by Wu et al. (PCE = 12.4 %) for similar device.[172] In general, all the champion devices with GO/Cdots as HTL showed far superior PV performances: 15.6 %, 16.2 % and 15.4 % for Cdots loading at 0.025, 0.05 and 0.1 mg/mL, respectively. The improved performances of GO/Cdots are due mainly to their increased J_{SC}. Higher J_{SC} in GO/Cdots devices were confirmed by the IPCE spectra (**Figure 7.9 b)**. The calculated J_{SC} values from the IPCE spectra are consistent with the J_{SC} values obtained from the *J–V* curve measurements. All the devices with Cdots show IPCE spectral features similar to those of the GO device, but with increased values in the entire wavelength range. Because of the weak absorption of Cdots relative to the perovskite film (**Figure 7.8**), a significant contribution of Cdots to the light harvesting of the perovskite films can be excluded.

Table 7.1. Photovoltaic parameters for the best devices containing three different amounts of Cdots, as well as the reference device.

Devices	Cdots Concentration (mg/mL)	J_{SC} (mA cm^{-2})	Integrated J (mA cm^{-2})	*V*oc (mV)	FF	PCE (%)
GO	0	20.0	17.7	935	0.79	14.7
GO/Cdots 0.025	0.025	20.2	18.2	935	0.82	15.6
GO/Cdots 0.05	0.05	21.0	18.7	953	0.80	16.2
GO/Cdots 0.1	0.1	20.6	18.2	922	0.81	15.4

The effect of introducing Cdots in a GO layer as HTL is clearly discernible in the statistical data. Twenty devices were fabricated under the same experimental conditions for devices based on GO and GO/Cdots (with varied Cdots concentration); the corresponding PV parameters are listed in Appendix III. **Figure 7.10 a-d** compares the J_{sc}, V_{oc}, FF and PCE distributions of these results with various hole extraction layers, giving mean PCE (%) = 13.4±0.7, 14.3±0.7, 14.9±0.7 and 14.45±0.9 for devices made of GO, GO/Cdots 0.025, GO/Cdots 0.05 and GO/Cdots 0.1, respectively. At the optimum amount of 0.05 mg/mL of Cdots on GO, all the functional parameters (V_{oc}, J_{sc}, FF and PCE) show the highest values. GO/Cdots 0.1 devices in general present the lowest values among the Cdot-based PSC, because of the poor wettability of the

perovskite solution on the surface of the GO/Cdots; this condition can also explain the large variation from the best value for this dataset.

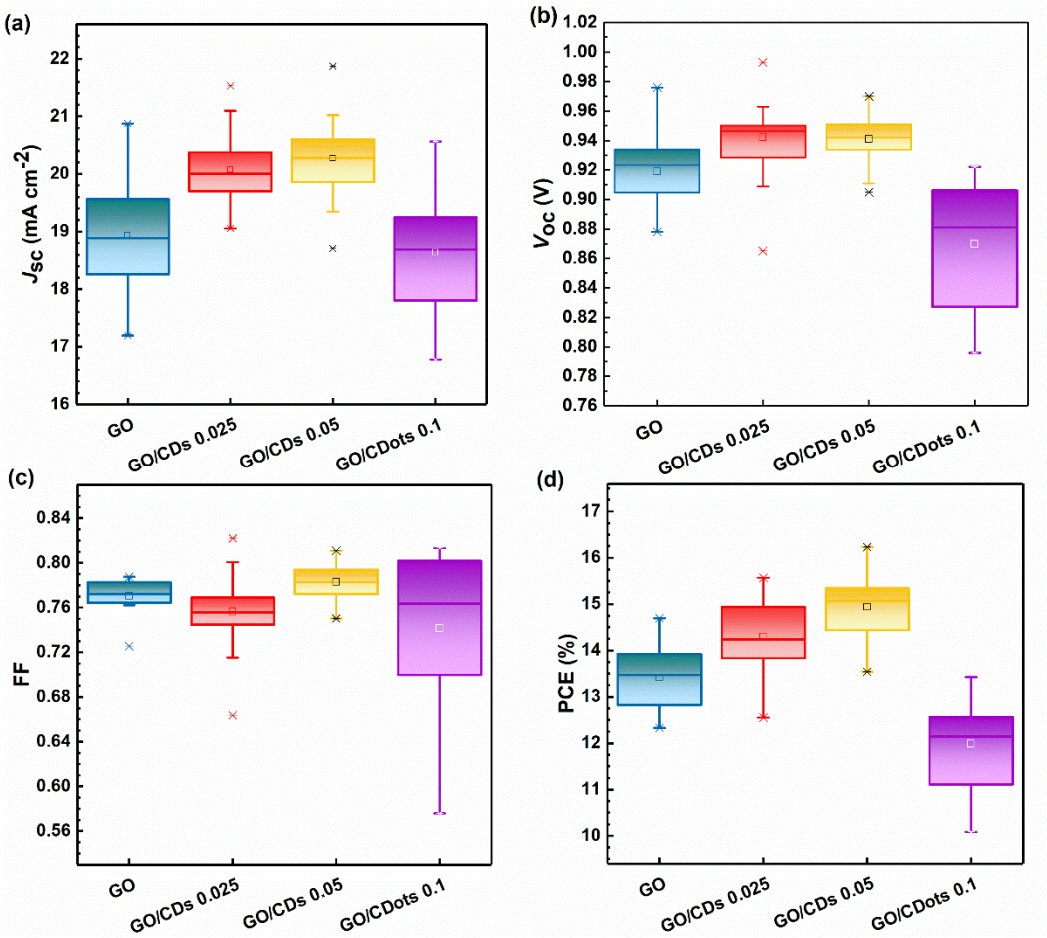

Figure 7.10. a-d) Statistical box plots of photovoltaic parameters for inverted perovskite solar cells with Cdots at varied concentration on GO as HTL that were fabricated under the same experimental conditions for cells of each type. Top and bottom of the boxes is the 75–25 percentile and the cross symbols represent outliers in box plot.

The poor wettability is confirmed by contact angle measurements (**Figure 7.11**). By increasing the amount of non-polar Cdots deposited, the hydrophobicity of the layer increases (higher contact angle), making more difficult the deposition of uniform perovskite films prepared by spin coating technique.

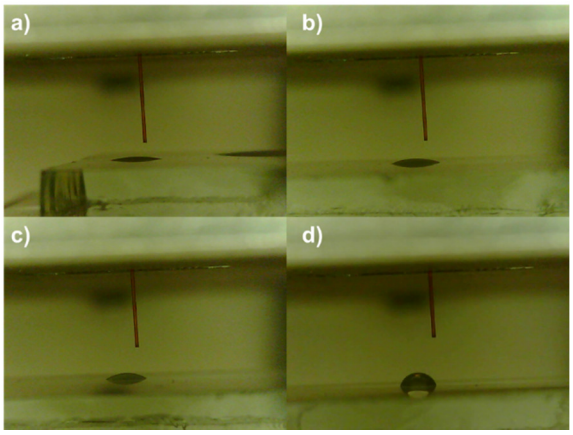

Figure 7.11. Contact angle measurements of most representative samples: a) FTO/GO, b) FTO/GO/Cdots_0.025, c) FTO/GO/Cdots_0.05 and d) FTO/GO/Cdots_0.1

7.1.4 Investigation of the role of Cdots in the charge transfer

From these observations, we deduced that the addition of Cdots at an optimum amount on GO nanosheets increases the hole-extraction ability of a GO layer. To acquire further understanding of the mechanisms for the enhanced PCE, PL decay lifetimes and transient open-circuit photovoltage (TPV) decays were measured. To elucidate the dynamics of charge-transfer processes at the GO/Cdots composite layer, we applied steady-state PL and transient PL decays with time-correlated single-photon counting (TCSPC) techniques; the results for representative samples are depicted in **Figure 7.12**. Samples were prepared with a perovskite layer deposited on either an ITO/GO or an ITO/GO/Cdots layer while an ITO/PSK sample served as reference. All samples presented the characteristic perovskite excitonic emission feature centered about 770 nm **(Figure 7.12 a**). When GO or GO/Cdots were introduced at the interface of the PSK layer, a strong PL quenching was observed, maximized at 0.05 mg mL^{-1} Cdots concentration with the PL intensities following the order ITO/PSK > ITO/GO/PSK > ITO/GO/0.025Cdot/PSK > ITO/GO/0.025Cdot/PSK > ITO/GO/0.05Cdot/PSK. The steady-state PL quenching indicates a substantial contribution of Cdots to hole extraction from the perovskite film.

For a more direct confirmation of their role in the charge transfer, the PL lifetime was measured by TCSPC technique. Normalized transient PL decays of the corresponding samples (λ_{ex} = 635 nm, λ_{em} = 770 nm) are shown in **Figure 7.12 b**. A similar trend to the steady-state PL is observed, with the shortest decay being associated with the sample with GO/Cdots at 0.05 mg mL^{-1}. All PL transients were fitted with a bi-exponential decay model; the corresponding lifetimes and relative amplitudes are summarized in Table 7.2.

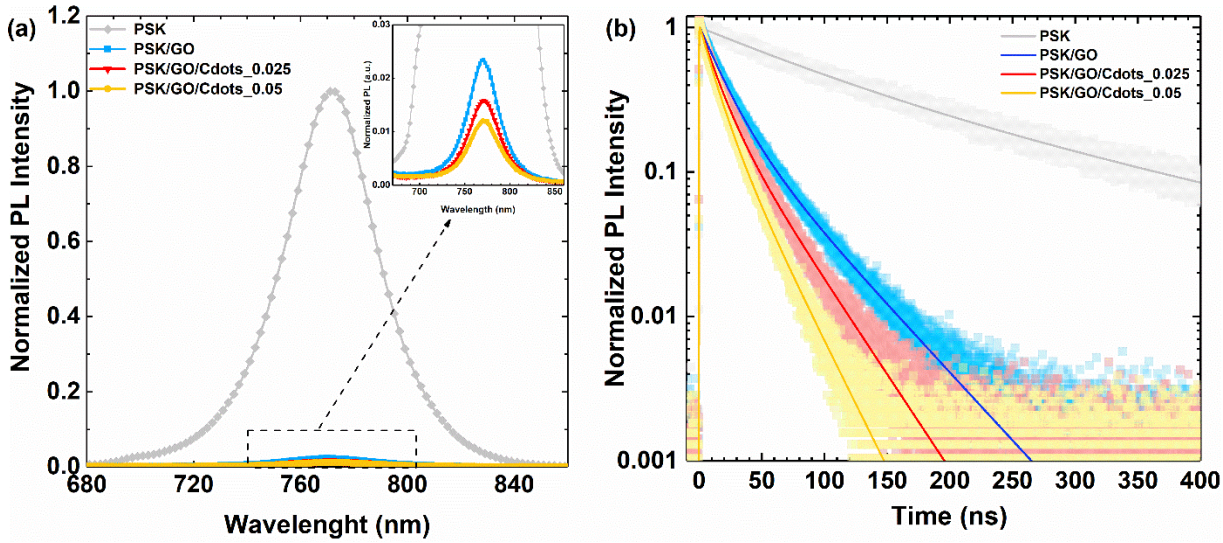

Figure 7.12. a) Steady-state photoluminescence spectra of perovskite thin films deposited on ITO, on GO and on GO/Cdots with varied loading, collected with excitation λ_{exc} = 635 nm, b) transient PL decays obtained using the TCSPC technique with excitation at 635 nm and probe at 770 nm.

For perovskite films fitted with a bi-exponential function, the first decay component corresponds to a non-radiative relaxation of the surface state in the grain boundaries of the perovskite while the second decay component is assigned to recombination events in the bulk.[299] The sample with 0.05 mg mL^{-1} Cdots contents has the smallest τ_1, 25 ns, compared with the GO sample, 46 ns. This supports the hypothesis of an enhanced charge transfer in the presence of an optimal amount of Cdots.

Table 7.2. Corresponding lifetimes and relative amplitudes of the bi-exponential fit of the transient lifetime of Figure 7.12.

	τ_1 (A_1)	τ_2 (A_2)	Average τ
$MAPbI_3$	95.50 (0.63)	250.95 (0.37)	153.02
$MAPbI_3$+GO	46.2 (0.30)	17.25 (0.70)	25.94
$MAPbI_3$+GO/Cdot(0.025)	30.43 (0.40)	12.11 (0.60)	19.44
$MAPbI_3$+GO/Cdot(0.05)	24.97 (0.35)	11.24 (0.65)	16.04

To increase our understanding of the effect of Cdots on the hole-extraction mechanism in complete devices, we measured the TPV, which is a measure of the rate of carrier recombination within the cells. In the TPV measurements, to achieve a steady-state equilibrium the solar cell was first illuminated under a white light bias, then a weak laser pulse was applied to generate an additional amount of charges in the devices. The

TPV associated with the charge population perturbation was then monitored to study the charge recombination processes. All photovoltage decay profiles were fitted with a single-exponential decay model; the values of the decay coefficient (τ_{rec}) for charge recombination are shown in **Figure 7.14 a**. The rate of recombination of the carriers is proportional to the inverse of the decay lifetime; a greater lifetime hence indicates less recombination inside the device.[300] An increase in charge-recombination lifetime can be observed for all the cells incorporating the Cdots. In particular the cell with the optimum content of Cdots, GO/Cdots 0.05, showed the longest lifetimes, indicating that a lower charge recombination rate was achieved. The TPV results suggests that a more favorable energy level alignment and good electron blocking capability of the hybrid GO/Cdots 0.05 HTL could effectively suppress the charge recombination process.

EIS served to elucidate the electronic properties and interfacial recombination in the solar cell with Cdots in varied amounts (**Figure 7.14 b**). For all samples, only one large semicircle is visible in the Nyquist plot; this arc, typically observed at medium frequencies, is related to the charge recombination inside the solar cell.[301, 302]

Generally, two semicircles can be observed. However in a high conductivity case (as in this case), in which either one of the transport resistances for electrons or holes is negligible, the geometric arc will not appear in the IS spectra in the high frequency region.[301] The most remarkable feature in the Nyquist plots is that the cell treated with 0.05 mg/mL Cdots leads to the larger arc indicating a reduced recombination phenomena. This is in agreement with the J-V measurement that showed a highest efficiency for this cell.

In particular, the response at different bias (V_{bias}) can be fitted to the simple circuit shown in **Figure 7.13**.[301,302] For the reason aforementioned, the model employed will not take into account the geometric capacitance. In addition, fitting the semicircle with a simple model containing only the series resistance (R_s), the recombination resistance (R_{rec}), and a capacitance (C_μ, chemical capacitance) gave a good fit and showed identical trends in the recombination resistance.

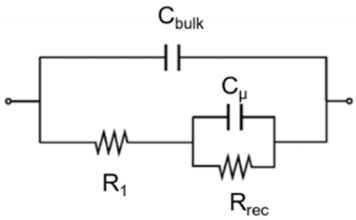

Figure 7.13. Circuit employed for fitting the EIS data

A further confirmation of the reduced recombination phenomena for the optimum amount of Cdots, comes from the analysis of R_{rec} when varying the voltage bias **(Figure 7.14 c)**. In all the range of V_{bias}, the value of R_{rec} for the best cell (with 0.05mg/mL Cdots) is higher compared to the others. The value of R_{rec} is inversely proportional to the charge recombination rate, so a higher value implies a significant suppression of the recombination rate. As the cells differs only for the HTL, we can attribute the reduced recombination to a better injection of holes in the ITO with a notable increment in the final PCE (as seen in the J-V analysis). Introducing Cdots increased the charge recombination resistance, in agreement with the TPV results.

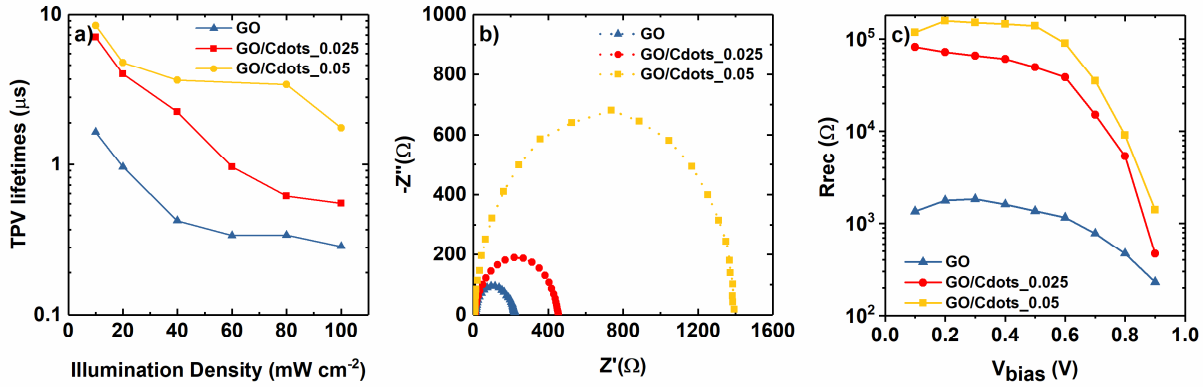

Figure 7.14. a) Transient photovoltage measurement of representative samples at varied illumination densities; b) Nyquist plot at 900 mV in dark of three representative samples with varied HTL: GO, GO/Cdots 0.025 and GO/Cdots 0.05; (c) recombination resistance of the of three representative samples.

The presence of a hole-transfer potential barrier between the perovskite and GO interface was previously established.[287] Based on all PL decay, TPV measurements and EIS, we conclude that the addition of Cdots into the GO HTL enhances the electronic coupling for efficient mediation of the hole transfer from the perovskite to the ITO front contact, decreasing the recombination at this interface, and consequently increasing J_{SC}.

To improve the understanding of the actual role of Cdots on GO nanosheets, we evaluated the band diagram of the Cdots using cyclic voltammetry (CV) (**Figure 7.15**). The measurements were performed at ~23 °C under an inert atmosphere with a three-electrode system consisting of a Pt foil as the counter electrode, an Au disk as working electrode and a Ag/AgCl as reference electrode. The band positions of the Cdots was obtained from the onset oxidation potential (E_{ox}) and the onset reduction potential (E_{red}) of the nanocrystals with equations reported in the experimental section. The HOMO and LUMO of Cdots were found to be −5.26 eV vs Vacuum and −3.55 eV vs Vacuum (**Figure 7.15 b**), respectively. The band position alignment of the Cdots supports the hypothesis of an improved hole transfer from the perovskite layer to the GO and

their ability to provide band bending and shifting the GO work function downward towards more negative values, as reported in **Figure 7.16 b**.

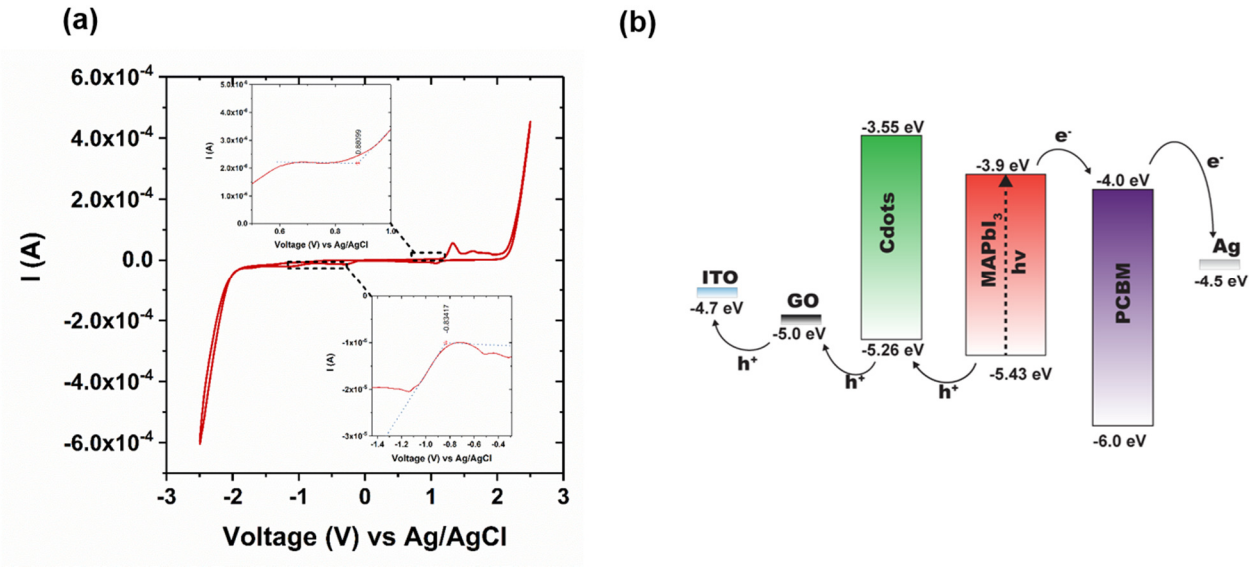

Figure 7.15. a) Cyclic Voltammetry of Cdots in TBAP/Acetonitrile. The insets highlight the onset of the oxidation and reduction used to calculated the HOMO/LUMO of the Cdots. b) Energy diagram of the perovskite cell (the energy values are reported vs Vacuum Level).

KPFM imaging supports this hypothesis: a shift of the contact potential difference towards more positive values was observed when the measurement was performed on a Cdot/GO sample. (**Figure 7.16 a**). In the KPFM system employed, the potential was applied on the tip, meaning that CPD = φ_{tip}-φ_{sample}. A shift towards less positive value of the CPD, considering that the work function of the tip does not vary, means that the work function of the sample increased.

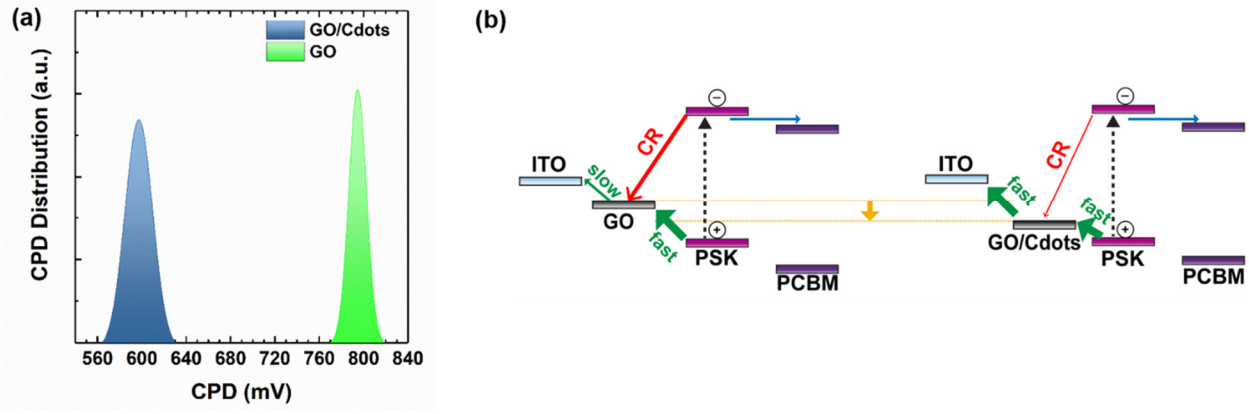

Figure 7.16. a) Contact Potential Difference (CPD) distribution of two representative samples: GO and GO/Cdots 0.05 on Si substrate. b) Schematic illustration of a mechanism of charge transfer for GO and GO/Cdots to rationalize the observed hole-extraction kinetics at the HTL/PSK interface and the corresponding photovoltaic performance.

To confirm the band position of Cdots, we conducted tests with Cdots and PCBM. PCBM has HOMO/LUMO energies of -6.0 eV vs Vacuum and -4.0 eV vs Vacuum, respectively. In theory, Cdots, with a LUMO energy of – 3.55 eV vs Vacuum, would inject carriers into the PCBM layer, but they would create a barrier for the electrons from the perovskite to the electron-transport layer as their LUMO level is less negative than the one of the PSC layer (**Figure 7.17**).

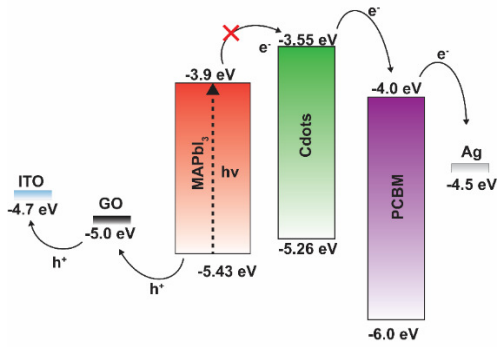

Figure 7.17. Energy diagram of the perovskite cell with the Cdots layer deposited over the PSC one. The charge transfer fron the perovskite to PCBM is blocked by the higher LUMO level of the Cdots.

Figure 7.18 a reports the steady-state PL of a solution of Cdots with added PCBM; as expected, when PCBM was added, the emission was quenched. A solar cell was then assembled with a layer of Cdots deposited over the perovskite layer and covered with PCBM. As reported in **Figure 7.18 b**, the short-circuit current of the cell decreases, yielding a PCE of 7.0 %, confirming the barrier effect of the Cdots between the PSK layer and the PCBM.

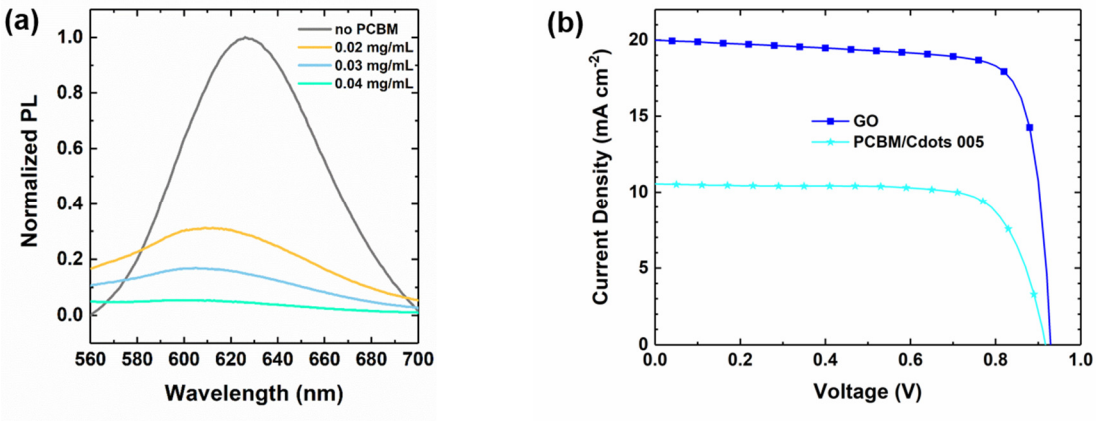

Figure 7.18. a) Fluorescence spectra of Cdots in Chlorobenzene solution at different PCBM concentrations. λex=540nm. b) J-V curve of solar cells with 0.05 mg/mL Cdots added between the PSK and PCBM compared to the normal device with a structure ITO/GO/PSK/PCBM/Ag.

7.1.5 Stability measurements

An important aspect for the commercialization of perovskite-based devices is their long-term stability. The performance as a function of storage duration for two devices, GO and GO/Cdots, was measured for 1200 h at 25 °C and relative humidity 25-30 % with no encapsulation; the results are reported in **Figure 7.19**. Both devices maintained almost 90 % of their initial efficiencies after storage for 1500 h, indicating the excellent stability of the GO-based devices relative to an organic HTL material such as PEDOT:PSS.[303]

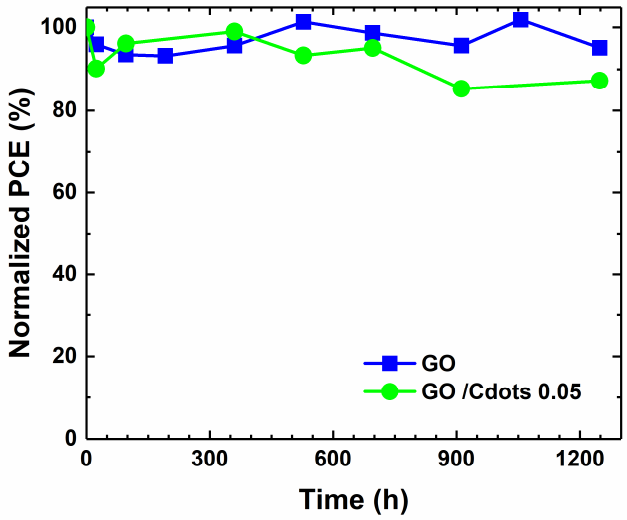

Figure 7.19. Profiles of efficiency stability of the PHJ devices with HEL made of GO and GO / Cdots 0.05 as a function of storage period.

Another challenge related to the stability of PSCs is the stability of perovskite to ultraviolet light.[134, 288, 289] To address this condition and to increase the long-term stability of our devices, we exploited the unique optical properties of Cdots. As mentioned before, the optical properties of Cdots can be tuned through the preparation method: in this case, a different type of Cdots was synthesized with the same precursors yet using a microwave method. This batch of Cdots presented strong down-converting properties, with absorption in the UV region and emission around 450 nm (**Figure 7.20 a**). In this way, the photon in the UV region of Sun spectrum can be absorbed, removing the soaking effect on the perovskite film, re-emitted in the visible spectral region (λ_{em} in the 450-500 nm region), and photoconverted into electric power. Cdots dispersed in isopropanol were subsequently mixed with polyvinylpyrrolidone (PVP) and spin-coated on the glass side of the PSC devices. Adding the protective layer of Cdots not only improved the stability of the device but also increased the PCE of the cell: the Cdots film removed the UV part of the spectrum and

downshifted it to a more suitable range of wavelength that can be absorbed by the perovskite film (**Figure 7.20 b**).

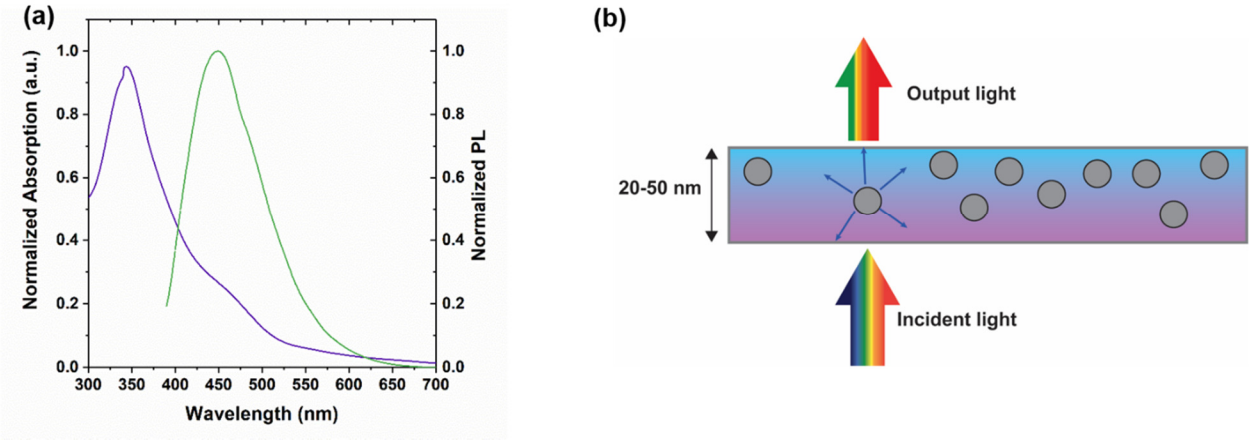

Figure 7.20. a) Absorption and emission spectra of UV Cdots. b) Schematic of the downshifting layer made of UV Cdots.

This synergistic effect is clearly observed in the device, as shown in **Figure 7.21**. The presence of an external thin film of Cdots increased J_{sc} by 3.8 %, increasing the final PCE to 16.8 %. The enhancement of the J_{sc} due to the effect of the downshifting of the UV light, is confirmed by the IPCE, in which the efficiency of photons to electrons in the range 350-500 nm is increased (**Figure 7.21 b**). To verify the light-soaking stability, we maintained the devices with or without a UV filter under illumination at 1 sun without capsulation in an ambient condition (RH = 45-50 %, T = 25 ˚C) (**Figure 7.21 c**). The device with the Cdots layer as UV filter exhibited increased UV stability. The normalized PCE retained more than 62 % of the initial PCE after 30 min of continuous operation under full irradiation. In contrast, the stability of the solar cell without a protective layer decreased to 48 % of the initial PCE under the same testing conditions.

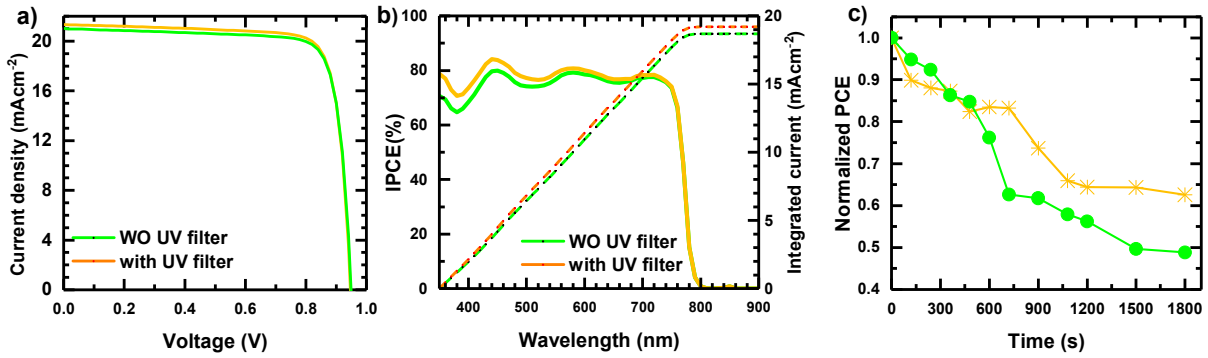

Figure 7.21. a) *J-V* curve of the best samples with GO/Cdots 0.05 as HTL and with or without an external protective UV-Cdots layer; b) corresponding IPCE and integrated curves; c) light-soaking stability for the two samples.

7.2 Conclusions

In summary, a rapid and highly reproducible method to prepare an efficient and stable HTL for planar-heterojunction PSCs based on Cdots/GO was demonstrated. These results show that the use of Cdots at an optimum amount improved the PCE of the device to 16.2 %. In the reference cell containing only GO, the transfer of the localized holes into the ITO surface can be a bottleneck that increases the recombination at the PSK/GO interface. As evidence shown via PL lifetime decay, TPV decay, EIS, CV and KPFM, the addition of the Cdots shifted down the work function of GO, increasing the rate of hole injection and decreasing charge recombination so that the collection of photogenerated charges improved significantly. Moreover, employing appropriate UV-absorbing Cdots as a protective film on the exterior side of the PSC improved the stability against UV radiation by more than 20 % while increasing the PCE up to 16.8 %. The present work provides important indications for further investigation in exploiting the properties of carbonaceous nanomaterials as high-conductive CTL alternatives for improving the efficiency of planar PSCs. Moreover, the versatility of the Cdots shown here, with their environmental friendliness, non-toxicity, and low-cost fabrication, can represent a practical and low-cost way to realize highly stable and efficient PSC.

7.3 Materials and methods

7.3.1 Synthesis of Carbon Dots

Cdots were synthesized via a solvothermal method with citrate and urea as precursors, following previous work.[290] Citric acid (1 g) and urea (2 g) were typically dissolved in 10 mL of dimethylformamide (DMF) under stirring. When all precursors were dissolved, the transparent solution was transferred into an autoclave (volume 30 mL); the reaction proceeded for 6 h at 160 °C. After natural cooling to ~23 ºC, the mixture was added dropwise to hexane (50 mL) to precipitate the Cdots. The precipitates were collected and dispersed in methanol (60 mL, MeOH_Cdots). For Cdots modified with oleamine (OLA) - OLA-modified C-dots, MeOH_Cdots (5 mL) were added to 1-Ethyl-3-(3-dimethylaminopropyl)carbodiimide (EDC) (250 mg) and OLA (1 mL). The mixture was stirred for at least 15 h near ~23 ºC. After the reaction, additional hexane (20 mL) was mixed with the solution. The OLA-modified Cdots were transferred into the hexane phase after standing for 5 min. For purification of the OLA-modified C-dots, the product was kept at -10 °C for 1 h; at that temperature, the residual OLA precipitated and was removed. The OLA-modified Cdots were then dried at 70 °C in a vacuum oven and redispersed in chlorobenzene (CB_Cdots).

We used a different approach for the synthesis of optical UV absorbing Cdots: citric acid (3.0 g) and urea (1.5 g) were dissolved in water (10 mL) under stirring. The precursors were subsequently placed in a

microwave oven for 4 min; the obtained green slurry was dried in a vacuum oven at 60 °C. The obtained powder was dispersed in isopropyl alcohol and centrifuged at 5000 rpm for 30 min; the supernatant was retained.

7.3.2 Device Fabrication

CH_3NH_3I (MAI) was synthesized as reported elsewhere.[304] To prepare the perovskite precursor solution, MAI and PbI_2 (molar ratio 1:1) powders were mixed in anhydrous DMF at concentration 50 mass %. The solution was stirred for more than 4 h at 70 °C and filtered through a polyvinylidene difluoride (PVDF) membrane (0.45 μm) before device fabrication. The devices were fabricated with a p–i–n configuration ITO/GO (GO/Cdots) /$CH_3NH_3PbI_3$/PCBM/BCP/Ag. The etched ITO substrates were cleaned and exposed to ultraviolet light and O_3 for 18 min. A GO solution (1 mg mL^{-1} in DMF, synthesized according to the method of Hummers explained in a previous report [303]) was spin-coated onto the substrates at 4000 rpm for 40 s. After annealing at 120 °C for 15 min, the substrates were transferred into a glove box for subsequent deposition of perovskite and an electron-transport layer. Before perovskite deposition, Cdots_CB solutions (concentrations 0.025, 0.05 and 0.1 mg mL^{-1} in chlorobenzene) were spin-coated on the GO film at 3000 rpm for 30 s and annealed at 60 °C for 5 min. These films as prepared are labeled here as GO/Cdots 0.025, GO/Cdots 0.05 and GO/Cdots 0.1, respectively. The perovskite precursor solution was dripped onto the ITO/GO (GO /Cdot) substrate spinning at a rate of 5000 rpm. The total duration of spin-coating was 15 s; chlorobenzene serving as antisolvent was injected onto the substrate after spinning 5 s. The perovskite film was then annealed at 100 °C for 2 min; the samples were treated with solvent annealing technique under DMF vapor for 10 min at the same temperature. Afterward, Methanofullerene Phenyl-C61-Butyric-Acid-Methyl-Ester (PCBM, 20 mg, FEM Tech) was dissolved in chlorobenzene (1 mL) and spin-coated on top of the perovskite layer at 1000 rpm for 30 s. Bathocuproine (BCP) (concentration 0.5 mg/mL in isopropyl alcohol, IPA) was spin-coated at 400 rpm on top of the PCBM layer. The silver back-contact electrode (100 nm) was eventually deposited via thermal evaporation in a vacuum chamber.

7.3.3 Preparation of an UV-protective layer

The Cdots dispersed in isopropanol were mixed with polyvinylpyrrolidone (PVP) polymer (final concentration 200 mg/mL). The concentration of Cdots was about 2 mg/mL. The solution was then spin-coated at 800 rpm for 30 s on the back side of an assembled PSC (thickness 50-100 μm). Before spin-coating, the active area was protected with a tape.

7.3.4 Characterization of Materials and Devices

The current–voltage characteristics were measured with a digital source meter (Keithley 2400) with the device under one-sun illumination (AM 1.5G, 100 mW cm^{-2}) from a solar simulator (XES-40S1, SAN-E1). The spectra of the IPCE of the corresponding devices were recorded with a system consisting of a Xe lamp (PTiA-1010, 150W), a monochromator (PTi, containing a grating with 1200 g mm^{-1} blazed at 500 nm) and a source meter (Keithley 2400). XRD patterns were recorded with an X-ray diffractometer (Bruker AXS, D8 Advance, Cu K_α, λ = 1.5418 Å). A scanning electron microscope (SEM, Hitachi SU-8010) was used to investigate the morphology of the films. Absorption spectra were recorded with a spectrophotometer (JASCO V-570);

The PL transient spectra were recorded with a time-correlated single-photon counting (TCSPC) system (Picoharp 300, PicoQuant) with excitation at 635 nm from a picosecond pulsed-diode laser (LDH-635, PicoQuant, FWHM ~70 ps). The rate of repetition of the laser used for all experiments was 25 MHz; the pulse energy per unit area was 4 μJ cm^{-2}. The PL temporal profiles were collected at 770±16 nm, using a microchannel-plate photomultiplier tube (MCP-PMT, R3809U-50). Transient open-circuit photovoltage (TPV) decays were measured with a home-built setup. The sample was biased under a white-light light-emitting diode (LED, HP-HC30W3, Createk) at varied intensities; a small perturbation was introduced with a blue LED (HP-HC30B3, Createk) modulated at 1 kHz with a function generator (AFG-2225, GW Instek). The V_{OC} transient decay was recorded with an oscilloscope (HDO 4034, Teledyne Lecroy).

Cyclic voltammetry (CV) measurements were performed under N_2 with a Ag/AgCl reference electrode, a Au disc as working electrode and a Pt foil as auxiliary electrode in a computer-controlled electrochemistry system (Solartron 1087). Before use, the working electrode was polished with alumina powder (1, 0.3, 0.1 μm), rinsed with copious amounts of water (Milli-Q), and cleaned electrochemically with H_2SO_4 (0.5 M) with electrolyte tetrabutylammonium perchlorate (TBAP, 0.1 M in acetonitrile). Before use, TBAP was dried *in vacuum* for at least 4 h at 80 °C. Cdots (5 μL) were dried on the Au electrode; CV was performed in a potential window [-2.5 V; +2.5 V] at scan rate 5 mV/s. The HOMO/LUMO of the Cdots were calculated using the following formula:

$$E(HOMO) = -(E_{ox,onset} + E_{vac,ferrocene} - E_{redox,ferrocene})$$

$$E(LUMO) = -(E_{red,onset} + E_{vac,ferrocene} - E_{redox,ferrocene})$$

These potentials are relative to a Ag/AgCl reference electrode; $E_{vac,ferrocene}$ is taken equal to 4.8 eV; $E_{redox,ferrocene}$ was calculated to be 0.42 V vs Ag/AgCl.[305, 306]

8 Summary and outlook

Photovoltaic devices based on nanomaterials have emerged as a credible alternative to conventional solar cells. In the last years, impressive improvement in the conversion efficiencies have been achieved, however they still lag behind the traditional silicon technology. Although they show lower efficiencies, the nanostructured cells offer several advantages over their competitors. As we have seen in Chapter 1, in the next years it is of fundamental importance to have technologies with low carbon footprint in order to reduce the emission of greenhouses gases and limit the climate change. Under these premises, DSSCs, QDSCs and PSCs can play a major role for transition to greener technologies. In fact they can be produced more cheaply and with processes less energy-intensive than silicon cells, for which 5 GJ have to be spent to make 1 m^2 of collector area.[307] Unlike silicon, their efficiency increases with temperature, narrowing the efficiency gap under normal operating conditions. They usually have a bifacial configuration, allowing them to capture light from all angles. DSSCs and QDSCs can have also different colours and transparency that could serve as windows in buildings. As seen in Chapter 2, one of the main factors that limit their performance, is the charge recombination and collection processes. The next breakthrough will come if the control of these processes will be improved. The challenge will be to find a facile and robust method to realize the control of the charge dynamics inside the solar cells, and therefore to significantly reduce the energy loss during the charge-transfer and transport phenomena.

In this thesis, the charge dynamics and light management of different architecture, such as DSSC, QDSC and PSC have been explored.

In Chapter 4 the effects of incorporation of different concentrations of F-MWCNTs into TiO_2 active layers for DSSCs have been explored. It has been shown that the presence of 2 wt% F-MWCNTs in the photoanodes increases the PCE up to 7.95% and J_{sc} up to 17.5 mA cm^{-2} while standard DSSCs with bare TiO_2 exhibit a PCE of 6.05% and a J_{sc} of 13.3 mA cm^{-2}. The improved performances can be assigned to the combined effect of increased dye loading and reduced charge recombination (as clarified by dye loading and EIS measurements), due to the conformal coverage of F-MWCNTs, which allows fast and efficient charge collection in operating solar cells. These results can help in improving the PCE in DSSCs in an elegant and straightforward way, minimizing the need of additional steps (e.g. pre and post treatment with $TiCl_4$) for photoanode preparation.

In Chapter 5, the traditional Pt CE has been replaced with a nanofiber-based CE made of Pt/Pd hollow nanofibers. The nanofibers were obtained by sputtering a Pt/Pd alloy (80/20 wt.%) onto electrospun polymer nanofibers, used as sacrificial template. The optimized CE can increase the short circuit current density, leading to a ~15% enhancement PCE compared to flat CE. The processes that contribute to the

PCE were an increased surface area provided by the high aspect ratio hollow nanofibers and an improved electro-catalytic performance, as validated by EIS measurements. These results suggest a simple and straightforward strategy to increase PCE in DSSCs, to minimize the use of precious metals used in this kind of devices and, more generally, to tailor the CE structure in photoelectrochemical systems to boost their functional properties, thanks to the advantages afforded by this complex morphology.

In Chapter 6, Kelvin Probe Force Microscopy was used to investigate the electrical properties of individual metal chalcogenide QDs with different size and composition grown via a successive ionic layer absorption and reaction (SILAR) on graphene-like material. This model system allows to investigate the properties of individual QDs, minimizing any other collective effect and/or QD-QD interaction. By using KPFM, it was possible to observe the local variation of the Fermi Level inside an individual QD and to distinguish the different materials from an electronic point of view, without interference from the morphology of the sample. The implications of this study are relevant to processes related to exciton dynamics, which are determined by the local environment at the interface of composite systems.

In Chapter 7, the effect of the integration of Cdots in high-performance inverted planar-heterojunction perovskite solar cells was investigated. By introducing Cdots on graphene oxide as HTL, the efficiency of the PSC improved significantly from 14.7% in the case of bare GO to 16.2% of the best device with optimized Cdots content. The efficiency and stability of the PSC were further improved with the application of a downshifting layer based on Cdots with an engineered absorption in the UV range. The final PSC attained a maximum PCE of 16.8% (+14%) and, compared to the PSC without DSL, the stability of the device was also enhanced of more than 20%. To understand the mechanism behind the PCE improvement, the electronic band alignment at the interface between GO/Cdots and the perovskite film was analyzed. Holes were extracted and transferred to the conductive substrate more efficiently in the presence of Cdots, thus delaying charge recombination. Photoluminescence (PL), transient PL decays and transient photovoltage (TPV) decays investigated the charge-transfer kinetics and proved the retardation of charge recombination. This work reveals an effective and easy method to enhance the charge extraction and thus of performance of planar PSCs by using a Cdots/GO hybrid as HTL.

8.1 Perspectives

To further promote the development of low environmental impact solar cells, the PCE and stability of the cells together with the toxicity of various constituents should be taken into consideration simultaneously, and improved to satisfactory level. A prerequisite for the ‘real world’ applications of a new kind of solar cell, it is that the whole device is environmentally friendly. In particular for QDSC and PSC, there are concerns related to the use of toxic materials such as Cd and Pb while for DSSC the main concern is the

iodine electrolyte. Alternative such as Cd-free QDs based on ternary I-III-VI group materials such as CuInS and CuInSe have been proposed and they are promising for future applications. Lately, there have been immense efforts to replace Pb with nontoxic elements for various Pb-free perovskites. Tin (Sn), closely analogous in many respects to Pb, has been investigated as a possible alternative to produce lead-free perovskites. However, Sn-based PSC have still issues of stability as Sn^{2+} can be easily oxidized to Sn^{4+} in air, producing detrimental effect on the PCE of the cell. Aqueous DSSC, based on water-based electrolyte have been also introduced, however the efficiency are still far behind compared to standard DSSC.

Recently, Cdots started to attract interests not only for their optical properties but also as possible alternative to organic dyes in DSSC and QDs in QDSC. Even though some Cdots have shown promising results, their performance are still limited. For example, as a proof-of-concept, recently Cdots have been used as sensitizer to realize a DSSC device reaching efficiency of 0.24%, far from the 13.4% obtained with dye-molecules. In general, in literature there is a lack of investigation on the charge transfer properties of the Cdots. Investigating and understanding fundamental charge-transfer properties of Cdots will be of fundamental importance for all the applications in which Cdots are used as photosensitizers.

Until now the adoption of new and environmental friendly resources was mainly determined by economic considerations, rather than technological challenges. This is why a solar cell, to be economically viable, should offer high efficiency combined with low cost as well as an extended lifetime. The current stability of nanostructured solar cells is still far from the standard needed for real applications. Further effort is thus required to improve their long-term stability. The improvement of the device sealing technique for liquid-junction devices or the fabrication of all-inorganic-solid-state could be enough to reach satisfactory long-term stability for DSSC and QDSC. PSC, in particular Pb-free devices, still present issues of stability, that encapsulation alone could not address. Recent studies on the incorporation of 2D perovskite structure on top of the 'standard' perovskite are showing promising results towards longer stability against humidity.

More importantly, even if these kind of PV solar cells will not be able to reach the required standard 25 years lifetime, it does not mean that they cannot be commercially competitive. In fact, recent work has highlighted that emerging PV technologies with lifetime shorter than 25 years could still be cost-effective, since solar panels become more efficient and cost-effective over time, so that periodically replacing panels may become economically advantageous.[308] Furthermore, to asses in the correct way the lifetime, further development of accelerated test procedures is needed. The most common procedures are adapted from silicon cells, however there is still a lot discussion of how accurate the rather old standardized procedures are in determining acceleration factors and product life. Some recent papers are trying to define standard for example for PSC but further studies are required.[309]

Reduction of recombination processes are keys to achieve high efficiency and long term stability. Full coverage of the ETLs is of fundamental importance to enhance the light absorption capability and reduce the uncovered area of metal oxide to minimize the metal oxide/electrolyte interface. The coating of the mesoporous oxide electrode with a thin wide band gap material can still be further improved. Advanced techniques, such as Atomic Layer Deposition (ALD), are showing promising results in this direction, giving higher control on the film thickness and uniformity.

A deeper understating of the mechanisms of charge dynamics is still also need it. Due to the high complexity (physical and chemical) of systems such as DSSC, QDSC and PSC, up to now, it is still not possible to predict accurately how a small change to the system, that is, replacing one component will affect the performance. Future research direction is to understand and master the mechanisms happening in particular at the oxide/dye/electrolyte (HTM) interface. For example, in DSSCs, it has been estimated that a reduction in loss-in potential of 0.1-03 eV could improve the efficiencies over 15%.[310] The control of the disorder at the interface and heterogeneity of the electron transfer process, together with faster hole transfer processes, could help to achieve that.

In this regard, the use of 1D and 2D materials, such as CNTs and graphene has shown promising result in facilitating the charge extraction. Further research direction should be focused on the understanding of the mechanism behind the increment of performance with these kind of materials, for example by making comparative studies on similar cells using advanced techniques such as EIS, intensity modulated photovoltage spectroscopy (IMPV), intensity-modulated photocurrent spectroscopy (IMPS), etc. Furthermore, the same principle of integration in the TiO_2 matrix could be applicate to 2D materials, starting from transition metal dichalcogenide (TMD) such as MoS_2. Preliminary results are already showing remarkable results and further exploration of the plethora of 2D materials should bring fascinating results.

It is worth to note that the advancement in solar technology and power conversion efficiency must go together with the progression of storage technologies. In fact, up to now, there is not a satisfactory solution to store efficiently the energy generated by PV. Innovative approaches to storage technologies are needed to compensate for the intermittency of sunlight and allow for development of a full clean-energy system. One of the promising solution is the conversion of solar light in solar fuels, such as hydrogen.

9 BIBLIOGRAPHY

1. P. Friedlingstein, M. W. Jones, M. O'Sullivan, R. M. Andrew, J. Hauck, G. P. Peters, W. Peters, J. Pongratz, S. Sitch and C. Le Quéré, *Earth System Science Data Discussions*, 2019.
2. H. E. Murdock, D. Gibb, T. André, F. Appavou, A. Brown, B. Epp, B. Kondev, A. McCrone, E. Musolino and L. Ranalder, *REN 21, Renewables 2019 Global Status Report*, 2019.
3. G. P. Peters, R. M. Andrew, J. G. Canadell, P. Friedlingstein, R. B. Jackson, J. I. Korsbakken, C. Le Quéré and A. Peregon, *Nature Climate Change*, 2019, DOI: 10.1038/s41558-019-0659-6.
4. C. Figueres, C. Le Quéré, A. Mahindra, O. Bäte, G. Whiteman, G. Peters and D. Guan, *Nature*, 2018, **564**, 27-30.
5. H. R. a. M. Roser, *Our World in Data*, 2019.
6. T. W. Bank, *Journal*, 2019.
7. N. S. Lewis, *Science*, 2016, **351**, aad1920.
8. W. Shockley and H. J. Queisser, *Journal of Applied Physics*, 1961, **32**, 510-519.
9. J. Jean, P. R. Brown, R. L. Jaffe, T. Buonassisi and V. Bulović, *Energy & Environmental Science*, 2015, **8**, 1200-1219.
10. R. Frischknecht, N. Jungbluth, H.-J. Althaus, R. Hischier, G. Doka, C. Bauer, R. Dones, T. Nemecek, S. Hellweg and S. Humbert, *Implementation of life cycle impact assessment methods. Data v2. 0 (2007). Ecoinvent report No. 3*, Ecoinvent Centre, 2007.
11. J. Gong, S. B. Darling and F. You, *Energy & Environmental Science*, 2015, **8**, 1953-1968.
12. N. A. Ludin, N. I. Mustafa, M. M. Hanafiah, M. A. Ibrahim, M. A. M. Teridi, S. Sepeai, A. Zaharim and K. Sopian, *Renewable and Sustainable Energy Reviews*, 2018, **96**, 11-28.
13. M. Pehl, A. Arvesen, F. Humpenöder, A. Popp, E. G. Hertwich and G. Luderer, *Nature Energy*, 2017, **2**, 939.
14. V. Fthenakis, H. Kim, R. Frischknecht, M. Raugei, P. Sinha and M. Stucki, *International Energy Agency (IEA) PVPS Task 12*, 2011.
15. J. Peng, L. Lu and H. Yang, *Renewable and sustainable energy reviews*, 2013, **19**, 255-274.
16. H. L. Raadal, L. Gagnon, I. S. Modahl and O. J. Hanssen, *Renewable and Sustainable Energy Reviews*, 2011, **15**, 3417-3422.
17. R. Turconi, A. Boldrin and T. Astrup, *Renewable and sustainable energy reviews*, 2013, **28**, 555-565.
18. A.-E. Becquerel, *CR Acad. Sci*, 1839, **9**, 145-149.
19. W. Brattain and C. Garrett, *Bell System Technical Journal*, 1955, **34**, 129-176.
20. H. Gerischer, *Journal of the electrochemical society*, 1966, **113**, 1174-1182.
21. A. Fujishima and K. Honda, *Nature*, 1972, **238**, 37.
22. C. Kittel, P. McEuen and P. McEuen, *Introduction to solid state physics*, Wiley New York, 1996.
23. S. M. Sze and K. K. Ng, *Physics of semiconductor devices*, John wiley & sons, 2006.
24. X. Pan, M.-Q. Yang, X. Fu, N. Zhang and Y.-J. Xu, *Nanoscale*, 2013, **5**, 3601-3614.
25. P. T. Landsberg, *Recombination in Semiconductors, by Peter T. Landsberg, pp. 617. ISBN 0521543436. Cambridge, UK: Cambridge University Press, October 2003.*, 2003, 617.

26. A. J. Bard, *Journal of Photochemistry*, 1979, **10**, 59-75.
27. R. Van de Krol and M. Grätzel, *Photoelectrochemical hydrogen production*, Springer, 2012.
28. A. D. McNaught, *Compendium of chemical terminology*.
29. R. A. Marcus, *The Journal of Chemical Physics*, 1956, **24**, 966-978.
30. H. Gerischer, *Photochemistry and Photobiology*, 1972, **16**, 243-260.
31. R. Memming, *Semiconductor electrochemistry*, John Wiley & Sons, 2015.
32. A. J. Nozik and R. Memming, *The Journal of Physical Chemistry*, 1996, **100**, 13061-13078.
33. H. Sato, M. Kawasaki, K. Kasatani, Y. Higuchi, T. Azuma and Y. Nishiyama, *The Journal of Physical Chemistry*, 1988, **92**, 754-759.
34. N. Vlachopoulos, P. Liska, J. Augustynski and M. Graetzel, *Journal of the American Chemical Society*, 1988, **110**, 1216-1220.
35. B. O'Regan and M. Grätzel, *Nature* 1991, **353**, 737-740.
36. M. Grätzel, *J. Photochem. Photobiol., C*, 2003, **4**, 9.
37. K. Lee, S. W. Park, M. J. Ko, K. Kim and N.-G. Park, *Nature materials*, 2009, **8**, 665-671.
38. A. Yella, H. W. Lee, H. N. Tsao, C. Y. Yi, A. K. Chandiran, M. K. Nazeeruddin, E. W. G. Diau, C. Y. Yeh, S. M. Zakeeruddin and M. Gratzel, *Science*, 2011, **334**, 629-634.
39. B. E. Hardin, H. J. Snaith and M. D. McGehee, *Nat. Photonics*, 2012, **6**, 162-169.
40. S. Mathew, A. Yella, P. Gao, R. Humphry-Baker, B. F. Curchod, N. Ashari-Astani, I. Tavernelli, U. Rothlisberger, M. K. Nazeeruddin and M. Gratzel, *Nat Chem*, 2014, **6**, 242-247.
41. G. Boschloo and A. Hagfeldt, *Accounts of chemical research*, 2009, **42**, 1819-1826.
42. M. Grätzel, *Inorganic chemistry*, 2005, **44**, 6841-6851.
43. A. Hagfeldt, G. Boschloo, L. Sun, L. Kloo and H. Pettersson, *Chemical reviews*, 2010, **110**, 6595-6663.
44. L. Alibabaei, B. H. Farnum, B. Kalanyan, M. K. Brennaman, M. D. Losego, G. N. Parsons and T. J. Meyer, *Nano letters*, 2014, **14**, 3255-3261.
45. S. Chappel, L. Grinis, A. Ofir and A. Zaban, *The Journal of Physical Chemistry B*, 2005, **109**, 1643-1647.
46. A. B. F. Martinson, J. W. Elam, J. Liu, M. J. Pellin, T. J. Marks and J. T. Hupp, *Nano letters*, 2008, **8**, 2862-2866.
47. X. Feng, K. Zhu, A. J. Frank, C. A. Grimes and T. E. Mallouk, *Angewandte Chemie International Edition*, 2012, **51**, 2727-2730.
48. E. Hendry, M. Koeberg, B. O'Regan and M. Bonn, *Nano letters*, 2006, **6**, 755-759.
49. K. Zhu, N. R. Neale, A. Miedaner and A. J. Frank, *Nano letters*, 2007, **7**, 69-74.
50. S. Lee, I. J. Park, D. H. Kim, W. M. Seong, D. W. Kim, G. S. Han, J. Y. Kim, H. S. Jung and K. S. Hong, *Energy & Environmental Science*, 2012, **5**, 7989-7995.
51. K. Zhu, T. B. Vinzant, N. R. Neale and A. J. Frank, *Nano letters*, 2007, **7**, 3739-3746.
52. J. Liu, X. Sheng, F. Guan, K. Li, D. Wang, L. Chen and X. Feng, *Chemical science*, 2018, **9**, 7400-7404.
53. W.-Q. Wu, H.-L. Feng, H.-S. Rao, Y.-F. Xu, D.-B. Kuang and C.-Y. Su, *Nature communications*, 2014, **5**, 3968.
54. J. Jiu, S. Isoda, F. Wang and M. Adachi, *The Journal of Physical Chemistry B*, 2006, **110**, 2087-2092.

55. S. So, I. Hwang, J. Yoo, S. Mohajernia, M. Mačković, E. Spiecker, G. Cha, A. Mazare and P. Schmuki, *Advanced Energy Materials*, 2018, **8**, 1800981.
56. E. J. W. Crossland, N. Noel, V. Sivaram, T. Leijtens, J. A. Alexander-Webber and H. J. Snaith, *Nature*, 2013, **495**, 215-219.
57. A. Zaban, S. Chen, S. Chappel and B. Gregg, *Chemical communications*, 2000, 2231-2232.
58. E. Barea, X. Xu, V. González-Pedro, T. Ripollés-Sanchis, F. Fabregat-Santiago and J. Bisquert, *Energy & Environmental Science*, 2011, **4**, 3414-3419.
59. M. K. Nazeeruddin, A. Kay, I. Rodicio, R. Humphry-Baker, E. Müller, P. Liska, N. Vlachopoulos and M. Grätzel, *Journal of the American Chemical Society*, 1993, **115**, 6382-6390.
60. B. C. O'Regan, J. R. Durrant, P. M. Sommeling and N. J. Bakker, *The Journal of Physical Chemistry C*, 2007, **111**, 14001-14010.
61. P. M. Sommeling, B. C. O'Regan, R. R. Haswell, H. J. P. Smit, N. J. Bakker, J. J. T. Smits, J. M. Kroon and J. A. M. van Roosmalen, *The Journal of Physical Chemistry B*, 2006, **110**, 19191-19197.
62. S. Ito, P. Liska, P. Comte, R. Charvet, P. Péchy, U. Bach, L. Schmidt-Mende, S. M. Zakeeruddin, A. Kay and M. K. Nazeeruddin, *Chemical communications*, 2005, 4351-4353.
63. A. Burke, S. Ito, H. Snaith, U. Bach, J. Kwiatkowski and M. Grätzel, *Nano letters*, 2008, **8**, 977-981.
64. P. J. Cameron, Peter, L. M., & Hore, S. , *The Journal of Physical Chemistry. B*, 2005, **109**, 930-9366.
65. M. S. Góes, E. Joanni, E. C. Muniz, R. Savu, T. R. Habeck, P. R. Bueno and F. Fabregat-Santiago, *The Journal of Physical Chemistry C*, 2012, **116**, 12415-12421.
66. Y. Cao, Y. Liu, S. M. Zakeeruddin, A. Hagfeldt and M. Grätzel, *Joule*, 2018, **2**, 1108-1117.
67. V. Georgakilas, J. A. Perman, J. Tucek and R. Zboril, *Chemical reviews*, 2015, **115**, 4744-4822.
68. S.-R. Jang, R. Vittal and K.-J. Kim, *Langmuir : the ACS journal of surfaces and colloids*, 2004, **20**, 9807-9810.
69. P. Brown, K. Takechi and P. Kamat, *The Journal of Physical Chemistry C*, 2008, **112**, 4776-4782.
70. K. T. Dembele, G. S. Selopal, C. Soldano, R. Nechache, J. C. Rimada, I. Concina, G. Sberveglieri, F. Rosei and A. Vomiero, *Journal of Physical Chemistry C*, 2013, **117**, 14510−14517.
71. T. Sawatsuk, A. Chindaduang, C. Sae-Kung, S. Pratontep and G. Tumcharern, *Diamond and Related Materials*, 2009, **18**, 524-527.
72. J. Chen, B. Li, J. Zheng, J. Zhao and Z. Zhu, *The Journal of Physical Chemistry C*, 2012, **116**, 14848-14856.
73. K. T. Dembele, G. S. Selopal, R. Milan, C. Trudeau, D. Benetti, A. Soudi, M. M. Natile, G. Sberveglieri, S. Cloutier and I. Concina, *Journal of Materials Chemistry A*, 2015, **3**, 2580-2588.
74. T. Chen, W. Hu, J. Song, G. H. Guai and C. M. Li, *Advanced Functional Materials*, 2012, **22**, 5245-5250.
75. B. Tang and G. Hu, *Journal of Power Sources*, 2012, **220**, 95-102.
76. R. Vogel, K. Pohl and H. Weller, *Chemical Physics Letters*, 1990, **174**, 241-246.

77. E. M. Sanehira, A. R. Marshall, J. A. Christians, S. P. Harvey, P. N. Ciesielski, L. M. Wheeler, P. Schulz, L. Y. Lin, M. C. Beard and J. M. Luther, *Science Advances*, 2017, **3**, eaao4204.
78. A. Braga, S. Giménez, I. Concina, A. Vomiero and I. Mora-Seró, *The Journal of Physical Chemistry Letters*, 2011, **2**, 454-460.
79. I. Concina, C. Manzoni, G. Grancini, M. Celikin, A. Soudi, F. Rosei, M. Zavelani-Rossi, G. Cerullo and A. Vomiero, *The Journal of Physical Chemistry Letters*, 2015, **6**, 2489-2495.
80. Q. Dai, Y. Wang, X. Li, Y. Zhang, D. J. Pellegrino, M. Zhao, B. Zou, J. Seo, Y. Wang and W. W. Yu, *ACS Nano*, 2009, **3**, 1518-1524.
81. I. Moreels, K. Lambert, D. Smeets, D. De Muynck, T. Nollet, J. C. Martins, F. Vanhaecke, A. Vantomme, C. Delerue, G. Allan and Z. Hens, *ACS Nano*, 2009, **3**, 3023-3030.
82. H. Zhao, Z. Fan, H. Liang, G. Selopal, B. Gonfa, L. Jin, A. Soudi, D. Cui, F. Enrichi and M. Natile, *Nanoscale*, 2014, **6**, 7004-7011.
83. A. P. Alivisatos, *Science*, 1996, **271**, 933-937.
84. J. Tian and G. Cao, *The journal of physical chemistry letters*, 2015, **6**, 1859-1869.
85. D. V. Talapin, J. S. Lee, M. V. Kovalenko and E. V. Shevchenko, *Chemical reviews*, 2010, **110**, 389-458.
86. Y. Yin and A. P. Alivisatos, *Nature*, 2005, **437**, 664-670.
87. L. Jin, H. Zhao, D. Ma, A. Vomiero and F. Rosei, *Journal of Materials Chemistry A*, 2015, **3**, 847-856.
88. A. Salant, M. Shalom, I. Hod, A. Faust, A. Zaban and U. Banin, *Acs Nano*, 2010, **4**, 5962-5968.
89. H. Lee, M. Wang, P. Chen, D. R. Gamelin, S. M. Zakeeruddin, M. Grätzel and M. K. Nazeeruddin, *Nano letters*, 2009, **9**, 4221-4227.
90. P. K. Santra and P. V. Kamat, *Journal of the American Chemical Society*, 2012, **134**, 2508-2511.
91. H. Zhu and T. Lian, *Energy & Environmental Science*, 2012, **5**, 9406-9418.
92. N. D. Bronstein, L. Li, L. Xu, Y. Yao, V. E. Ferry, a. P. Alivisatos and R. G. Nuzzo, *ACS Nano*, 2014, **8**, 44-53.
93. F. Meinardi, A. Colombo, K. A. Velizhanin, R. Simonutti, M. Lorenzon, L. Beverina, R. Viswanatha, V. I. Klimov and S. Brovelli, *Nature Photonics*, 2014, **8**, 392-399.
94. F. García-Santamaría, Y. Chen, J. Vela, R. D. Schaller, J. A. Hollingsworth and V. I. Klimov, *Nano Lett.*, 2009, **9**, 3482-3488.
95. H. Zhao, M. Chaker, N. Wu and D. Ma, *J. Mater. Chem.*, 2011, **21**, 8898-8904.
96. S. Jiao, Q. Shen, I. Mora-Seró, J. Wang, Z. Pan, K. Zhao, Y. Kuga, X. Zhong and J. Bisquert, *ACS Nano*, 2015, **9**, 908-915.
97. K. Zhao, Z. Pan and X. Zhong, *The Journal of Physical Chemistry Letters*, 2016, **7**, 406-417.
98. H. McDaniel, N. Fuke, N. S. Makarov, J. M. Pietryga and V. I. Klimov, *Nature communications*, 2013, **4**, 2887.
99. J. Yang, J. Wang, K. Zhao, T. Izuishi, Y. Li, Q. Shen and X. Zhong, *The Journal of Physical Chemistry C*, 2015, **119**, 28800-28808.
100. Z. Pan, I. n. Mora-Seró, Q. Shen, H. Zhang, Y. Li, K. Zhao, J. Wang, X. Zhong and J. Bisquert, *Journal of the American Chemical Society*, 2014, **136**, 9203-9210.

101. Y. Chen, J. Vela, H. Htoon, J. L. Casson, D. J. Werder, D. A. Bussian, V. I. Klimov and J. A. Hollingsworth, *Journal of the American Chemical Society*, 2008, **130**, 5026-5027.
102. Y.-S. Park, J. Lim, N. S. Makarov and V. I. Klimov, *Nano letters*, 2017, **17**, 5607-5613.
103. G. S. Selopal, H. Zhao, X. Tong, D. Benetti, F. Navarro-Pardo, Y. Zhou, D. Barba, F. Vidal, Z. M. Wang and F. Rosei, *Advanced Functional Materials*, 2017, **27**, 1701468.
104. Z. Du, Z. Pan, F. Fabregat-Santiago, K. Zhao, D. Long, H. Zhang, Y. Zhao, X. Zhong, J.-S. Yu and J. Bisquert, *The journal of physical chemistry letters*, 2016, **7**, 3103-3111.
105. Z. Pan, L. Yue, H. Rao, J. Zhang, X. Zhong, Z. Zhu and A. K. Y. Jen, *Advanced materials*, 2019, 1903696.
106. J. Du, Z. Du, J.-S. Hu, Z. Pan, Q. Shen, J. Sun, D. Long, H. Dong, L. Sun and X. Zhong, *Journal of the American Chemical Society*, 2016, **138**, 4201-4209.
107. X.-F. Gao, H.-B. Li, W.-T. Sun, Q. Chen, F.-Q. Tang and L.-M. Peng, *The Journal of Physical Chemistry C*, 2009, **113**, 7531-7535.
108. D. R. Baker and P. V. Kamat, *Advanced Functional Materials*, 2009, **19**, 805-811.
109. P. Sudhagar, T. Song, D. H. Lee, I. Mora-Seró, J. Bisquert, M. Laudenslager, W. M. Sigmund, W. I. Park, U. Paik and Y. S. Kang, *The Journal of Physical Chemistry Letters*, 2011, **2**, 1984-1990.
110. J. H. Bang and P. V. Kamat, *Advanced Functional Materials*, 2010, **20**, 1970-1976.
111. A. Kongkanand, K. Tvrdy, K. Takechi, M. Kuno and P. V. Kamat, *Journal of the American Chemical Society*, 2008, **130**, 4007-4015.
112. H.-L. Feng, W.-Q. Wu, H.-S. Rao, L.-B. Li, D.-B. Kuang and C.-Y. Su, *Journal of Materials Chemistry A*, 2015, **3**, 14826-14832.
113. Y.-F. Xu, W.-Q. Wu, H.-S. Rao, H.-Y. Chen, D.-B. Kuang and C.-Y. Su, *Nano Energy*, 2015, **11**, 621-630.
114. J. Tian, Q. Zhang, E. Uchaker, Z. Liang, R. Gao, X. Qu, S. Zhang and G. Cao, *Journal of Materials Chemistry A*, 2013, **1**, 6770-6775.
115. S.-m. Yang, C.-h. Huang, J. Zhai, Z.-s. Wang and L. Jiang, *Journal of Materials Chemistry*, 2002, **12**, 1459-1464.
116. L. J. Diguna, Q. Shen, J. Kobayashi and T. Toyoda, *Applied Physics Letters*, 2007, **91**, 023116.
117. Q. Shen, J. Kobayashi, L. J. Diguna and T. Toyoda, *Journal of Applied Physics*, 2008, **103**, 084304.
118. N. Guijarro, J. M. Campiña, Q. Shen, T. Toyoda, T. Lana-Villarreal and R. Gómez, *Physical Chemistry Chemical Physics*, 2011, **13**, 12024-12032.
119. F. Huang, L. Zhang, Q. Zhang, J. Hou, H. Wang, H. Wang, S. Peng, J. Liu and G. Cao, *ACS applied materials & interfaces*, 2016, **8**, 34482-34489.
120. F. Huang, J. Hou, Q. Zhang, Y. Wang, R. C. Massé, S. Peng, H. Wang, J. Liu and G. Cao, *Nano Energy*, 2016, **26**, 114-122.
121. F. Huang, Q. Zhang, B. Xu, J. Hou, Y. Wang, R. C. Massé, S. Peng, J. Liu and G. Cao, *Journal of Materials Chemistry A*, 2016, **4**, 14773-14780.
122. Z. Tachan, I. Hod, M. Shalom, L. Grinis and A. Zaban, *Physical Chemistry Chemical Physics*, 2013, **15**, 3841-3845.
123. K. Zhao, Z. Pan, I. Mora-Seró, E. Cánovas, H. Wang, Y. Song, X. Gong, J. Wang, M. Bonn, J. Bisquert and X. Zhong, *Journal of the American Chemical Society*, 2015, **137**, 5602-5609.

124. Z. Ren, J. Wang, Z. Pan, K. Zhao, H. Zhang, Y. Li, Y. Zhao, I. Mora-Sero, J. Bisquert and X. Zhong, *Chemistry of Materials*, 2015, **27**, 8398-8405.
125. K. E. Roelofs, T. P. Brennan, J. C. Dominguez, C. D. Bailie, G. Y. Margulis, E. T. Hoke, M. D. McGehee and S. F. Bent, *The Journal of Physical Chemistry C*, 2013, **117**, 5584-5592.
126. D. B. Mitzi, C. A. Feild, W. T. A. Harrison and A. M. Guloy, *Nature*, 1994, **369**, 467.
127. H. L. Wells, *Zeitschrift für anorganische Chemie*, 1893, **3**, 195-210.
128. A. Kojima, K. Teshima, Y. Shirai and T. Miyasaka, *Journal of the American Chemical Society*, 2009, **131**, 6050-6051.
129. H.-S. Kim, C.-R. Lee, J.-H. Im, K.-B. Lee, T. Moehl, A. Marchioro, S.-J. Moon, R. Humphry-Baker, J.-H. Yum, J. E. Moser, M. Grätzel and N.-G. Park, *Scientific reports*, 2012, **2**, 591.
130. M. Lee, Teuscher, J., & Miyasaka, T. , *Science*, 2012, **338**, 643-647.
131. W. S. Yang, B.-W. Park, E. H. Jung, N. J. Jeon, Y. C. Kim, D. U. Lee, S. S. Shin, J. Seo, E. K. Kim, J. H. Noh and S. I. Seok, *Science*, 2017, **356**, 1376-1379.
132. National Renewable Energy Laboratory, https://www.nrel.gov/pv/assets/images/effciency-chart.png, (accessed December, 2019).
133. J. M. Ball, M. M. Lee, A. Hey and H. J. Snaith, *Energy & Environmental Science*, 2013, **6**, 1739.
134. M. Grätzel, *Accounts of Chemical Research*, 2017, **50**, 487-491.
135. T. Liu, K. Chen, Q. Hu, R. Zhu and Q. Gong, *Advanced Energy Materials*, 2016, **6**, 1600457.
136. S. S. Shin, W. S. Yang, J. H. Noh, J. H. Suk, N. J. Jeon, J. H. Park, J. S. Kim, W. M. Seong and S. I. Seok, *Nature communications*, 2015, **6**, 7410.
137. Q. Lin, A. Armin, R. C. R. Nagiri, P. L. Burn and P. Meredith, *Nature Photonics*, 2015, **9**, 106.
138. T. S. Sherkar, C. Momblona, L. n. Gil-Escrig, J. Ávila, M. Sessolo, H. J. Bolink and L. J. A. Koster, *ACS energy letters*, 2017, **2**, 1214-1222.
139. G. Xing, N. Mathews, S. Sun, S. S. Lim, Y. M. Lam, M. Grätzel, S. Mhaisalkar and T. C. Sum, *Science*, 2013, **342**, 344-347.
140. S. D. Stranks, V. M. Burlakov, T. Leijtens, J. M. Ball, A. Goriely and H. J. Snaith, *Physical Review Applied*, 2014, **2**, 034007.
141. J.-Y. Jeng, Y.-F. Chiang, M.-H. Lee, S.-R. Peng, T.-F. Guo, P. Chen and T.-C. Wen, *Advanced materials*, 2013, **25**, 3727-3732.
142. Z. Chu, M. Yang, P. Schulz, D. Wu, X. Ma, E. Seifert, L. Sun, X. Li, K. Zhu and K. Lai, *Nature communications*, 2017, **8**, 2230.
143. A.-F. Castro-Méndez, J. Hidalgo and J.-P. Correa-Baena, *Advanced Energy Materials*, 2019, **9**, 1901489.
144. J. S. Yun, A. Ho-Baillie, S. Huang, S. H. Woo, Y. Heo, J. Seidel, F. Huang, Y.-B. Cheng and M. A. Green, *The journal of physical chemistry letters*, 2015, **6**, 875-880.
145. Z. Xiao, C. Bi, Y. Shao, Q. Dong, Q. Wang, Y. Yuan, C. Wang, Y. Gao and J. Huang, *Energy & Environmental Science*, 2014, **7**, 2619-2623.
146. W. Zhang, M. Saliba, D. T. Moore, S. K. Pathak, M. T. Hörantner, T. Stergiopoulos, S. D. Stranks, G. E. Eperon, J. A. Alexander-Webber and A. Abate, *Nature communications*, 2015, **6**, 6142.

147. W. Zhang, S. Pathak, N. Sakai, T. Stergiopoulos, P. K. Nayak, N. K. Noel, A. A. Haghighirad, V. M. Burlakov, D. W. DeQuilettes and A. Sadhanala, *Nature communications*, 2015, **6**, 10030.
148. J. H. Heo, H. J. Han, D. Kim, T. K. Ahn and S. H. Im, *Energy & Environmental Science*, 2015, **8**, 1602-1608.
149. Z. Xiao, Q. Dong, C. Bi, Y. Shao, Y. Yuan and J. Huang, *Advanced materials*, 2014, **26**, 6503-6509.
150. Y. Yu, C. Wang, C. R. Grice, N. Shrestha, D. Zhao, W. Liao, L. Guan, R. A. Awni, W. Meng and A. J. Cimaroli, *ACS Energy Letters*, 2017, **2**, 1177-1182.
151. C.-H. Chiang, M. K. Nazeeruddin, M. Grätzel and C.-G. Wu, *Energy & Environmental Science*, 2017, **10**, 808-817.
152. M. Stolterfoht, C. M. Wolff, J. A. Márquez, S. Zhang, C. J. Hages, D. Rothhardt, S. Albrecht, P. L. Burn, P. Meredith and T. Unold, *Nature Energy*, 2018, **3**, 847.
153. H. Kim, K.-G. Lim and T.-W. Lee, *Energy & Environmental Science*, 2016, **9**, 12-30.
154. F. Fu, T. Feurer, T. P. Weiss, S. Pisoni, E. Avancini, C. Andres, S. Buecheler and A. N. Tiwari, 2016.
155. D. B. Khadka, Y. Shirai, M. Yanagida, J. W. Ryan and K. Miyano, *Journal of Materials Chemistry C*, 2017, **5**, 8819-8827.
156. Z. Liu, L. Krückemeier, B. Krogmeier, B. Klingebiel, J. A. Márquez, S. Levcenko, S. Öz, S. Mathur, U. Rau, T. Unold and T. Kirchartz, *ACS Energy Letters*, 2019, **4**, 110-117.
157. J. Lee, H. Kang, G. Kim, H. Back, J. Kim, S. Hong, B. Park, E. Lee and K. Lee, *Advanced materials*, 2017, **29**, 1606363.
158. F. Zhang, J. Song, R. Hu, Y. Xiang, J. He, Y. Hao, J. Lian, B. Zhang, P. Zeng and J. Qu, *Small*, 2018, **14**, 1704007.
159. C. Bi, Q. Wang, Y. Shao, Y. Yuan, Z. Xiao and J. Huang, *Nature communications*, 2015, **6**, 7747.
160. X. Liu, Y. Cheng, C. Liu, T. Zhang, N. Zhang, S. Zhang, J. Chen, Q. Xu, J. Ouyang and H. Gong, *Energy & Environmental Science*, 2019, **12**, 1622-1633.
161. C. Huang, W. Fu, C.-Z. Li, Z. Zhang, W. Qiu, M. Shi, P. Heremans, A. K.-Y. Jen and H. Chen, *Journal of the American Chemical Society*, 2016, **138**, 2528-2531.
162. J. You, L. Meng, T.-B. Song, T.-F. Guo, Y. Yang, W.-H. Chang, Z. Hong, H. Chen, H. Zhou, Q. Chen, Y. Liu, N. De Marco and Y. Yang, *Nature Nanotechnology*, 2016, **11**, 75-81.
163. J. H. Kim, P. W. Liang, S. T. Williams, N. Cho, C. C. Chueh, M. S. Glaz, D. S. Ginger and A. K. Y. Jen, *Advanced materials*, 2015, **27**, 695-701.
164. Z. Zhu, Y. Bai, T. Zhang, Z. Liu, X. Long, Z. Wei, Z. Wang, L. Zhang, J. Wang and F. Yan, *Angewandte Chemie*, 2014, **126**, 12779-12783.
165. W. Sun, Y. Li, S. Ye, H. Rao, W. Yan, H. Peng, Y. Li, Z. Liu, S. Wang and Z. Chen, *Nanoscale*, 2016, **8**, 10806-10813.
166. S. Ye, W. Sun, Y. Li, W. Yan, H. Peng, Z. Bian, Z. Liu and C. Huang, *Nano letters*, 2015, **15**, 3723-3728.
167. J. A. Christians, R. C. M. Fung and P. V. Kamat, *Journal of the American Chemical Society*, 2014, **136**, 758-764.
168. Q. Wang, C. C. Chueh, T. Zhao, J. Cheng, M. Eslamian, W. C. Choy and A. K. Y. Jen, *ChemSusChem*, 2017, **10**, 3794-3803.

169. J. Liu, S. K. Pathak, N. Sakai, R. Sheng, S. Bai, Z. Wang and H. J. Snaith, *Advanced Materials Interfaces*, 2016, **3**, 1600571.
170. J. W. Jung, C. C. Chueh and A. K. Y. Jen, *Advanced materials*, 2015, **27**, 7874-7880.
171. W. Chen, F. Z. Liu, X. Y. Feng, A. B. Djurišić, W. K. Chan and Z. B. He, *Advanced Energy Materials*, 2017, **7**, 1700722.
172. Z. Wu, S. Bai, J. Xiang, Z. Yuan, Y. Yang, W. Cui, X. Gao, Z. Liu, Y. Jin and B. Sun, *Nanoscale*, 2014, **6**, 10505-10510.
173. I. Jung, D. A. Dikin, R. D. Piner and R. S. Ruoff, *Nano letters*, 2008, **8**, 4283-4287.
174. C. K. Chua and M. Pumera, *Chemical Society reviews*, 2014, **43**, 291-312.
175. J.-S. Yeo, R. Kang, S. Lee, Y.-J. Jeon, N. Myoung, C.-L. Lee, D.-Y. Kim, J.-M. Yun, Y.-H. Seo and S.-S. Kim, *Nano Energy*, 2015, **12**, 96-104.
176. E. Jokar, Z. Y. Huang, S. Narra, C. Y. Wang, V. Kattoor, C. C. Chung and E. W. G. Diau, *Advanced Energy Materials*, 2018, **8**, 1701640.
177. M. Grätzel, *Nature*, 2001, **414**, 338.
178. B. Liu and E. S. Aydil, *Journal of the American Chemical Society*, 2009, **131**, 3985-3990.
179. S. H. Kang, S. H. Choi, M. S. Kang, J. Y. Kim, H. S. Kim, T. Hyeon and Y. E. Sung, *Advanced materials*, 2008, **20**, 54-58.
180. J. B. Baxter and E. S. Aydil, *Applied Physics Letters*, 2005, **86**, -.
181. S. Gubbala, V. Chakrapani, V. Kumar and M. K. Sunkara, *Advanced Functional Materials*, 2008, **18**, 2411-2418.
182. X. Feng, K. Shankar, O. K. Varghese, M. Paulose, T. J. Latempa and C. A. Grimes, *Nano letters*, 2008, **8**, 3781-3786.
183. A. Vomiero, V. Galstyan, A. Braga, I. Concina, M. Brisotto, E. Bontempi and G. Sberveglieri, *Energy & Environmental Science*, 2011, **4**, 3408-3413.
184. O. K. Varghese, M. Paulose and C. A. Grimes, *Nature Nanotechnology*, 2009, **4**, 592-597.
185. V. Galstyan, A. Vomiero, I. Concina, A. Braga, M. Brisotto, E. Bontempi, G. Faglia and G. Sberveglieri, *Small*, 2011, **7**, 2437-2442.
186. G. K. Mor, K. Shankar, M. Paulose, O. K. Varghese and C. A. Grimes, *Nano letters*, 2006, **6**, 215-218.
187. S. Iijima, *Nature*, 1991, **354**.
188. H. Zhu, J. Wei, K. Wang and D. Wu, *Solar Energy Materials and Solar Cells*, 2009, **93**, 1461-1470.
189. J. Wilder, L. Venema and A. Rinzler, *Nature*, 1998, **584**, 1996-1999.
190. C. Y. Yen, Y. F. Lin, S. H. Liao, C. C. Weng, C. C. Huang, Y. H. Hsiao, C. C. M. Ma, M. C. Chang, H. Shao, M. C. Tsai, C. K. Hsieh, C. H. Tsai and F. B. Weng, *Nanotechnology*, 2008, **19**, 375305.
191. Y. F. Chan, C. C. Wang, B. H. Chen and C. Y. Chen, *Progress in Photovoltaics: Research and Applications*, 2013, **21**, 47-57.
192. K. T. Dembele, G. S. Selopal, R. Milan, C. Trudeau, D. Benetti, A. Soudi, M. M. Natile, G. Sberveglieri, S. Cloutier, I. Concina, F. Rosei and A. Vomiero, *Journal of Materials Chemistry A*, 2015, **3**, 2580-2588.
193. N. Yang, J. Zhai, D. Wang, Y. Chen and L. Jiang, *Acs Nano*, 2010, **4**, 887-894.
194. J. Durantini, P. P. Boix, M. Gervaldo, G. M. Morales, L. Otero, J. Bisquert and E. M. Barea, *Journal of Electroanalytical Chemistry*, 2012, **683**, 43-46.
195. T. C. A. Jitianu, R. Benoit, S. Delpeux, F. B eguin, S. Bonnamy, *Carbon*, 2004, **42**, 5.

196. I. C. L. S. A.G. Osorio, V.L. Bueno, C.P. Bergmann, *Applied Surface Science*, 2008, **255**, 5.
197. S. Costa, E. Borowiak-Palen and A. Bachmatiuk, *Materials Science-Poland*, 2008, **26**, 433-441.
198. E. Flahaut, C. Laurent and A. Peigney, *Carbon*, 2005, **43**, 375-383.
199. J. Wang, Y. Lin, M. Pinault, A. Filoramo, M. Fabert, B. Ratier, J. Bouclé and N. Herlin-Boime, *ACS applied materials & interfaces*, 2015, **7**, 51-56.
200. S. P. S. Porto, P. A. Fleury and T. C. Damen, *Phys. Rev.*, 1967, **154**, 522-526.
201. C. Y. Yen, Y. F. Lin, C. H. Hung, Y. H. Tseng, C. C. Ma, M. C. Chang and H. Shao, *Nanotechnology*, 2008, **19**, 045604.
202. M. Grätzel, *Pure and Applied Chemistry*, 2001, **73**, 459-467.
203. K. T. Dembele, R. Nechache, L. Nikolova, A. Vomiero, C. Santato, S. Licoccia and F. Rosei, *Journal of Power Sources*, 2013, **233**, 93-97.
204. S. R. Raga, E. M. Barea and F. Fabregat-Santiago, *Journal of Physical Chemistry Letters*, 2012, **3**, 1629-1634.
205. Y.-B. Tang, C.-S. Lee, J. Xu, Z.-T. Liu, Z.-H. Chen, Z. He, Y.-L. Cao, G. Yuan, H. Song, L. Chen, L. Luo, H.-M. Cheng, W.-J. Zhang, I. Bello and S.-T. Lee, *Acs Nano*, 2010, **4**, 3482-3488.
206. P. Brown, K. Takechi and P. Kamat, *J. Phys. Chem. C*, 2008, **112**, 4776-4782.
207. M.-Y. Yen, M.-C. Hsiao, S.-H. Liao, P.-I. Liu, H.-M. Tsai, C.-C. M. Ma, N.-W. Pu and M.-D. Ger, *Carbon*, 2011, **49**, 10.
208. F. Fabregat-Santiago, *The Journal of Physical Chemistry C*, 2007, **2**, 6550-6560.
209. J. Bisquert, I. Mora-Sero and F. Fabregat-Santiago, *ChemElectroChem*, 2014, **1**, 289-296.
210. F. Fabregat-Santiago, J. Bisquert, G. Garcia-Belmonte, G. Boschloo and A. Hagfeldt, *Solar Energy Materials and Solar Cells*, 2005, **87**, 117-131.
211. M. Adachi, M. Sakamoto, J. Jiu, Y. Ogata and S. Isoda, *The journal of Physical Chemistry B*, 2006, **110**, 13872-13880.
212. L. M. Peter, N. W. Duffy, R. L. Wang and K. G. U. Wijayantha, *Journal of Electroanalytical Chemistry*, 2002, **524-525**, 127-136.
213. H. Wang, J. He and G. Boschloo, *The journal of Physical Chemistry B*, 2001, 2529-2533.
214. I. Mora-Sero and J. Bisquert, *Nano letters*, 2003, **3**, 945-949.
215. F. M. P. Kubelka, *Z. Tech. Physik*, 1931, **12**, 593-601.
216. G. Kortüm, *Reflectance Spectroscopy*, Springer, New York, 1969.
217. G. Calogero, P. Calandra, A. Irrera, A. Sinopoli, I. Citro and G. Di Marco, *Energy Environ. Sci.*, 2011, **4**, 1838-1844.
218. R. Zhou, W. Guo, R. Yu and C. Pan, *J. Mater. Chem. A*, 2015, **3**, 23028-23034.
219. V.-D. Dao, S.-H. Kim, H.-S. Choi, J.-H. Kim, H.-O. Park and J.-K. Lee, *The Journal of Physical Chemistry C*, 2011, **115**, 25529-25534.
220. D. J. Kim, J. K. Koh, C. S. Lee and J. H. Kim, *Adv. Energy Mater.*, 2014, **4**, n/a-n/a.
221. Y. Hu, A. Yella, S. Guldin, M. Schreier, F. Stellacci, M. Grätzel and M. Stefik, *Advanced Energy Materials*, 2014, **4**, 1400510.
222. F. Gong, H. Wang, X. Xu, G. Zhou and Z.-S. Wang, *Journal of the American Chemical Society*, 2012, **134**, 10953-10958.
223. J. Han, H. Kim, D. Y. Kim, S. M. Jo and S.-Y. Jang, *ACS Nano*, 2010, **4**, 3503-3509.
224. Y. Duan, Q. Tang, J. Liu, B. He and L. Yu, *Angewandte Chemie International Edition*, 2014, **53**, 14569-14574.

225. Y. Li, Q. Tang, L. Yu, X. Yan and L. Dong, *Journal of Power Sources*, 2016, **305**, 217-224.
226. Q. Tang, H. Zhang, Y. Meng, B. He and L. Yu, *Angewandte Chemie International Edition*, 2015, **54**, 11448-11452.
227. J. Wang, Q. Tang, B. He and P. Yang, *Journal of Power Sources*, 2016, **328**, 185-194.
228. Q. Yang, P. Yang, J. Duan, X. Wang, L. Wang, Z. Wang and Q. Tang, *Electrochimica Acta*, 2016, **190**, 85-91.
229. R. Zhou, W. Guo, R. Yu and C. Pan, *Journal of Materials Chemistry A*, 2015, **3**, 23028-23034.
230. J. Kim, J. Kang, U. Jeong, H. Kim and H. Lee, *ACS applied materials & interfaces*, 2013, **5**, 3176-3181.
231. H. Wu, D. Kong, Z. Ruan, P.-C. Hsu, S. Wang, Z. Yu, T. J. Carney, L. Hu, S. Fan and Y. Cui, *Nature nanotechnology*, 2013, **8**, 421.
232. C.-C. Wang, J.-G. Chen, K.-C. Huang, H.-W. Chen, Y.-C. Wang, C.-Y. Hsu, R. Vittal, J.-J. Lin and K.-C. Ho, *Journal of Power Sources*, 2013, **239**, 496-499.
233. X. Fang, T. Ma, G. Guan, M. Akiyama, T. Kida and E. Abe, *Journal of Electroanalytical Chemistry*, 2004, **570**, 257-263.
234. J. Bisquert, A. Zaban and P. Salvador, *The Journal of Physical Chemistry B*, 2002, **106**, 8774-8782.
235. I. Montanari, J. Nelson and J. R. Durrant, *The Journal of Physical Chemistry B*, 2002, **106**, 12203-12210.
236. A. Zaban, M. Greenshtein and J. Bisquert, *Chemphyschem : a European journal of chemical physics and physical chemistry*, 2003, **4**, 859-864.
237. S. Huang, G. Schlichthörl, A. Nozik, M. Grätzel and A. Frank, *The Journal of Physical Chemistry B*, 1997, **101**, 2576-2582.
238. W.-Y. Lee, V.-D. Dao and H.-S. Choi, *RSC Advances*, 2016, **6**, 38310-38314.
239. A. Hauch and A. Georg, *Electrochimica acta*, 2001, **46**, 3457-3466.
240. Q. Wang, J.-E. Moser and M. Grätzel, *The Journal of Physical Chemistry B*, 2005, **109**, 14945-14953.
241. M. Adachi, M. Sakamoto, J. Jiu, Y. Ogata and S. Isoda, *The Journal of Physical Chemistry B*, 2006, **110**, 13872-13880.
242. M. Wang, A. M. Anghel, B. Marsan, N.-L. Cevey Ha, N. Pootrakulchote, S. M. Zakeeruddin and M. Grätzel, *Journal of the American Chemical Society*, 2009, **131**, 15976-15977.
243. F. Rosei, *Journal of Physics: Condensed Matter*, 2004, **16**, S1373.
244. Q. Zhang, E. Uchaker, S. L. Candelaria and G. Cao, *Chemical Society reviews*, 2013, **42**, 3127-3171.
245. L.-s. Li, J. Hu, W. Yang and A. P. Alivisatos, *Nano letters*, 2001, **1**, 349-351.
246. D. J. Norris and M. G. Bawendi, *Physical Review B*, 1996, **53**, 16338-16346.
247. I. Concina, Z. H. Ibupoto and A. Vomiero, *Advanced Energy Materials*, 2017, **7**, 1700706.
248. R. J. Ellingson, M. C. Beard, J. C. Johnson, P. Yu, O. I. Micic, A. J. Nozik, A. Shabaev and A. L. Efros, *Nano letters*, 2005, **5**, 865-871.
249. S. Ruhle, M. Shalom and A. Zaban, *Chemphyschem : a European journal of chemical physics and physical chemistry*, 2010, **11**, 2290-2304.
250. J. M. Caruge, J. E. Halpert, V. Wood, V. Bulovic and M. G. Bawendi, *Nat Photon*, 2008, **2**, 247-250.

251. H. M. Chen, C. K. Chen, Y. C. Chang, C. W. Tsai, R. S. Liu, S. F. Hu, W. S. Chang and K. H. Chen, *Angewandte Chemie*, 2010, **122**, 6102-6105.
252. L. Jin, B. AlOtaibi, D. Benetti, S. Li, H. Zhao, Z. Mi, A. Vomiero and F. Rosei, *Advanced Science*, 2016, **3**, 1500345.
253. C.-H. M. Chuang, P. R. Brown, V. Bulović and M. G. Bawendi, *Nature materials*, 2014, **13**, 796-801.
254. I. Mora-Seró, S. Giménez, F. Fabregat-Santiago, R. Gómez, Q. Shen, T. Toyoda and J. Bisquert, *Accounts of Chemical Research*, 2009, **42**, 1848-1857.
255. Z. Yufeng, B. Daniele, F. Zhiyuan, Z. Haiguang, M. Dongling, G. A. O., V. Alberto and R. Federico, *Advanced Energy Materials*, 2016, **6**, 1501913.
256. S. A. McDonald, G. Konstantatos, S. Zhang, P. W. Cyr, E. J. Klem, L. Levina and E. H. Sargent, *Nature materials*, 2005, **4**, 138.
257. B.-R. Hyun, Y.-W. Zhong, A. C. Bartnik, L. Sun, H. D. Abruna, F. W. Wise, J. D. Goodreau, J. R. Matthews, T. M. Leslie and N. F. Borrelli, *ACS nano*, 2008, **2**, 2206-2212.
258. W. A. Tisdale, K. J. Williams, B. A. Timp, D. J. Norris, E. S. Aydil and X.-Y. Zhu, *Science*, 2010, **328**, 1543-1547.
259. B.-R. Hyun, A. C. Bartnik, L. Sun, T. Hanrath and F. W. Wise, *Nano letters*, 2011, **11**, 2126-2132.
260. B. Alperson, I. Rubinstein, G. Hodes, D. Porath and O. Millo, *Applied physics letters*, 1999, **75**, 1751-1753.
261. U. Banin, Y. Cao, D. Katz and O. Millo, *Nature*, 1999, **400**, 542-544.
262. W. Wu, J. R. Tucker, G. S. Solomon and J. S. Harris Jr, *Applied physics letters*, 1997, **71**, 1083-1085.
263. A. Liscio, V. Palermo and P. Samorì, *Accounts of chemical research*, 2010, **43**, 541-550.
264. Y. Rosenwaks, R. Shikler, T. Glatzel and S. Sadewasser, *Physical Review B*, 2004, **70**, 085320.
265. E. M. Tennyson, C. Gong and M. S. Leite, *ACS Energy Letters*, 2017, **2**, 2761-2777.
266. V. Palermo, M. Palma and P. Samorì, *Advanced materials*, 2006, **18**, 145-164.
267. H. Jacobs, P. Leuchtmann, O. Homan and A. Stemmer, *Journal of applied physics*, 1998, **84**, 1168-1173.
268. S. Shusterman, A. Raizman, A. Sher, Y. Paltiel, A. Schwarzman, E. Lepkifker and Y. Rosenwaks, *Nano letters*, 2007, **7**, 2089-2093.
269. W. Melitz, J. Shen, A. C. Kummel and S. Lee, *Surface science reports*, 2011, **66**, 1-27.
270. Y. Zhang, O. Pluchery, L. Caillard, A. F. Lamic-Humblot, S. Casale, Y. J. Chabal and M. Salmeron, *Nano letters*, 2015, **15**, 51-55.
271. Y. Zhang, D. Zherebetskyy, N. D. Bronstein, S. Barja, L. Lichtenstein, D. Schuppisser, L. W. Wang, A. P. Alivisatos and M. Salmeron, *Nano letters*, 2015, **15**, 3249-3253.
272. E. M. Miller, D. M. Kroupa, J. Zhang, P. Schulz, A. R. Marshall, A. Kahn, S. Lany, J. M. Luther, M. C. Beard, C. L. Perkins and J. van de Lagemaat, *ACS Nano*, 2016, **10**, 3302-3311.
273. I. Kang and F. W. Wise, *J. Opt. Soc. Am. B*, 1997, **14**, 1632-1646.
274. D. Schooss, A. Mews, A. Eychmüller and H. Weller, *Physical Review B*, 1994, **49**, 17072.
275. F. Fabregat-Santiago, G. Garcia-Belmonte, J. Bisquert, P. Bogdanoff and A. Zaban, *Journal of The Electrochemical Society*, 2003, **150**, E293-E298.
276. Y.-L. Lee, C.-F. Chi and S.-Y. Liau, *Chemistry of Materials*, 2010, **22**, 922-927.

277. J. Gao, J. M. Luther, O. E. Semonin, R. J. Ellingson, A. J. Nozik and M. C. Beard, *Nano letters*, 2011, **11**, 1002-1008.
278. P. Y. Yu and M. Cardona, *Fundamentals of semiconductors: physics and materials properties*, Springer, 2010.
279. A. Liscio, V. Palermo, K. Müllen and P. Samorì, *The Journal of Physical Chemistry C*, 2008, **112**, 17368-17377.
280. M. Gratzel, *Nature*, 2001, **414**, 338-344.
281. Y.-J. Yu, Y. Zhao, S. Ryu, L. E. Brus, K. S. Kim and P. Kim, *Nano letters*, 2009, **9**, 3430-3434.
282. M. Auffan, J. Rose, J.-Y. Bottero, G. V. Lowry, J.-P. Jolivet and M. R. Wiesner, *Nat Nano*, 2009, **4**, 634-641.
283. S. Y. Lim, W. Shen and Z. Gao, *Chemical Society reviews*, 2015, **44**, 362-381.
284. H. Li, W. Shi, W. Huang, E.-P. Yao, J. Han, Z. Chen, S. Liu, Y. Shen, M. Wang and Y. Yang, *Nano letters*, 2017, **17**, 2328-2335.
285. Z. Jia, Y. Yue, L. Gaolin and Y. Shu-Hong, *Advanced Science*, 2015, **2**, 1500002.
286. C.-C. Chung, S. Narra, E. Jokar, H.-P. Wu and E. Wei-Guang Diau, *Journal of Materials Chemistry A*, 2017, **5**, 13957-13965.
287. E. Jokar, Z. Y. Huang, S. Narra, C.-Y. Wang, V. Kattoor, C.-C. Chung and E. W.-G. Diau, *Advanced Energy Materials*, 2018, **8**, 1701640.
288. Y. Rong, L. Liu, A. Mei, X. Li and H. Han, *Advanced Energy Materials*, 2015, **5**, 1501066-n/a.
289. W. Li, W. Zhang, S. Van Reenen, R. J. Sutton, J. Fan, A. A. Haghighirad, M. B. Johnston, L. Wang and H. J. Snaith, *Energy & Environmental Science*, 2016, **9**, 490-498.
290. Y. Zhou, D. Benetti, X. Tong, L. Jin, Z. M. Wang, D. Ma, H. Zhao and F. Rosei, *Nano Energy*, 2018, **44**, 378-387.
291. A. Privitera, M. Righetto, D. Mosconi, F. Lorandi, A. A. Isse, A. Moretto, R. Bozio, C. Ferrante and L. Franco, *Physical Chemistry Chemical Physics*, 2016, **18**, 31286-31295.
292. M. Fu, F. Ehrat, Y. Wang, K. Z. Milowska, C. Reckmeier, A. L. Rogach, J. K. Stolarczyk, A. S. Urban and J. Feldmann, *Nano letters*, 2015, **15**, 6030-6035.
293. H. Ding, J.-S. Wei, N. Zhong, Q.-Y. Gao and H.-M. Xiong, *Langmuir : the ACS journal of surfaces and colloids*, 2017, **33**, 12635-12642.
294. X. Dong, Y. Su, H. Geng, Z. Li, C. Yang, X. Li and Y. Zhang, *Journal of Materials Chemistry C*, 2014, **2**, 7477-7481.
295. P. Yu, X. Wen, Y.-R. Toh, Y.-C. Lee, K.-Y. Huang, S. Huang, S. Shrestha, G. Conibeer and J. Tang, *Journal of Materials Chemistry C*, 2014, **2**, 2894-2901.
296. Z. Yu and L. Sun, *Advanced Energy Materials*, 2015, **5**, 1500213.
297. A. Poglitsch and D. Weber, *The Journal of chemical physics*, 1987, **87**, 6373-6378.
298. P. Whitfield, N. Herron, W. Guise, K. Page, Y. Cheng, I. Milas and M. Crawford, *Scientific reports*, 2016, **6**, 35685.
299. D. Shi, V. Adinolfi, R. Comin, M. Yuan, E. Alarousu, A. Buin, Y. Chen, S. Hoogland, A. Rothenberger, K. Katsiev, Y. Losovyj, X. Zhang, P. A. Dowben, O. F. Mohammed, E. H. Sargent and O. M. Bakr, *Science*, 2015, **347**, 519-522.
300. N. F. Montcada, J. M. Marín-Beloqui, W. Cambarau, J. Jiménez-López, L. Cabau, K. T. Cho, M. K. Nazeeruddin and E. Palomares, *ACS Energy Letters*, 2017, **2**, 182-187.

301. A. Guerrero, G. Garcia-Belmonte, I. Mora-Sero, J. Bisquert, Y. S. Kang, T. J. Jacobsson, J.-P. Correa-Baena and A. Hagfeldt, *The Journal of Physical Chemistry C*, 2016, **120**, 8023-8032.
302. A. Pockett, G. E. Eperon, T. Peltola, H. J. Snaith, A. Walker, L. M. Peter and P. J. Cameron, *The Journal of Physical Chemistry C*, 2015, **119**, 3456-3465.
303. E. Jokar, Z. Y. Huang, S. Narra, C.-Y. Wang, V. Kattoor, C.-C. Chung and E. W.-G. Diau, *Advanced Energy Materials*, 2018, **8**, n/a-n/a.
304. J. Qiu, Y. Qiu, K. Yan, M. Zhong, C. Mu, H. Yan and S. Yang, *Nanoscale*, 2013, **5**, 3245-3248.
305. V. V. Pavlishchuk and A. W. Addison, *Inorganica Chimica Acta*, 2000, **298**, 97-102.
306. R. R. Gagne, C. A. Koval and G. C. Lisensky, *Inorganic Chemistry*, 1980, **19**, 2854-2855.
307. M. Grätzel, *Nature*, 2001, **414**, 338-344.
308. J. Jean, M. Woodhouse and V. Bulović, *Joule*, 2019, DOI: https://doi.org/10.1016/j.joule.2019.08.012.
309. M. Saliba, M. Stolterfoht, C. M. Wolff, D. Neher and A. Abate, *Joule*, 2018, **2**, 1019-1024.
310. H. J. Snaith, *Advanced Functional Materials*, 2010, **20**, 13-19.

10 ANNEXE I

10.1 ORIGINAL CONTRIBUTIONS

10.1.1 First and Co-First Authored Publications:

Presented in this thesis

1. **D. Benetti**[+], E. Jokar[+], C. Yu, A. Fathi, H. Zhao, A. Vomiero, E. W. Diau, F. Rosei "Hole-extraction and photostability enhancement in highly efficient inverted perovskite solar cells through carbon dot-based hybrid material". *Nano Energy*, **2019**, 62, 781–790

2. **D. Benetti**, D. Cui, H. Zhao, F. Rosei, A. Vomiero "Direct Measurement of Electronic Band Structure in Single Quantum Dots of Metal Chalcogenide Composites". *Small* **2018**, 14 (51), 1801668 **(VIP, Front Cover)**

3. F. Navarro Pardo[+], **D. Benetti**[+], H. Zhao, V.M Castano, A. Vomiero, F.Rosei. "Platinum/Palladium hollow nanofibers as high-efficiency counter electrodes for enhanced charge transfer", *Journal of Power Sources*, **2016,** 355, 138-145.

4. **D. Benetti**[+], K. T. Dembele[+], J. Benavides, H. Zhao, S. G. Cloutier, I. Concina, A. Vomiero, F. Rosei. "Functionalized multi-wall carbon nanotubes/TiO_2 composites as efficient photoanodes for dye sensitized solar cells". *Journal of Materials Chemistry C,* **2016,** 4, 3555.

Not presented in this thesis

5. **D Benetti**, F Rosei, "A bridge for charge carriers", *Nature Energy*, **2019**, 4 (11), 910-911 (News & Views)

6. **D. Benetti**, R. Nouar, R. Nechache, H. Pepin, A. Sarkissian, F. Rosei, J. MacLeod. "Combined magnetron sputtering and pulsed laser deposition of TiO2 and BFCO thin films". *Scientific Reports*, **2017**, 7: 2503.

10.1.2 Co-Authored Publications

During my PhD I could collaborate and work on different projects, such as DSSC, QDSC, multiferroic materials, photoelectrochemical cells for hydrogen production (PEC) and Luminescent Solar Concentrators (LSC). Here are listed, divided per typology the publication I have co-authored. At the same time I also started to supervise some students.

Supervision of Students, Co-Corresponding Authors (*)

1. L. Shi, **D. Benetti***, F. Li, Q. Wei*, F. Rosei*. "Phase-junction design of MOF-derived TiO_2 photoanodes sensitized with quantum dots for efficient hydrogen generation" Applied Catalysis B: Environmental, **2020,** 263: 118317

2. X. Liu, B. Luo, J. Liu, D. Jing, **D. Benetti***, F. Rosei*. "Eco-friendly quantum dots for liquid luminescent solar concentrators" (under review), *Journal of Material Chemistry A*

3. Y. Zhou, X. Tong, **D. Benetti***, Z. M. Wang, D. Ma, H Zhao*, F. Rosei,* "Electron transfer in semiconductor heterostructure interface through electrophoretic deposition and linker-assisted method" (under review) *CrystEngComm*

Works on LSC

4. Y. Zhou, **D. Benetti**, X. Tong, L. Jin, Z.M. Wang, D. Ma, H. Zhao, F. Rosei. "Colloidal carbon dots based highly stable luminescent solar concentrators". *Nano Energy,* **2018,** 44, 378-387

5. H. Zhao, **D. Benetti**, X. Tong, H. Zhang, Y. Zhou, G. Liu, D. Ma, S. Sun, Z. M. Wang, Y. Wang, F. Rosei. " Efficient and stable tandem luminescent solar concentrators based on carbon dots and perovskite quantum dots". *Nano Energy* **2018**, 50, 756-765

6. H. Zhao, Y. Zhou, **D. Benetti**, D. Ma, F. Rosei. " Perovskite Quantum Dots integrated in Large-area Luminescent Solar Concentrators" *Nano Energy*, **2017**, 37, 214-223

7. L. Tan, Y. Zhou, F. Ren, **D. Benetti**, F. Yang, H. Zhao, F. Rosei, M. Chaker, D. Ma. " Ultrasmall PbS quantum dots: a facile and greener synthetic route and their high performance in luminescent solar concentrators", *Journal of Materials Chemistry A,* **2017***,* 5 (21), 10250-10260

8. H.Zhao, **D. Benetti**, L.Jin, Y. Zhou, F.Rosei, A. Vomiero, "Absorption Enhancement in "Giant" Core/Alloyed-Shell Quantum Dots for Luminescent Solar Concentrator". *Small*, **2016,** 12 (38), 5354-5365 (**Back cover)**

9. Y. Zhou, **D. Benetti**, Z. Fan, H. Zhao, D. Ma, A.O Govorov, A Vomiero, F. Rosei. "Near Infrared, Highly Efficient Luminescent Solar Concentrators". *Advance Energy Materials*, **2016**, 6, 11 **(Frontispiece)**

Works on QDs-PEC for hydrogen production

10. R. Akilimali, G. S. Selopal, **D. Benetti**, M. Mohammadnezhad, H. Zhao, Z. M. Wang, B. Stansfield, F. Rosei. "Graphene nanoribbon-TiO2-quantum dots hybrid photoanode to boost the performance of photoelectrochemical for hydrogen generation". *Catalysis Today*, **2019**

11. F. Navarro-Pardo, L. Jin, R Adhikari, X. Tong, **D. Benetti**, K Basu, S Vanka, HG Zhao, ZT Mi, SH Sun, VM Castano, A. Vomiero, F. Rosei " Nanofiber-supported CuS nanoplatelets as high efficiency counter electrodes for quantum dot-based photoelectrochemical hydrogen production". *Materials Chemistry Frontiers*, **2017**,1 (1), 65-72

12. F. Navarro-Pardo, L. Jin, R Adhikari, X. Tong, **D. Benetti**, K Basu, S Vanka, HG Zhao, ZT Mi, SH Sun, VM Castano, A. Vomiero, F. Rosei " Nanofiber-supported CuS nanoplatelets as high efficiency counter electrodes for quantum dot-based photoelectrochemical hydrogen production". *Materials Chemistry Frontiers*, **2017**,1 (1), 65-72

13. R. Adhikari, L. Jin, F. Navarro-Pardo, **D. Benetti**, B. AlOtaibi, S. Vanka, H. Zhao, Z. Mi, A. Vomiero, F.Rosei. " High efficiency, Pt-free photoelectrochemical cells for solar hydrogen generation based on "giant" quantum dots", *Nano Energy*, **2016,** 27, 265-274

14. L. Jin, B. AlOtaibi, **D. Benetti**, S. Li, H. Zhao, Z. Mi, A. Vomiero, F. Rosei. "Near-Infrared Colloidal Quantum Dots for Efficient and Durable Photoelectrochemical Solar-Driven Hydrogen Production". *Advance Science*, **2016**, 3, 1500345. **(Back Cover)**

Works on DSSC

15. G. S. Selopal, R. Chahine, M. Mohammadnezhad, F. Navarro-Pardo, **D. Benetti**, H. Zhao, Z. M Wang, F. Rosei "Highly efficient and stable spray assisted nanostructured Cu2S/Carbon paper counter electrode for quantum dots sensitized solar cells" *Journal of Power Sources*, **2019**, 436: 226849.

16. R. Akilimali, G. S. Selopal, **D. Benetti**, I. Serrano-Esparza, P. A Algarabel, J. M. De Teresa, Z. M. Wang, B. Stansfield, H. Zhao, F. Rosei. "Hybrid TiO2-Graphene nanoribbon photoanodes to improve the photoconversion efficiency of dye sensitized solar cells". *Journal of Power Sources,* **2018**, 396, 566-573

17. F. Navarro-Pardo, **D. Benetti**, J Benavides, H.G. Zhao, S.G. Cloutier, VM Castano, A. Vomiero, F. Rosei "Nanofiber-structured TiO2 nanocrystals as a scattering layer in dye-sensitized solar cells". *ECS Journal of Solid State Science and Technology*, **2017**, 6 (4), N32-N37

18. K. Basu, **D. Benetti**, H. Zhao, L. Jin, F. Vetrone, A. Vomiero, F. Rosei. "Enhanced photovoltaic properties in dye sensitized solar cells by surface treatment of SnO_2 photoanodes". *Scientific Reports*, **2016**, 6, 23312.

19. K.T. Dembele, G.S. Selopal, R. Milan, C. Trudeau, **D. Benetti**, A. Soudi, M.M. Natile, G. Sberveglieri, S.G. Cloutier, I. Concinca, F. Rosei, A. Vomiero. "Graphene below the percolation

threshold in TiO_2 for dye-sensitized solar cells". *Journal of Materials Chemistry A,* **2015**, 3, 2580-2588. **(Back Cover)**

Works on QDSC

20. G. S. Selopal, H. Zhao, X. Tong, **D. Benetti**, F. Navarro-Pardo, Y. Zhou, D. Barba, F. Vidal, Z. M. Wang, F. Rosei. "Highly Stable Colloidal "Giant" Quantum Dots Sensitized Solar Cells". *Advanced Functional Materials*, **2017**, 27 (30), 1701468

21. H. Zhang, G. S. Selopal, Y. Zhou, X. Tong, **D. Benetti**, L. Jin, F. Navarro-Pardo, Z. Wang, S. Sun, H. Zhao, F. Rosei. "Controlled synthesis of near-infrared quantum dots for optoelectronic devices". *Nanoscale*, **2017**, 9(43), 16843-16851

Works on Multiferroic perovskite oxide and organic-inorganic perovskite

22. W. Huang, C. Harnagea, X. Tong, **D. Benetti**, Sh. Sun, M. Chaker, F. Rosei, R. Nechache "Epitaxial Bi_2FeCrO_6 Multiferroic Thin-Film Photoanodes with Ultrathin p-Type NiO Layers for Improved Solar Water Oxidation". *ACS applied materials & interfaces*, **2019**, *11*(14), 13185-13193

23. D. Gedamu, I.M. Asuo, **D.Benetti**, M. Basti, I Ka, S.G. Cloutier, F. Rosei, R. Nechache. "Solvent-antisolvent ambient processed large grain size perovskite thin films for high-performance solar cells". *Scientific reports*, **2018**, 8 (1), 12885

24. J. Chakrabartty, D. Barba, L. Jin, **D. Benetti**, F. Rosei, R. Nechache "Photoelectrochemical properties of $BiMnO_3$ thin films and nanostructures", **2017**, *Journal of Power Sources* 365, 162-168

25. W. Huang, C. Harnagea, **D. Benetti**, M. Chaker, F. Rosei, R. Nechache. "Multiferroic Bi 2 FeCrO 6 based pin Heterojunction Photovoltaic devices". *Journal of Materials Chemistry A,* **2017**,5 (21), 10355-10364

10.1.3 Patents

1. *Luminescent solar concentrator using a metal-free emitter*
   Application number: WO2018CA50176 20180216

2. *Thin film coating and method of fabrication thereof*
   Application Number: U.S. Patent Application No 15/840,407

11 ANNEXE II

Table 11.1 Photovoltaic parameters of inverted planar heterojunction perovskite solar cells fabricated with GO as HTL under simulated AM-1.5G illumination (power density 100 mW cm^{-2}) with active area 0.0225 cm2.

Cell NO.	*J*sc /mAcm^{-2}	*V*oc / V	FF	PCE /%
1	18.7	0.881	0.763	12.6
2	18.1	0.882	0.771	12.3
3	18.2	0.878	0.778	12.4
4	18.7	0.891	0.787	13.1
5	18.5	0.913	0.765	12.9
6	19.5	0.904	0.781	13.8
7	19.55	0.905	0.784	13.9
8	18.9	0.939	0.764	13.5
9	19.05	0.913	0.780	13.6
19	19.25	0.914	0.772	13.6
11	19.6	0.934	0.764	14.0
12	18.9	0.931	0.762	13.4
13	18.3	0.932	0.771	13.2
14	17.8	0.933	0.779	13.0
15	17.2	0.934	0.787	12.7
16	19.9	0.976	0.727	14.1
17	20.9	0.932	0.725	14.1
18	20.0	0.935	0.787	14.7
19	17.8	0.916	0.772	12.6
20	20.0	0.935	0.787	14.7
Average	18.9±0.9	0.919±0.024	0.770±0.017	13.4±0.7

Table 11.2 Photovoltaic parameters of inverted planar heterojunction perovskite solar cells fabricated with GO/Cdots 0.025 as HTL under simulated AM-1.5G illumination (power density 100 mW cm^{-2}) with active area 0.0225 cm^2.

Cell NO.	*J*sc /mAcm^{-2}	*V*oc /V	FF	PCE /%
1	20.6	0.990	0.715	14.58
2	20.3	0.993	0.773	15.57
3	21.1	0.946	0.745	14.88
4	21.5	0.928	0.763	15.24
5	20.0	0.943	0.664	12.55
6	19.9	0.950	0.760	14.36
7	20.0	0.947	0.801	15.14
8	20.2	0.923	0.744	13.9
9	20.0	0.947	0.799	15.12
19	19.4	0.946	0.750	13.76
11	19.7	0.949	0.751	14.07
12	20.3	0.929	0.747	14.09
13	19.05	0.926	0.766	13.53
14	19.95	0.937	0.755	14.11
15	19.2	0.952	0.744	13.63
16	19.4	0.909	0.764	13.47
17	20.1	0.947	0.737	14.02
18	19.7	0.950	0.7715	14.41
19	20.5	0.865	0.822	14.55
20	20.6	0.963	0.756	15
Average	20.1±0.6	0.942±0.027	0.756±0.032	14.3±0.7

Table 11.3 Photovoltaic parameters of inverted planar heterojunction perovskite solar cells fabricated with GO/Cdots 0.05 as HTL under simulated AM-1.5G illumination (power density 100 mW cm^{-2}) with active area 0.0225 cm^2.

Cell NO.	*J*sc /mAcm^{-2}	*V*oc /V	FF	PCE /%
1	19.891	0.97	78.2	15.09
2	20.498	0.93	78.99	15.05
3	20.668	0.947	81.06	15.86
4	21.022	0.953	80.99	16.23
5	20.238	0.905	78.35	14.35
6	20.362	0.947	79.12	15.26
7	20.761	0.934	80.08	15.53
8	19.567	0.937	79.64	14.6
9	20.314	0.962	77.56	15.15
19	19.344	0.949	78.25	14.37
11	18.708	0.954	75.84	13.54
12	19.825	0.941	81.07	15.12
13	19.918	0.948	75.56	14.27
14	20.529	0.943	78.24	15.15
15	21.872	0.933	78.04	15.92
16	21.8	0.938	75.03	15.42
17	19.669	0.911	76.79	13.75
18	20.147	0.926	78.32	14.6
19	19.929	0.954	76.23	14.5
20	20.456	0.935	78.66	15.05
Average	20.3±0.75	0.941±0.016	0.783±0.018	14.9±0.7

Table 11.4 Photovoltaic parameters of inverted planar heterojunction perovskite solar cells fabricated with GO/Cdots_0.1 as HTL under simulated AM-1.5G illumination (power density 100 mW cm^{-2}) with active area 0.0225 cm^2.

Cell NO.	*J*sc /mAcm^{-2}	*V*oc /V	FF	PCE /%
1	17.1	0.908	0.789	12.2
2	16.8	0.922	0.812	12.6
3	19.1	0.891	0.755	12.9
4	19.25	0.871	0.770	12.9
5	20.6	0.922	0.81	15.4
6	18.1	0.827	0.813	12.1
7	18.7	0.796	0.745	11.1
8	19.0	0.801	0.70	10.7
9	18.0	0.825	0.679	10.1
10	20.3	0.906	0.576	10.6
11	17.4	0.84	0.778	11.35
12	17.5	0.843	0.794	11.7
13	18.1	0.827	0.813	12.1
Average	18.44±1.75	0.860±0.045	0.756±0.069	12.0±0.1.35